Dynamics of CO$_2$ in coal as a reservoir

Proefschrift

Ter verkrijging van de graad van doctor
aan de Technische Universiteit Delft,
op gezag van de Rector Magnificus Prof. dr. ir. J.T. Fokkema,
voorzitter van het College voor Promoties,
in het openbaar te verdedigen op donderdag 29 maart 2007 te 15:00 uur

door

Saikat MAZUMDER

Master of Science and Technology in Applied Geology,
Indian School of Mines, Dhanbad, India
geboren te Durgapur, India

To my father, my mother and my wife

This thesis is based on the following articles:
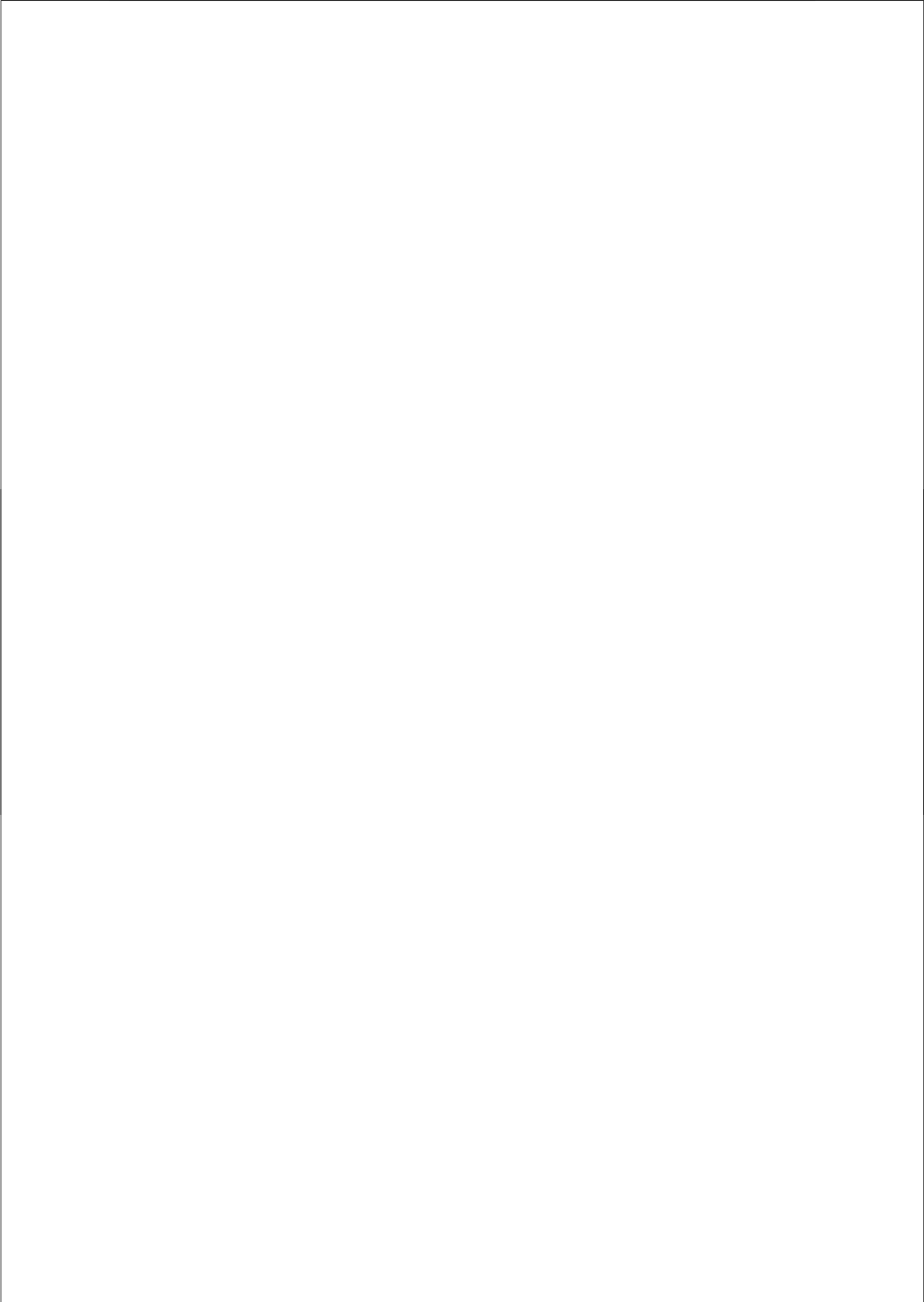
1. Mazumder, S., K-H. A. A Wolf and P. van Hemert,. "Laboratory experiments on environmental friendly means to improve coalbed methane production by carbon dioxide / flue gas injection" Accepted for "Transport in Porous Media", submitted February, 2006.

2. Shi, Ji-Quan, Mazumder, S., K-H. A. A Wolf., & Durucan, S., "Competitive Methane Desorption by Supercritical CO_2 Injection in Coal", Accepted for "Transport in Porous Media", submitted May, 2006.

3. Mazumder, S., K-H. A. A Wolf and P. van Hemert,. "CO_2 and Flue-Gas Coreflood Experiments for Enhanced Coalbed Methane" Accepted for "SPE Journal", submitted February, 2006.

4. Mazumder, S., R. Ephraim, K-H. A. A Wolf and Elewaut, K.,. "Application of X-Ray Computed Tomography for analysing cleat spacing and cleat aperture in coal samples", International Journal of Coal Geology 68, 205 - 222, 2006.

5. Mazumder, S., P. van Hemert, A. Busch, K-H. A. A Wolf and P Tejera Cuesta.,. "Flue gas and pure CO_2 sorption properties of coal: A comparative study", International Journal of Coal Geology 67, 267 - 279, 2005.

6. Mazumder, S., Siemons, N., and K-H. A. A Wolf.,. "Differential swelling and permeability change of coal in response to CO_2 injection for ECBM", Accepted for SPE Journal, SPE-98475-USMS, submitted June, 2005.

7. Willem-Jan Plug., Mazumder, S. & J. Bruining., "Capillary Pressure and Wettability Behavior of the Coal-Carbon Dioxide-Water System at High Pressures", Under review for SPE Journal. SPE-108161-USMS, submitted November, 2006.

8. Mazumder, S., Karnik, A., and K-H. A. A Wolf.,. "Swelling of Coal in Response to CO_2 Sequestration foe ECBM and its Effect on Fracture Permeability", SPE Journal, SPE-97754-RMS, September, 2006.

9. Mazumder, S., P. van Hemert, J. Bruining, K-H. A. A Wolf., & Drabe, K. "Insitu CO_2 - Coal reactions in view of carbon dioxide storage in deep unminable coal seams", Fuel 85, 1904 - 1912, 2006.

10. Mazumder, S., K.H.A.A. Wolf; "An overview of the potentials and prospects of coalbed methane exploration and exploitation in the permo-carboniferous coal measures of the Barakar Formation, the Jharia basin, India" Geologica Belgica, 7/3-4, 147 – 156, 2004.

Contents

1 Introduction

1.1 Background

The IEA's World Energy Outlook 2002 Reference Scenario shows that, according to the Organization for Economic Co-operation and Development (OECD), fossil fuel use and carbon emissions continue to increase through 2030 (IPCC Special report on Carbon Dioxide Capture and Storage, 2005). The World Energy Assessment, (2004) also includes an Alternative Policy Scenario that anticipates a levelling off and decline of OECD emissions as a result of additional energy policies. They are considered, however, not yet adopted. This levelling off of OECD emissions will not occur before 2025 (Fig. 1.1). In the meantime, carbon emissions from non-OECD countries will increase rapidly as compared to the present day rate of CO_2 emissions. Since atmospheric concentrations of green house gas emissions continue to increase, the "business-as-usual" emissions scenario results in greenhouse gas concentrations that may cause substantial climate changes. The policy actions for long-term changes cannot be delayed, if atmospheric concentrations are to be stabilized within the next 50 to 75 years.
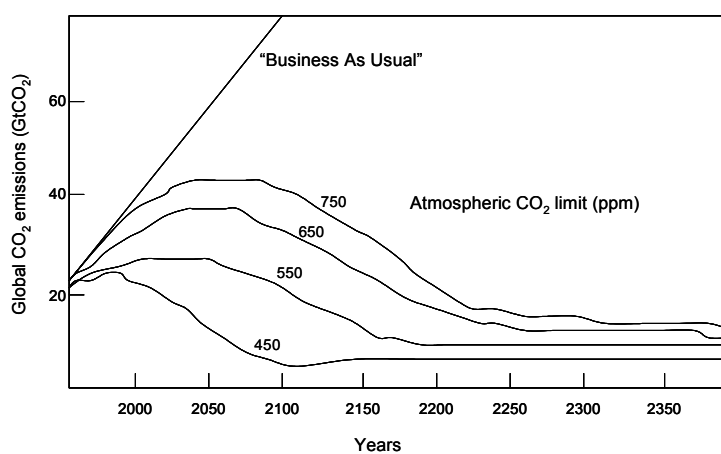
Fig. 1.1 Emissions Trajectory (Source: The Intergovernmental Panel on Climate Change)

An attempt to reduce Green House Gases (GHG) for the future generation is what nations are attempting, under the international treaty, "The Kyoto Protocol". Primarily there are three main ways to reduce CO_2 concentrations in the atmosphere:

(i) To promote energy efficiency in order to produce less CO_2 per unit of energy service (industrial, transportation and residential);

(ii)   De-carbonation of energy - development of technologies related to renewable sources or alternative energy;

(iii)   CO$_2$ capture and storage/sequestration.

CO$_2$ sequestration with available technologies is not economically feasible. The Kyoto protocol addresses this issue and solves the problem by means of carbon credits, technically known as the Clean Development Mechanism (CDM). CDM is one of the project-based flexible mechanisms, designed to make it easier and cheaper for industrialized countries to meet the greenhouse gas (GHG) emission reduction targets. CDM is also mandated to assist developing countries in achieving sustainable development. Under CDM, an industrialized country with a GHG reduction target can invest in a project in a developing country, without a target, and claim credit for the emissions that the project achieves. For example, an industrialized country may invest in a CO$_2$ sequestration project or in renewables in a developing country. The industrialized country then claims credit for the emissions that have been avoided, and uses these credits to meet its own target. For industrialized countries, this method reduces the cost for reduction commitments.

1.1.1   What is CO$_2$ capture and storage?

CO$_2$ capture and storage involves capturing the CO$_2$ from the combustion of fossil fuels, as in power generation, or from the preparation of fossil fuels, as in natural gas processing. It can also be applied to the combustion of biomass-based fuels and in certain industrial processes, such as the production of hydrogen, ammonia, iron and steel, or cement. Capturing CO$_2$ involves separation of the CO$_2$ from other gas mixtures. The CO$_2$ is transported to a site where it is stored, away from the atmosphere. In order to have a significant effect on atmospheric concentrations of CO$_2$, storage capacity needs to be large relative to annual emissions (40 GtCO$_2$/year).

The modern power plant in the west operates at high efficiencies and at relatively low costs. Use of CO$_2$ capture technology with such a plant would reduce CO$_2$ emissions by more than 80% whilst still providing reliable and relatively low cost power (IEA Greenhouse Gas R&D Programme). Solvent absorption technology has been used for many years in the oil industry to remove CO$_2$ from mixtures of gases. There are several installations where CO$_2$ is captured from the flue gases of power plants, to supply CO$_2$ to the food industry and other industrial users. This process is based on a reversible chemical reaction between CO$_2$ and a solvent, typically an amine compound. Thus the technology to "de-carbonize" electricity generation is already available. It could be done using either pre or post combustion techniques. The pre-combustion method is applied to the flue gas stream of any fossil fuel-fired power station and captures most of the CO$_2$ in the flue gas. However, due to the large amount of flue gases to be processed, the equipment will be very large in size. Such plants have a large demand for steam, reducing the overall generation efficiency. Costs of capturing CO$_2$ on such a scale would be more expensive than the cost of storage. Developments in post-combustion capture

of CO$_2$ are focused on cost reduction by improved energy efficiency, better liquid-gas contacting and improved solvents. Two recent developments are the use of sterically hindered amine solvents, and a combination of membrane technology and solvent absorption (IEA Greenhouse Gas R&D Programme, 2004).

1.1.2 Geological storage of CO$_2$ in unminable coal seams

CO$_2$ produced by major sources, such as power plants, fertilizer plants etc., can be captured and stored underground. The IEA Greenhouse Gas R&D Programme estimated the global potential for CO$_2$ storage (Table 1.1). The most stable mode of storing CO$_2$ is in unminable coal seams. In nature, coal seams contain gases such as methane, held in pores on the surface of the coal and in fractures in the seams. When CO$_2$ is injected into a coal seam, it displaces the methane, which can be recovered. The CO$_2$ remains stored in the seam, provided that the coal is never mined. In addition, the sale of the methane helps to reduce the cost of injecting the CO$_2$. Undisturbed coal seams contain up to 25 cubic meters of methane per ton of coal. The coal suitable for CBM and ECBM operations lie between 300 and 1500m below the surface and measure a proved capacity of over 4000 billion tons (IEA Special Report on Carbon Dioxide Capture and Storage, 2005). Typically 50% of the methane in the coal can be recovered using standard techniques (Rice, 1997). The methane often has a high purity (>90% by volume) and can be supplied directly to a natural gas distribution system or used for power generation or heating.

The replacement process, known as CO$_2$-enhanced coalbed methane production (CO$_2$-ECBM), providing a potential underground storage facility, as the CO$_2$ remains stored within the seam. Laboratory measurements prove that twice as much CO$_2$ can be stored in coal as methane desorbs. Early indications from actual applications suggest this ratio might be even higher (Reeves et al., 2001). This technique is capable of recovering 90% or more of the methane in the coal seam.

For an enhanced recovery project, the operating income from increased methane production compensates part of the additional costs associated with CO$_2$ separation and injection (IEA Special Report on Carbon Dioxide Capture and Storage, 2005). Far more CO$_2$ (perhaps 20 to 50 times as much) can be stored in less favourable coal basins, but costs will be higher. A key factor determining the attractiveness of a particular site is the permeability of the coal and its proximity to the source of CO$_2$. The cost of capturing CO$_2$, transporting for 300 km and storing it has been estimated to be between $30-50/tonne CO$_2$ (Reeves et al., 2004).

Two main advantages of CO_2 storage in coal above other options are:

(i)   Injected CO_2 replaces adsorbed CH_4 at the internal coal surface and absorbs firmly to the coal at near liquid density. Since the process of gas adsorption has proven its stability through geological time periods, the chances of CO_2 release from coal over the period of the next 10000 years are minimized,

(ii)   Both laboratory experiments and field tests show that for two sequestered CO_2 molecules, one CH_4 molecule can be produced.

1.2   Problem statement

Although the experience gained by the oil industry represents a starting point, several problems are to be studied and solved before CO_2-ECBM production is feasible, e.g.

(i)   what are the conditions under which the fluid in the micro-pores of the coal, in the presence of competitive adsorption, is displaced by the CO_2;

(ii)   what is the efficiency of the sequestration in relation to swelling and shrinkage characteristics of coal;

(iii)   how does mobile and immobile water in coal affect the exchange process;

(iv)   how do the wetting properties of coal affect the adsorption rate;

Worldwide capacity of potential CO_2 storage sites	
Sequestration option	Worldwide capacity
Ocean	1000^s GtC
Deep Saline Formations	$100^s – 1000^s$ GtC
Depleted Oil and Gas Reservoirs	100^s GtC
Coal Seams	$10^s – 100^s$ GtC
Terrestrial Ecosystems	10^s GtC
Utilization	< 1 GtC / yr
1 GtC = 1 billion metric tons	

Table 1.1 The global potential for CO_2 storage (Source: IEA Greenhouse Gas R&D Programme, 2004)

(v)   how does swelling of coal as a result of the viscoelastic relaxation of the macro molecular network structure of coal, affect the diffusion process;

(vi)   what is the effect of swelling on cleat aperture and by that on porosity and permeability of coal.

These questions are partly answered by laboratory experiments, which are capable of measuring some of the related coupled process of multiphase flow, competitive sorption, geo-mechanics and wetting properties of coal towards water, CH_4 and supercritical CO_2.

1.3 Motivation, Objective and Thesis outline

This thesis deals with three practical aspects related to enhanced coalbed methane recovery. These aspects are (i) the permeability history in the coal during the methane recovery process alongside the injection of CO_2, (ii) the effect of flue gas as an alternative injectant, and the overall efficiency of the coal to separate CO_2 from other gases and to produce methane. There is a need of additional thorough experimental and theoretical work on these issues.

It is the objective of this thesis to provide additional quantitative experimental data and theoretical insight interrelating to these three aspects. In addition we want to clarify the relevance of some ensuing fundamental aspects that can help to improve the operational feasibility of CO_2 enhanced recovery of coalbed methane.

Therefore the research was divided into two programs. First program relates to the permeability issue. The structure of the coal and its relation to the variety of permeability is described in Chapter 2. Chapter 4 gives the theoretical background to swelling. As a spin-off of this research also stress induced diffusion is modelled. Chapter 5 describes swelling measurements related to the absolute effect of CO_2 sorption. Chapter 6 describes the differential swelling measurements related to the incremental strain due to CO_2 sorption over CH_4 on a unit concentration basis. Secondly we deal with the option of flue gas injection. Chapter 3 describes experiments related to sorption capacity of flue gas in comparison of CO_2. For the first time the density of flue gas in the relevant pressure and temperature range was measured. Chapter 7 shows the data obtained from the flooding experiments and the interpretation of the data in terms of a dual porosity model. Here the main components of flue gas, i.e., CO_2 and N_2 are compared. Each chapter involves a specific experimental and/or theoretical issue and carries its own conclusions.

A schematic of thesis outline is shown in Fig. 1.2, and contributes to the following objectives:

Swelling / shrinkage and coal characterization	Characterization and up scaling of the natural fracture system of coal	Gas & water transport processes in coal

Investigation of the basic scientific phenomena of CO_2 injection and retention in coal towards the development of a CO_2- ECBM recovery and CO_2 sequestration simulator

Wetting properties of coal, CO_2 – coal – water	Two phase flow experiments under simulated reservoir conditions	Anomalous diffusion in coal

Fig. 1.2 A summary of the research methodology for achieving the overall objective of this work

The outline of the research described in this thesis touches upon the aspects, described below. The cleat network as showed in Fig. 1.3 plays an important role in the production of methane from coal beds. They are the principal contributors to permeability for fluid flow. Coalbeds have two major fracture systems called face cleats and butt cleats. Key cleat properties include size, spacing, connectivity, aperture, degree of mineral filling and orientation both on a seam scale (mm-m) and regional scale (km). Chapter 2 deals with two different techniques to measure cleat spacing and cleat aperture by using X-ray computed tomography (Mazumder et al., 2006).

In the context of geological storage of CO$_2$, as an alternative, the direct injection of flue gases can be considered. This improves the cost-effectiveness of the projects by eliminating separation costs in comparison to pure CO$_2$. Sorption behaviour of flue gas lacks the attention. Little experimental data is available on the density of flue gas. The different existing mixed gas equations of state (EOS) published for CH$_4$/ CO$_2$, or components associated with flue gas, are inconsistent and are difficult to apply. Chapter 3 shows a method to experimentally determine the density of flue gas under isothermal conditions and varying pressures. This has been published in the "International Journal of Coal Geology", vol. 67, 2005 (Mazumder et al., 2005).

The swelling of coal by a penetrant is described as an increase in the volume occupied by the coal as a result of the viscoelastic relaxation of its highly cross-linked macromolecular structure. The similarities in structure between coal and glassy polymers led to the perception that CO$_2$ sorption in coal has many analogous features that are observed for organic sorbents penetrating into glassy polymers (Mazumder et. al., 2006). The diffusion in glassy polymers often does not fit the Fickian diffusion model. Hence a second limiting case is under consideration, where the rate of transport is controlled by molecular relaxation. This diffusion process is strongly coupled to the mechanical response of coal. A mechanistic model is proposed and an implicit numerical solution to the model is presented in Chapter 4.

Volumetric swelling associated with CO$_2$ sorption on coal has a significant influence on the fracture porosity and permeability under constrained reservoir conditions. Cleat permeability of coal is the most important parameter for methane production. Sorption induced coal swelling decreases the permeability of the coal and the volume increase is compensated by a reduction in the secondary porosity. This detrimental effect of matrix swelling on cleat permeability is quantified and relations between concentration, strain, pressure and permeability are characterized in the Chapters 5 and 6. This has been published in SPE Journal, 2006 (SPE 97754).

The effect of mobile and immobile water in the exchange process of CO$_2$ and CH$_4$ are presented as core flood experiments in Chapter 7. These experiments were performed under simulated reservoir conditions, with different water saturations and injection rates. This has been accepted for publication in "Transport in Porous Media" (Mazumder et al., 2006 and Shi et

al., 2006). The experiments exhibit the processes occurring in a transition zone, where CO$_2$ is injected in coal.

It can be expected that CO$_2$-ECBM is a slow process unless operated at pressures such that the coal becomes CO$_2$ wet (Plug et al., 2006). In water wet coal, the micro-fracture system is filled with water. The kinetics of CO$_2$ adsorption and CH$_4$ desorption is determined by the speed of diffusion in the water filled fractures and coal. However, capillary diffusion is two or three orders of magnitude faster and fills the small fractures proportionally faster for CO$_2$ wet conditions (Mazumder et.al., 2005). Wettability experiments with CO$_2$-coal-water have been conducted under high pressure and temperature conditions. This work was done in cooperation with Willem-Jan Plug and is explained in combined papers (Mazumder et.al., 2003) and his thesis work.

The list of the output of different projects is provided in the bibliography.
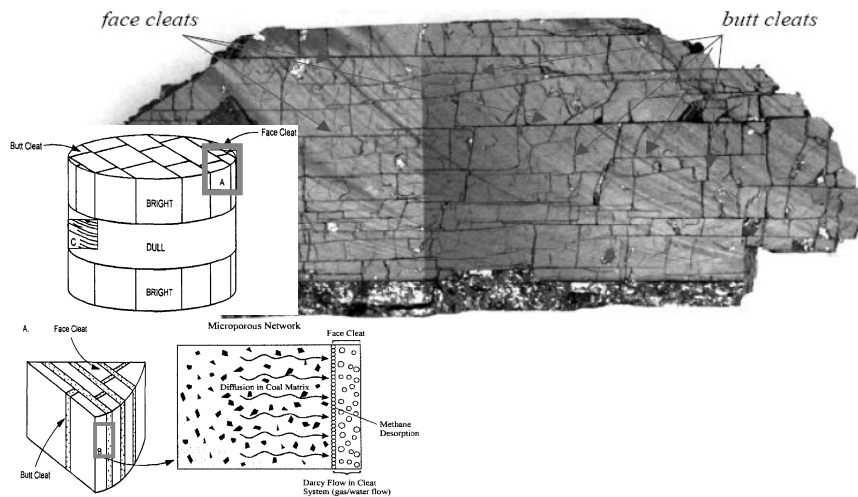
Fig. 1.3 Planar and 3D representation of the coal cleat system. Two orthogonal cleat system is shown. Methane sorbs out of the coal matrix by the process of diffusion and then flows in the open fracture system along with water to the wellbore. (revised after De Haan, 1998 and Law et. al., 1993)

2 Application of X-ray computed tomography for analyzing cleat angle, spacing and aperture

2.1 Introduction

The cleat network of coal plays an important role in the production of methane from coalbeds. Micropores are responsible for most of the porosity in coal, the cleats provide the principal source of permeability for fluid flow. Coal beds usually have two major orthogonal joint systems called face cleats and butt cleats. The key cleat characteristics include height, spacing, connectedness, aperture, degree of mineral filling, and patterns of preferred orientation on sample and km scale (Close et al., 1991). These values provide flow parameters for coal reservoir models. The dominant flow direction is related to the existing cleat system and is controlled by the Darcy permeability. Few data is available on the aperture, height, length, and connectivity of cleats. Bertheux, 2000, and Wolf et al., 2004, determined cleat angle distributions in coal seams by using image analysis techniques. With coal particles and cuttings, cleat angle distribution was analyzed for face cleats, butt cleats and bedding planes. In addition a first attempt was made to determine cleat spacing distribution, based on differences in fracture behaviour of the macerals and ash. However, applied to cuttings, which are affected by transport, only angle distribution can be reconstructed.

Cleat spacing is maceral type and ash content dependent and is in the order of millimeters to centimeters. Many fracture sizes are present in coal cores, but core observations rarely distinguish the hierarchy of fracture sizes. Recognizing the range of cleat sizes present in coal, it is only meaningful when cleat size is included in an analysis.

Contrasts in coalbed methane well production also may reflect variable development of cleats. Variability in spacing (or intensity of fracture development) of cleats in coal beds has been recognized by Kendall and Briggs, 1933. Cleat spacing varies with coal rank, decreasing from lignite through medium volatile bituminous coal (Ammosov et al., 1963, Ting et al., 1977 and Law, 1993) and increasing through the anthracite range, forming a bell shaped distribution of cleat spacing. Based on outcrop and core data from North American coal, Law, 1993 found that face cleat spacing ranges from approximately 22 cm in lignites (% Rr 0.25 - 0.38%) to 0.2 cm in anthracites (% Rr greater than 2.6%). Many authors have noted that cleat spacing varies with coal type and ash content (Tremain et al., 1991 and Law, 1993). Bright coal lithotypes (vitrain) generally have smaller cleat spacings than dull coal lithotypes (durain) (Kendall et al.,1933 and Stach, 1982). Most of these correlations are very qualitative and basin specific. Coals with low ash content tend to have smaller cleat spacings than those with high ash contents (Laubach et al., 1998). The average cleat spacing is linearly proportional to coal lithotype layer thickness (Tremain et al., 1991, Close et al., 1991 and Law, 1993). This study avoids the limitation of hierarchy of fracture sizes based on coal petrology, and proposes a

technique to measure and compare cleat spacing distributions from Computer Tomography (CT) scan images of coal blocks. Since the accuracy of cleat determination from CT-images depends on the pixel size, images have to be enhanced to obtain the smallest cleats possible. Fractures are recognized by either change in the CT-number (attenuation coefficient) and/or low number grey values, which can be followed in a certain direction.

Cleat aperture width under in situ conditions is important for the cleat geometry and permeability, but the collection of aperture data under stressed conditions is difficult to determine because of the low resolution of the scanned images. However, cleat aperture data under stress free conditions are available and is of importance for spatial analysis. For example, face cleat aperture measurements of six relaxed Fruitland coal cores from the northern San Juan basin vary in range from 0.01 mm to 0.30 mm (Close et al., 1991). Cleat aperture widths under in situ confining pressure probably vary from less than 0.05 mm to less than 0.0001 mm. We used non-destructive CT-scanning technique to obtain cleat aperture distribution from a Polish and an English coal cores under unstressed conditions. Karacan et al., 2000 did a similar study to understand the cleat aperture distributions for some Turkish coal samples.

In this chapter alternative methods are introduced to determine cleat aperture, cleat orientation and cleat spacing distribution with CT-scans.

2.2   Sample details

The samples used for cleat spacing measurements were from a French Lorraine coal mine (France 495) and from the Upper Silezia mine in Poland (Brzeszcze LW 405). Both samples were blocks of coal and were scanned as obtained. The Brzeszcze LW 405 was one of the target seams for CO_2 injection, as part of the "RECOPOL" project. It has a vitrinite reflectance of 0.74%. The Brzeszcze mine is situated in the southeastern part of the Upper Silesian Coal Basin. This coal seam is of Carboniferous-Westphalian age.

Of the two coal core samples used for cleat aperture measurement, one was from the Silezia mine in the Upper Silesian Basin in Poland (Silesia 315). The coal was obtained as an in-situ sample from a depth of 900 m. The coal seam was also selected for CO_2 injection in the RECOPOL project. It is a high volatile bituminous coal from Carboniferous- Westphalian with a vitrinite reflectance of 0.68%. A cylindrical core of 7 cm in diameter and 25 cm in length was drilled out of the block. The other coal core (Tupton) used for this purpose has similar dimensions and was obtained from the Nottinghamshire and North Derbyshire coal mines in UK. The Tupton sample is of Carboniferous- Westphalian A age. It has a vitrinite reflectance of 0.53%. The sample details are listed in Table 2.1.

Samples	VR₀ max (%)	Liptinite (%)	Vitrinite (%)	Inert. (%)	Moisture Cont. (%)	Ash (%)	Mineral Matter (%)	Volatile Matter (%)	Density (%)	TOC (%)
Brzeszcze 405	0.75	8.0	39.0	53.0	1.85	4.57	4.98	34.17	1.33	68.80
Silesia 155-315	0.68	7.0	70.0	24.0	7.00	20.05	21.85	40.13	1.38	60.73
Tupton	0.53	14.0	59.4	25.8		2.05	0.8	36.15		73.01

Table 2.1 Sample details

2.3   Data acquisition and processing procedure

When a CT-scanner is operated, X-rays penetrate a thin volumetric slice of an object at different angles, as the X-ray source rotates around the object. A series of detectors then records the transmitted X-ray intensity. Thus, many different X-ray attenuations are made available for mathematical reconstruction and image enhancement. The basic quantity measured in each volume element (voxel) of a CT image is the linear attenuation coefficient, μ, which is defined as:

$$\mu[cm^{-1}] = \left(\frac{1}{L}\right)\ln\left(\frac{I}{I_0}\right), \qquad (2.1)$$

where L is the path length in cm, I_0 is the incident X-ray intensity and I is the transmitted intensity or the intensity remaining after the X-ray passes through a thickness of homogeneous sample. Measurement of the attenuation of multiple ray projections provides the data to solve multiple equations for the attenuation coefficient. Images are usually reconstructed with a filtered back propagation method. The method projects a uniform value of attenuation over each ray path so that the calculated value is proportional to the measured attenuation. Each matrix element receives a contribution from each ray passing through it. Images obtained are blurred, partly because of the assumption that attenuation is uniform over the entire length of the ray. Hence, a convolution or filtering process is used to modify the ray sum data, which improve images.

After image reconstruction, values of linear attenuation coefficient are known for each pixel. The computer converts attenuation coefficients into corresponding numerical values, or CT numbers, by normalizing them with the attenuation coefficient of water, μ_w,

$$CT_N = K\left(\frac{\mu - \mu_w}{\mu_w}\right), \qquad (2.2)$$

where K is a constant equal to 1000, μ is the linear attenuation coefficient of the material in the pixel where the CT number is measured. μ_w is the linear attenuation coefficient of water. The units of Eq. 2.2 are Hounsfield (H) units, where each Hounsfield unit is 0.1% change in density with respect to calibration density scale.

Measurements with X-ray CT are subject to a variety of errors and image artifacts including beam hardening, X-artifacts, positioning errors, and machine errors. The majority of the CT scanners are developed for medical purposes and were originally intended for qualitative imaging and not for quantitative analysis. The X-ray source delivers a polychromatic spectrum of X-ray energies rather than monochromatic energy. The lower energy, (soft, portion) are absorbed preferentially at the air / sample interface but also in the sample. Through the sample X-ray spectrum attenuates towards the lower energy part of the spectrum. An open fracture, which is presumably filled with air, shows this effect along the edges of the fracture in the spatial resolution of the reconstructed image. This will be seen as a distinct contrast in the grey tone of the image along the fracture edges. This effect has a major limitation to our study.

2.3.1 Cleat orientation and cleat spacing distribution from CT scans

For cleat spacing and orientation measurements, CT scan images were produced by the Institute Francais du Petrol in Paris. Using a General Electric, SX/I high-speed sequential CT scanner, the images were made as sequential scans in RAW and JPEG format at a resolution of 512 x 512 pixels with 256 grey levels. Each pixel in the XY plane represents an area of 0.7 x 0.7 mm. The distance between two images in the scan direction was 1 mm. The images were enhanced in order to increase the contrast between matrix, fracture and mineral filled fracture. This enhancement provides a better discrimination of increased artifacts, like scattered noise and a diagonal linear pattern (Keller, 1998).

A set of images from a CT scan session is called an image stack. The section plane is the XY plane and the scan direction is the Z axis. For viewing and for extracting 3D information from the image stacks, 3D visualization and modeling software Amira™ was used. Image stacks in the orthogonal YZ and XZ directions were generated, saved as JPG images, providing a complete set of images in the orthogonal directions (Fig. 2.1a). QWIN™, image analysis software was used to correct for linear pattern and for the beam hardening effects, which were induced by "high density" bright spots in the sample. In each image the cleat spacing, coal matrix and mineral matter were separated by grey tones. Then, each image was processed in order to suppress details that were not contributing to the required information, i.e. lines and spots. Thereafter the resulting binary images for cleats, mineral matter and matrix were used for measurements. The flowchart showing the scheme to process the CT scans is shown in Fig. 2.1b.

The mentioned artifacts introduced two difficulties:

(i) Incomplete cleat detection, and

(ii) Scattered vesicles, detected as cleats but with a high ambiguity.
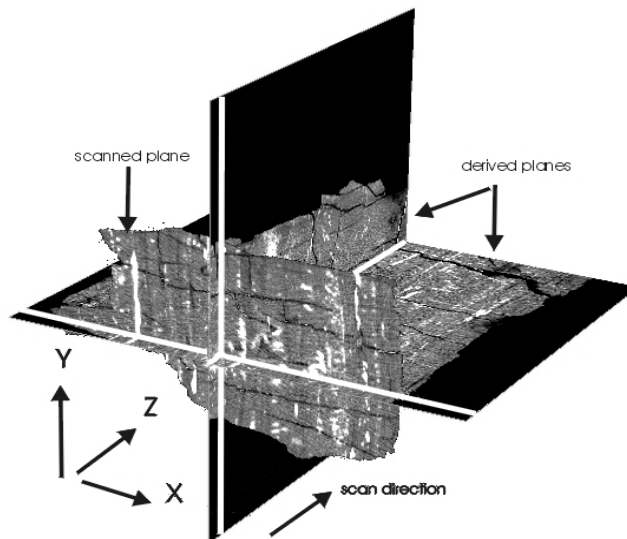
Fig. 2.1a Orthoslices of France 495

The described binary image heterogeneity made it necessary to improve each image automatically and manually. The automatic procedure consists of a sequence of image analysis processes called erosion and dilation, to enhance elongate cleat elements. Linear operators (or kernels, or structuring elements) are used in eight different directions, to suppress all non linear binary objects, leaving the continuous cleat lines unaffected. The manual procedure, (editing) was used to complete detected cleat structures that, otherwise visible in the original image, were erased because of the poor resolution of the features. In addition all remaining artifacts were erased. Thereafter, cleat lines were thinned by an erosion procedure called skeletonisation, leaving lines of 1 pixel wide through the axis of the cleats. Next, where two cleats crossed or a cleat suddenly changed direction, the lines were split, making orientation and distance measurements possible on the resulting segmented lines. This sequence of enhancement techniques provided images, which were saved for further analysis.

In order to find the two main cleat directions, the orientation and lengths of all cleat line segments were measured. This was necessary for measuring the cleat spacings of sub-parallel cleats. A histogram of the frequency distribution gives the expected bimodal behavior (Fig. 2.5). Next, a QWIN^{TM} program was developed to find the cleat spacings for all cleats in a particular

direction, i.e. face, butt or bedding, using the images in the XY, YZ and XZ plane in the following steps (Fig. 2.1 a, b),

```
        ┌─────────────────────────┐
        │        CT scans         │
        └─────────────────────────┘
                     │
                     ▼
        ┌─────────────────────────┐
        │        AMIRA™           │
        │       YZ and XZ         │
        │     reconstruction      │
        └─────────────────────────┘
                     │
                     ▼
        ┌─────────────────────────┐
        │        QWIN™            │
        │    Image enhancement    │
        └─────────────────────────┘
                     │
                     ▼
        ┌─────────────────────────┐
        │        QWIN™            │
        │  Cleat detection, binary│
        │      enhancements       │
        └─────────────────────────┘
                     │
                     ▼
        ┌─────────────────────────┐
        │        QWIN™            │
        │   Orientation and length│
        │      measurement        │
        └─────────────────────────┘
                     │
                     ▼
        ┌─────────────────────────┐
        │         EXCEL           │
        │  Face / butt cleat analysis│
        └─────────────────────────┘
                     │
                     ▼
        ┌─────────────────────────┐
        │        QWIN™            │
        │     Cleat distance      │
        │      measurements       │
        └─────────────────────────┘
                     │
                     ▼
        ┌─────────────────────────┐
        │         EXCEL           │
        │      Data analysis      │
        └─────────────────────────┘
```
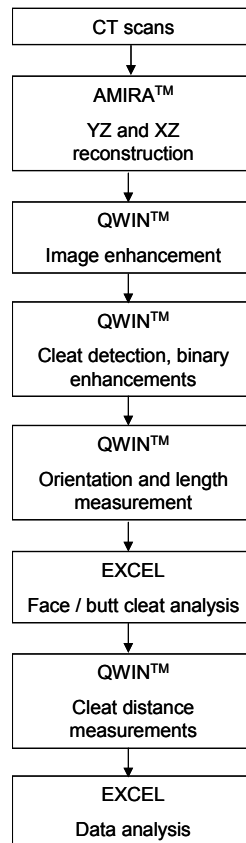
Fig. 2.1b Flowchart showing the image analysis scheme to process the CT scan for cleat orientation and spacing analysis

(i) Input of the orientation of the cleats for which the spacings were measured (Fig. 2.2).

(ii) Suppressing cleats outside the direction of the pre-defined orientation and a spread around this value i.e. the specified direction $\pm$ spread in degrees.

(iii) Adding a grid of parallel lines to the image with the orientation perpendicular to the pre-defined cleat direction and with a spacing of 4 pixels corresponding to the smallest cleat length measured.

(iv) Only accepting lines or line segments that have connections from two sub-parallel cleats.

(v) Measuring all accepted line segments giving the desired cleat spacings and produce the frequency distributions.
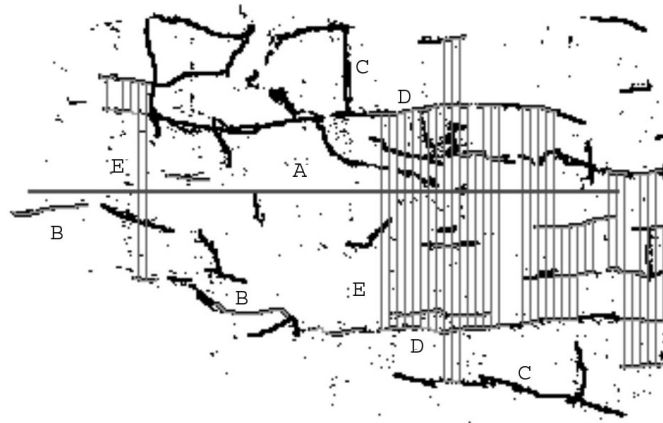
Fig. 2.2 Cleat spacing measurements on a XY-section plane, showing all cleats after image analysis on cleat spacing. A. The chosen cleat direction, B. Cleats within the direction of choice without a parallel cleat for spacing measurements, C. For orientation neglected cleats, D. preferred cleats with parallel cleats for spacing measurements. E. Cleat spacing line segments

In order to relate the measured and distributed cleat spacings to the cleat lengths involved, the originally measured number of spacing line segment per class (bin) is recalculated to the summed cleat length used for cleat spacing, using the following equation:

$$U = ((F-1)*G) + 1 + n. \qquad (2.3)$$

As U is based on counting the number of line segments with a space of 3 pixels between the grid lines, (resulting in an accuracy of +/- 6 pixels) the constant n (here is 3) expresses the integer of the average accuracy range in pixels.

Adding U of all images in a specific direction for all distribution frequencies, gives a value for the total cleat length involved in the spacing measurement. These result are in Table 2.2; the column "sum cleat lengths for spacings (px)". It expresses an estimation of the total length of cleats within the preferred orientation range. Its length is at least 4 pixels and opposites another accepted cleat to measure the cleat distance.

Occasionally a cleat runs parallel with two other cleats at both sides (Fig. 2.2). In such case the cleat length related to the spacing is included only once. Therefore, the cleat density and the discussed cleat length values are estimations.

px = pixels	nr. of images available	nr. of images used	total nr. of cleats segm.	cleat length summed (px)	max. cleat length (px)	cleat orientation according to the fit	total nr. of cleats segm.	sum oriented cleat lengths (px)	sum cleat lengths for spacings (px)	relevant cleat length (ratio)
France 495										
XY	295	60	8926	130007	187	**0° +/- 10°**	3157	60132	33184	0.26
						90° +/- 10°	1859	27647	17592	0.14
ZX	130	26	1746	17513	112	**6° +/- 15°**	571	6251	1976	0.11
						94° +/- 10°	719	8611	3636	0.21
ZY	320	32	1531	27497	179	**0° +/- 15°**	330	4027	1200	0.04
						90° +/-15°	950	21764	14732	0.54
Brzeszce LW405										
XY	135	28	417	8412	108	**10° +/- 10°**	186	4248	644	0.08
						95° +/- 20°	102	2172	252	0.03
ZX	310	31	410	6625	120	**0° +/- 20°**	297	4982	620	0.09
						90° +/- 20°	79	1419	388	0.06
ZY	110	22	250	9666	205	**5° +/- 20°**	31	747	36	0.00
						92° +/- 20°	153	7980	3660	0.38

Table 2.2 Distribution of the total cleat length, relevant cleat length and orientation of the samples

2.3.2   Cleat aperture measurement from CT scans

The X-ray CT scanner used in this study is SOMATOM Volume Zoom quad-slice, manufactured by Siemens. In this third generation apparatus, the X-ray source-detector system rotates continuously for whole object examinations using a traversing slice method. The imaging system uses the Somaris software to reconstruct the images of the subject, from multidirectional transmission data. The scanner operated at 120 KV and 165 mA. The scanning time was 2 seconds per slice (multi-scan technique). The reconstruction matrix consisted of 512 by 512 pixels. The X-ray source has a 0.8 x 0.9 mm spot size and the detector is made of 768 multi-used chambers. The apparatus allows a minimum slice thickness of 0.5 mm. Slice thickness of 0.5 and 1 mm have been used for this study. Each pixel in the XY plane represents an area of 0.29 x 0.29 mm.

Cleat apertures are detected as a reduction in the CT number for the pixel(s) containing the cleat, relative to pixels which are 100% coal matrix. Since the images are usually seen as monochromatic, with the lowest CT number set to black and the highest to white, the reduction in CT number is seen as a darker grey, as shown in Fig. 2.3a. This image presents a typical scan of a cleated coal. Air is considered to be black, with CT_{air} = -1000. As can be seen from Fig. 2.3b a dip in the profile is noticed where the cleat is present. In theory, the image of a

cleat can be seen as a convolution of a rectangular fracture profile with a point spread function (PSF), which is Gaussian (Fig.2.4), Vandersteen et al., 2003.
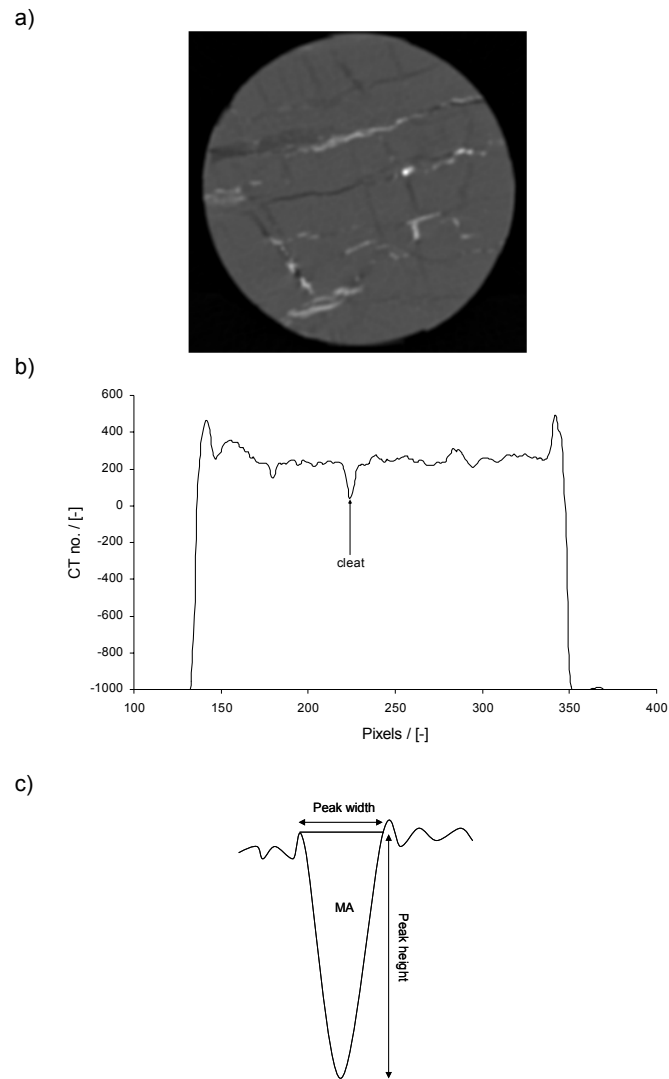
a)

b)

c)

Fig. 2.3 (a) CT image of a cleated coal core, (b) A profile across the CT image with a dip in the CT number showing the presence of a cleat and (c) Different methods to quantify a cleat aperture

The variability in the matrix CT numbers is due to the heterogeneous maceral composition of the coal. The CT scanner is calibrated with a water phantom. Using Eq. 2.2, this yields values of 0 for water and -1000 for air. Although it is also possible to calibrate the CT scanner using other materials e.g. carbon, as a material close in density to coal, this does not affect the data, but the scale on which the data is presented. Rescaling by using a coal analogue phantom, changes the amplitude of the dataset enhancing the signal of features such as cleats. At the same time this rescaling, affects the expressed values of noise artifacts that in the end are more dominant in the resolving limit for cleat aperture measurement. Although the cleat features in the coal stand out at higher amplitude and are in theory easier to distinguish, the shift caused by noise artifacts is also increased by the same amplitude.

The parameters used to quantitatively describe the cleat apertures, are shown in Fig. 2.3c. These parameters are listed and compared by Vandersteen et al., 2003. A missing rock mass or a missing attenuation (MA) is described as the integrated loss of the attenuation coefficient due to the presence of the cleat. Missing attenuation needs to be measured perpendicular to the direction of the fracture plane (Van Geet, 2001). Alternatively peak height value (PH) of the attenuation profile was used to measure the aperture (Verhelst et al., 1995). The advantage of peak height (PH) is that it's independent of the direction of measurement in the cleat. In this study both parameters are used to describe cleat aperture with a calibration technique. In images with a very high signal to noise ratio, the missing attenuation (MA) and peak height (PH) can be directly estimated. However, the heterogeneities of coal give the images a very low signal to noise ratio. Hence, an alternative fitting procedure is used to calculate the MA and the PH of a cleat in coal.

The dip in the attenuation profile is fitted by a Gaussian point spread function. The background noise by heterogeneities can be equalized to derive a CT bulk host rock response. The averaging was done using a certain tolerance in the measurements. An attenuation profile 'Y' containing a cleat can be described as,

$$Y = PH \exp\left[-\frac{1}{2}\left(\frac{X - xp}{\Delta xp}\right)^2\right] + CT_{coal}, \qquad (2.4)$$

where xp is the position of the peak, Δxp is the width of the peak within 68% confidence interval, CT_{coal} is the mean attenuation value in the bulk coal and PH is the peak height. Missing attenuation (MA) can be described as,

$$MA = \sqrt{2\pi . PH . \Delta xp}. \qquad (2.5)$$

Eqs 2.4 and 2.5 are referenced in Vandersteen et al., 2003. As shown in Fig. 2.4b, this fitting technique approximates the measured data. Fig. 2.4a represents the original data with the solid

line as the mean CT of the coal matrix and the dotted line as the tolerance to calculate the average.
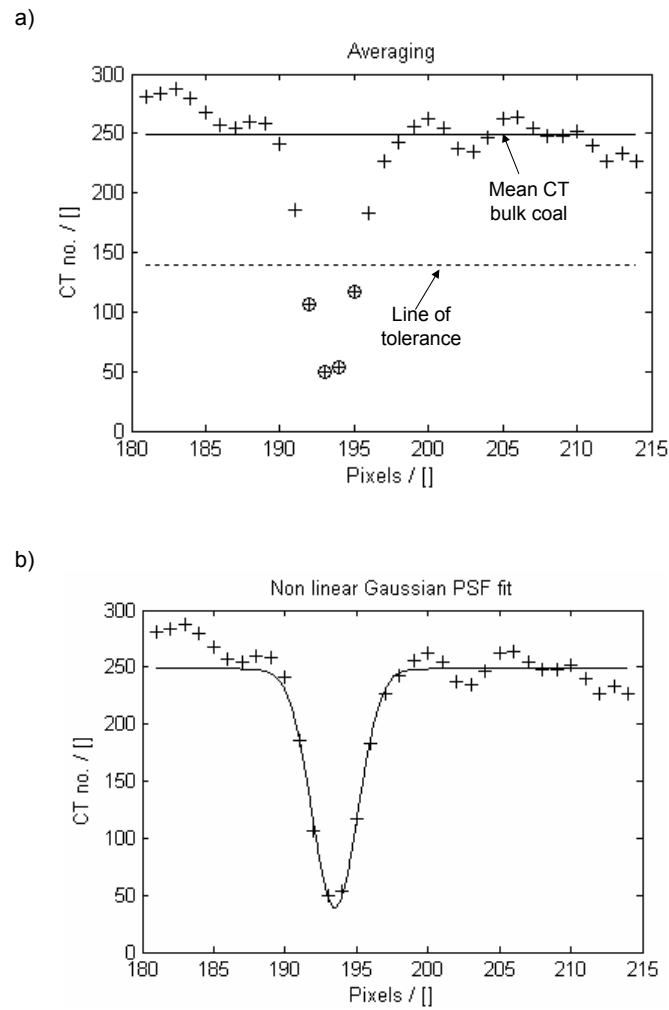
a)

b)

Fig. 2.4 (a) The image of a cleat seen as the convolution of a rectangular fracture profile with a point spread function (PSF), which is Gaussian and (b) A fitting technique approximating the measured data

The tolerance was calculated to be half the difference between the CT_{coal} and the CT value corresponding to the peak at xp. Thereafter, we assume a Gaussian function of the form

$$f(x) = A\exp(-Bx^2), \qquad (2.6)$$

Following the procedure to minimize the least square error leads to a set of non-linear equations for the coefficients A and B. To generate a solution, the sum of the least-square error was minimized using a MATLAB routine.

$$E_2 = \sum_{k=0}^{n} \left| A\exp(-Bx_k^2) - y_k \right|^2, \qquad (2.7)$$

A, B are the coefficients of the Gaussian point spread function and x_k, y_k are the x and the y values, which correspond to each attenuation profile. An initial guess of the parameters was used for minimization i.e. non-linear Gaussian fit to the data from each attenuation profile (Fig. 2.4b) to provide optimized values of PH, MA and xp.

Using the whole set of optimized values of PH and MA from each of the scanned coal cores, a calibration was used to translate the data to aperture measurements. Cleat aperture calibration standards were prepared for this purpose. The calibration standard comprised two halves of the same coal type. The adjoining flat surfaces were polished, to reduce surface roughness. To produce a "fracture" of known aperture, two metal feeler gauges of calibrated thickness were placed between the two flat surfaces. The two halves were firmly clamped together during scanning and the lower polished surface was leveled, to produce a horizontal fracture plane. The scan was done perpendicular to the longitudinal axis of the calibration standard, between the two feeler gauges. Fracture apertures ranging from 0.05 mm to 0.63 mm were scanned.

2.4   Results and discussion

2.4.1   Cleat orientation and spacing measurements

For two samples, France 495 and Brzeszce LW405, the cleat spacing distribution was measured in the three orthogonal directions. The France 495 sample was scanned in one direction. The Polish sample was scanned in two orthogonal directions because of the image quality. Of the French sample, the Voxel calibration values are known (0.7 mm per pixel in the XY plane, 1 mm per pixel in the YZ and ZX planes). From the Polish sample there is no calibration information. Hence for comparison, all results are discussed in pixel units. Moreover, to describe a method to measure cleat spacing distribution, it is not needed to give results in absolute values other than pixels.
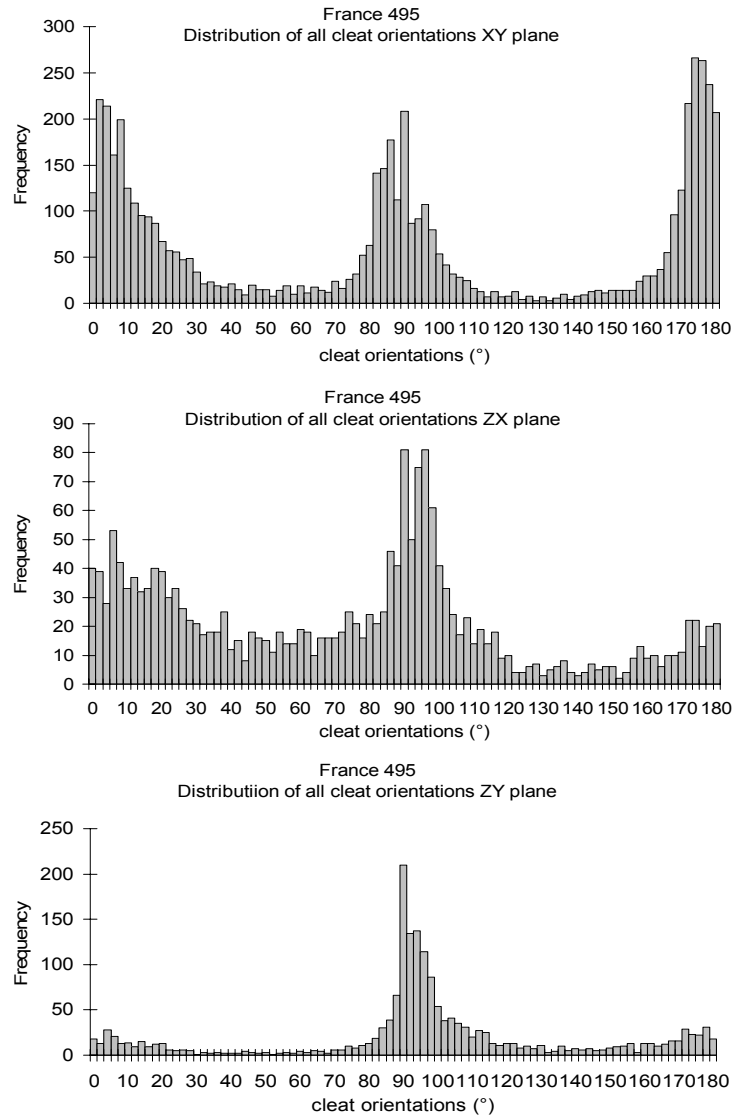
Fig. 2.5 France 495. Distribution of all cleat orientations measured in the XY, ZX and ZY plane

Brzeszzce LW405
Distribution of all cleat orientations XY plane

Brzeszzce LW405
Distribution of all cleat orientations ZX plane

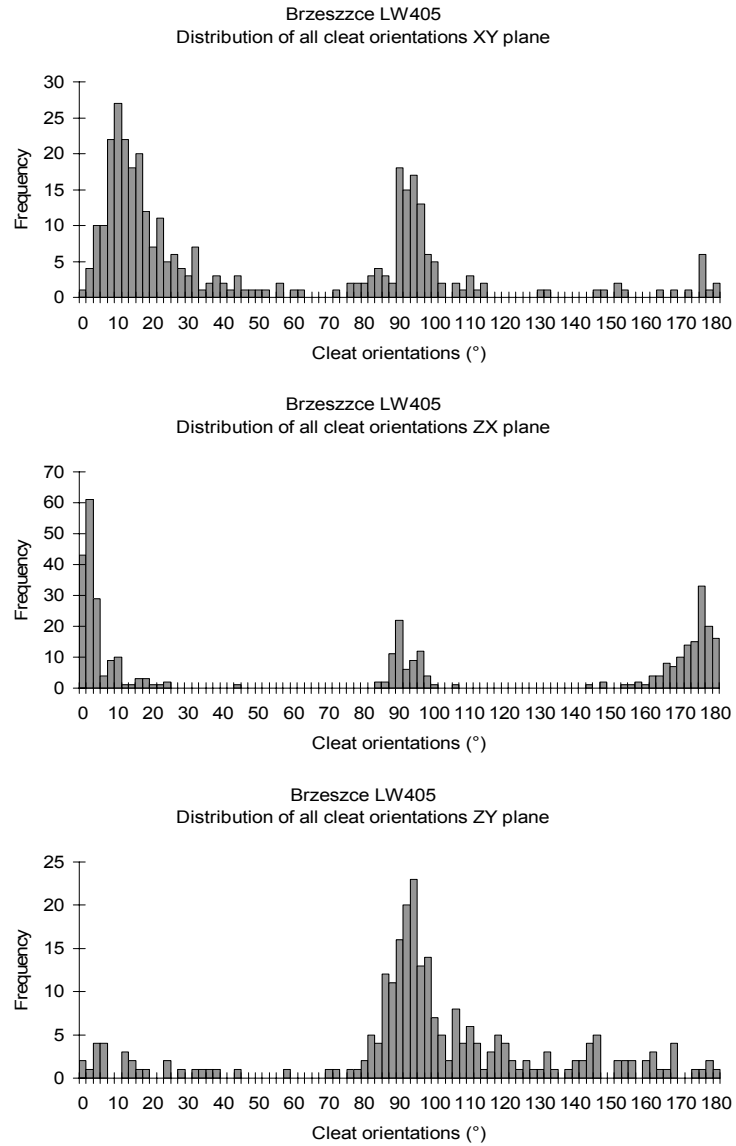Brzeszce LW405
Distribution of all cleat orientations ZY plane

Fig. 2.6 Brzeszce LW405. Distribution of all cleat orientations measured in the XY, ZX and ZY plane

To recognize the statistical value of the outcomes, the results are split up in:

(i) *Total lengths of open cleats and cleat orientation distribution.* All cleats are measured in all directions within a stack. Cleat orientation distribution is related to the section plane in which an image stack is oriented. In all images the zero orientation points horizontal, the angles turning clockwise.

(ii) *Lengths of cleats in the preferred orientations.* From the orientation distribution (Figs. 2.5 and 2.6) the preferred angles are selected with a spread of $\pm 18^0$. The cleats within the defined angle range are used for cleat length measurements.

(iii) *Total cleat lengths used for cleat spacing measurement.* Those oriented sub-parallel cleat segments that can be used for cleat spacing measurements. They are selected on summarized cleat length and spacing distribution. Total cleat lengths used for cleat spacing measurement divided by the total lengths of open cleats, give the relevant cleat length ratio.

Table 2.2 shows for both samples the major cleat orientations, divided in face and butt cleats in the XY and ZX directions respectively, and relaxation fractures (sub-) parallel to the bedding, for the ZY planes. Table 2.2 shows that reconstructed cleat systems can be recognized by cleat length ratios. The results show that a face cleat and a butt cleat system are recognized by a continuous reduction of grey values in a specific direction. When measured and ordered according to the preferred cleat orientations, the same fracture set should give similar results in two directions (Fig. 2.1). For example, for France 495 the XY plane 0° and the ZY plane 90° have a relevant cleat length of 0.26 and 0.54 respectively. When looking at Fig. 2.7a and f, the summed cleat spacing distributions are high with maximum values of 12000 and 5500 pixels respectively (Fig. 2.7). It can be concluded that the face cleat system, which is oriented sub-parallel to the ZX plane, has a regular spacing distribution. Considering the butt cleat system, which is more random and here oriented sub-parallel to the XY plane, the relevant cleat length has a lower ratio for the ZX plane 0° and ZY plane 0° of respectively 0.11 and 0.04. For the bedding, oriented according to the ZY plane, maximum ratios are measured of 0.14 in the XY plane 90° and 0.21 in the ZX plane 94°. Also for the orientations of the butt cleats (Fig. 2.7c and e) and bedding planes (Fig. 2.7b and d) the cleat spacing distributions in different directions show similar shapes. From these shapes it can be concluded that the cleat spacing distribution, measured over the same volume in perpendicular distances, give comparable results. However, pixel counts can be different, since the XY plane and Z direction have different resolutions attributed to the pixel size and different amounts of images analyzed. The spreading and summed pixel counts for the spacing in the three directions are a measure for the regularity of the cleat texture: (i) Higher counts mean more relevant cleat length in a specific direction (Fig. 2.7a and f). (ii) Wide peak distributions count for a large spread in cleat spacing (Fig. 2.7b and d). (iii) An irregular spacing pattern represents dispersed cleat spacing in one specific direction (Fig. 2.7c and e).

a) Cleat spacing distribution in the XY plane
preferred cleat orientation 0° +/- 10 °
Analyzed cleat lengths 66368 pixels
Face Cleats

b) Cleat spacing distribution in the XY plane
preferred cleat orientation 90° +/- 10°
Analyzed cleat lengths 35184 pixels
Fractures parallel to bedding

c) Cleat spacing distribution in the ZX plane
preferred preferred cleat orientation 6° +/- 15 °
Analyzed cleat lengths 3952 pixels
Butt Cleats

d) Cleat spacing distribution in the ZX plane
preferred cleat orientation 94° +/- 10 °
Analyzed cleat lengths 7272 pixels
Fractures parallel to bedding

e) Cleat spacing distribution in the ZY plane
preferred cleat orientation 0° +/- 15 °
Analyzed cleat lengths 2400 pixels
Butt Cleats

f) Cleat spacing distribution in the ZY plane
preferred cleat orientation 90° +/- 15 °
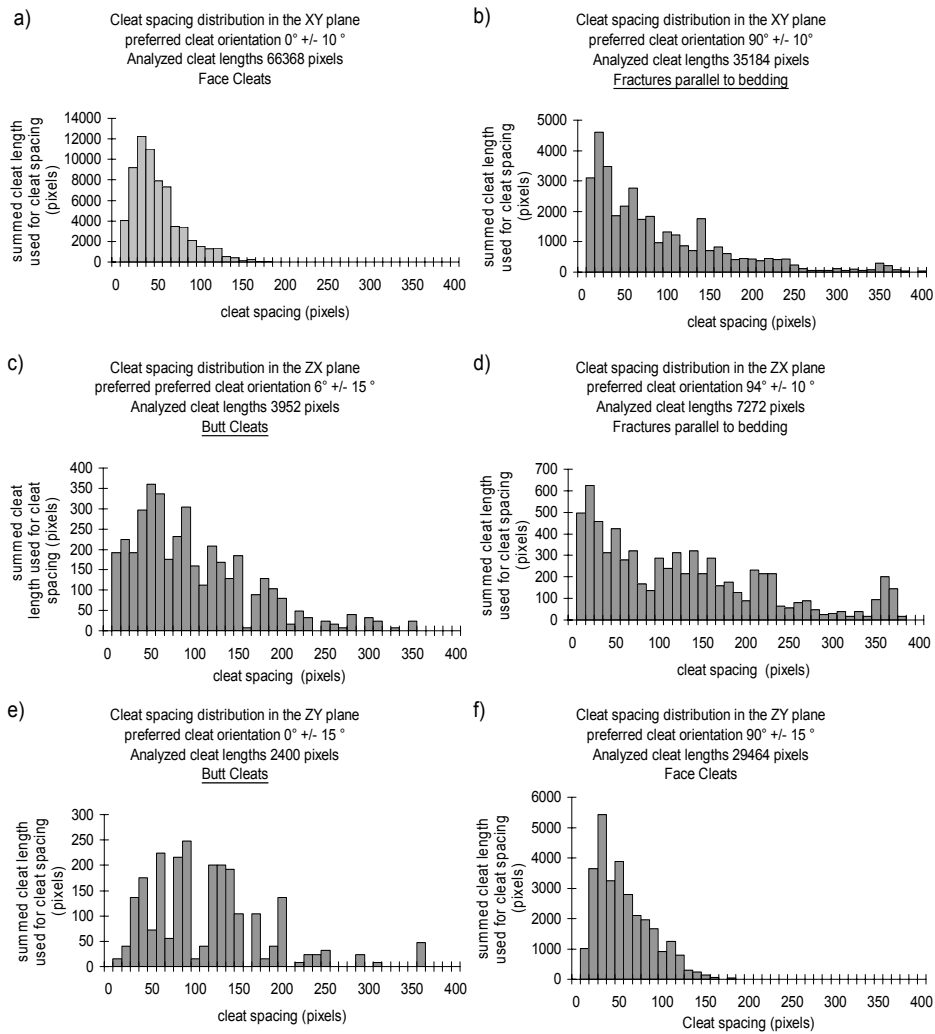Analyzed cleat lengths 29464 pixels
Face Cleats

Fig. 2.7 France 495. Distribution of cleat spacings against cleat lengths in the 3 orthogonal planes and in the two preferred cleat directions in each plane
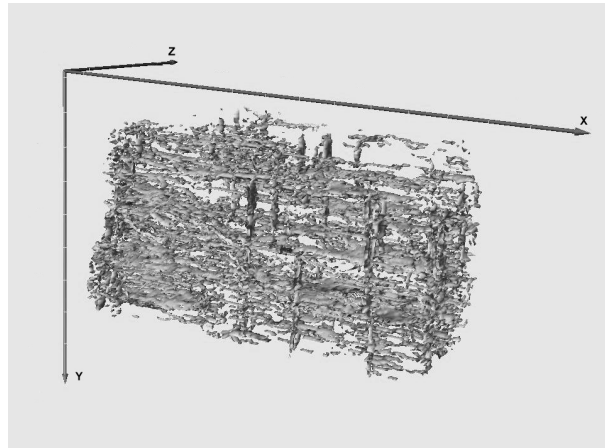
Fig. 2.8 Rendered cleat system of France 495, using every 5th CT-scan in the stack direction (Z)
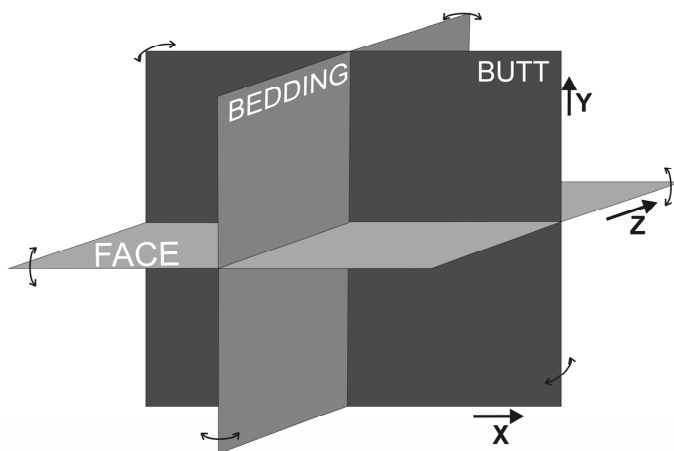

Fig. 2.9 Orientation of the cleats and bedding related to the orientation of the CT-scan axis

For the France 495 series, the most pronounced cleat spacing distribution is found for the face cleats. Fig. 2.8 shows a rendered pseudo 3D representation of the detected cleats structure in the France 495 sample. Fig. 2.9 shows a schematic drawing of the resulting cleat and bedding directions.

Fig. 2.10 shows for the Brzeszce LW405 sample the spacing distributions parallel to the cleats and bedding. The spacing distribution in all directions is poorly pronounced when compared to the France sample. Table 2.2, Figs. 2.5 and 2.6 shows that the values for cleat length, relevant cleat length and cleat orientation distribution are low, which point to more random cleat dispersion. This is clearly visible in the spacing distributions of the bedding plane cleats (Fig. 2.10b and d), face cleats (Fig. 2.10a and f) and butt cleats (Fig. 2.10c and e). The moderate quality of the CT scan images caused that, only the face cleats in the XY-plane and butt cleats in the XZ-plane could be used.

The reasons of the poor cleat distribution properties of the Polish sample are:

- Less cleats are present in the coal block, so less total cleat length is available (Table 2.2).

- Less cleats are measured (one order of magnitude less) in cleat orientation measurements for Brzeszce compared to the French sample.

Since the samples are from different regions, they have different burial history and consequently a difference in cleat orientation and in cleat spacing behavior.

The cleat orientations of the France 495 and the Brzeszce LW405 sample (Figs. 2.5 and 2.6) show comparable major cleat orientations. So, the cleat planes in both samples run sub-parallel to the XYZ planes. However, the difference between the samples can be found in the spread which is much higher for the France 495. Based on frequency distributions this sample also shows a higher cleat density. When considered the angle orientations between 30° and 80° and between 110° and 160°, the Brzeszce 405 sample shows a more pronounced cleat system. Also better image reconstruction was possible for France 495 sample.

The cleat spacing distributions of the France 495 sample are, as with cleat orientation, more detailed compared to the results of the Brzeszce sample. We observed that the spread in cleat orientations also results in a larger spread of cleat spacings. The results of cleat spacing distributions are all negatively skewed. It is not understood whether it is common to have cleat spacing distributions log-normally distributed or that the skewness is because of image quality.
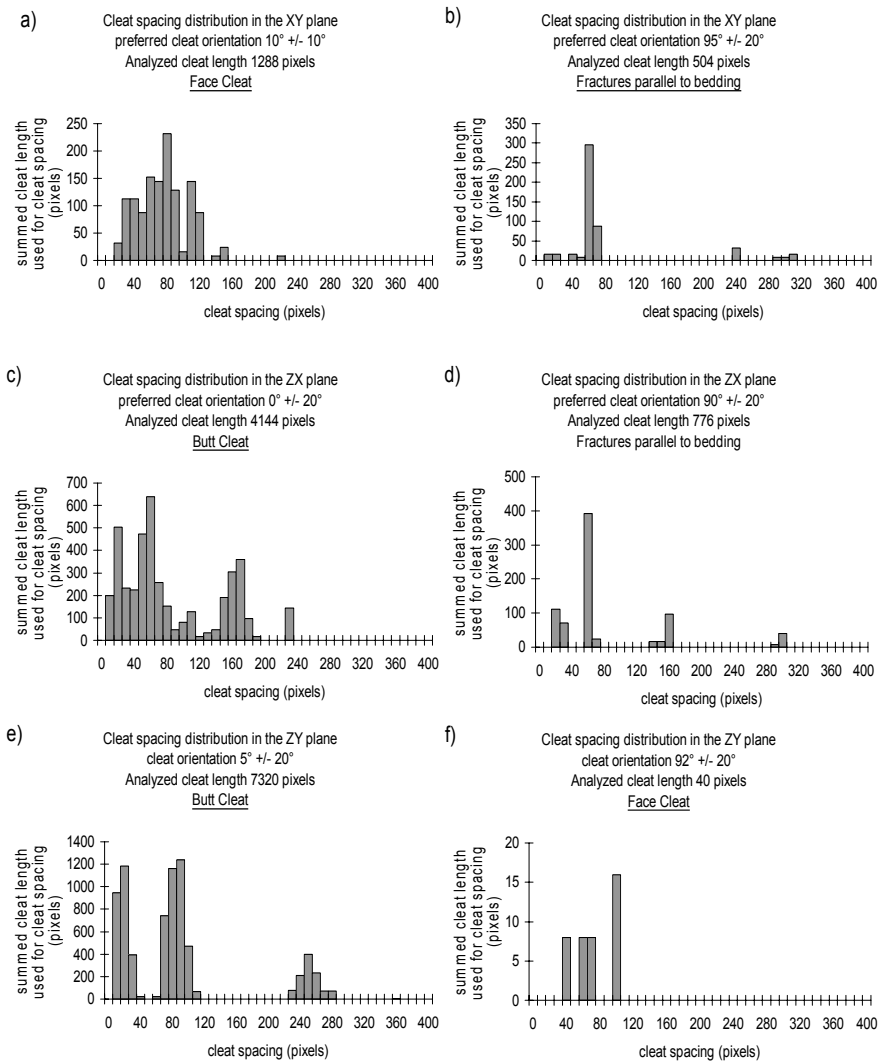
a)

Cleat spacing distribution in the XY plane
preferred cleat orientation 10° +/- 10°
Analyzed cleat length 1288 pixels
Face Cleat

b)

Cleat spacing distribution in the XY plane
preferred cleat orientation 95° +/- 20°
Analyzed cleat length 504 pixels
Fractures parallel to bedding

c)

Cleat spacing distribution in the ZX plane
preferred cleat orientation 0° +/- 20°
Analyzed cleat length 4144 pixels
Butt Cleat

d)

Cleat spacing distribution in the ZX plane
preferred cleat orientation 90° +/- 20°
Analyzed cleat length 776 pixels
Fractures parallel to bedding

e)

Cleat spacing distribution in the ZY plane
cleat orientation 5° +/- 20°
Analyzed cleat length 7320 pixels
Butt Cleat

f)

Cleat spacing distribution in the ZY plane
cleat orientation 92° +/- 20°
Analyzed cleat length 40 pixels
Face Cleat

Fig. 2.10 Brzeszce LW405. Distribution of cleat spacings against cleat lengths in the 3 orthogonal planes and in the two preferred cleat directions in each plane

2.4.2   Cleat aperture measurements

Using the calibration method described above, fracture apertures ranging from 0.05 mm to 0.63 mm were scanned for coal to obtain a calibration curve. The calibration curves for peak height (PH) and missing attenuation (MA) are shown in Fig. 2.11a. The figure also shows that missing attenuation (MA) as a function of the cleat aperture, yields a more curvilinear relationship as compared to the peak height (PH). The slope of MA initially has a higher value and decreased with increasing cleat apertures. The missing attenuation is more sensitive than peak height (PH), since the missing attenuation is more sensitive to the direction in which the profiling is done. Also the fact that MA is a derived parameter and is a function of PH and Δxp, it carries over the error from multiple parameters and increases it. For near vertical cleats, the calibration profile for MA should be orthogonal to the cleat trace, whereas peak height is insensitive to the profiling direction. For non orthogonal cleats, MA has to be multiplied with the co-sine value of the inclination of the cleat plane. 80 to 90 cleat attenuation profiles were analyzed for each cleat aperture calibration point. Fig. 2.11b is a plot of the coefficient of variation for both peak height and missing attenuation as a function of the aperture width. Missing attenuation (MA) is a better parameter for the determination of fractures with larger aperture widths. For lower aperture widths (Fig. 2.11a), MA is highly sensitive and thus peak height (PH) is a better parameter to calculate cleat apertures. Hence for smaller apertures, where the measurement error for MA is large, the data should be used with skepticism.

Using peak height and missing attenuation as parameters to calculate cleat aperture widths, all measurements for the Silesia and the Tupton coals were used to derive the cleat aperture frequency distributions. Figs. 2.12a and 2.13a are the aperture distributions of the Silesia and the Tupton coal, using PH as a parameter. Figs. 2.12b and 2.13b are the aperture distributions of the Silesia and the Tupton coal, using MA as a parameter to calculate cleat apertures. For the Silesia coal (Fig. 2.12a and b), using peak height and missing attenuation as parameters to calculate cleat aperture, a variability of the aperture distribution is observed; the mean aperture using PH was calculated to be 0.087 mm, using MA as a parameter it is 0.052 mm. For the Silesian coal, the aperture distribution calculated with PH as a parameter is more reliable. For the Tupton coal, the aperture measurements using PH and MA are in good agreement. The mean cleat aperture using PH as a parameter is 0.225 mm, using MA gives 0.247 mm.
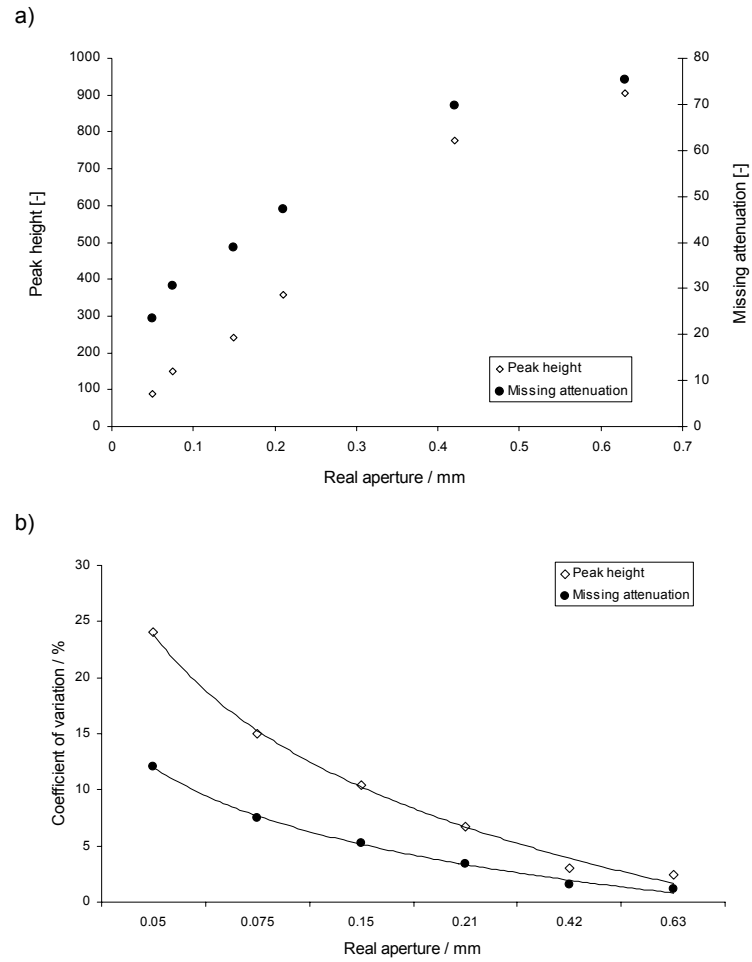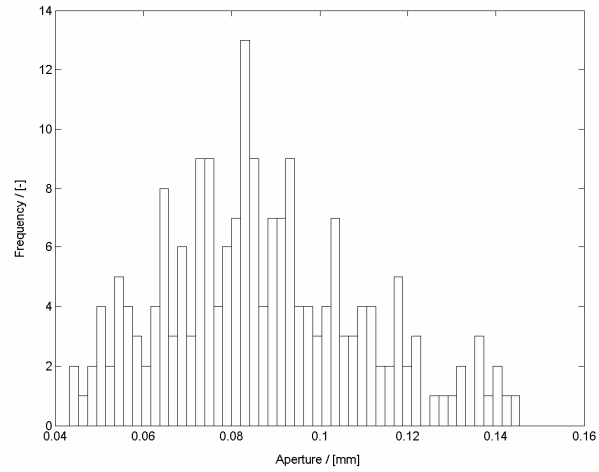
a)

b)

Fig. 2.11(a) The calibration curves for peak height (*PH*) and missing attenuation (*MA*) and (b) A plot of the coefficient of variation for both peak height and missing attenuation as a function of the aperture width
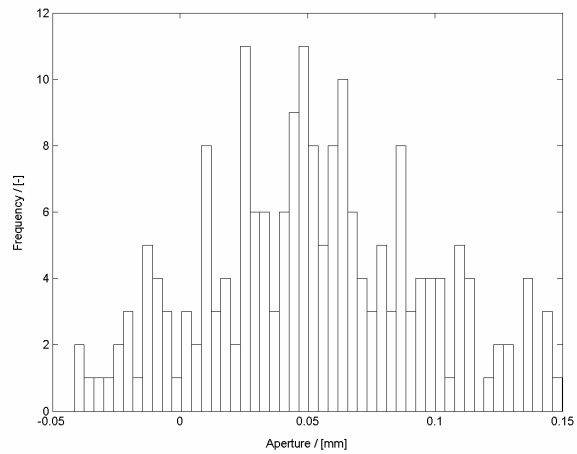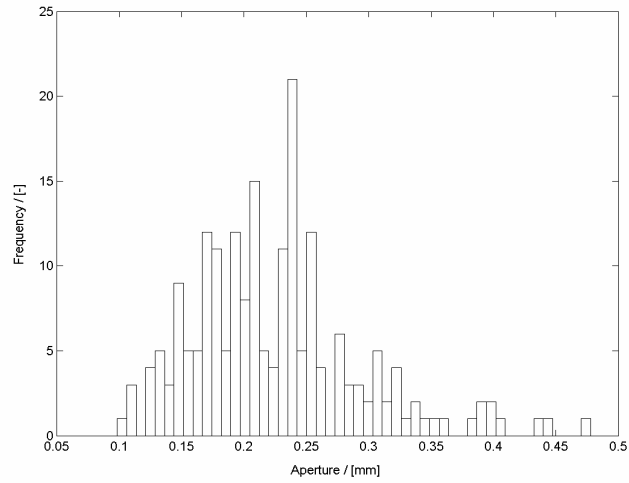
a)

b)

Fig. 2.12 Cleat aperture frequency distributions for the Silesia coal using (a) peak height and (b) missing attenuation as parameters to calculate the fracture aperture
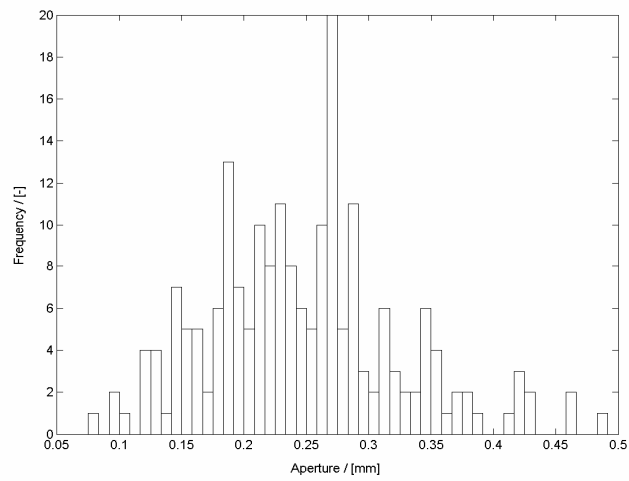
a)

b)

Fig. 2.13 Cleat aperture frequency distributions for the Tupton coal using (a) peak height and (b) missing attenuation as parameters to calculate the fracture aperture

2.4.2.1   Error analysis

The uncertainty principle was used to estimate the experimental error in measuring the missing attenuation and the peak height. The principle is based on the concept of calculating the uncertainty in the final value of the calculated parameter from the uncertainties of each measured variables (Holman, 1994 and Taylor, 1997). The effects of each measured variables on the final calculated variable value is derived from the concept of propagation of errors

Applying this concept for our case and starting with the equation for missing attenuation (Eq. 2.5), the measured independent variables are: PH and Δxp. Thus taking the partial derivative of MA with respect to the above mentioned independent variables, the uncertainty in missing attenuation is then derived as,

$$\partial \mathbf{MA} = \sqrt{\left(\pi \frac{\Delta xp}{\sqrt{2\pi . PH . \Delta xp}} \partial PH \right)^2 + \left(\pi \frac{PH}{\sqrt{2\pi . PH . \Delta xp}} \partial \Delta xp \right)^2} , \qquad (2.8)$$

where ∂MA, ∂PH and $\partial \Delta xp$ are the average measured standard deviations for each parameter. The independent variable PH (peak height) depends directly on how good is the averaging technique. An estimate of the standard deviations of all the "near host rock CT number" for the Silesia sample, has been made, The result is shown in Fig.2.14. The average measured standard deviation for all 196 measured profiles is 28.4 (∂PH). The least error minimization leads to optimized values for PH, MA and xp. A pessimistic estimate of $\partial \Delta xp$ was around 0.2. Using Eq. 2.8 the values of ∂MA is calculated and has been plotted in Fig. 2.15. The average calculated error for the missing attenuation (MA) was 15.8%. A realistic estimate of $\partial \Delta xp$ would be around 0.1 and that would yield an average error of 14.09 % for the MA calculation. The averaging technique used to derive the mean host rock response has an error of 11.4 %. Thus the error imposed by the averaging is well within the limit of standard experimental error. The error analysis completely justifies this.
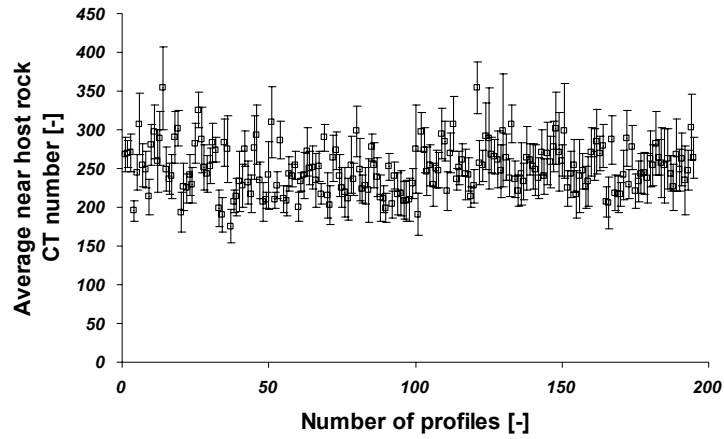
Fig. 2.14 Error estimate of the average near host rock CT number for the Silesia coal sample
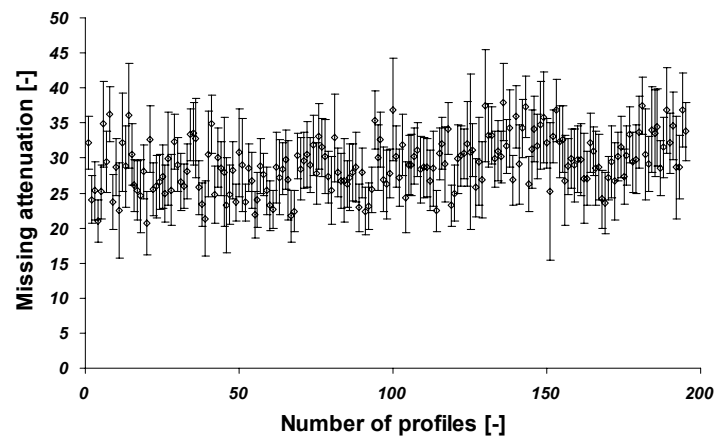
Fig. 2.15 Error estimate of the missing attenuation (*MA*) for the Silesia coal sample

2.5   Conclusions

- A method to determine cleat spacing in coal was difficult to find. Existing methods for cleat aperture measurements in coal were not exact because the image resolution was too low. Hence we developed a method based on a Gaussian Point Spread Function (PSF), to determine cleat aperture measurements from CT scans of coal samples.

- Peak height and missing attenuation measurements were used to generate the aperture distributions.

- In addition, a method to determine the cleat orientation and cleat spacing distribution from CT scans of coal samples was developed.

- Regarding the cleat orientation and relevant cleat spacings, we observe configuration dependent spacing distributions in both samples, which can be used for fracture modeling in coal specimens up to one cubic foot in size.

- The method combines these two different techniques, and gives a better understanding of the cleat framework. Upscaling to seam size is not investigated. This combined procedure also proves that it is possible to distinguish face cleat, the butt cleat and the bedding system.

- However it should be remembered that, fractions of a pixel are not physical domains, and the length measurements within this domain can not be exact. Thus no measurement can be exact in the sub-pixel level, including the method described above. At best the error in the approximations can be reduced by choosing the right method. Further image quality will be essential.

Nomenclature

I = transmitted intensity, [keV]

I_0 = incident intensity, [keV]

L = path length, $[cm]$

μ = measured linear attenuation coefficient, $[cm^{-1}]$

μ_w = linear attenuation coefficient of water, $[cm^{-1}]$

K = constant equal to 1000, [-]

U = summed cleat length used for cleat spacing measurement per spacing class, [-]

F = frequency per spacing class, [-]

G = grid spacing, distance between the line segments used for spacing measurement (4 pixels), [-]

n = integer of the average accuracy range in pixels, [-]

xp = position of the peak, [-]

Δxp = width of the peak within a 68% confidence level, [-]

CT_{coal} = mean CT response of the coal matrix, [H]

PH = peak height, [-]

MA = missing attenuation, [-]

3 Flue gas and pure CO$_2$ sorption properties of coal: A comparative study

3.1 Introduction

One of the most promising alternative options for CO$_2$ emissions reduction is the storage of CO$_2$ in deep, unmineable coal layers. These deep (300 to 1500 m) coal layers are known to contain vast quantities of gas, primarily methane (CH$_4$), adsorbed to the coal or dispersed into the pore spaces of the coal seam. Enhanced Coalbed Methane (ECBM) projects aim to replace the coal gas by CO$_2$. Approximately double the amount of CO$_2$ can be stored in comparison to the amount of CH$_4$ that can be produced.

In the context of the geological storage of CO$_2$, a few projects consider the direct injection of flue gases from power plants or other flue gas emitting industries. The aim of this research is to investigate how to use industrial flue gas as an alternative to pure CO$_2$ as an injectant and how it influences the sequesterable amount of CO$_2$ in dry and water saturated coal. The use of flue gas instead of CO$_2$ in the ECBM projects may improve the cost-effectiveness of the ECBM projects considerably.

3.1.1 Previous work

A considerable amount of literature is available on the physical adsorption of gases and vapors on activated carbon. Among others, the sorption isotherms have been studied for methane, ethane, and hydrogen as well as their binary mixtures, at elevated temperatures and pressures. Martin-Martinez et al., 1995 studied the sorption mechanisms of CO$_2$ in anthracite. They concluded from these isotherms that the adsorption in micropores with molecular dimensions is a micropore filling process, and produces a curved CO$_2$ isotherm. The adsorption that occurs in pores larger than two molecular diameters takes place via surface coverage and is associated with a linear isotherm. Clarkson et al., 1997 applied the monolayer (Langmuir), multilayer (BET), and the potential (Dubinin-Radushkevich and Dubinin-Astakhov) theories to the high temperature, high pressure (up to 10 MPa) CH$_4$ adsorption isotherms and low pressure CO$_2$ isotherms in order to determine the best fit for the experimental data. They found that the three-parameter D-A equation yielded the best fit to the high pressure CH$_4$ isotherms. They concluded that one of the postulates of the Langmuir theory, the assumption of the energetically homogeneous adsorption cavities, does not apply to coal. They also concluded that, although the adsorption potential theory applies to low-pressure CO$_2$ isotherms, high-pressure adsorption isotherms for CO$_2$ need further attention.

DeGance et al., 1993 investigated pure and multicomponent adsorption isotherms of CH$_4$, N$_2$, and CO$_2$ on a wet coal sample under high pressures. They applied a two-dimensional equations of state, (2-D EOS), the Ideal Adsorbed Solution Theory (IAS), and an extended Langmuir equation to the data. They concluded that the EOS approach does match partly to the experimental data for wet coals. However the simplicity of the 2-D EOS made it useful for modelling efforts. Chaback et al., 1996 measured sorption isotherms of N$_2$, CH$_4$ and CO$_2$ on wet bituminous coals at in situ conditions (46^{0}C and pressures up to 11 MPa). They concluded that the Langmuir equation and its extended form satisfactorily represent the adsorption isotherms of both pure components and gas mixtures. They also showed that the relative adsorption capacities of CO$_2$:CH$_4$:N$_2$ are about 4:2:1, respectively.

Historically, the adsorption of CO$_2$ on coal has been used to estimate surface areas and micropore structures. These measurements have been conducted under sub-atmospheric pressures and low temperatures (-78^{0}C). Krooss et al., 2002 have recently reported CH$_4$ and CO$_2$ adsorption isotherms on dry and moisture-equilibrated Pennsylvanian coal at temperatures of 40, 60, and 80^{0}C and at pressures up to 20 MPa. They showed that excess sorption isotherms of CO$_2$ yielded a minimum between 8 and 12 MPa, tending even to negative sorption values. This is indeed not possible from the point of thermodynamics. Regrettably, they could not compare their high pressure adsorption isotherm data with the literature due to the lack of published data on high pressure CO$_2$ isotherms except for the work of Hall et al., 1994. These negative sorption values are attributed to the swelling of the coal matrix.

Only a few experimental studies have been made on sorption of mixed gases on coal and on flue gas. Stevenson et al., 1991 measured, and also examined, adsorption of binary and ternary mixtures of CH$_4$, CO$_2$, and N$_2$ on dry Australian coals at 303.15K and pressures up to 5.2 MPa. Greaves et al., 1993 studied mixed gas sorption isotherms on dry Sewickley seam coal at 296.15 K. The study demonstrates the importance of sorption isotherm hysteresis in predicting sorbed phase compositions. Studies on wet coal directly reflect the sorption behavior under field conditions. The presence of moisture significantly changes the sorption equilibrium characteristics of mixed gases. Arri et al., 1992 collected binary (CH$_4$ – N$_2$ and CH$_4$ – CO$_2$) gas isotherm data at 46^{0}C at different pressures for a moisture-equilibrated coal system. Recently sorption and desorption behavior of pure CO$_2$, CH$_4$, and CH$_4$ – CO$_2$ mixtures has been studied by Busch et al., 2003 and Ozdemir et al., 2004 on a set of well characterized coals from the Argonne Premium Coal Programme. From the experiments, it was concluded that each component gas does not adsorb independently, but competes for adsorption space. The extended Langmuir isotherm provided a reasonable fit to the Arri et al., 1992 data. Harpalani and Pariti, 1993 obtained ternary adsorption / desorption data from a moisture equilibrated coal system at 319.15 K. A reasonable fit was also obtained. Hall et al. (1994) applied several models to pure- and mixed-gas Fruitland coal isotherm data and quantitatively assessed different model predictions. They found that, although all models used for pure gas adsorption,

performed well, the IAS theory of Myers and Prausnitz, 1965 and 2-D equation of state (EOS) models were more accurate than the extended Langmuir model for mixed gas adsorption. Stevenson et al., 1991, also found IAS theory to be adequate for predicting binary and ternary mixed gas adsorption on dry coal. Clarkson and Bustin, 2000 made a comparison of model predictions to experimental data. They used the IAS theory in conjunction with the Dubinin-Astakhov single component isotherm equations, with an extended Langmuir model. They found that the IAS model is more accurate. However, it is strongly dependent upon the choice of pure component equation.

A dual-sorption mechanism has been, at times, used to predict the sorption behavior of coal, both for single component and mixed gas systems (Barrer, 1984). This model makes an attempt to explain the solubility of small molecules in the glassy matrix. The model assumes that a polymer consists of a continuous chain matrix, along with micro voids (holes) frozen in the matrix. These microvoids, present in discrete as well as continuous domains, are caused by the non-equilibrium state of the glassy matter. Koros, 1980, presented an extension of the dual mode sorption model. The extension is based on the assumption that the primary effect due to the presence of other gases would be the competition between the individual components for the fixed free volume in the polymer. The dual-sorption mechanism is defined in terms of Henry's law of solubility (dissolution in continuous chain matrix) and extended Langmuir-type of sorption (sorption in microvoids).

None of the later predictive sorption models are able to explain the swelling behavior of coal when exposed to gas. During molecular transport of solvents at low or moderate temperatures, as molecules enter the macromolecular network of coal, the network density decrease. This results in an increase of the large molecular chain motions (Ritger et al., 1987). This increase of the molecular concentration of the network can be viewed as an effective decrease of the glass transition temperature (Hsieh, 1987). Structural changes induced during this process include swelling, microcavity formation, and primary phase transition, creating rearrangements of the chain segments. Such changes are dominated by relaxational phenomena. The best experimental study regarding heterogeneous sorption and swelling of coal due to CO_2 sorption has been conducted by Karacan, 2003. He studied the changes in the sorbed gas concentration and coal matrix properties using a dual energy X-ray computed tomography and demonstrated that CO_2 dissolution enabled rapid structural changes of coal. The diffusion in glassy polymeric matrix often does not fit the Fickian diffusion model. Alfrey et al., 1966 have presented a second limiting case for sorption, where the rate of transport is entirely controlled by molecular relaxation. This type of transport mechanism is designated as Case II transport.

The following sections describe the sorption experiments that were conducted on wet and dry Silesia coals, with pure CO_2 and flue gas. Desorption tests with flue gas were conducted to study the degree of preferential sorption of the individual components. In addition

to the sorption experiments, the density of the flue gas mixture has been determined upto 18 MPa at 318 K.

3.2   Material and methods

3.2.1   Sample description and preparation

All experiments reported here were performed on one single coal sample from the Silesia mine in the Upper Silesian Basin in Poland. The coal was obtained as a lump from a depth ~ 900 m. This coal seam was selected for CO_2 injection under the project "RECOPOL". It is a Pennsylvanian high volatile bituminous coal with a vitrinite reflectance (R_{max}) of 0.68%. Table 3.1 summarizes information on rank and maceral composition.

Coal sample	Silezia 315 II
Depth of origin [m]	~ 900
Geological age	Pennsylvanian
Mine or origin	Poland
% R_r	0.68
Vitrinite [%]	71.6
Liptinite [%]	6.8
Inertinite [%]	15.0
Minerals [%]	6.8
Micropore volume [cm^3/g]	0.064
Specific surface [m^2/g]	190
Porosity [%]	8.3

Table 3.1. Sample description

A core, 69.5 mm in diameter, was drilled out of the block of coal and was cut into three equal pieces of 5 cm in length. These cylindrical coal core samples were dried at 40^{0}C for a period of 2 weeks at a pressure of ± 0.3 bars. The samples were sealed in plastic bags to minimize oxidation. Before the start of the experiments, the samples were saturated with double distilled water for 3 hours at a temperature of 30^{0}C according to a modified ASTM procedure (Mavor et al., 1990).

3.2.2 Experimental setup

The experiments were performed in a volumetric sorption setup, similar to the one described by Mavor et al., 1990 and Levy et al., 1997, but adapted for cylindrical core samples. Fig. 3.1 shows a schematic diagram of the experimental setup, consisting of two stainless steel sample cells, a set of valves, a couple of high precision pressure transducer (maximum pressure of 12 MPa) and a reference volume between the two sample cells. The reference volume includes the dead volume between the two sample vessels and a reference vessel. The dead volume of the whole setup has been determined by helium expansion in a calibration procedure. The coal cores were placed inside the calibrated sample cell. The sample cells, along with the reference volume, were placed inside a thermostatic bath, maintained at 353 K. The pressure (sample and reference cell) and temperature (sample cell and thermostatic bath) were registered on a computer every 10 seconds.
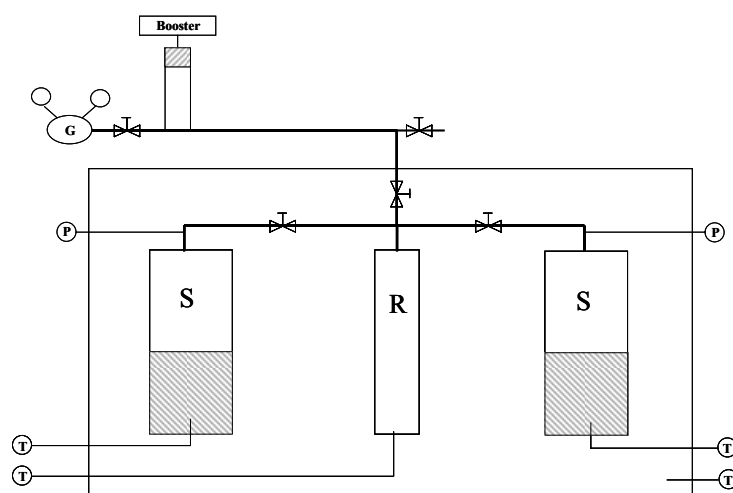

Fig. 3.1 Schematic of the experimental setup to conduct pure CO2 and preferential sorption measurements with flue gas using volumetric method. P indicates pressure measurement, T indicates temperature measurement, G indicates gas chromatography, S indicates sample cell and R indicates Reference cell. The distance between the sample cell and the gas chromatograph is 1 m.

To determine the preferential sorption behavior of flue gas on dry and wet coal, a micro-GC was used. The gas chromatograph was an Agilent 3000^{TM} micro GC with a TCD (Thermal Conductivity Detector). The micro GC is fitted with two types of columns, a Molsieve column and a Poraplot U column. For data acquisition and analysis the software of "Agilent

Cerity TM" was used. The specifications of the flue gas sample are in Table 3.2. The carrier gas used for measurements was argon. The Molsieve column allowed measurement of hydrogen, oxygen, N_2, CH_4, and CO. The poraplot U column separated and measured CO_2, ethylene, ethane, acetylene and sulfur dioxide. CO could not be measured because it has approximately the same thermal conductivity as that of argon. Both columns were cleaned for at least 12 h on a weekly basis. The micro GC was calibrated repeatedly with the Universal Gas Calibration Standard.

Component name	Gravimetric Conc. (mole %)	Used Column	Carrier Gas
CO_2	10.9	Porapack Q	He
CO	0.01	-	-
H_2	9.0	Mole-Sieve	Ar
CH_4	3.01	Mole-Sieve / Porapack Q	Ar/He
O_2	3.00	Mole-Sieve	Ar
SO_2	0.106	-	-
N_2	73.974	Mole-Sieve	Ar

Table 3.2. Flue gas specification and used columns/carrier gas for chromatographic analysis and density determination.
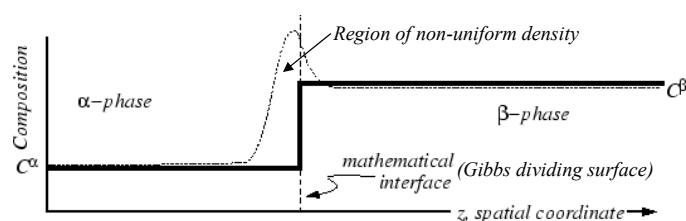

Fig. 3.2 Schematic of Gibbs dividing surface. In this case the two phases are the solid (coal) and the fluid phase (CO_2 / flue gas).

To determine the flue gas EOS, a separate volumetric setup, in combination with a gas chromatograph was used. Fig. 3.3 shows a schematic overview of this experimental setup. It was placed in an oven under a constant temperature of 45^0C. The GC used for the flue gas density measurements is different from the one used in the volumetric sorption setup. To

convert GC peak areas into molar densities, it is essential to calibrate the GC for each specific component in the flue gas mixture. Different sample loops are used (3.7µl, 13µl, 75µl, 152µl and 495µl) to achieve detector responses covering the complete peak area range that was necessary for the density measurements. The micro sampling valve (Swagelok, 0.06µl ±~20%) was also calibrated.
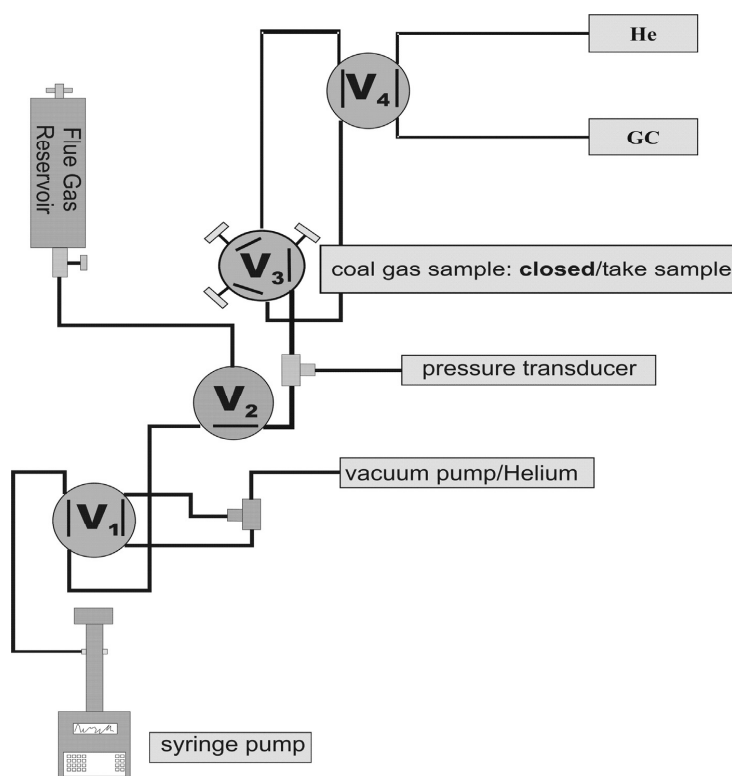

Fig. 3.3 Schematic of the experimental setup to conduct flue gas density measurements

3.2.3   Experimental procedure

Clarkson et al., 1997, have discussed the experimental procedure and theoretical background for the volumetric measurement for gas sorption isotherms on coal. Based on the experimental procedures of Mavor et al., 1990, the sorption experiments (pure CO$_2$ and flue gas) were performed at 353 K. At this temperature, pure CO$_2$ is in the supercritical state (T_c: 304.1 K; P_c: 7.38 MPa). The experimental method employed the mass balance principle, based

on careful volumetric measurements. After the removal of helium under vacuum, the reference cell was pressurized with CO_2 / flue gas. Where the required reference cell pressure was higher than the pressure in the gas bottle, a gas booster (Fig. 3.1) was used to achieve the required pressure. Once a stable pressure in the reference cell was obtained, a portion of the gas was transferred from the reference cell to the sample cell. Pressure and temperature were monitored constantly on the two sample cells and one reference cell to verify thermal and adsorption equilibration. Pressure equilibration times for the coal core varied between 48 to 72 h. After achieving pressure equilibration the reference volume was pressurized with additional gas and the process was repeated 5 to 7 times to reach the desired pressure.

For the preferential desorption measurements with flue gas, gas samples were extracted during desorption steps for chromatographic analysis. Ten gas samples were extracted and sampled in a gas sample bag for analysis. Care was taken to avoid air contamination. Each gas sample was analysed 50 times with the gas chromatograph.

3.2.3.1 *Volumetric method for adsorption capacity*

The process of adsorption removes sorbate gas molecules from the free gas phase, resulting in a decrease of the gas pressure within the sample cell. The operational procedure is the Gibbs approach, which assumes that the concentration of the gas is uniform up to a mathematical surface (Gibbs dividing surface) separating the homogeneous solid and the fluid phases. The Gibbs approach assumes a constant ratio of the condensed phase volume and void volume throughout (Krooss et al., 2002). Sorption results in a non-uniform concentration in the near vicinity of the solid surface and the formation of a sorbed phase (Fig. 3.2). At low pressures, this non-uniform density effects can be neglected. At higher pressures this problem is very perceptible as the amount of sorbed gas concentration increases. A correction for this sorbed phase volume gives the "absolute sorption" isotherm. But even such a correction does not take the effect of volumetric swelling of coal into account. This prompted us to present the data as a "Gibbs excess sorption" isotherm. The procedure for the multi-component isotherms is identical to the procedure for the pure gas isotherms. Mass balance considerations are used to calculate the adsorbed amounts at each pressure step j, where the total moles in the system at $n_{s,tot}^{j}$ is given as.

$$n_{s,tot}^{j} = n_{s,tot}^{j-1} + n_{ref,start}^{j} - n_{ref,end}^{j},$$ (3.1)

where the total moles in the system n_{s}^{j} is the sum of the adsorbed, free and dissolved in water

$$n_{s,tot}^{j} = n_{s,ads}^{j} + n_{s,free}^{j} + n_{s,water}^{j} + n_{s,leak}^{j}$$ (3.2)

where the cumulative leak $n_{s,leak}^{j}$ is given as

$$n_{s,leak}^{j} = n_{s,leak}^{j-1} + c^{j} * t^{j}$$ (3.3)

and the amount of dissolved water is given as

$$n_{s,water}^{j}(t) = m(P,T) * Mass_{water}$$ (3.4)

Pressures were converted to moles using the Redlich-Kwong EOS for CO_2 and the Peng-Robinson EOS for the flue gas and extracted mixtures. An EOS has been specifically worked out for flue gas and is in good correspondence with Peng-Robinson. The EOS for flue gas will be discussed in section 3.2.3.3. The solubility of CO_2 was calculated by using the CO_2 solubility model developed by Diamond, 2003.

3.2.3.2   Preferential sorption measurements with flue gas

Preferential sorption measurements with flue gas require an additional step to determine the relative concentrations of each component in the free gas phase. During the desorption step, free gas from the sample cell is expanded into the empty reference cell (Fig. 3.1). After equilibrium in the reference cell is reached, the gas is sampled and analyzed with the micro-GC. Since all gas concentration measurements are being carried out at near atmospheric conditions, the calibration of the micro-GC was rather easy.

3.2.3.3   Flue gas Equation of State

Generally, Equations of State (EOS) for single and mixed gases are based on theoretical or empirical studies. Besides EOS for several single gases (CH_4, N_2, CO_2, etc.), the different existing mixed gas EOS published for CH_4/CO_2, or components associated with flue gases, are inconsistent near the critical pressure. Therefore an experimental procedure to determine the flue gas EOS of a given composition was developed under isothermal conditions (45^0C) and pressures up to 180 bars. The method is based on a volumetric setup, in combination with gas chromatographic analysis. The chromatographic analysis measured the component concentrations in a known volume as a function of the pressure.

Initially a very precise leakage test was performed, because of the very small volumes used in this experimental setup. Helium was used to do the leakage tests. A flue gas reservoir (2000 cc at about 40 bar) was connected to the syringe pump via valves V1 and V2 (Fig. 3.3). Opening V1 and V2 filled the syringe pump. After filling, V2 was switched to get the pump connected to valve V3. Starting pressure in the pump was around 30 bars. Thereafter, valve V3 was switched and the flue gas was allowed to enter the sample loop as well as the micro-sampling valve V4. For the pressure dependent density measurements, the pump was used to set the pressure corresponding to a sampling step. Data acquisition was automated.

Density measurements were performed up to a pressure of 180 bars, at 5 bar steps below 30 bar and at 10 bar steps above 30 bars. At each pressure step, the flue gas composition was analyzed by the gas chromatograph. The details regarding the column and

the carrier gas used are provided in Table 3.2. The amount injected in the gas chromatograph (GC) was too small to detect the very low concentrations of SO$_2$ (0.106%) and CO (0.01%). These low concentrations have been considered irrelevant for the determination of the density of the gas mixture.

3.3 Results and discussion

Three single component CO$_2$ and four flue gas sorption experiments were performed at medium to high pressures (5 to 11 MPa) and at temperatures of 353 K. A set of volumetric gas chromatographic measurements was also performed to determine the flue gas equation of state. The experiments with the corresponding experimental conditions are listed below.

- Two with CO$_2$ on dry Silesia coal: Dry CO$_2$ (1) and Dry CO$_2$ (2) ~ 8 MPa.

- One with CO$_2$ on wet Silesia coal: Wet CO$_2$ (1) ~ 11 MPa.

- Two with flue gas on dry Silesia coal: Dry flue (1) ~ 6 MPa and Dry flue (2) ~ 10 MPa.

- Two with flue gas on wet Silesia coal: Wet Flue (1) and Wet Flue (2) ~ 11 MPa.

3.3.1 Comparison of CO$_2$ and flue gas excess sorption capacities

The results of the sorption measurements performed with CO$_2$ at pressures up to 11 MPa on dry and wet Silesia coal are in Fig. 3.4 and Fig. 3.5. The CO$_2$ isotherms on dry coal show some distinct differences (Fig. 3.4) in the shape of the isotherms and the absolute values of the excess sorption capacities. The deviation is either due to the heterogeneity of the large coal core or due to experimental inaccuracies. No duplicate experiment was performed for CO$_2$ (Fig. 3.5) on the wet coal. The sorption capacity of coal for CO$_2$ is higher for dry coal (~1.9 mmole CO$_2$/g coal) than for wet coal (~1.3 mmole CO$_2$/g coal). Thus the presence of water reduces CO$_2$ sorption. Both the CO$_2$ isotherm on dry and wet coal does tend to achieve limiting values at 8 and 10 MPa respectively. One of the possible reasons for this deviation might be because of the sequential measurements on a single sample. Each cycle of CO$_2$ sorption removes a considerable amount of the mobile molecular phase from the coal.

The flue gas isotherms on dry and wet coal (Figs. 3.6 and 3.7) do agree with each other. At low pressures the difference in sorption capacity of dry and wet coal for flue gas is within the experimental error of the measurements. No significant difference between the dry and wet coal isotherm at low pressures was observed. At higher pressures (> 8 MPa) the sorption capacity of dry coal is significantly higher than for wet coal. Again, at high pressure the presence of water reduces the number of available sorption sites. Because so little gas adsorbs in the flue gas experiments, the reduction in sorption sites by the presence of water is negligible. No limiting value was achieved in this case.

The sorption capacity of coal is much higher for pure CO$_2$ than for flue gas. The shape of the adsorption isotherms also differs significantly. Addition of extra components reduces the sorption capacity, mainly by decreasing the partial pressure of the main adsorbing component.
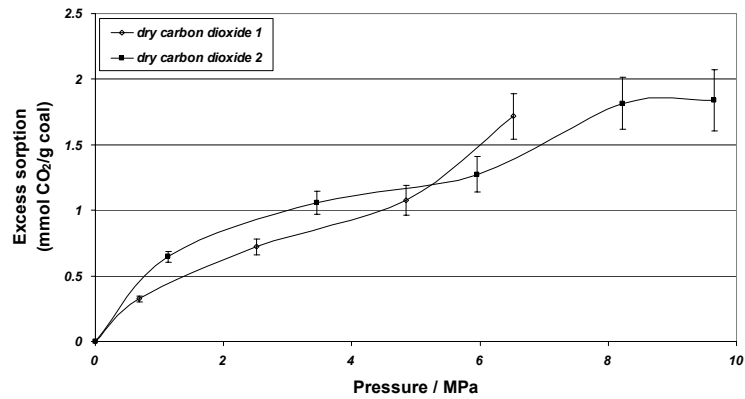

Fig. 3.4 CO$_2$ sorption isotherms on dry Silesia coal. The error bars are a measure of the experimental inaccuracies.
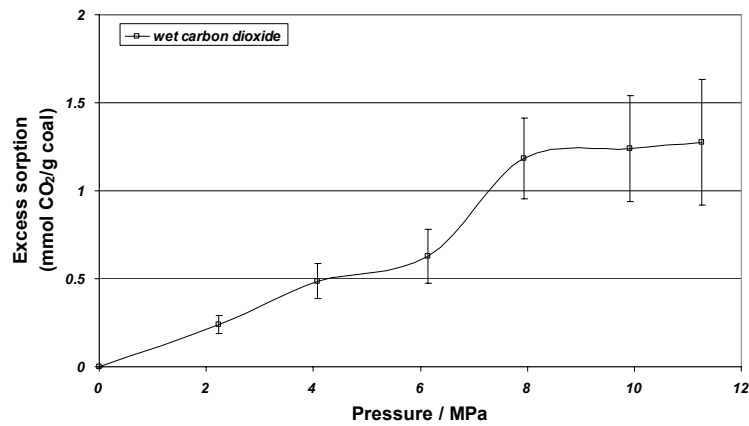

Fig. 3.5 CO$_2$ sorption isotherm on wet Silesia coal

Volumetric sorption measurements are highly sensitive to experimental uncertainties, because the actual adsorbed amount is only a fraction of the total amount of gas in the setup. Therefore small deviations in the total gas content can cause large deviations in the calculated

sorption. This sensitivity is evident not only in the influence of random uncertainties, but also in the influence of systematic uncertainties.
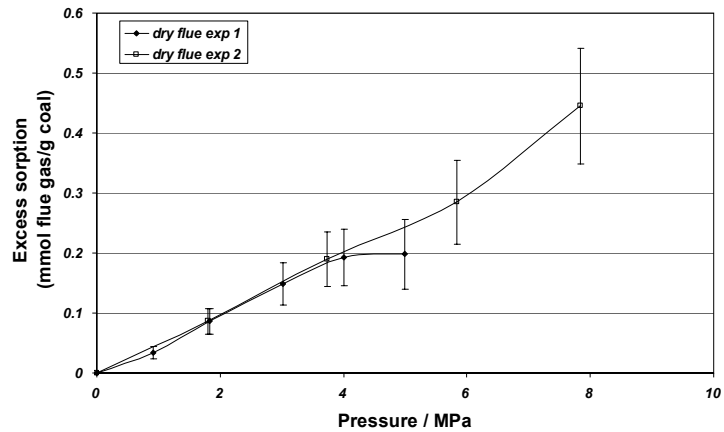

Fig. 3.6 Flue gas sorption isotherms on dry Silesia coal. The error bars from both the experiments suggest that the error is more systematic in nature and tends to grow with increasing pressure.
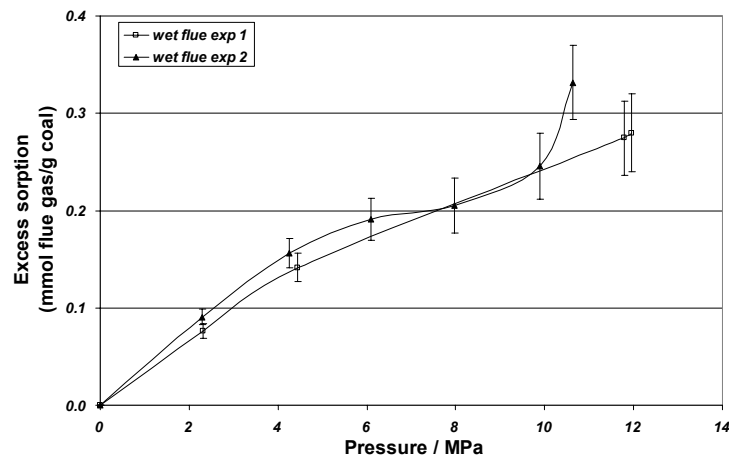

Fig. 3.7 Flue gas sorption isotherms on wet Silesia coal. The errors are reproducible inaccuracies that are consistent in magnitude with increasing pressures. These are systematic errors, probably due to a problem with the pressure and temperature measuring devices, which persists throughout the entire experiment.

Inaccuracies in the volumes or pressure and temperature calibration will introduce a systematic deviation in the measured sorption. This effect becomes even more pronounced for CO$_2$, due to its variability of density with pressure and temperature. Another cause of inaccuracy in the measured sorption is the inaccuracy of cubic EOS'^{s} to predict CO$_2$ density as a function of pressure and temperature.

Due to the preliminary nature of the investigation, the uncertainty was estimated to be 10% of the total gas content. Successfully completed duplicate isotherms correspond within this uncertainty, except for the dry CO$_2$ isotherms in Fig. 3.4. Possible causes for this deviation are legion, ranging from different pre-treatment to systematic uncertainties. Since the aim of the investigation was to experimentally verify the preferred sorption to coal of CO$_2$ from a flue gas, no attempt was made to isolate and eliminate the cause of experimental inaccuracies in the CO$_2$ sorption isotherms.

3.3.2   Preferential sorption measurements with flue gas on dry and wet coal

The measured composition of the extracted gas samples is shown in Fig's. 3.8-3.11. The composition of the extracted (non-adsorbed) gas from the first and the last pressure steps is shown in Table 3.3. The first and the last extraction step correspond to high and low pressure respectively. The noted compositions are normalized to 100% with respect to the total gas content. Any component concentration being reported higher than its initial concentration in the flue gas refers to the preferential presence of that component in the free gas phase.

	Unit	flue gas	Dry Flue (1)		Dry Flue (2)		Wet Flue (1)		Wet Flue (2)	
			first	last	first	last	first	last	first	last
H$_2$	mole%	9.00	9.8	5.3	9.4	6.1	8.7	8.8	9.1	8.0
O$_2$	mole%	3.00	n.r.	n.r.	n.r.	n.r.	n.r.	n.r.	n.r.	n.r.
N$_2$	mole%	73.974	82.6	80.4	85.0	80.9	79.6	64.6	78.5	72.2
CH$_4$	mole%	3.01	2.4	3.4	2.6	3.3	3.1	4.2	3.0	3.5
CO$_2$	mole%	10.90	4.4	9.2	2.5	8.9	7.5	21.7	8.8	16.0
SO$_2$	mole%	0.11	n.r.	n.r.	n.r.	n.r.	n.r.	n.r.	n.r.	n.r.
CO	mole%	1.0E-04	n.d.	n.d.	n.d.	n.d.	n.d.	n.d.	n.d.	n.d.

Table 3.3. Composition of the first and the last extraction step from all four flue gas desorption experiments on wet and dry coal core.

The measured SO$_2$ concentrations vary between 0.03 and 0.89 mole percent of the total gas in all measurements. The SO$_2$ concentration does not show a trend with consecutive extraction steps. Measured SO$_2$ concentrations are considered unreliable, due to a lack in

repeatability. The measured O$_2$ concentrations vary between 0.06 and 1 mole percent of the total gas extracted in all experiments. It does not show a trend with consecutive extraction steps. Therefore they are also considered unreliable. However, it is discernible that most of the O$_2$ added to the sample cell is not extracted. This indicates that the O$_2$ reacts or chemisorbs on the coal. Some O$_2$ measurements are missing due to experimental constraints.

The results of preferential sorption measurements of flue gas on dry coal are documented in Figs. 3.8 and 3.9. All reliable gas measurements show similarities in both the dry experiments. N$_2$ and hydrogen show decreasing concentrations, and CO$_2$ and CH$_4$ show increasing concentrations with decreasing pressures. In absolute terms the N$_2$ concentrations show excellent agreement. The concentration is perpetually higher than the original
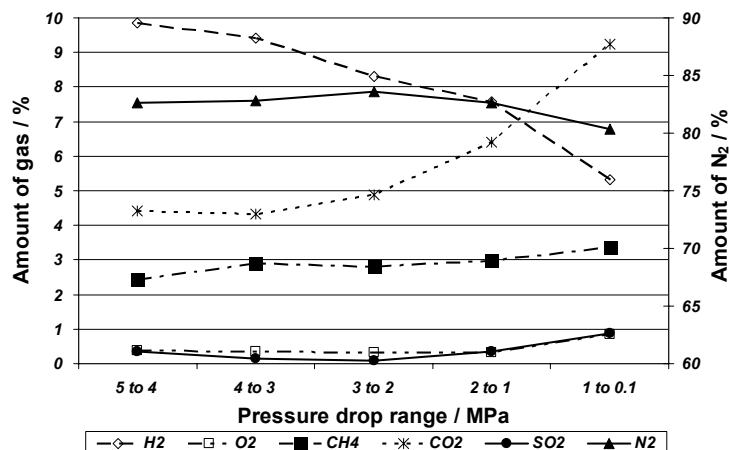

Fig. 3.8 Gas composition for different extraction steps in Dry flue (1). The points on the far left represents the initial condition before desorption starts.

concentration in the injectant. For CH$_4$ an increasing trend from 2.4 and 2.6 mole % to 3.4 and 3.3 mole % is seen. The concentration starts below the CH$_4$ injectant concentration and ends higher. Also for CO$_2$, an increasing concentration trend from 4.4 and 2.6 to 9.2 and 8.9 mole % is seen. The concentration is perpetually below the original concentration in the flue gas. For H$_2$ a decreasing trend from 9.8 and 9.4 mole % to 5.3 and 6.1 mole % is measured. The concentration starts above the original concentration in the flue gas and ends below it. The low CO$_2$ concentrations in the first extraction step (4.4% and 2.5% for the dry coal; 7.5% and 8.8% for the wet coal) indicate that CO$_2$ is being preferentially sorbed over all other components under both dry and wet conditions. A high N$_2$ concentration in the first extraction step (82.6%

and 85.0% for the dry coal; 79.6% and 78.5% for the wet coal) indicates the preferential presence of N$_2$ in the free gas phase.
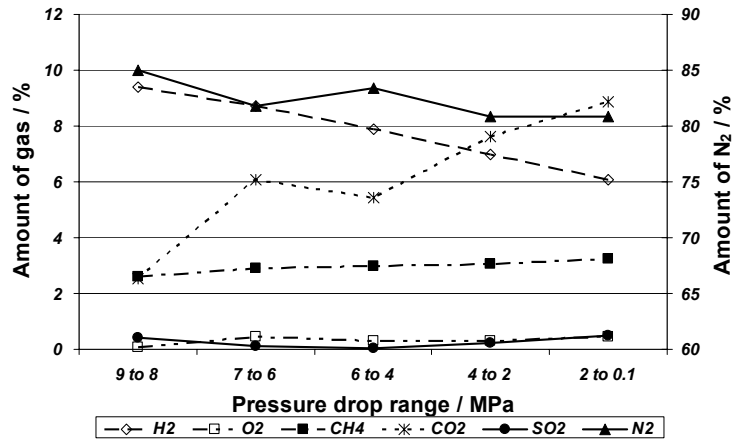

Fig. 3.9 Gas composition for different extraction steps in Dry flue (2)

The results of preferential sorption measurements of flue gas on wet coal are documented in Figs. 3.10 and 3.11. All measurements of the gas concentration show approximately the same trend in both wet experiments; N$_2$ shows a decreasing trend, and CO$_2$ and CH$_4$ show an increasing trend. Hydrogen concentrations show a very small decreasing trend. The N$_2$ concentration shows a decreasing trend from 79.6 and 78.5 to 64.6 and 72.2 mole %. The N$_2$ concentration starts above the starting conditions and ends below that. The CH$_4$ concentration shows an increasing trend from 3.1 and 3.0 to 4.2 and 3.5 mole %. The concentration starts above the original concentration in the flue gas and ends higher, suggesting that CH$_4$ is preferentially desorbed at lower pressures. The CO$_2$ concentration also shows an increasing trend from 7.5 and 8.8 to 21.7 and 15.0 mole %. The concentration starts below the original concentration and ends much above, it suggesting preferential desorption at low pressures. The H$_2$ concentration shows acceptable correspondence, from 8.7 and 9.1 to 8.8 and 8.0 mole %. The concentration is nearly constant in Wet Flue (1) and decreases slightly in Wet Flue (2).
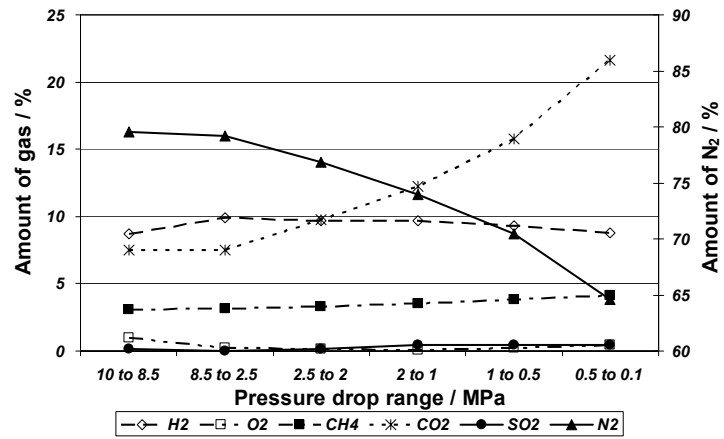
Fig. 3.10 Gas composition for different extraction steps in Wet flue (1)
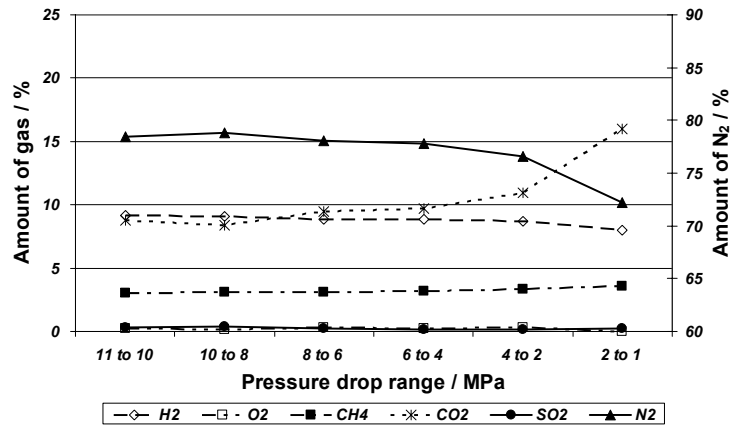
Fig. 3.11 Gas composition for different extraction steps in Wet flue (2)

3.3.3 Density measurements of flue gas and its components

Density measurements at 45^0C and pressures up to ~18 MPa were performed for N_2, CO_2, CH_4, H_2 and O_2 using two different chromatographic columns as shown in Table 3.1. The results of the partial densities of the single components are shown in Fig. 3.12. The regressions of the different density curves with pressure are good, ranging between 0.9944 and 0.9999.

Fig. 3.13 shows a direct comparison of the flue gas density obtained in this study with reference data from the literature for pure N_2 (Span et al., 2000) and the same flue gas composition analyzed (Peng and Robinson, 1976). It shows that all three density curves are in good agreement with each other, demonstrating that N_2 (74%) controls the density of the flue gas and that additional components have only a negligible effect on the density curves.
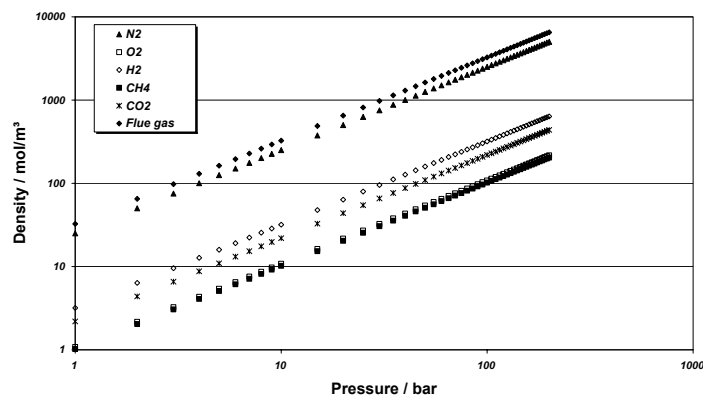

Fig. 3.12 Experimentally determined partial densities as a function of pressure for N_2, H_2, O_2, CO_2 and CH_4.
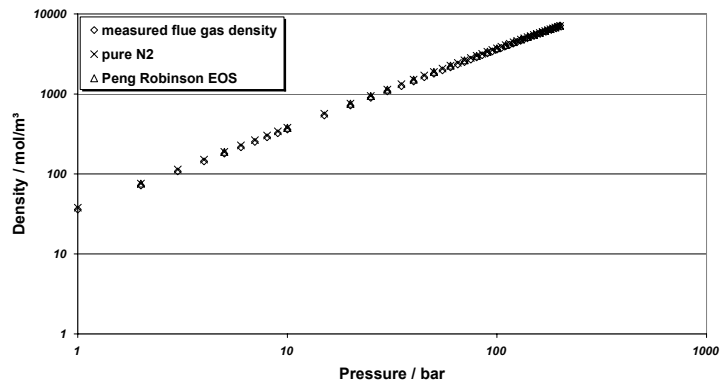

Fig. 3.13 Comparison of measured flue gas density with pure N_2 (Span et al., 2000) and Peng and Robinson, 1976.

3.4 Conclusions

- CO$_2$ compared to CH$_4$ is the most preferred adsorbed component in both the wet and dry experiments: CO$_2$ shows the largest decrease in concentration at the end of the adsorption experiment and shows the largest increase (preferentially desorbed) at the end of the extraction steps. The preference has decreased with the addition of water to the coal. Thus a considerable amount of CO$_2$ can be stripped off the flue gas by making it sorb onto coal at high pressures.

- CH$_4$ is the second most preferred component: CH$_4$ shows a slight preferential desorption at the end of the extraction steps. Its preference has decreased slightly with the addition of water to the coal.

- The density measurement of the flue gas has been successfully performed, suggesting a close resemblance to the pure N$_2$ behavior.

- H$_2$ hardly adsorbed to the coal. It adsorbed the least in the dry experiments, and showed the largest decrease. The preference increased with the addition of water, dissolution of H$_2$ in water having a significant effect (k_H = 121.2 x 10^6 Pa dm^3/mol).

- N$_2$ adsorbs very little to the coal. It adsorbs even less in the wet experiments, as is evident from the large decrease during the wet extraction experiment. The preference of sorption is thus decreased with the addition of water.

- The good correspondence of the single CO$_2$ sorption points in the flue gas experiments to the pure CO$_2$ isotherms indicate that adsorption of CO$_2$ to coal is not significantly hindered by the addition of other gases, other than dilution effect of the pressure.

- For the injection of flue gas on an industrial scale, it means that coal may be successfully used to filter the CO$_2$ in. Large volumes of flue gas could be directly sequestered in coal. Enhancement of CH$_4$ production via flue gas adsorption could not be established in these experiments.

Nomenclature

$n_{s,tot}^{j}$ = total amount of gas in the sample cell at step *j* [moles],

$n_{s,tot}^{j-1}$ = total amount of gas in the sample cell at step *j-1* [moles],

$n_{s,ads}^{j}$ = amount of gas adsorbed in the sample cell at step *j* [moles],

$n_{s,water}^{j}$ = amount of gas dissolved in the water in the sample cell at step *j* [moles],

$n_{s,leak}^{j}$ = amount of gas leaked (if any) from the sample cell at the end of step *j* [moles],

$n_{s,free}^{j}$ = amount of gas in the free phase at step j [moles],

$n_{ref,end}^{j}$ = amount of gas in the reference cell before step j [moles],

$n_{ref,start}^{j}$ = amount of gas in the reference cell after step j [moles],

c^{j} = leak rate after step j [Pa/s],

t^{j} = time at step j [s],

$Mass_{water}$ = mass of water in the sample cell [g],

$m(P,T)$ = Henry's constant

4 Swelling and anomalous diffusion mechanisms of CO$_2$ in coal

4.1 Introduction

Pressure induced diffusion plays an important part in many engineering applications, such as polymer sciences and biomedical applications. It is of interest to investigate its importance in CO$_2$ induced swelling of coal in carbon sequestration applications. It is shown that the transport equation, used in the literature, can be derived from extended non-equilibrium thermodynamics. This equation is critically evaluated to explore the possible occurrence of super-diffusion. An implicit numerical model is derived and the model is validated using analytical solutions for both the linearized case, but including a jump in the diffusion coefficients.

The "swelling" of coal by a penetrant can be referred to as, an increase in the volume occupied by the coal as a result of the viscoelastic relaxation of it's highly crosslinked macromolecular structure. Although the macro molecular network structure does not dissolve, the penetrant is almost universally termed as "solvent". Thus a coal - coal hydrogen bond or any other weaker bond will be replaced by a coal - solvent bond only if the new coal - solvent bond is thermodynamically favored. If intramolecular bonding in the coal contributes significantly to its structural integrity, then strong coal - solvent bonding should disrupt such a structure, which results into coal swelling.

A CO$_2$ molecule placed between the polymer chains of coal disrupts partly the original structure if the sorption takes place in locations where the available volume between the chains is smaller than the actual volume of the CO$_2$ molecule. This disruption requires energy to overcome attractive forces between the chains, which can be described in the form of Lennard-Jones potentials and coulombic electrostatic potentials. Furthermore, the energy which is required to change the conformation of the polymer chains: rotational alterations of sp^3- bonds and out-of-plane bending of sp^2-bonds will be responsible for the change of the chain conformation.

The similarities in structure between coal and glassy polymers have led to the perception that CO$_2$ penetration has many analogous features that are observed for organic sorbents penetrating into glassy polymers. In other words, the application of theories of sorption behavior of polymers to coals has been proposed. For the interpretation of the experiments we assume that a matrix slab of more or less constant thickness exists between cleats.

During penetrant transport at low or moderate temperatures into the macromolecular network of coal, the network density decreases which results into an increase of the large

molecular chain motions (Ritger and Peppas, 1987). This increase of the penetrant concentration of the network can be viewed as an effective decrease of the glass transition temperature (Hsieh and Duda, 1987). Structural changes induced during this process include swelling, microcavity formation and primary phase transition requiring rearrangements of each chain segments. Such changes are dominated by relaxational phenomenon.

The diffusion of gas into glassy polymers varies between two extremes. If the diffusion is controlled by the concentration gradient between the centre and the outside of the coal matrix, the diffusion mechanism is Fickian. If the transport is controlled by a stress gradient induced by the penetration of molecules, the diffusion mechanism is anomalous. For polymers the following observations are made.

The diffusion in glassy polymers often does not fit the Fickian diffusion model. Alfrey, Gurnee and Lloyd, 1966 have presented a second limiting case for sorption, where the rate of transport is entirely controlled by molecular relaxation. This type of transport mechanism is designated as Case II transport. The characteristics of Case II diffusion in coal are considered to be as follows:

(a) The penetrant is observed to advance through the macromolecular glassy substance with a sharp upstream boundary to a rubber zone. Downstream the penetrant concentration is zero. Upstream the rubber zone the penetrant is at equilibrium concentration. The rubber part is substantially swollen with respect to the glassy part.

(b) After some initializing effects a semi-steady state occurs, where a given concentration profile travels through the slab

(c) The boundary between the swollen matrix and the glassy material advances at a constant velocity.

(d) The initial weight gain of the sample has a linear propagation with time.

(e) The swollen matrix behind the advancing front is at an uniform state of swelling.

(f) Many authors state that the Fickian flux of solvent must be supplemented by a flux due to stress gradient which exists across the moving boundary.

(g) Some process of molecular relaxation are possible for control of the front velocity.

(h) Peterlin, 1977 suggests that the sharp diffusion front, characteristic of the Case II process, is preceeded by a region of penetrant at low concentration which forms a precursor to the front and results from Fickian diffusion into the glassy material ahead of the front. He recognizes that the velocity of the front is controlled by some independent material property, and suggests time dependent rupture and disentanglement of molecular chains as possible process.

(i) Thomas and Windle (1982) proposed that the rate controlling step at the penetrant front is the time dependent mechanical deformation of the glassy polymer in response to the thermodynamic swelling stress.

Most transport processes in coal can be represented by a coupling of the Fickian and Case II transport mechanisms. A simple expression of this observation can be written for long term behavior by adding the diffusion controlled to relaxation controlled uptakes:

$$\frac{M_t}{M_e} = k_1\sqrt{t} + k_2 t \approx kt^n, \tag{4.1}$$

where M_t is the mass uptake at time t and M_e is the equilibrium mass uptake, k is a constant incorporating characteristics of the macromolecular network system and the penetrant, and n is the diffusional exponent, which is indicative of the transport mechanism. Eq. 4.1 is valid for the first 60% of the normalized penetrant uptake. Fickian diffusion and Case II transport for a thin slab are defined by n equal to 0.5 and n equal to 1 respectively. Anomalous transport behavior is intermediate between Fickian and Case II, and has a value of n between 0.5 and 1. The geometry of the sample plays an important role in determining the value of the diffusion exponent, n. An analysis of the geometry of the particle with the diffusion exponent has been done by Ritger et al., 1987. The results from this analysis show that Fickian diffusion and Case II transport in a cylindrical sample (inside to outside) are defined by n = 0.451 ± 0.004 and n = 0.89 ± 0.02 respectively. Similar analysis was performed on the first 60% of the sorption process for Fickian diffusion and Case II transport in a spherical sample.

Diffusional exponent (n)			De	Transport mechanism
Plane sheet	Cylinder	Sphere		
0.5	0.45	0.43	>>1 or <<1	Fickian
1.0>n >0.5	0.89>n >0.45	0.85>n >0.43	0	Anomalous
1.0	0.89	0.85	1.0	Case II
n>1.0	n>0.89	n>0.85	-	Super case II

Table 4.1 Dependence of diffusion exponent on sample geometry

The results of this analysis show that Fickian diffusion and Case II transport are defined by n = 0.432 ± 0.007 and 0.85 ± 0.02 respectively.

Vrentas et al. (1975, 1977) introduced the Deborah number (D_e) as a means of characterizing penetrant uptake. In terms of D_e, the nature of the sorption process can be distinguished by the ratio of two characteristic times, namely (i) λ, for the macromolecular

penetrant system is a relaxation time; and (ii) a characteristic diffusion time, θ. The Deborah number is written as,

$$D_e = \frac{\lambda}{\theta}. \tag{4.2}$$

The dependence of Deborah number and diffusional exponent on sample geometry is shown in Table. 4.1. For $D_e \gg 1$, i.e. relaxation time much larger than diffusion time, there is effectively no time variation of the macromolecular structure during the diffusion process. Such a sorption process can be described by Fickian diffusion. For $D_e \ll 1$, i.e. relaxation time much smaller than diffusion time, conformational changes in the macromolecular structure occur instantaneously with respect to the time scale of diffusion. This type of sorption process is also described by Fickian diffusion. Hence, in relation to the diffusional exponent n, systems exhibiting $D_e \gg 1$ or $D_e \ll 1$ can be characterized by n equal to 0.5 (for slab geometry). When D_e = 0(1), i.e. the relaxation and diffusion times are of the same order of magnitude, case II diffusion becomes relevant. As the penetrant diffuses into the macromolecular network, rearrangement of the chains does not occur immediately. Thus, the instantaneous macromolecular configuration may differ from the equilibrium network structure at the same water concentration. This situation represents anomalous transport behavior, which is defined by values of n between 0.5 and 1. When $D_e = 1$, uptake is controlled by macromolecular chain relaxation only. This value of D_e represents Case II transport where the diffusional exponent is equal to 1. It has been reported that the transport mechanism observed for a coal / penetrant system depends on the sample dimensions. This phenomenological observation can be interpreted in terms of the diffusional Deborah number in the following way. A characteristic diffusion time for one dimensional diffusion in thin films is defined as,

$$\theta = \frac{\delta^2}{D}, \tag{4.3}$$

where the characteristic diffusion length, δ, is the film half thickness, $l\,/\,2$, and D is the gas diffusion coefficient in the macromolecular structure. Thus, the diffusional Deborah number can be written as,

$$\frac{\lambda D}{\delta^2} = \frac{4\lambda D}{l^2}. \tag{4.4}$$

This presumption, that anomalous diffusion is the prevailing transport mechanism for CO_2 in coal, is to be verified in our experiments.

4.2   Dynamic volumetric swelling experiments

The diffusion process is closely interlinked to the dynamic volumetric swelling (DVS) of coal. The increase in volume of a coal sample is a function of time. Only the adsorbent that has diffused into the "bulk" structure induces coal swelling. The increase in volume is proportional to the amount of material that has diffused into the "bulk". This process disregards all occluded sorbents. At any time t, the amount of adsorbent that has diffused into the "bulk" is proportional to the volumetric swelling. S_t is the amount of volumetric swelling at time t, and S_e is the equilibrium swelling. The variation of mass uptake with time has the same apparent functional variation for Fickian and relaxation diffusion. To distinguish graphically between the extreme modes of diffusion (bounds) it is conventional to plot the dimensionless mass uptake
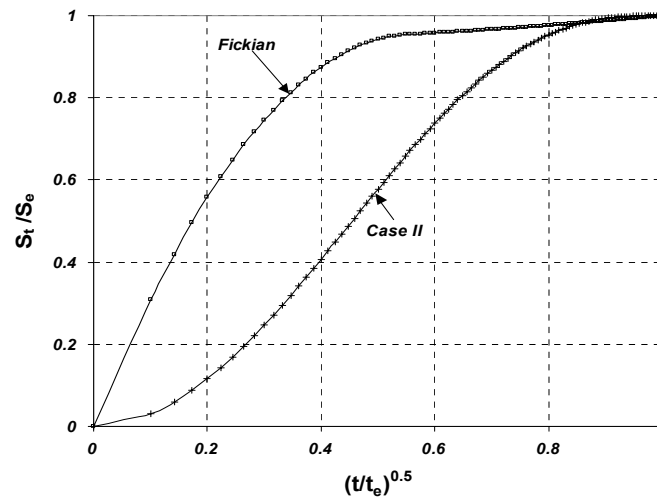

Fig. 4.1 Generalized plots of the dynamic volumetric swelling, plotted as dimensionless mass uptake vs. square root of dimensionless time for limiting Fickian and relaxation controlled Case II diffusion in a spherical particle (inside – outside).

(S_t / S_e) as a function of the square root of the dimensionless time (t / t_e) (Carslaw and Jaeger, 1986). The Fickian curve increases monotonically, whereas the relaxation controlled mode has an inflection at low $(t / t_e)^{1/2}$ (Fig. 4.1). It needs to be noted that the functional dependence is related to a constant boundary condition. However, for long times the behavior can still be proportional to the square root of time.

A set-up was designed to measure volumetric strain due to changes in sorbed gas concentration while keeping the net stress on the coal sample constant. Details regarding the

construction of the set-up, procedure to measure the linear and the radial strain and the experimental procedure have been discussed in Chapter 5. The schematic of the set-up is shown in Fig. 5.1a.

Assuming isotropic stress conditions, the volumetric strain for the coal core was calculated as follows,

$$\epsilon_v = (1 + \epsilon_a)(1 + \epsilon_r)^2 - 1, \tag{4.5}$$

Sample	Warndt Luisenthal
Carbon [%]	81.3
Hydrogen [%]	5.58
Nitrogen [%]	1.88
Sulphur [%]	0.69
Oxygen (diff.) [%]	5.47
H/C	0.82
O/C	0.05
Rmax [%]	0.71
Vitrinite [%]	74.4
Liptinite [%]	15.6
Inertinite [%]	9
Minerals [%]	1
Specific surface [m²/g]	104
Micropore volume [cm³/g]	0.03545
Diameter [mm]	74.48
Length [mm]	154

Table 4.2 Sample properties

where ϵ_v , ϵ_a and ϵ_r are volumetric, axial and radial strains respectively.

4.2.1 Results and discussion

Dynamic volumetric swelling (DVS) experiments were performed on a Warndt Luisenthal coal core (0.71% R_{max}) with CO_2 at 45°C. The tests start with a complex procedure of mounting the coal core sample in a rubber sleeve and loading it in the high-pressure cell; leak free. The sample cell was connected to a vacuum pump, for at least a week, to eliminate any form of residual gas or moisture. Prior to the start of the experiment, strain gauges were calibrated for

temperature variations. During an experiment the CO$_2$ is fed in the pressure cell to a certain pressure and the pressure is allowed to equilibrate over time. A DVS measurement on the first Warndt Luisenthal experiment is shown in Fig. 4.2.
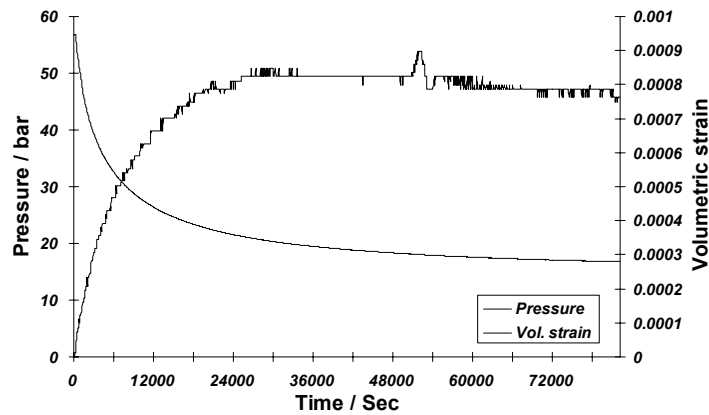

Fig. 4.2 Dynamic Volumetric Swelling (DVS), plotted as the volumetric strain and the pressure against time from the first pressure step of the swelling experiment on Warndt Luisenthal coal (0.71% R$_{max}$) at 45°C with CO$_2$

The plots correspond to the experimental data from the first pressure step. The pressure decline curve corresponds to the uptake of CO$_2$ and is assumed to be proportional to the dynamic volumetric swelling. A repeat Warndt Luisenthal experiment is performed and the the DVS measurement is shown in Fig. 4.5. In Figs. 4.3 and 4.6 the equilibrium swelling ratio is plotted against the square root of the dimensionless time. Assuming that mass uptake is proportional to the amount of swelling observed, and using Eq. 4.1, the transport phenomenon of CO$_2$ in coal can be determined. Plots of $\ln\left[\left(S_e - S_t\right)/S_e\right]$ against time, for the first and the repeat Warndt Luisenthal experiments are shown in Figs. 4.4 and 4.7. To determine the mechanism of initial diffusion of CO$_2$ into the coal, the data from the initial CO$_2$ swelling region were fitted to Eq. 4.1, where k is a constant and n is the diffusion exponent. Values of 0.5 < n < 1 the diffusion is anomalous. For the first and the repeat Warndt Luisenthal experiment, diffusion exponents of 0.78 and 0.72 were calculated respectively. These results are an indication towards the fact that CO$_2$ diffusion in coal might be anomalous in nature. However this transport process is highly dependent on the geometry of the sample. The time dependence is further complicated by the fact that the boundary condition in these experiments is not constant. The other complication is the fact that there is a start-up time. Judging the existence of anomalous diffusion requires a much more complicated analysis than performed in the literature.
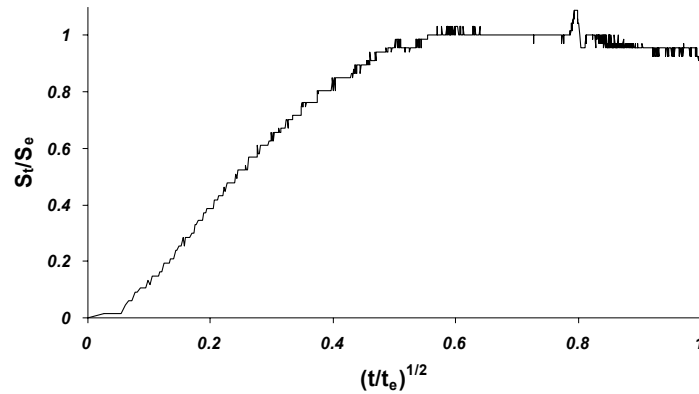
Fig. 4.3 Plot of the Dynamic Volumetric Swelling, plotted as dimensionless mass uptake against the square root of dimensionless time from the swelling experiment of Warndt Luisenthal coal (0.71% R_{max}) at 45°C with CO_2. The time dependence is complicated by the fact that the boundary condition of these experiments is not constant. The other complication seen is the fact that there is a start-up effect.

Fig. 4.4 Variations of ln[(S_e-S_t)/S_e] with time for the swelling of Warndt Luisenthal coal (0.71% R_{max}) at 45°C with CO_2
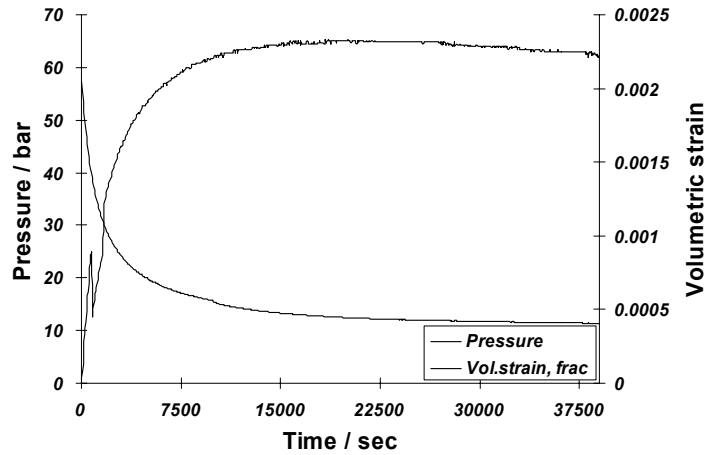
Fig. 4.5 Dynamic Volumetric Swelling (DVS), plotted as the volumetric strain and the pressure against time from the first pressure step of the repeat swelling experiment on Warndt Luisenthal coal (0.71% R$_{max}$) at 45°C with CO$_2$.

Fig. 4.6 Plot of the Dynamic Volumetric Swelling, plotted as dimensionless mass uptake against the square root of dimensionless time from the repeat swelling experiment of Warndt Luisenthal coal (0.71% R$_{max}$) at 45°C with CO$_2$. The time dependence is complicated by the fact that the boundary condition of these experiments is not constant. The other complication seen is the fact that there is a start-up effect.
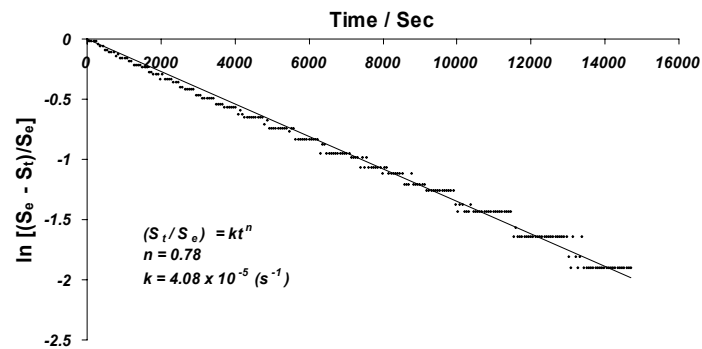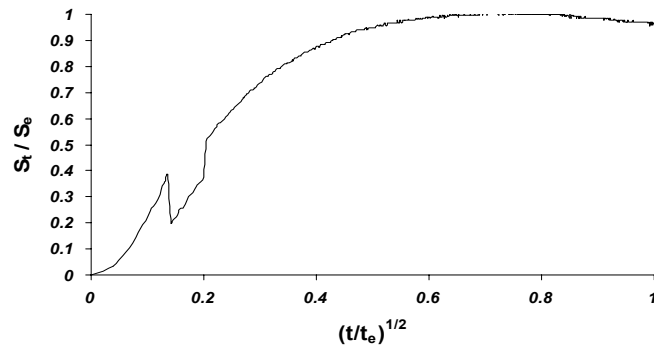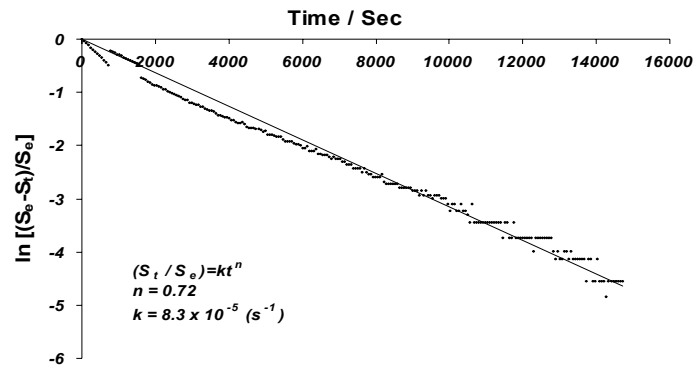
Fig. 4.7 Variations of $\ln[(S_e - S_t)/S_e]$ with time for the repeat swelling of Warndt Luisenthal coal (0.71% R_{max}) at 45°C with CO_2

To understand the physics behind such a complex relaxation driven diffusion process, a fully implicit numerical scheme has been presented. No validation of the experimental results has been done with the present model.

4.3 A Case II diffusion model in coal

4.3.1 Introduction

Coal has a large capacity to sorb, and transform in the process from a stiff glassy coal to a rubbery solid. Unlike the Fickian diffusion, the penetration of a sorbent molecule into coal is accompanied by swelling. The Thomas and Windle model stimulated experimental research of Case II sorption, particularly by Kramer et al. (1988, 1991) on a number of polymer / sorbent systems using the Rutherford backscattering technique. Hui et al. (1987) dealt with both the initial transient penetration of the sorbent and the final steady state motion of the sorption front - all within the framework of the Thomas and Windle model. The experiments and these more detailed models showed that while the Thomas and Windle model has a successful qualitative framework of most of the important mechanistic factors, it is unable to provide a quantitatively accurate statement of the kinetics of the sorbent penetration. The latter requires a more highly non-linear material deformation resistance. There has been a number of other model developments of Case II sorption such as, e.g. of Govindjee et al. (1993) that emphasize the representation of the thermodynamic driving forces arising from activity gradients and a glass to rubber transition. A distinguishing feature of Case II sorption is the associated material misfit produced by the sorbent; the development of internal stresses must be an important

component of the process. Alternatively, there must be other effects of applied external stresses or pressures, which accelerate or retard the diffusion process. Thomas and Windle have rightly noted that the presence of an imposed stress will suppress the equilibrium of the sorbent in the glassy coal at a given temperature significantly. Durning (1985) extended the Thomas and Windle model using irreversible thermodynamics. They replaced the viscous model with the Maxwell viscoelastic model, so that a relaxation time can be defined. The relation between osmotic pressure and the stresses on the coal was analyzed using the force balance. Argon et al. (1999) presented a mechanistic model, which considers the conditions that govern the self-similar propagation of fully developed Case II sorption fronts, combined with their Fickian precursors. The principal point of departure from all other models is the specific considerations of the effects of the sorbent induced material misfit and the non-linear viscoelastic response of the constrained coal matrix to the misfit induced effective stresses. This stress has been termed as the swelling stress (P_{xx}), and is defined as the pressure of an element of coal matrix saturated with the adsorbent (CO$_2$ / CH$_4$ / N$_2$) avoiding at the same time deformation. The very definition makes it clear that the measurement, or measurement methodology of swelling stress, is not a matter to be easily accomplished. From the viewpoint of thermodynamics, swelling stress represents a kind of energy. In the case of free swelling (unconstrained laboratory conditions) it turns out to be a volume change (dV). Swelling stress only occurs in the case of constrained swelling. The concept of swelling stress has been described in Chapter 5, Fig. 5.10. Considering a deformed domain, a process of back compaction can be visualized to understand the swelling stress (P_{xx}).

The Thomas and Windle model is able to predict successfully the essential aspects of Case II diffusion. The model proposes that the diffusive process is strongly coupled to the mechanical response of coal. This happens such that the rate at which the penetrant is absorbed must be compatible with the swelling rate, controlled by the creep deformation of the surrounding coal. It is a diffusion which is stress driven. The creep deformation depends on both the osmotic pressure, which drives the swelling, and the viscosity of the material. The viscosity and diffusivity of the coal are extremely sensitive to the concentration of the penetrant. The penetrant produces very large decreases in viscosity and increases in diffusivity within a very narrow range of concentration (Fig. 4.8). These changes are due to plasticization caused by sorption of the penetrant, which produces a decrease in coal segmental relaxation times from very large, glassy behaviour, to very short, rubbery behaviour. It is this strong dependence of viscosity and diffusivity on penetrant concentration that produces the sharp front which is a characteristic of Case II or anomalous diffusion (Thomas and Windle, 1982).
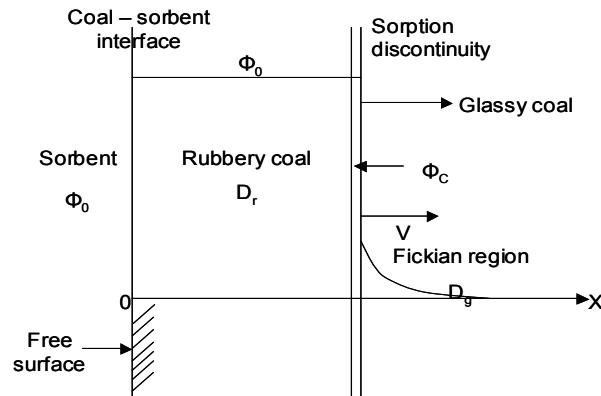
Fig. 4.8 Idealized concentration profile proposed by Argon et al. (1999) for Case II sorption into an infinite sheet with a Fickian diffusion front preceding the advancing boundary between swollen rubbery and the essentially unpenetrated glassy coal

4.3.2   Derivation of the equations

The salient features of the Thomas and Windle (TW) model are well summarized by Hui et al. (1987). Since Case II diffusion is introduced for coal for the first time, a short explanation is needed. According to the TW model, the concentration (volume fraction) ϕ of the penetrant only depends on one spatial dimension x, i.e. $\phi = \phi(x,t)$, where t denotes time. The increase in the concentration occurs by the penetrant molecules occupying "interstitial" sites between polymer chains in the coal. To a good approximation the glassy coal is a random close-packed arrangement of chain segments with little "free volume". There are only a limited number of such sites that may be occupied without the concurrent motion of the cross-links. If the equilibrium volume fraction of penetrant is larger than the volume fraction of the existing interstitial sites, there is a kinetic problem associated with the sorption. As compared to the glassy state of coal, in the rubbery state the crosslink polymeric chains can move separately and rapidly by a process involving rotation of main chain bonds so that the equilibrium is obtained almost instantaneously. Thus, the initial penetrant volume ϕ will be less than the equilibrium volume fraction ϕ_0. ϕ approaches this value only as permitted by the motion of the polymeric chains in coal.

Thomas and Windle (1982) treat the swelling rate, or the rate of change of volume fraction of penetrant, as the rate of linear viscous creep deformation driven by the osmotic

pressure, P_{xx}. The amount of penetrant is expressed in terms of the volume fraction ϕ, which is related to the concentration by $\phi = c / \Omega$, where Ω is the partial molecular volume.

We summarize their derivation here with the help of the article by Hui et al. (1987) and Landau and Lifshitz, 1975, i.e. the molar (diffusive) flux J is not only driven by the volume fraction gradient $\partial \phi / \partial x$, but also by the stress gradient $\partial P_{xx} / \partial x$ (Landau and Lifshitz, 1975) i.e.

$$J = -D \frac{\partial}{\partial x} \left(\phi + \frac{\Omega \phi}{k_B T} P_{xx} \right). \tag{4.6}$$

The coefficients are determined by comparison to CIT. P_{xx} is interpreted as the stress that balances the osmotic pressure Π i.e. $P_{xx} = -\Pi$.

Extended non-equilibrium thermodynamics suggests that vice-versa also the stress is related to molar flux gradient as (Jou et al., 2001)

$$P_{xx} = -\eta_l \frac{\partial J}{\partial x} = \eta_l \frac{\partial \phi}{\partial t}, \tag{4.7}$$

where η_l is the elongational viscosity. The second equation follows from the mass balance equation

$$\frac{\partial \phi}{\partial t} + \frac{\partial J}{\partial x} = 0. \tag{4.8}$$

The diffusion coefficient depends on the concentration. Below a critical volume fraction ϕ_c a diffusion coefficient D_g characteristic of a glassy state is used, and above ϕ_c the diffusion coefficient D_r characteristic of the rubber (swollen) state is used. It can be expected that $D_r / D_g >> 1$. In the model an abrupt change of the diffusion coefficients at ϕ_c is used, and D_r and D_g are considered constant for $\phi > \phi_c$ and $\phi < \phi_c$ respectively.

Therefore we find after substituting into Eq. 4.6,

$$J = -D \frac{\partial}{\partial x} \left(\phi + \frac{\eta_l \Omega \phi}{k_B T} \frac{\partial \phi}{\partial t} \right) \tag{4.9}$$

and after substituting into the mass balance equation, Eq. 4.8, we arrive at

$$\frac{\partial \phi}{\partial t} = \frac{\partial}{\partial x} D \frac{\partial}{\partial x} \left(\phi + \frac{\eta_l \Omega \phi}{k_B T} \frac{\partial \phi}{\partial t} \right). \tag{4.10}$$

The elongational viscosity η_l is supposed to depend on the volume fraction of the penetrant as

$$\eta_l = \eta_o \exp(-m\phi), \tag{4.11}$$

where m is a material constant and η_0 is the volumetric viscosity of the un-swollen coal sample. The final equilibrium concentration is reached when the coal has swollen to make the stress P_{xx} equal to zero. In this case the volume fraction of CO_2 in the coal is in equilibrium with the CO_2 in the fluid phase outside the coal. Also the CO_2 in the stressed coal is in equilibrium with the CO_2 in the fluid phase. The change in chemical potential $d\mu = \Omega dP_{xx} + k_B T d\ln\phi$. Equating the chemical potential in the unstressed ($P_{xx}^{(0)} = 0$) and stressed state leads to:

$$\Omega P_{xx} + k_B T \ln\phi = \Omega P_{xx}^0 + k_B T \ln\phi_o \tag{4.12}$$

Substitution of Eq. 4.7 and Eq. 4.11 into Eq. 4.12 leads to

$$\ln\phi/\phi_o = -\frac{\eta_0\Omega}{k_B T}\exp(-m\phi)\frac{d\phi}{dt}. \tag{4.13}$$

The solution of this equation is

$$t = -\phi_o\frac{\eta_0\Omega}{k_B T}\int\limits_0^{\phi/\phi_o}\frac{\exp(-m\phi_o y)}{\ln y}dy, \tag{4.14}$$

where we use the boundary condition that $\phi = 0$ at $t = 0$.

4.3.3 Steady-state solution

Hui et al. (1987) claim that Eq. 4.10 can have a traveling wave like solution if the diffusion coefficient in the glass state (initial coal) approaches zero. This means that the velocity of the volume fraction ϕ_c at which the transition between the glass state and the rubber state occurs, is initially proportional to time. To solve the problem of a steadily moving front, the following assumptions are made regarding the diffusivity. Let D_g and D_r denote the diffusivity of the coal in the glassy and the rubbery states respectively, brought about by the plasticization of the coal with the imbibition of CO_2. They assume that there exists a critical concentration ϕ_c, such that, for $\phi < \phi_c$, $D(\phi) \approx D_g$ and for $\phi > \phi_c$, $D(\phi) \approx D_r$ and that $D_r \gg D_g$. They also assume that the transition from D_g to D_r takes place within a narrow range of ϕ about ϕ_c, and $D(\phi)$ is a monotonically increasing function of ϕ.

It is possible to derive a conventional finite volume representation of Eq. 4.10 as shown in the appendix. The initial conditions are that $\phi\langle x\rangle$ and $\partial\phi/\partial t\langle x\rangle$ are zero. The boundary condition at the end of the slab ($x = L$) is $(\partial\phi/\partial x)(L) = 0$ (see Appendix B). At $x = 0$, it is possible to obtain the volume fraction $\phi(x = 0)$ from Eq. 4.14. However we assume a constant volume fraction, as we are interested to see whether anomalous diffusion is

not an artifact of the initial loading effects at the boundary (see Eq. 4.14). The parameters used for the simulation are summarized in Table 3. The results of the simulation are shown in Fig. 4.11. When $B = kT / \Omega \eta_o$ is big, the contribution of the relaxation term is small we obtain, the curve shows good agreement with the Sherwood and Pigford solution (see Appendix B). Dimensional analysis shows that this is also the solution obtained for long times. In this case the adsorption flux shows $\sqrt{t}$ behavior.

Parameter	
D_g	10^{-11} m^2/s
D_r	10^{-10} m^2/s
m	10-30
T_g	350°C
Ω	1.68 x 10^{-29} m^3/molecule
η_0	10^{15} Ns/m^2
Φ_0	0.205
Φ_c	0.10 x Φ_0
Length	10^{-2} m
T	45°C

Table 4.3 Parameters used in simulation for a CO₂ – coal system.

Fig. 4.10 shows the numerical solution for the case that the relaxation term also contributes. It appears that the relaxation term retards the penetration rate, but it is not yet analyzed whether the fully implicit code is adequate for this equation. Here we used the following parameters where ϕ is the CO₂ volume fraction, D the diffusion coefficient, $m \sim 10$ is a constant stress relaxation parameter and $B \sim 2.6 \times 10^{-9} \left[s^{-1} \right]$ is a stress dissipation rate parameter. Below a critical volume fraction ϕ_c the diffusion coefficient $D = D_g \sim 10^{-13} \left[m^2 / s \right]$ characteristic of a glassy state is used, and above $\phi_c \sim 0.1$ the diffusion coefficient $D = D_r \sim 10^{-10} \left[m^2 / s \right]$ characteristic of the rubber (swollen) state is used. D_r and D_g are considered constant for $\phi > \phi_c$ and $\phi < \phi_c$ respectively. The penetration will be in the $1mm - 1cm$ range. Initially $\phi(x, t = 0) = 0$. The boundary conditions of interest are $\phi(x = 0, t) = 0.16$ and $\phi(x \to \infty, t) < \infty$.
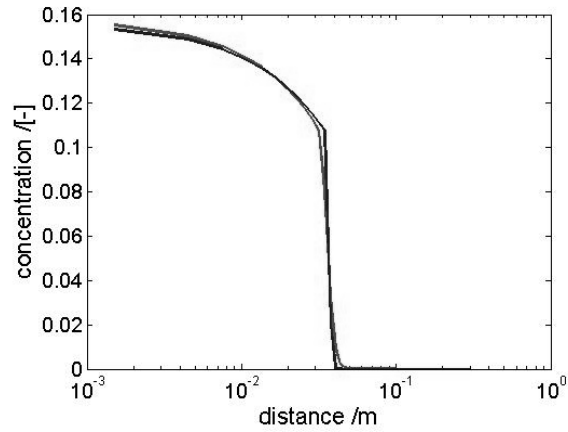
Fig. 4.9 Concentration profile when the relaxation term is negligible. The numerical solution (in red) shows good agreement with the analytical solution of Sherwood and Pigford (in blue)
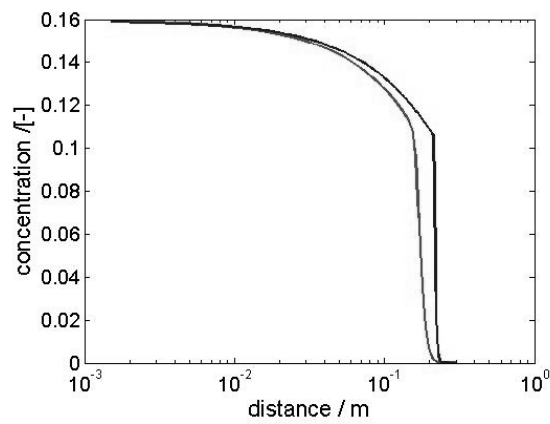

Fig. 4.10 Concentration profile for the case that the relaxation term contributes (in red). The blue curve shows again the Sherwood and Pigford solution, which disregards the relaxation term. It appears that the relaxation retards rather than enhances the penetration rate

Also in Appendix B we present a linearized form of the equation. Using a steady state initial condition with a constant concentration and using numerical Laplace inversion we observe that almost immediately a high penetration occurs, but after that hardly any penetration occurs. This appears to be non-physical behavior.
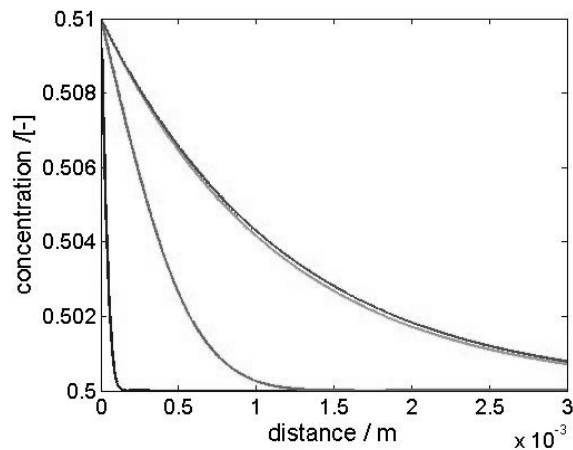

Fig. 4.11 Comparison of simple and stress driven diffusion at different times. Blue curve represents simple diffusion at time (t); purple curve is simple diffusion at time (100 t); green curve represents stress driven diffusion at time (t); red curve represents diffusion at time (100 t)

4.4 Conclusions

- Details about the highly crosslinked macromolecular nature of coal have been presented.

- Experiments have been conducted to determine the diffusion exponent (n) in coal, with respect to CO$_2$ sorption. The first pressure steps and the corresponding mass uptake curves have been used. Diffusion exponent between 0.7 and 0.8 have been calculated and it suggests an anomalous diffusion process. More experiments to understand the diffusion process under stressed condition needs to be carried out.

- A theory is introduced that accounts for the phenomenon of anomalous diffusion which is observed when bituminous coal swells in CO$_2$. The theory explains the process in terms of the contrast in the diffusion coefficients (D_r and D_g) and the viscosity of the un-swollen coal (η_o).

- A solution to the TW model pertaining to Case II diffusion has also been presented. The derivation of the model with inputs from extended non-equilibrium thermodynamics have been used in conjunction with the work of Hui et al. (1987).

- Parameter estimation for the model corresponding to the diffusion of CO2 in coal has been done.

- Sharp concentration fronts in line with the theory of Case II diffusion has been observed in the simulation results.

- Eq. 4.10 is derived from conservation law, combined with mass transport both due to concentration and stress gradients. Moreover the derivation uses that the stress is proportional to the mass flux gradient, a typical result obtained from extended non-equilibrium thermodynamics (Jou et al., 2001).

- It is claimed that Eq. 4.10 describes so called super-diffusion i.e. that the penetration rate is faster than $t^{\frac{1}{2}}$.

- The statement is based on (poorly described) numerical simulations and the assertion that approximately a traveling wave solution of Eq. 4.10 can be obtained.

- Our implicit finite volume model of the equation is not able to reproduce these results

- A dimensional analysis shows that the behavior converges to the Sherwood-Pigford solution, which shows $t^{\frac{1}{2}}$ behavior.

- The solution of a linearized equation, applied to situation where there is a finite initial concentration shows non-physical behavior.

- It is not yet clear whether the t^m (with $m > 1/2$) behavior occurs due to relaxation enhanced transport or due to the finite saturation time of the exposed surface described by Eq. 4.14.

Nomenclature

$M_t =$ dimensionless mass uptake [-],

$M_e =$ equilibrium mass uptake [-],

$k =$ constant incorporating characteristics of the macromolecular network system and the penetrant [-],

$n =$ diffusional exponent [-],

$D_e =$ Deborah number [-],

$\lambda =$ characteristic time for the macromolecular penetrant system [s],

$\theta =$ characteristic diffusion time [s],

$\delta = $ characteristic diffusion length [m],

$l = $ film thickness [m],

$D = $ gas diffusion coefficient [m^2 / s],

$\epsilon = $ strain [-],

$S_t = $ amount of volumetric swelling at time t [-],

$S_e = $ equlibrium swelling at time t_e [-],

$\phi = $ volume fraction of the penetrant [-],

$\phi_o = $ equilibrium volume fraction [-],

$P_{xx} = $ viscous stress [kg / m^2],

$\eta_l = $ elongational viscosity of coal [Ns / m^2],

$\eta_0 = $ volumetric viscosity of the unswollen coal sample [Ns / m^2],

$\Omega = $ partial molar volume of CO₂ [$m^3 / molecule$],

$m = $ material constant [-],

$D_g = $ diffusion coefficient characteristic of a glassy coal [m^2 / s],

$D_r = $ diffusion coefficient characteristic of a swollen (rubbery) coal [m^2 / s],

$\phi_c = $ critical volume fraction [-],

$k_B = $ Boltzman constant [1.37983 x $10^{-23} J / molecule / K$],

$T = $ temperature [K],

$\mu = $ chemical potential,

$L = $ slab length [m]

5 Absolute swelling of coal in response to CO$_2$ injection and its effect on fracture permeability

5.1 Introduction

Cleat permeability of coal is an important parameter for coalbed methane production. Being normal to the bedding plane and orthogonal to each other, the face and butt cleats in coal seams are usually sub-vertically orientated. Thus, changes in the cleat permeability are primarily controlled by the prevailing effective horizontal stresses that act across the cleats, rather than the effective vertical stress, defined as the difference between the overburden stress and pore pressure (Harpalani et al., 1997). Coal swelling accompanying CO$_2$ sorption would decrease the permeability of the coal as the volume increase is compensated within the fracture porosity.

Field evidence suggests that the well injectivity has indeed declined at early stages of CO$_2$ injection. It has been reported that CO$_2$ is adsorbed in higher concentration by coal than CH$_4$. A medium rank coal can sorb double the amount of CO$_2$ as compared to CH$_4$ (Mazumder et al., 2003). Even on a unit of concentration basis, CO$_2$ causes more swelling than CH$_4$. Thus, 20 cm^3/g of CO$_2$ causes more swelling than 20 cm^3/g of CH$_4$ (Reeves et al., 2002). This differential swelling behavior has severe consequences for field injection projects. For required injection rates, the increased pressure may lead to uncontrolled fracturing of the reservoir beyond a certain pressure. The detrimental effect of matrix swelling on cleat permeability is elaborated in this work. Similar work to assess the permeability damage on Canadian coals, from volumetric swelling experiments, have been carried out by Laxminarayana, 2004 using N$_2$, CH$_4$, CO$_2$ and H$_2$S.

Swelling / shrinkage coefficients have been reported in different units by different authors. Seidle et al., 1995 calculated the swelling coefficient assuming the swelling to be proportional to the amount of gas sorbed and relating the sorbed gas to pressure by the Langmuir equation. The sorption induced strain of the coal sample was corrected for mechanical compliance and this value was then used to calculate the swelling coefficient. The details regarding the mechanical compliance test and the correction procedure is explained later in this chapter. Seidle et al., 1995 reported the swelling coefficient in dimensions of μ-strain - ton / Scf.

Other authors have calculated the shrinkage/swelling coefficients after Levine, 1996 by using a Langmuir type equation. They assume that the shrinkage / swelling coefficient is a measure of strain with change in pressure. This was assumed since the pressure vs. strain curve follows the trend of an isotherm. The values reported by all other authors are in dimensions of MPa^{-1}. The swelling coefficient's reported are all from experiments conducted on

coal core or plugs. Table 5.1 gives an overview of the swelling and shrinkage coefficients of coal for CO_2 and CH_4 reported to date by various authors.

Shrinkage Coefficient, C_m	Gas type	Unit	Author
$9.5(10)^{-3}$	CO_2	MPa^{-1}	Reucroft & Patel (1986)
$2.39(10)^{-3}$	CO_2	MPa^{-1}	Zutshi & Harpalani (2004)
$5.19(10)^{-3}$	CO_2	MPa^{-1}	George & Barkat (2000)
$4.0-10.0(10)^{-4}$	CH_4	MPa^{-1}	Gunther (1968)
$2.03-10.0(10)^{-4}$	CH_4	MPa^{-1}	Wubben, et al. (1986)
$1.25(10)^{-4}$	CH_4	MPa^{-1}	Gray(1987)
$3.72(10)^{-2}$	CH_4	MPa^{-1}	Juntgen (1990)
$8.99(10)^{-4}$	CH_4	MPa^{-1}	Harpalani & Scraufnagel (1990)
$1.3(10)^{-4}$	CH_4	MPa^{-1}	George & Barkat (2000)
$11.99(10)^{-4}$	CH_4	MPa^{-1}	George & Barkat (2000)
$2.47(10)^{-4}$	CH_4	MPa^{-1}	Moffat & Weale (1995)

Table 5.1. The shrinkage coefficients for CO_2 and CH_4 reported till date by various authors

Sorption induced swelling and simultaneous permeability measurements were done as part of this work. The objectives to perform these experiments are:

(i) To measure the mechanical compliance of the coal core as a function of mean pore pressure using helium. The effective stress ($P_{eff} = P_{ann} - P_{pore}$) is to be kept constant while changing the pore pressure.

(ii) To determine the absolute swelling of coal with CO_2 as a function of the mean pore pressure at constant P_{eff}. To establish the matrix swelling effect alone, the mechanical effect measured from step (i) has to be subtracted.

(iii) To get an indication of the dependence of permeability on mean CO_2 pore pressure. The effective pressure (P_{eff}) is kept constant during the experiment.

5.2   Equipment design

A high-pressure core flooding setup was constructed. The schematic of the setup is shown in Fig. 5.1a. The pressure cell can reach a maximum confining pressure of 50 MPa. The

confining pressure was applied as an outside mechanical stress exerted by hydraulic oil. During the course of the experiment this confining pressure was controlled manually.
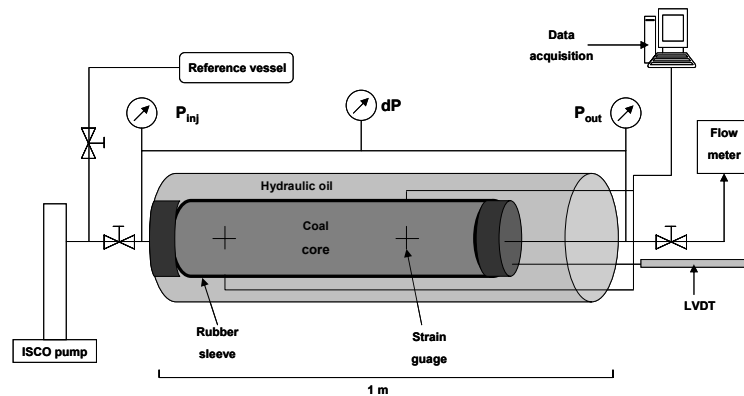

Fig. 5.1a Schematic of the entire setup. The axial displacement of the sample was measured by the Linear Variable Displacement Transducer (LVDT).

For each pressure step the expected pore pressure was calculated and then the confining pressure was added manually by means of a pressure actuated valve to keep the effective stress (P_{eff}) constant throughout the experiment. The confining pressure was applied on the coal core, inside a rubber sleeve. To prevent the gas from diffusing through the rubber sleeve, a lead foil was wrapped around the coal core. To simulate downhole conditions the temperature in the pressure cell was maintained at 45^{0}C. The sample diameter is 72 mm. The length of the core varied from sample to sample. To limit scaling-up problems, it was preferred to use large cores and this makes the setup complex. The cores were drilled parallel to the bedding plane, thus ensuring that the axial strain measured was parallel to the bedding. For the first experiment a high rank coal core of 268 mm in length and for the second and third experiment a low rank coal core of 154 mm in length was used. To avoid mechanical end effects on the core permeability, two sieperm plates are fixed at either ends of the core. The injection & production tubings were attached to the end plates. These sieperm plates have a porosity of 33% and a permeability of 10^{-13} m^2.

Apart from the high pressure cell, the rest of the setup can be broadly grouped as injection, production, strain and data acquisition equipments. The equipments used are:

(i)   An ISCO^{TM} plunger pump connected to a bottle of the required gas to be injected. The ISCO plunger pump injects CO$_2$, CH$_4$, N$_2$ and / or flue gas into the coal core at a constant injection rate. The differential pressure gauge measurements were used for the calculation of the Darcy permeability.

(ii)   A reference vessel, outside the reactor was used to feed the gas. The gas was fed to this reference vessel by an ISCO pump. Then the gas was boosted into the reference cell, to get the required pressures. Time was needed to stabilize the temperature in the reference cell.

(iii)   At the production end, a back pressure valve controlled the flow out. A constant pressure difference was maintained during the experiment.

(iv)   A digital flow meter unique to measure CO_2 flow was used at the production end to monitor the flow rate.

(v)   Strain gauges were attached on the sample surface to measure the sorption induced volumetric strain in the coal (Fig. 5.1b). The procedure followed is explained in the following section. The strain measurements were stored, through an amplifier and a data acquisition system, into a computer. A linear variable displacement transducer (LVDT) was used in addition to the strain gauges to measure the axial changes in the sample dimension.

Fig. 5.1b Photo of strain gauges on the surface of the coal core

(vi)   The operation panel, the data-acquisition system and safety devices were installed in the control room. During the test, two thermocouples were used to measure temperatures above and below the core inside the pressure cell. In addition, the (differential) pressure, sample expansion and flows were registered every 30 s. The arrangement of the whole experimental setup is shown in Fig. 5.1c.
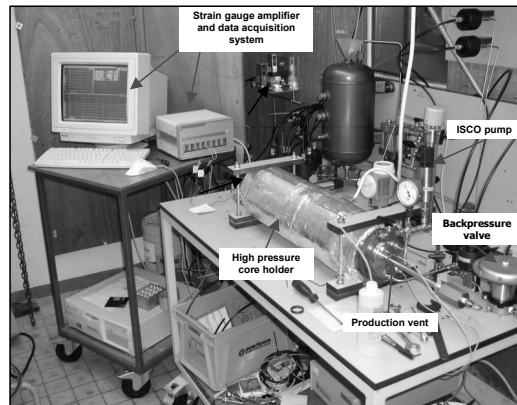
Fig. 5.1c Laboratory setting of the experimental setup along with the data acquisition system for the strain measurements

5.3   Sample description and preparation

The samples used for these experiments were from the South Wales coalfield (Selar Cornish) in UK and the Warndt Luisenthal coalfield in Germany. Some properties of the samples are shown in Table 5.2. The samples selected were quite diverse in their rank and internal properties. To mount the strain gauges the following procedure was used:

(i)   A smooth cleat free part of the coal core surface was selected. If needed, this surface was polished. Grooves of about 2 mm deep were made to prevent the strain gauges from coming off the surface due to the shear force of the rubber sleeve. The groove surfaces were also polished. The surface, on which the strain gauge needs to be attached, was cleaned with industrial tissue paper or cloth soaked in a small amount of acetone. It was cleaned until no more free coal particles could be removed. A non-smooth surface area will not properly adhere to the strain gauge.

(ii)   The adhesive to be used for fixing the strain gauges on the coal surface was prepared. The adhesive was applied evenly on both the surfaces, i.e. on the strain gauge surface as well as the coal surface. A polyethylene sheet was placed onto it and pressed down on the gauge for about 10 minutes. Connectors were positioned at a distance of 3 to 5 mm from the gauge.

(iii)   The junction area was soldiered for both the gauge leads and the connecting terminals. To connect the extension, the lead wires were soldered to the connecting terminals. Two strain gauges were axially oriented and the two other oriented radially on the core surface. Copper wires of sufficient length were soldered to the terminals of each of

these strain gauges. A groove was made along the length of the core and the wires were guided through this groove. All the grooves were then filled with a mixture of coal puff and the adhesive. This further prevented the strain gauges from being sheared off the surface during the experiment.

Sample	Rank % R_{max}	Length mm	Diameter mm	Specific surface m²/g	Micropore volume cm³/g coal
Selar Cornish	2.41	268	72	208	0.071
Warndt Luisenthal	0.71	154	74.78	104	0.03545

Table 5.2. Sample properties

The strain gauges were of the rosette type (TML-PC-10) gauges, and a gauge factor of 2.07. The strain gauges had an accuracy of +/- 2 %. The gauge factor can be defined as

$$K = \frac{\Delta R / R}{\varepsilon}.$$ (5.1)

$\Delta R / R$ is indicated by specifying the Poisson's ratio of the test specimen. The gauges were connected to a (1/4) Wheatstone bridge, whose amplifier output is given by

$$\varepsilon = \frac{4 A_{op}}{K \mu_B A},$$ (5.2)

where K is the gauge factor, ε the mechanical strain, R the gauge resistance, ΔR the resistance variation, A_{op} the amplifier output, μ_B the bridge supply and A the amplification (1000 times in this case).

With this arrangement, the axial and radial strain in the coal sample due to swelling induced by the sorption of CO_2 was measured. The directional placements of the strain gauges, gives the measurement of the two horizontal strains (strain parallel to the bedding plane).

5.4   Sorption induced absolute swelling experiments

The setup is designed to measure volumetric strain as a function of the sorbed gas concentration while keeping the net stress on the coal sample constant. The tests start with mounting the coal core sample in a rubber sleeve and building it in the high-pressure cell. This requires a careful handling of the sample as otherwise leaks can occur. The sample cell is connected to a vacuum pump, for at least a week, to eliminate any form of residual gas or

moisture. Prior to the start of the experiment, strain gauges were calibrated for temperature variations.

A mechanical compliance test with helium is required at the start. Helium was injected in the coal in 20 bar steps of increasing pressure upto 160 bars. The effective pressure $(P_{pore} - P_{ann})$ was kept constant throughout the experiment. The pressure was reduced in a similar way. Each injection cycle ended after an equilibration time of 30 minutes. This test was done to measure the void volume of the set-up and to estimate the mechanical compliance coefficient of the coal (Seidle, 1995). Helium was selected because it is asserted that only negligible amounts are adsorbed. Thus the measured strain with helium is solely due to the mechanical compression of the solid coal resulting from the change in pressure.

The next set of experiments, were done to determine the absolute swelling of coal with CO_2 as a function of the mean pore pressure and constant P_{eff}. Here, CO_2 was used instead of Helium. The CO_2 sorption experiment was carried out at 45^0C. The pore pressure, P_{pore}, was increased in increments of 20 bars till the end pressure of 160 bars. After each pressure step an equilibration time of 4 to 7 days was given. Over the entire course of the experiment, the effective pressure, P_{eff}, was kept constant. Measurements are made for the strain in the system. Three experiments were performed, one with the Selar Cornish coal and two with the Warndt Luisenthal coal. The third experiment was a repetition of the second experiment. At the end of each experiment, the core was taken out, the length of the sample measured and the integrity of the coal checked. For all the three experiments the position of the strain gauges were checked for slip, but was found to be intact.

5.4.1   Data analysis

The axial and the radial strains were obtained from the strain gauges fixed on the sample. Strain gauge response from the duplicate Warndt Luisenthal experiment is shown in Fig. 5.7. For isotropic swelling, we have

$$\varepsilon_{volumtric} = \varepsilon_x + 2\varepsilon_y. \tag{5.3}$$

Following the helium injection, the volumetric strain response of the coal sample was used to calculate the mechanical compliance coefficient (C_p). C_p is defined as the strain with corresponding change in pressure and is primarily due to grain compression.

$$C_p = \frac{d\varepsilon_g}{dP}, \tag{5.4}$$

where ε_g is the strain due to grain compression.

Methane and carbon dioxide sorption data can be modeled using the empirical form of the Langmuir isotherm model (Levine, 1996). Therefore, an equation having the same form as the Langmuir equation was used in this study to fit the sorption strain data theoretically.

$$\frac{\varepsilon_s}{P} = \frac{\varepsilon_{max}}{P + P_\psi},$$ (5.5)

where ε_s is the sorption induced strain. ε_{max} and P_ψ were estimated by best fitting a linearized form of Eq. 5.5. The slope of this linearized form is equal to $1/P_\psi$ and the y-intercept is equal to ε_{max}/P_ψ. Matrix swelling coefficient is a measure of the strain change with the corresponding change in pressure.

$$C_m = \frac{d\varepsilon_s}{dP} = \frac{\varepsilon_{max}}{P + P_\psi} - \frac{\varepsilon_{max} P}{(P + P_\psi)^2}.$$ (5.6)

The coefficient derived from this equation has the units of MPa⁻¹, which quantifies the change in volumetric strain per unit pressure.

5.4.2   Results and discussion

The first part of the experiment is a mechanical compliance test for the coal core samples by injecting helium, in pressure steps of 20 bars and continuously monitoring the strain. The sample was considered to be in equilibrium if the strain remained constant for more than 30 minutes. The mechanical compliance test results are shown in Figs. 5.2 and 5.3. The linearity of the compression with pressure is quite evident. The mechanical compliance coefficient (C_p) for the Selar Cornish and the Warndt Luisenthal coal were calculated to be -5.0 x 10⁻⁴ MPa⁻¹ and -1.0 x 10⁻⁴ MPa⁻¹ respectively. Eq. 5.4 was used to calculate C_p. Various authors have reported various values of C_p. This holds true since C_p is a rank dependent property of coal. The linearity is because helium is not sorbed onto coal, and the entire strain observed is due to the compression of the coal matrix by the increasing gas pressure. This effect is subtracted to get the volumetric strain because of the sorption of CO₂.

In the second series of experiments, CO₂ was injected. The volumetric strain results from the three experiments are shown in Figs. 5.4, 5.5 and 5.6. It was recognized that these experiments with CO₂ showed a combined effect of grain compression and matrix swelling. Thus by subtracting the mechanical effects from the experimental results, only the effect due to swelling was retained. As can be seen from the volumetric strain results, matrix swelling is more dominant. Fig. 5.4 shows the experimental and the fitted volumetric strain measurements of the Selar Cornish coal. During this experiment, the effective pressure (P_{eff}) was kept constant at 4 MPa. With CO₂, the Selar Cornish coal showed a maximum volumetric strain of 1.48 % corresponding to an average pore pressure of 13 MPa. Matrix swelling coefficients (C_m) were

calculated from this experiment using Eq. 5.6 and have been plotted as a function of pressure in Fig. 5.7.
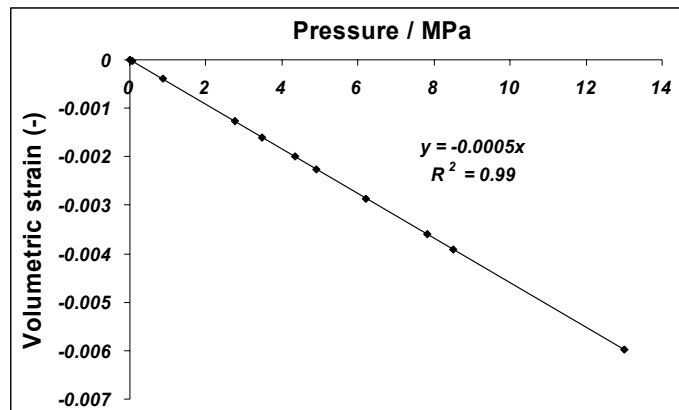

Fig. 5.2 Volumetric strain response for Selar Cornish coal following Helium

Similarly the experimental and fitted volumetric strain measurements of the Warndt Luisenthal coal are shown in Figs. 5.5 and 5.6. Fig. 5.6 shows a duplicate experiment, conducted on the same coal sample as the experiment shown in Fig. 5.5. The low rank Warndt Luisenthal coal exhibited higher strain of around 1.6 % compared to the high rank Selar Cornish. Thus the rank dependence of swelling holds true for these set of experiments. The duplicate Warndt Luisenthal experiment shows higher volumetric strain values for all pressure steps. A maximum volumetric strain of 1.9 % corresponding to a mean pore pressure of 14 MPa was measured. This incremental strain from the duplicate experiment suggests that the process of sequential swelling is occurring as suggested by Bodily et al., 1989. Sequential swelling confirms the highly cross-linked macromolecular nature of coal. It also suggests that the swelling of coal by all non-polar gases like CO_2 and CH_4 is caused by the dispersion force interaction between the gas and the coal macromolecular network. The cross-links broken at the first place are not completely reformed upon removal of the sorbent leading to incremental strains as shown in the duplicate experiment.

The matrix swelling coefficients (C_m) from the two Warndt Luisenthal experiments are plotted as a function of pressure in Fig. 5.8. The matrix swelling coefficients for the low and high rank coal differ. This was also reported by George and Barakat, 2001. For the Selar Cornish coal, an end strain of -0.45 % and for the Warndt Luisenthal coal an end strain of -0.92 % was measured.
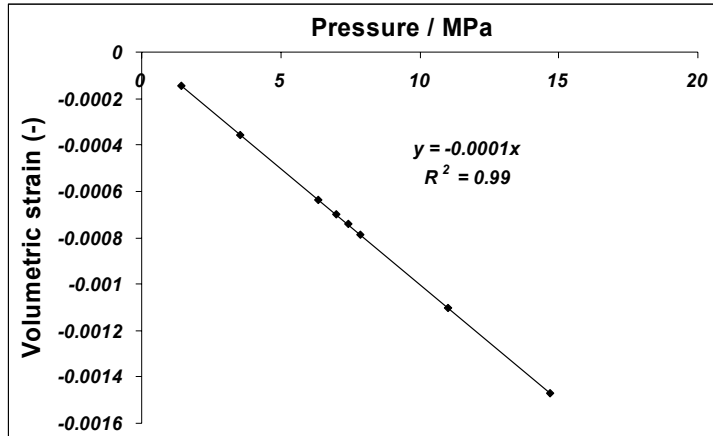
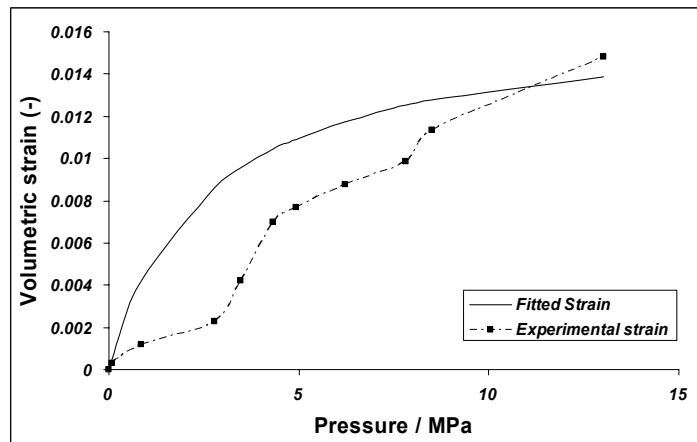Fig. 5.3 Volumetric strain response for Warndt Luisenthal coal following Helium injection.

Fig. 5.4 Experimental and fitted strain for Selar Cornish coal.

The curvy natures of the experimental strains are probably due to, short equilibration times or the heterogeneity in the coal. Fig. 5.9 demonstrates the strain change with time for the duplicate Warndt Luisenthal experiment. It also shows that reaching equilibrium in terms of strain measurement over all individual strain gauges was not possible. But the criterion to continue doing the next step was based on the equilibration of the strain over time. When the

change in pressure was observed to be less than 0.01 MPa over 12 hours, the experiment was ready for the next step.
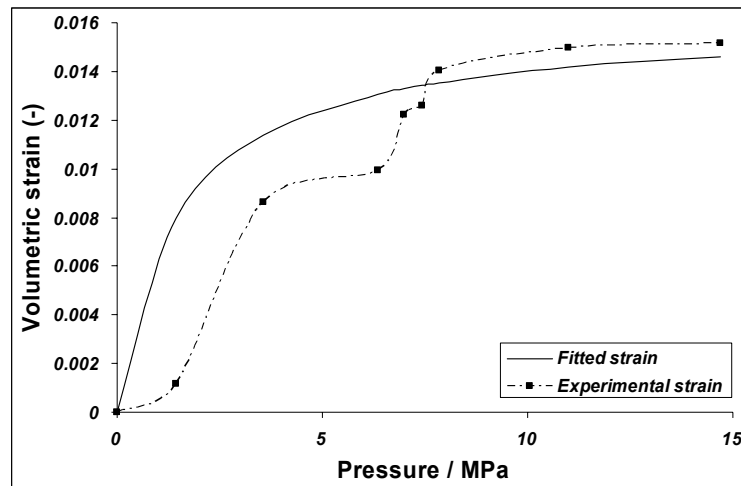

Fig. 5.5 Experimental and fitted strain for Warndt Luisenthal coal core experiment.
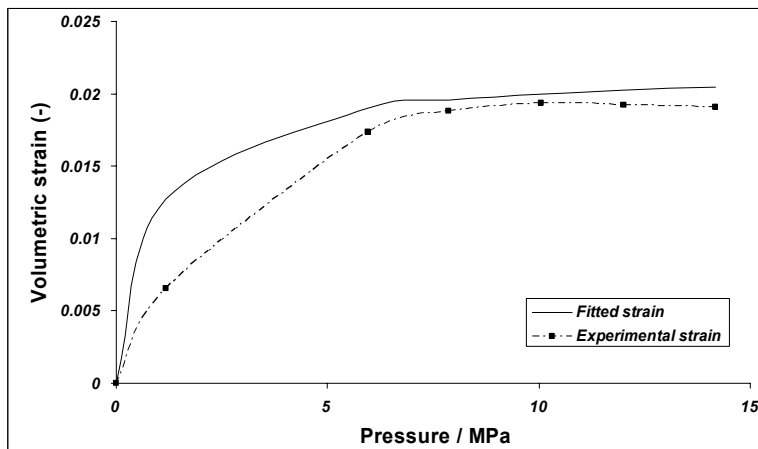

Fig. 5.6 Experimental and fitted strain for duplicate Warndt Luisenthal coal core experiment.

Moreover the non-equilibrium in the strain measurement (Fig. 5.9) is only observed in one pair of axial and radial strain measurements, which were coupled together at one particular point on the coal core. Considering the scale of the samples it is quite possible that a particular location

on the coal surface cannot be absolutely free of micro / meso cleats. Presence of such minor fractures will obviously affect the equilibrium strain measurements. The bad fit between the empirical and the experimental strain may otherwise suggest that a Langmuir type model is not enough to describe the process.
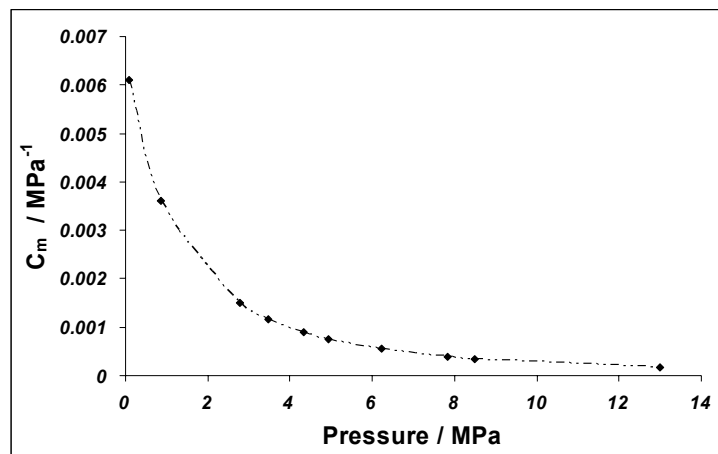

Fig. 5.7 Matrix swelling coefficients for the Selar Cornish experiment as a function of pore pressure.
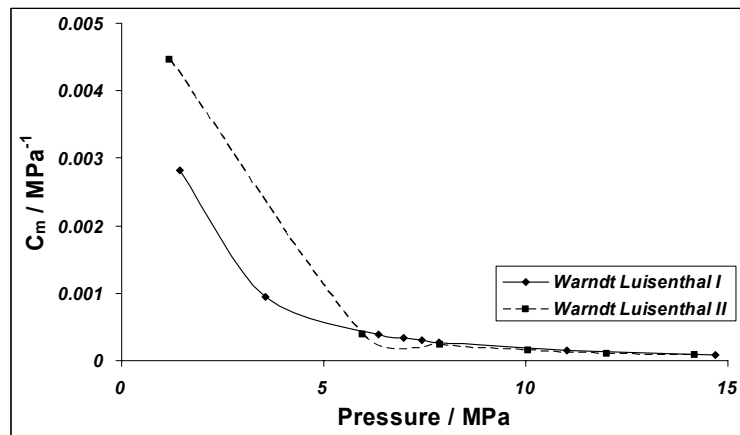

Fig. 5.8 Matrix swelling coefficients for the Warndt Luisenthal experiments as a function of pore pressure.
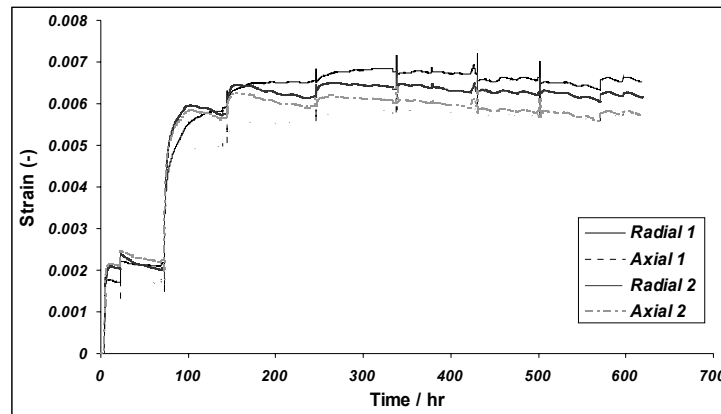
Fig. 5.9 Strain change with time for repeat Warndt Luisenthal coal core experiment.

The swelling experiments show that the transport process in coal is complex. The similarities in structure between coal and glassy polymers have led to the application of theories of sorption behavior of polymers to coals. During diffusive transport at low or moderate temperatures, gas enters the macromolecular network of coal, decreasing the network density. It results into an increase of the large molecular chain motions (Peppas et al., 1987). This increase of the gas concentration of the network can be considered as an effective decrease of the glass transition temperature. Structural changes induced during this process, includes swelling, micro cavity formation and primary phase transition requiring rearrangements of each chain segment. Such changes are dominated by relaxation phenomenon.

The diffusion of gas into glassy polymers may vary between two analytically treatable extremes. If the diffusion is controlled by the concentration gradient between the centre and the outside of the particle, the diffusion mechanism is Fickian. The diffusion in glassy polymers often does not fit the Fickian diffusion model. Alfrey, Gurnee and Lloyd, 1966 presented a second limiting case for sorption. Here the rate of transport is entirely controlled by molecular relaxation. This type of transport mechanism is designated as Case II transport. Thomas and Windle, 1982 proposed that the rate controlling step at the penetrant front is the time dependent mechanical deformation of the glassy polymer in response to the thermodynamic swelling stress.

5.5   Effect of matrix swelling on fracture porosity and permeability

The coal matrix is heterogeneous and is characterized by two distinct porosity systems; micropores and macropores. The permeability behavior is largely determined by the macro-pore system. The macro porosity in coal consists of the cleats. It is a well defined and uniformly distributed network of natural fractures. The cleat system can be subdivided into continuous face cleat, and discontinuous butt cleat, which terminate at intersections with the face cleat.

Cleat permeability is recognized as the most important parameter for coalbed methane production. Being normal to the bedding plane and orthogonal to each other, the face and butt cleats in coal seams are usually sub-vertically oriented. Changes in cleat permeability are primarily controlled by the prevailing effective horizontal stress that acts across the cleats.

The impact of increasing triaxial stress on permeability of coal samples has been investigated by a number of researchers (Somerton et al. 1975; Durucan and Edwards, 1986). Experimental measurements indicate that permeability of coal decreases exponentially with increasing effective stress (P_{eff}) McKee et al., 1987.

The permeability of the cleat structure in coal changes due to: (i) the phase relative permeability effects, whereby the degree of saturation will affect the gas and water relative permeability's of the reservoir. (ii) The permeability varies by a change in the effective stress within the seams. The effective stress tends to close the cleats and reduce permeability. It is likely that the permeability is related particularly to the "effective horizontal stress" (Gray, 1987) across the cleats because these appear to conduct most seam fluids. The "effective normal stress" is referred to as the total stress normal to the cleat minus the fluid pressure within the cleat. Under field condition the "effective normal stress" can also be termed as the "effective horizontal stress" (Shi et al., 2003) because the cleat system is sub-vertically oriented to the bedding plane and is orthogonal to each other. Under these circumstances, the permeability variations brought about by variations in fluid pressures are anisotropic, depending on the nature, frequency, and direction of the cleats. Such opening and closing of the cleats is also likely to change the phase relative permeability's and capillary pressures within the coal. (iii) The permeability varies due to shrinkage while methane is being desorbed or swelling while carbon dioxide is being injected. This aspect of permeability variation is being dealt with.

The test procedure in the laboratory involved confining a 20 cm long and 7 cm in diameter coal core sample under a number of isotropic stress levels in the cell and injecting carbon dioxide through the sample at a steady pressure until the flow came to equilibrium. 12 to 48 hours were required to reach equilibrium. A digital mass flow meter specially calibrated for CO_2 was used to measure the flow on the production end. To keep the downstream pressure constant and to create a pressure gradient a backpressure valve was used. The equation below was used to calculate the fracture permeability for compressible fluids (Dullien, 1992; Gray, 1987), and assumes ideal gas behavior.

$$k[m^2] = \frac{2qP_0L\mu}{A(P_i^2 - P_o^2)}.$$
(5.7)

The permeability measurements were conducted on the Selar Cornish and the Warndt Luisenthal coal core sample. The coal samples used had high cleat density. At the end of the absolute swelling measurements with CO_2, when the coal core reached equilibrium at pressures above 14 MPa, the permeability measurements were carried out at each step of decreasing pressure. For all measurements the cell was kept at a constant temperature of 45^0C. As shown in Fig. 5.1, the pressure vessel is a biaxial cell where the coal core is placed inside a rubber sleeve. The effective stress during the entire experiment was maintained around 4 MPa for the Selar Cornish coal and around 6 MPa for the Warndt Luisenthal sample. After the stress stabilized, the injection of CO_2 was done with the ISCO pump at a constant rate. The average of the injection and production pressure was taken as the core pressure for the calculation of the permeability. The flow measurements for a particular pressure step were only used when all equilibrium conditions were satisfied. When no change in flow rate was observed over a period of one hour, the flow was considered to be stable. Usually the flow stabilized between 12 to 30 hours after the start of injection. Considering the fact that the desorbing gas was also contributing to the production stream, upto a maximum of 48 hours, was given for the flow to stabilize. Doing the first permeability measurement at higher pressure ensured that the coal core sample equilibrated both in terms of its sorption capacity and sorption induced swelling. This arrangement does allow the coal to swell to its maximum under the respective mean pore pressure and the applied effective stress and can be better referred to as unconstrained swelling hereafter. The swelling of coal matrix results in a change in the cleat porosity and the permeability.

5.5.1 Results and discussion

The results of the permeability measurements in the laboratory are shown in Figs. 5.10 and 5.11. Under stress, both the coal samples have extremely low initial permeability in the range of 0.01 mD. The slight variation in the effective stress (P_{eff}) at lower pressures was unavoidable. Since the coal core was free to swell inside the pressure cell (unconstrained swelling), the measured permeability is higher at higher mean pore pressure. This whole process of free swelling in the laboratory in comparison to constrained swelling in the field is analogous to thermal expansion (Shi et al., 2003). A hollow steel pipe, when subjected to thermal expansion, encounters an increase in its free volume, which is analogous to an increase in the cleat porosity with increasing swelling in our case.

To understand why the permeability of the coal core increases with increasing pore pressure (P_{pore}), while the effective stress is kept constant, is a question of understanding what swelling stress (σ_{sw}) is. Swelling stress is defined as the pressure of an element of coal matrix saturated with the adsorbent (CO_2 / CH_4 / N_2) avoiding at the same time deformation. The very definition

makes it clear that the measurement, or measurement methodology of swelling stress, is not a matter to be easily accomplished. From the viewpoint of thermodynamics, swelling stress
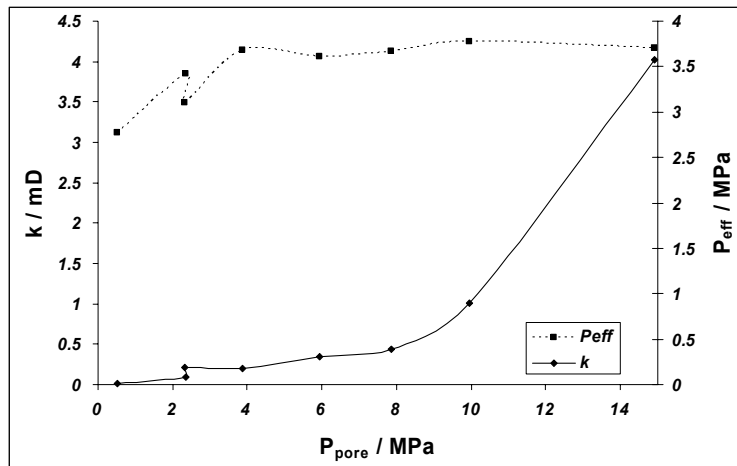

Fig. 5.10 Experimentally determined variation in permeability for Selar Cornish coal as a result of matrix swelling under unconstrained conditions
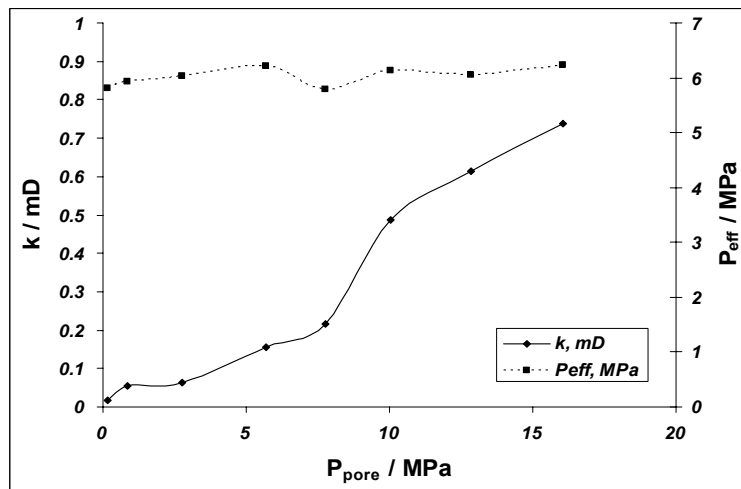

Fig. 5.11 Experimentally determined variation in permeability for Warndt Luisenthal coal due to matrix swelling under unconstrained conditions

represents a kind of energy. In the case of free swelling (unconstrained laboratory conditions) it turns out to be a volume change. Swelling stress only occurs in the case of constrained swelling. The concept of swelling stress is shown in Fig. 5.12.

Considering a deformed domain, a process of back compaction can be visualized to understand the swelling stress. With the present experimental setup, a case of free swelling will result in a volume change (dV). This volume change will see an incremental rise in the annular pressure (P_{ann}) of the cell. But, because the system is set so as to keep the effective stress (P_{eff}) constant, some of the oil from the annular space will drain out.
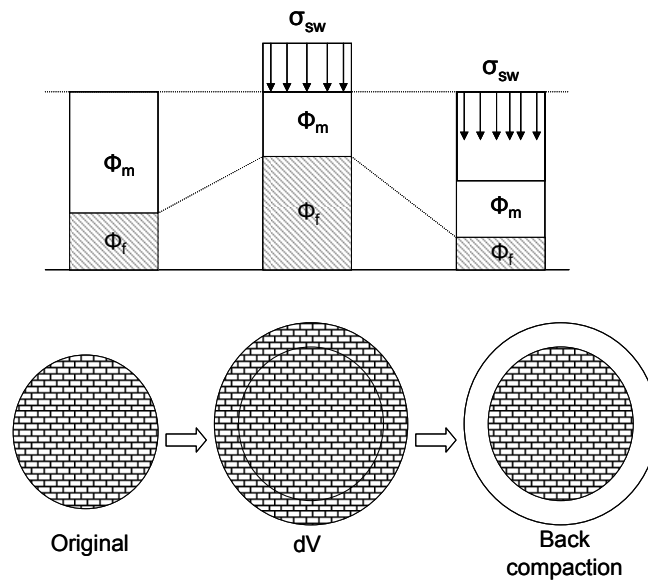

Fig. 5.12 Concept of swelling stress. In the case of free swelling (unconstrained laboratory conditions) swelling results in a volume change (dV). Swelling stress only occurs in the case of constrained swelling. Considering a deformed domain, a process of back compaction can be visualized to understand the swelling stress (σ_{sw}).

There are two sets of experimental data to validate a relationship between permeability and swelling, (i) permeability measurements under unconstrained conditions and (ii) volumetric strain measurements.

Using the experimentally determined permeability measurements under unconstrained conditions (Figs. 5.10 and 5.11) and using the empirical Carmen-Kozeny relation in the general form, the changes in cleat porosity were calculated. Moreover in coal, the distribution of the fractures gives the matrix a periodic structure. Arbogast, 1993 showed that for a dual-porosity system the permeability can be approximated as

$$k \sim \varphi_f \frac{\phi^3 d_p^{\,2}}{(1-\phi)^2},$$

where φ_f is the volume fraction of the fractures, ϕ the cleat porosity and d_p the grain diameter. It is assumed that the grain diameter d_p within the cleat is negligibly affected by the decrease in the cleat aperture due to swelling. Thus the permeability ratio can be written as

$$\frac{k_{new}}{k_{initial}} = \left(\frac{\varphi_f^{new}}{\varphi_f^{initial}}\right)\left(\frac{\phi_{new}}{\phi_{initial}}\right)^3 \frac{(1-\phi_{initial})^2}{(1-\phi_{new})^2} \approx \left(\frac{\phi_{new}}{\phi_{initial}}\right)^{\alpha}. \tag{5.8}$$

In Eq. 5.8 the first and the last term drops out because of very low fracture porosity in coal. α has a value of 3 for coal. The increase in coal cleat porosity due to unconstrained swelling is considered to be equal to the decrease in cleat porosity under field conditions with constrained swelling. The resulting decrease in the cleat porosities are shown in Figs. 5.13 and 5.14. This assumption is valid when the total volume of coal (matrix and cleats) remains constant with injection of CO₂. With the decrease in cleat porosity calculated and with a set of three different initial fracture porosity values, the permeability variation under constrained condition was determined. Although significant advances have been made, it is still difficult to measure cleat porosity accurately because of the very small volume of cleats in a core. For that reason, a range of three different initial cleat porosity (ϕ) values within 0.1 % to 1.0 % were used to estimate the change in permeability with sorption induced swelling. The resulting variations in permeability corresponding to a cleat porosity of 1 % are shown in Figs. 5.15 and 5.16. For all initial porosity cases, the fracture porosity attains near zero values, since the initial permeability of the sample is very low. Zutshi and Harpalani, 2004 have also reported this with a matchstick model (Reiss, 1980). Under laboratory conditions, the near zero permeability can be explained as the flow, which takes place through the coal matrix, can no longer be considered as a fracture or cleat flow. This injectivity problem can be anticipated at field scale injection projects in low permeability coal. Thus, injecting under such extremely poor permeability condition may result in very high bottom hole pressures, which exceeds fracture breakdown limit resulting in propagation of uncontrolled fractures.

With the second set of data on volumetric strain measurements and following the procedure described by Harpalani et al., 1992, 1997, 1995, 1992, 1995, changes in cleat porosity and permeability, as a result of changing volumes of the coal matrix, were calculated. This procedure, by using the matchstick model (Reiss, 1980), is briefly described below. The increase in coal matrix volume due to swelling was considered equal to the decrease in cleat aperture (b) as shown in Fig. 5.17, assuming that the total volume of coal remains constant upon injection of CO₂. Assuming a matchstick geometry, where $a = a_1 = a_2$, the initial fracture porosity ($\phi_{initial}$) is given by $2b/a$.
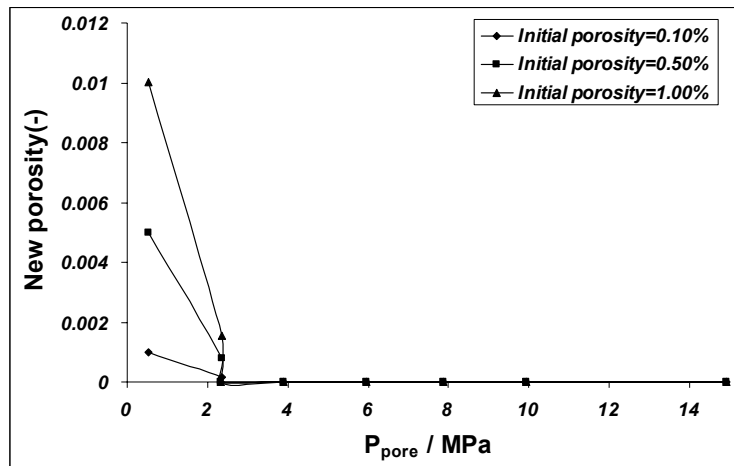
Fig. 5.13 Variation in fracture porosity for Selar Cornish coal as a result of matrix swelling under constrained conditions
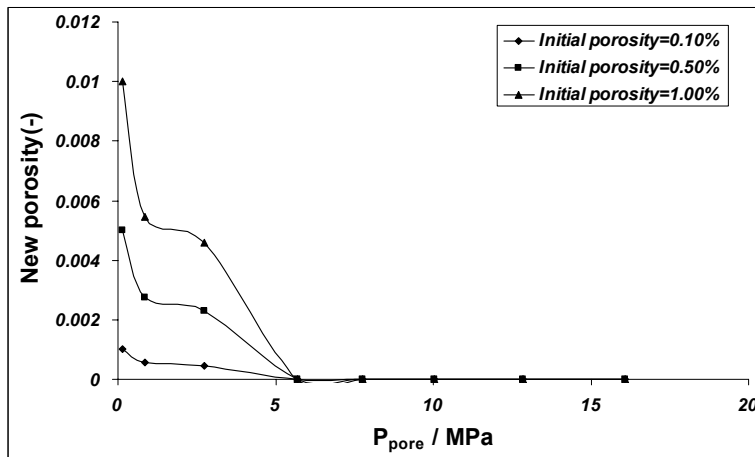
Fig. 5.14 Variation in fracture porosity for Warndt Luisenthal coal as a result of matrix swelling under constrained conditions

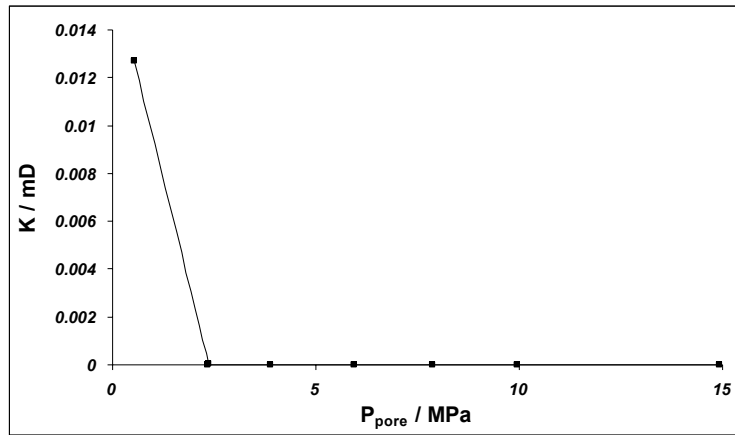Fig. 5.15 Variation in permeability for Selar Cornish coal as a result of matrix swelling under constrained conditions
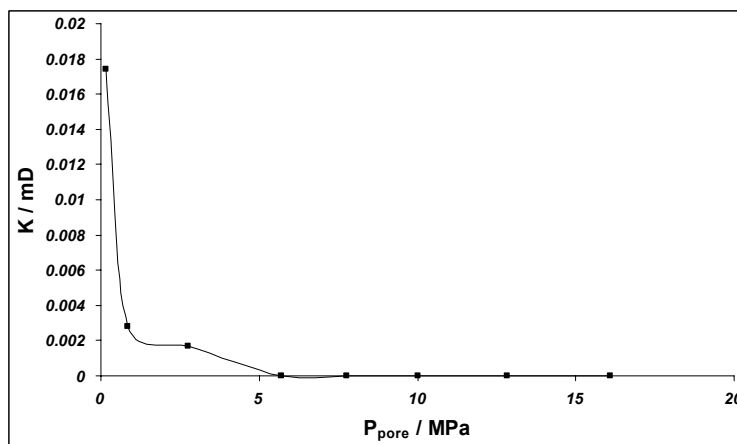
Fig. 5.16 Variation in permeability for Warndt Luisenthal coal as a result of matrix swelling under constrained conditions

The change in matrix dimension depends on the change in pressure and the swelling behavior of coal and is given by

$$\Delta a = a l_m \Delta P, \qquad\qquad (5.9)$$

where a is the initial cleat spacing, l_m is the change in dimension of the coal matrix in the horizontal direction per unit pressure, and ΔP is the change in pressure of the gas being injected. Since the flow of the gas is considered along the cleat systems perpendicular to the bedding plane, change in dimensions along the vertical cleats only has been taken into account necessitating the use of the term l_m.

Fig. 5.17 Matrix and cleat geometry for a matchstick model

After a pressure change of ΔP, the new cleat porosity (ϕ_{new}) can be written as

$$\phi_{new} = \frac{2(b - \Delta a)}{(a + \Delta a)}. \qquad (5.10)$$

Substituting the value of Δa, the porosity ratio can be written as:

$$\frac{\phi_{new}}{\phi_{initial}} = \frac{1-(2l_m\Delta P/\phi_{initial})}{(1+l_m\Delta P)}. \qquad (5.11)$$
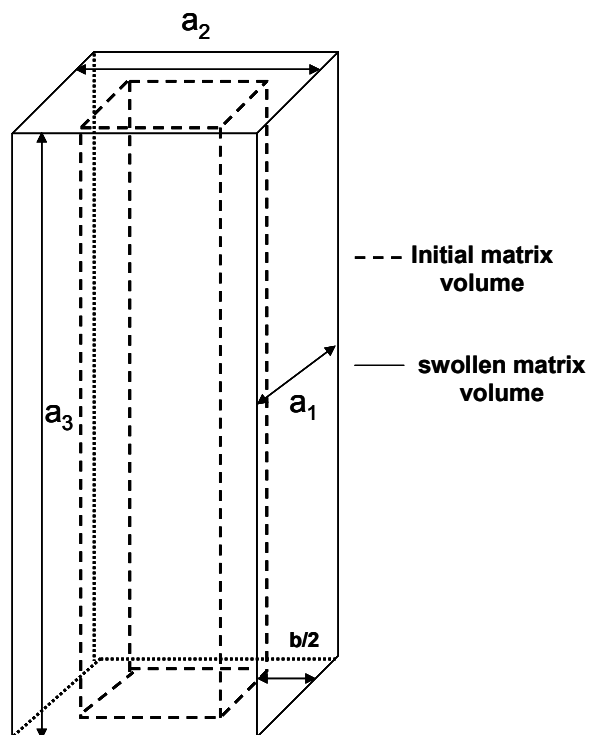
Using estimates for initial porosity and the experimental horizontal strain, pressure dependent cleat porosity can be estimated and compared to the experimentally derived porosity change. Moreover the change in cleat porosity by swelling will result in a change in cleat permeability. For the same matchstick geometry, and with the same set of assumptions, the initial cleat permeability ($k_{initial}$) is given by

$$k_{initial} = \frac{b^3}{12a}. \qquad (5.12)$$

Thus after a pressure change, the new cleat permeability (k_{new}) can be written as

$$k_{new} = \frac{(b-\Delta a)^3}{12(a+\Delta a)}. \qquad (5.13)$$

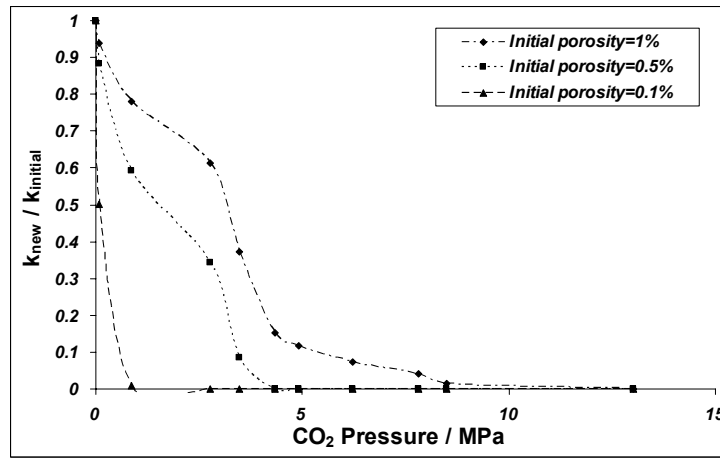The ratio of the modified cleat permeability can be written as

Fig. 5.18 Theoretically calculated permeability variation as a result of matrix swelling for Selar Cornish coal from matchstick model

$$\frac{k_{new}}{k_{initial}} = \frac{\left(1-(2l_m\Delta P/\phi_{initial})\right)^3}{(1+l_m\Delta P)}. \qquad (5.14)$$

The variations in permeability as a function of the initial porosity for both the Selar Cornish and Warndt Luisenthal coal core absolute swelling experiments are shown in Figs. 5.18 and 5.19. The permeability variation for both the experiments, have been worked out for three different porosity situations as shown in the figures. As expected the permeability in all the three situations decreases to zero. However these results showing a decrease in permeability are due to change in matrix volume alone. In our experiments the effective stress (P_{eff}) was kept constant. Under true field conditions the injection of CO$_2$ would also result in a simultaneous
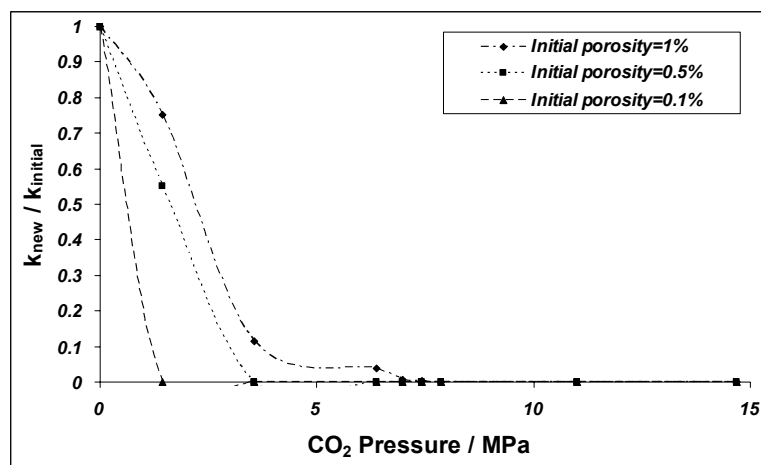
Fig. 5.19 Theoretically calculated permeability variation as a result of matrix swelling for Warndt Luisenthal coal from matchstick model

decrease in the P_{eff}, which would result in an increase in the cleat permeability and will thus counter a part of the permeability reduction due to volume increase.

5.6   Conclusions

- The major conclusion from this experimental study is that, injection of CO$_2$ in coal seams result into volumetric swelling. It has a profound effect on the fracture porosity and permeability of the coal.

- The swelling is rank dependent as was established by doing experiments with two coal samples differing in rank.

- Sequential swelling of coal holds true and is in line of comparing the coal structure with that of glassy polymers.

- Decrease in permeability due to change in matrix volume was studied under constant effective stress conditions. Swelling in coal has detrimental effects on its permeability.

- CO_2 injection in coal seams would turn up with serious injectivity problems near the well bore.

Nomenclature

K = Gauge factor [-],

ε = Mechanical strain [%],

R = Gauge resistance $[\Omega]$,

ΔR = Resistance variation

A_{op} = Amplifier output [volts],

μ_B = Bridge supply [volts],

A = Amplification, 1000 times in this case,

ε_s = Linear sorption strain at pressure P,

ε_{max} = Corresponds mathematically to the `Langmuir volume' and represents the theoretical maximum strain approached asymptotically at infinite pressure,

P_{ψ} = Corresponds mathematically to the 'Langmuir pressure' and represents the pressure at which the coal has attained 50 % of its maximum strain. The lower the value of P_{ψ}, the steeper is the sorption curve at low pressures,

k = Permeability [mD],

q = Flow rate [m^3/s],

P_0 = Production pressure [MPa],

P_i = Injection pressure [MPa],

P_{pore} = Pore pressure [MPa],

P_{ann} = Annular pressure [MPa],

P_{eff} = Effective stress [MPa],

σ_{sw} = Swelling stress [MPa],

φ_f = volume fraction of the fractures [-],

μ = Viscosity [*Pa s*],

A = Crossection area [*cm^2*],

L = Length of the core [*m*],

a = The initial cleat spacing [*m*],

l_m = Change in dimension of the cleat matrix in the horizontal direction per unit pressure,

ΔP = Change in the gas pressure,

ϕ = Cleat porosity [-],

C_m = Swelling coefficient [*MPa^{-1}*],

C_p = Mechanical compliance coefficient [*MPa^{-1}*].

6 Differential swelling and permeability change of coal in response to CO₂ injection (overlap with Chapter 5)

6.1 Introduction

The coal matrix is heterogeneous and is characterized by three different porosity systems - micropores, mesopores and macropores. The macropores are the cleats, which are sub-vertically oriented to the bedding plane in coal. The cleat system consists of the face cleats, continuous throughout the reservoir, and butt cleats, which are discontinuous and terminate against the face cleat.

Darcy flow through the cleats is the most important transport mechanism for gases and liquids through the seam. The cleat permeability is considered to be primarily controlled by the prevailing effective horizontal stress under uniaxial strain reservoir conditions.

Various methods have been proposed to improve the coalbed methane recovery. These methods are collectively called Enhanced Coalbed Methane Recovery (ECBM). One of the methods is based on the principle of inert gas stripping, where a low sorbing or non-sorbing gas like N_2 or H_2 is injected. Since sorption of CH_4 depends on the partial pressures, the process of stripping reduces the partial pressures of methane in the free gas phase and enhances desorption of methane from the adsorbed phase (Puri et al., 1990; Arri et al., 1992). As an alternative, injected CO_2 may preferentially sorb onto coal and compete with methane for the same sorption site. It enhances methane production both by reducing the partial pressure of CH_4 and by preferential sorption. Laboratory experiments, among others, by Kross et al., 2002, suggest that for every methane molecule produced, about two molecules of CO_2 are sequestered. Furthermore, this exchange ratio could be higher at pressures corresponding to supercritical CO_2 conditions (Hall et al., 1984). However this technique has its associated problem in the name of differential swelling.

Extensive lab data in the literature reveal that CO_2 causes a greater degree of coal matrix swelling than methane, even when measured on a unit concentration basis (Levine, 1996; Laxminarayana et al., 2004). This effect has been emphasized in the work of Pekot and Reeves, 2002. CO_2 adsorption causes more strain and swelling than CH_4, since it is adsorbed in higher concentrations. Differential swelling is caused by an excess strain produced by CO_2 over CH_4 on a unit concentration basis. This suggests that the physical change introduced in the macromolecular network structure of coal, as a result of CO_2 dissolution, is more pronounced than for CH_4. This observed difference in the swelling capacity is called differential swelling.

The chemical reasoning behind the process is explained in polymer sciences, where coal is compared to a glassy polymeric system. Reucroft and Patel, 1986 have looked into the

thermodynamic swelling theories for a cross-linked macromolecular network structure. This theory predicts that maximum swelling occurs when the solubility parameter of a gas molecule (δ_{gas}) is equal or close to the solubility parameter of the macromolecular network (δ_{coal}) (Lucht and Peppas, 1981). The solubility parameter (δ) is defined in terms of molar enthalpy of vaporization (H_v) and the molar volume (V).

$$\delta = \sqrt{\left(\frac{H_v - RT}{V}\right)}. \tag{6.1}$$

The solubility parameter of CO₂ ($\delta_{CO_2} \approx 6.1 cal^{0.5} cm^{-1.5}$) being closer to the solubility parameter of coal ($\delta_{coal} \approx 10 cal^{0.5} cm^{-1.5}$) yields higher swelling as compared to CH₄ and N₂ ($\delta_{CO_2} \approx 2.6 cal^{0.5} cm^{-1.5}$) on a unit concentration basis. The solubility parameter of organic solvents like pyridine and acetone are even higher than that of CO₂, thus yielding higher swelling of coal.

Laxminarayana et al., 2004 derives a linear relationship between volumetric strain and gas concentration for CO₂, CH₄, N₂ and H₂S. From his experiments on four different coal samples at any unit gas concentration, the volumetric strain for CO₂ was at least 1.5 times higher than for methane.

Differential swelling as a result of CO₂ injection can cause profound changes in fracture porosity and permeability with significant implication for enhanced methane recovery. Permeability of coal changes due to two reasons: a change in the effective horizontal stress and a change caused due to a differential matrix swelling / shrinkage.

The effect of matrix swelling and shrinkage on cleat permeability of coal samples has been investigated by a number of researchers (Somerton et al., 1975; Durucan et al., 1986; Gray, 1987; Harpalani et al., 1989; Sawyer et al., 1990; Seidle et al., 1995; Palmer et al., 1996; Gilman et al., 2000; Shi et al., 2003 and Chikatamarla et al., 2004). All proposed models, almost invariably have two terms to define the porosity change, (i) a term to account for the pressure dependent nature of the coal porosity, (ii) a term which accounts for porosity changes due to matrix shrinkage and swelling. Pekot and Reeves, 2002 and Laxminarayana et al., 2004 incorporated the effect of differential swelling on fracture porosity in coal. A recent effort by Mavor et al., 2004 to model the effect of differential swelling on secondary porosity and permeability of coal is commendable. He developed a model for estimating changes in secondary porosity and permeability as a function of the pressure and sorbed gas concentration. He used an iterative procedure to calibrate the model with the well test data. Most of the experimental data presented here can also be used to calibrate the model.

This chapter presents an experimental effort to measure the effect of differential swelling on coal permeability using the axial strain measurements on a coal core sample. A linear variable differential transformer (LVDT) has been used to measure the axial strain. The objectives to perform these experiments are:

(i) To determine the differential swelling as a result of CO_2 injection in an initially methane saturated coal core.

(ii) To determine the sweep efficiency of CO_2 as a function of the initial methane saturation at a constant mean pore pressure and constant P_{eff}.

(iii) To estimate and to establish the dependence of permeability on the differential swelling of coal i.e. the effect on permeability due to change in the partial pressures of CH_4 and CO_2 in the free gas phase. The effective stress (P_{eff}), the pressure difference ($P_{injection} - P_{production}$), the mean pore pressure (P_{mean}) and the injection rate are kept constant over the course of the flooding experiment.

This chapter also presents a model that describes the porosity change due to differential swelling as a function of the change in partial pressures using pressure - time relations.

6.2 Equipment design

A high-pressure core flooding setup was constructed. The schematic of the setup is shown in Fig. 5.1a. The pressure cell is 1m in length and can reach a maximum confining oil pressure of 50 MPa and a temperature of 420 K. The confining pressure was applied on the coal core, inside a rubber sleeve. To prevent the gas from diffusing through the rubber sleeve, 0.2 mm lead foil was wrapped around the coal core. To simulate downhole conditions the temperature in the pressure cell was maintained at around 45^0C. The pressure cell can handle samples up to a diameter of 120 mm and a core length of 500 mm. Smaller samples are not representative due to heterogeneity. The length of the core varied from sample to sample. The dimensions of the coal core used in our experiments are provided in Table 6.2. To avoid mechanical end effects on the core permeability, two sieperm plates are fixed at both ends of the core. The photo of the setup is shown in Fig. 6.1. These sieperm plates have a porosity of 33% and a permeability of 10^{-13} m^2. The injection and production tubing's were attached to the end plates.

The measurement of sorption related strain of coal is subject to experimental difficulties. To avoid a long and tedious sample preparation, a simple mechanical micrometer (LVDT) was used to measure the axial strain in the coal core. The cores were drilled parallel to the bedding plane, thus ensuring that the axial strain measured was parallel to this plane.

As described in chapter 5, the high pressure cell consists of the following peripheral devices. All description of peripheral devices is in order of the flow direction.
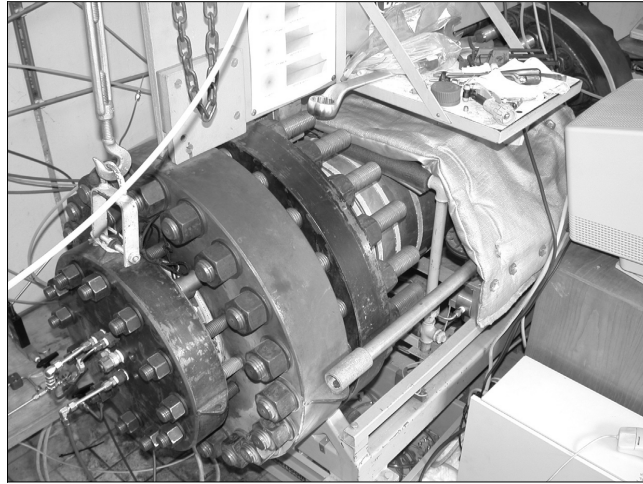
Fig. 6.1 Photo of the high pressure flow cell

- *An ISCO TM plunger pump* was used to inject the required gas. The ISCO plunger pump injects CO_2 into the coal core at a constant injection rate. The average of the injection and production pressure was taken as the pressure over the core and used for the calculation of the Darcy permeability. At the production end, a backpressure valve was used to ensure outflow at constant pressure. A constant pressure difference ($P_{injection} - P_{production}$) facilitates a continuous permeability measurement during the experiment.

- *A linear variable displacement transformer (LVDT)*. This device measured the axial changes of the core dimension (μ-strains) throughout the course of the experiment. The strain measurements were stored, through a data acquisition system, on a computer.

- *Gas analyzer (GC)*. The gas chromatograph used for analyzing the product gas was an Agilent TM 3000 micro GC with a TCD (Thermal Conductivity Detector). The details regarding micro GC and its measurement technique have been discussed in Appendix G.

- *Flow analyzer*. At the end of the line an analog flow analyzer, i.e. an Acataris TM water clock measured the remaining gases leaving the system. This type of analog flow analyzers runs at an accuracy of 0.1 ml/hr. The flow rate was camera recorded and afterward used for mass balance calculations and permeability measurements.

- *Operational panel, safety device and data acquisition system*. The operation panel, the data-acquisition system and safety devices were installed in the control room. During the test, two thermocouples were used to measure temperatures above and below the core inside the

pressure cell. In addition, the (differential) pressure, tube / sample expansion and flows were registered every 30 seconds.

6.3   Sample description

The unique properties of coal put constraints on preparation and preservation of coal samples. When exposed to air, the effect of drying and weathering would result in the alteration of structure of coal and development of induced fractures. The permeability and porosity values of such samples may be significantly different from the samples that are well preserved. The cores were drilled from big blocks of coal. Coal samples used for these experiments were kept in water to avoid contact with air and drying. Once drilled the cores were put in sealed polythene bags and cooled to prevent oxidation or loss of moisture. All the coal cores were drilled parallel to the bedding plane.

The samples used for these experiments were from the Beringen coal mines (Beringen 770) in Belgium, the Silezia coalfield in Poland (Silezia 315 II) and the Tupton coalfields in UK. The details of the samples are shown in Table 6.1. Five different flooding experiments were conducted on coal cores drilled from the samples mentioned above.

Sample	Rank [% R_{max}]	Maceral composition [%]		Specific surface [m^2/g]	Micropore volume [cm^3/g coal]
Beringen 770 (Belgium)	0.78	Vitrinite	37.8	151.53	0.055
		Liptinite	18.0		
		Inertinite	44.0		
		Mineral matter	0.2		
Silezia 315 II (Poland)	0.68	Vitrinite	71.6	190.00	0.064
		Liptinite	6.8		
		Inertinite	15.0		
		Mineral matter	6.8		
Tupton (UK)	0.53	Vitrinite	59.4	244.10	0.08294
		Liptinite	14.0		
		Inertinite	25.8		
		Mineral matter	0.8		

Table 6.1. Compositional and structural details of the coal samples used for the differential sorption experiments

The details of the coal cores and their experimental conditions are in Table 6.2.

Experiment	Length [mm]	Diameter [mm]	P_{mean} [MPa]	P_{eff} [MPa]	Injection rate [ml/hr]	Free CH_4 [moles]	Adsorbed CH_4 [moles]
I (Beringen 770)	334.00	69.50	4.3	3.61	6	0.43	0.61
II (Beringen 770)	178.30	69.50	8.12	2.01	0.7	0.402	0.83
III (Silezia 315 II)	200.50	69.50	8.325	2.25	1	0.1337	0.2913
IV (Silezia 315 II)	200.50	69.50	9.08	1.59	1	0.5176	0.409
V (Tupton)	227.00	75.00	22.85	3.195	1	1.5672	0.4318

Table 6.2. Details of the coal cores used for the differential sorption experiments, the experimental conditions, injection rates and methane saturation

6.4   Differential swelling experiments and permeability measurements

6.4.1   Experimental procedure

The difference in sorption capacities for different gases makes it important to study the effects of CH_4 and CO_2 on the strain, porosity and permeability of coal during the enhanced recovery process. The axial strain measurements give an estimate of the differential swelling of coal. The experiments start with a complex procedure of mounting the coal core sample in a rubber sleeve and building it in the high-pressure cell; leak free. A detailed procedure for volume measurement was then followed. The volume measurements were conducted with and without the sample built in the pressure cell. The tubing volume in the whole setup is of the same order as that of the sample. The effect of this dead volume is clearly observed in the results and has been discussed later in this section.

At the end of the volume measurement the sample cell was connected to a vacuum pump, for a week, to eliminate any form of residual gas or moisture. During this process, the temperature was kept constant. Thereafter the coal was filled with methane in increasing pressure cycles. After each injection cycle the methane was allowed to sorb onto the coal matrix until equilibrium was reached. To meet sub-surface conditions, the difference between the annular pressure and the pore pressure was usually kept at ratios in between 2:1 up to 5:3. The volume of injected methane was measured with a mass flow meter. Thereafter, the tubing system and the pump were brought again to the same pressure and temperature conditions as the methane filled sample. More methane would adsorb and again time was needed for this methane to reach a new equilibrium pressure. In the following injection cycle, the pump was filled with CO_2. Keeping a constant pressure gradient over the whole core with the help of a backpressure valve, the system was allowed to produce alongside injection. The gas analyzer would determine the relative amount of CH_4 and CO_2 in the product gas. The gas chromatograph measured the change in molar concentrations of CH_4 and CO_2 in free phase.

This is partly true, but is a reasonable assumption to understand the permeability variation. The moisture, if any, was separated using silica gel bottle connected to a balance.

Five different differential sorption experiments were conducted (Table 6.2). The experiments range from sub-critical to super-critical CO$_2$ conditions. Experiments I and II were conducted on the Beringen 770 sample from Belgium. Both experiments were conducted on dry coal samples. Experiments III and IV were conducted on the Silezia 315 II sample from Poland. Experiment III was carried out on a moisture equilibrated coal while Experiment IV was carried out on a dry coal. The effect of moisture is evident from the low sweep efficiency (Table 6.4). Experiment V was performed on a dry coal sample from UK (Tupton) at a very high mean pore pressure of 23 MPa.

CO$_2$ flooding (Beringen 770)	CO$_2$ = 1 %		CO$_2$ = 50 %		CO$_2$ = 90 %	
	Dry (6ml/hr)	Dry (0.7ml/hr)	Dry (6ml/hr)	Dry (0.7ml/hr)	Dry (6ml/hr)	Dry (0.7ml/hr)
Sweep efficiency [%]	43.6	22.9	58.8	46.7	69.1	58.7
Displaced volume [mole/mole]	0.91	1.77	1.36	5.1	2.06	10.63
Time after production [sec]	3.36×10^5	6.6×10^5	5.0×10^5	19.0×10^5	7.7×10^5	39.6×10^5

Table 6.3. Sweep efficiency, displaced volume and time of Experiment I and II

CO$_2$ flooding (Silesia 315 II)	CO$_2$ = 1 %		CO$_2$ = 50 %		CO$_2$ = 90 %	
	Dry	Wet	Dry	Wet	Dry	Wet
Sweep efficiency [%]	37.2	11.6	66.25	16.5	69.8	19.5
Displaced volume [mole/mole]	1.28	1.26	2.56	2.09	2.96	2.86
Time after production [sec]	3.8×10^5	2.7×10^5	7.6×10^5	4.5×10^5	8.8×10^5	6.1×10^5

Table 6.4. Sweep efficiency, displaced volume and time of Experiment III and IV

The permeability of the coal varies due to combined effects posed by the process of differential sorption. It varies due to shrinkage, while methane is being desorbed and due to swelling, while carbon dioxide is being injected. The effect of swelling due to CO$_2$ sorption is more profound, thus resulting in an excess volumetric strain. The test procedure to measure permeability change during the differential sorption experiments involved the simultaneous injection of CO$_2$ and production of the mixed gas under steady pressure conditions. The injection of CO$_2$ was done with the ISCO pump at a constant rate. A mass flow meter was used to measure the flow on the production end. To keep the downstream pressure constant and to create a pressure gradient, a back pressure valve was used. Because gas pressure varied

across the sample, the average of the injection and the production pressures was used in the calculation of the effective stress. As permeability is a function of the effective stress, it was kept constant during the experiment. The equation below was used to calculate the core permeability (Gray, 1987).

$$k[m^2] = \frac{2qP_0L\mu}{A(P_i^2 - P_o^2)}.$$ (6.2)

The flow measurements for a particular permeability step were only used when equilibrium conditions were satisfied. The differential swelling corresponding to the differential gas sorption is controlled by the change in the partial pressures of the individual components. Assuming Darcy's flow to be the primary means of gas transport through the cleats, ample care was taken to see that the adsorbed gas is in dynamic equilibrium with the free gas phase, although at times this was very difficult to attain. The difference between the injection and the production pressure was kept constant during the flow measurements.

6.4.2 Results and discussion

Differential swelling from all five experiments here, are reported as the measured linear strain in the axial direction of the core and not as volumetric strain. All the differential strain measurements are shown in the Figs. 6.2, 6.5, 6.8, 6.11 and 6.14. There was no need to correct the strain measurements for mechanical compliance as the injection and production scheme was at constant pore pressure and effective stress. In all five experiments, as can be seen from the plots, the coal does not start to swell right at the onset of CO_2 injection. The delay in the strain response is because of the fact that the injected CO_2 had to displace the tubing volume preceding the core, before it reached the coal.

The overview of the experimental conditions and sample details are given in Table 6.2. In order to compare the experiments, the relative amount as measured by the gas analyzer and sweep efficiency are plotted against the displaced volume. The displaced volume is used to make time dimensionless. The sweep efficiencies and the molar concentration changes have been plotted against the displaced volume for all five experiments in Figs. 6.3, 6.6, 6.9, 6.12 and 6.15. Sweep efficiencies of all four dry experiments ranged between 60 to 90 % of the methane initially in place. Sweep efficiency and displaced volume are defined as follows:

$$\text{Sweep effeciency (\%)} = \frac{\text{moles of } CH_4 \text{ produced}}{\text{moles of } CH_4 \text{ initially in place}} \times 100$$ (6.3)

$$\text{Displaced volume} = \frac{\text{moles of } CO_2 \text{ injected}}{\text{moles of } CH_4 \text{ initially in place}}$$ (6.4)

The results of Experiment I and II are shown in Table 6.3. The experimental conditions prior to the start of CO_2 injection have been shown in Table 6.2. Figs. 6.3 and 6.6 show

migration history of CH_4 and CO_2 during the course of the experiment. Both the experiments were conducted at a temperature of 45^0C.
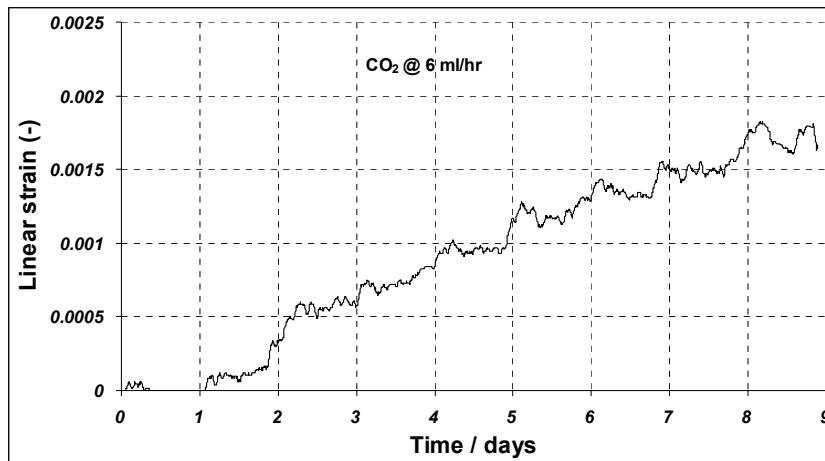

Fig. 6.2 Differential swelling measured as linear strain of the Beringen 770 from Experiment I
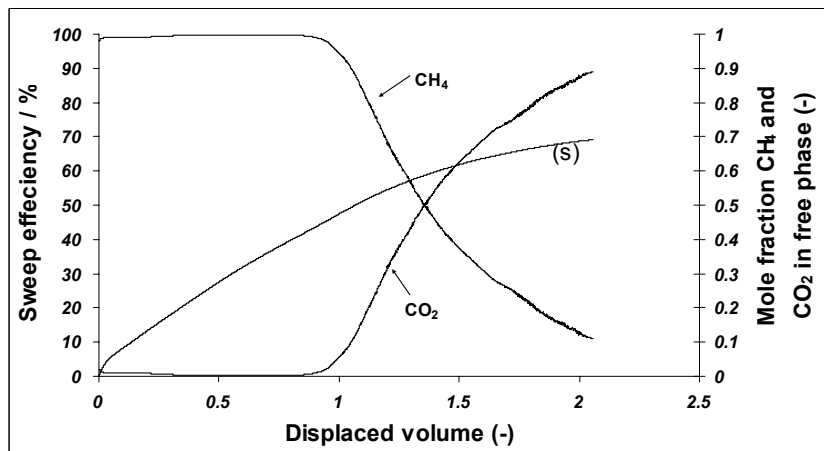

Fig. 6.3 Sweep efficiency (s) and molar concentrations of the produced gas against displaced volume from Experiment I

While the injection rate for Experiment I was 6 ml /h, that of Experiment II was set as low as 0.7 ml /h. Pressure and temperature conditions for both CH_4 and CO_2 were sub-critical in case of Experiment I, but were super-critical for Experiment II. As can be seen from the migration data

(Figs. 6.3 and 6.6) the injection pressure does not have a big influence on the methane recovery. Diffusion is much faster in the sub-critical gas phase than under super-critical conditions. CO_2 is five times denser than CH_4 under super-critical conditions. The coal core used in experiment I is twice as long as that of Experiment II (Table 6.2). As can be seen from Table 6.3, the breakthrough time for Experiment I is almost two times faster than Experiment II. Thus with an injection rate of 6 ml /h the sub-critical CO_2 is traveling four times as fast as compared to an injection rate of 0.7 ml /h . Also at breakthrough (1% CO_2), almost all the free methane in the system have been produced whereas only half the free volume of methane have been produced for the second case. From the displaced volume data it is evident that in terms of simple methane recovery, at 90% of product CO_2 concentration, Experiment I might look more efficient as it takes almost five times less time to remove equal concentration of CH_4 from the system. It can be seen that for better exchange and storage of CO_2, the residence time for CO_2 in the coal has to be longer. Diffusion is more predominant in Experiment II than in Experiment I. In Experiment I the injected CO_2 races through the core to get produced.
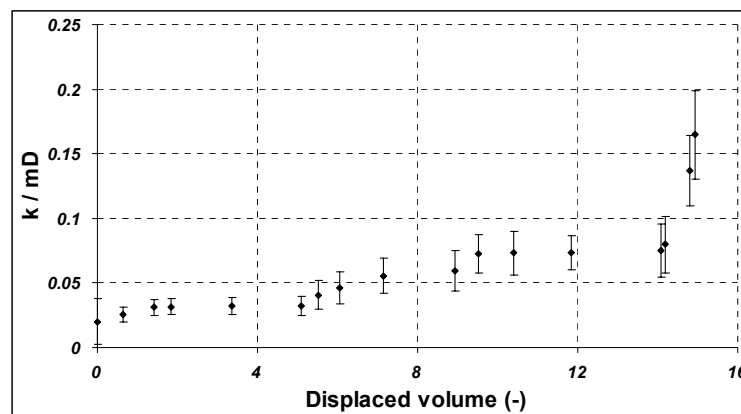

Fig. 6.4 Experimentally determined variation in permeability for the Beringen 770 coal as a result of differential swelling from Experiment II under unconstrained conditions

The results from Experiment III and IV can be used to compare the influence of water on the CO_2-CH_4 exchange process in the coal. The experimental conditions for these experiments have been shown in Table 6.2. Both the experiments were conducted on the same coal sample. Experiment II was conducted on a wet coal core where there was excess water present in the fracture system of the coal. No free water was present in the relatively dry Experiment IV. The comparative results of the experiments have been summarized in Table 6.4. The wet experiment was conducted for a much longer duration than the dry one.
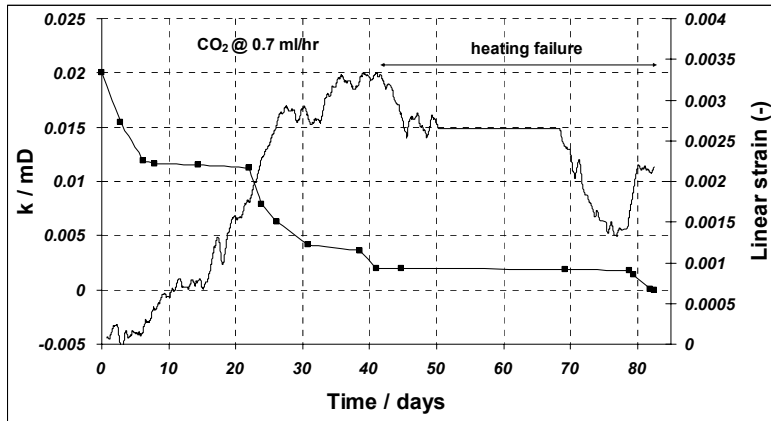
Fig. 6.5 Estimated permeability variations for Beringen 770 under constrained conditions using experimentally determined permeability data from Experiment II
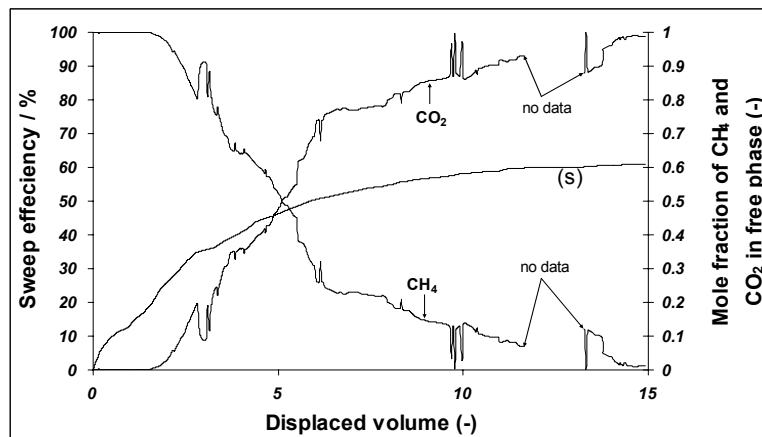

Fig. 6.6 Sweep efficiency (s) and molar concentrations of the produced gas against displaced volume from Experiment II. The period of no data on the plot is a result of electrical failure in the laboratory.

It is seen that only 34% of the CH$_4$ in place was produced at the end of the wet experiment, whereas almost 79% of the CH$_4$ in place was produced from the dry experiment. An estimate shows that, apart from the free methane that was produced, only 3% of the adsorbed methane was produced from the wet experiment, whereas 50% was produced from the dry experiment.

Fig. 6.7 Experimentally determined variation in permeability for a moist Silezia 315 II coal as a result of differential swelling from Experiment III under unconstrained conditions

Fig. 6.8 Estimated permeability variations for Silezia 315 II under constrained conditions using experimentally determined permeability data from Experiment III. The periodicity in the strain data is a consequence of the back pressure valve opening and closing at certain pressure thresholds. The initiation of the permeability drop coincides with the sharp rise in the linear strain measurement.
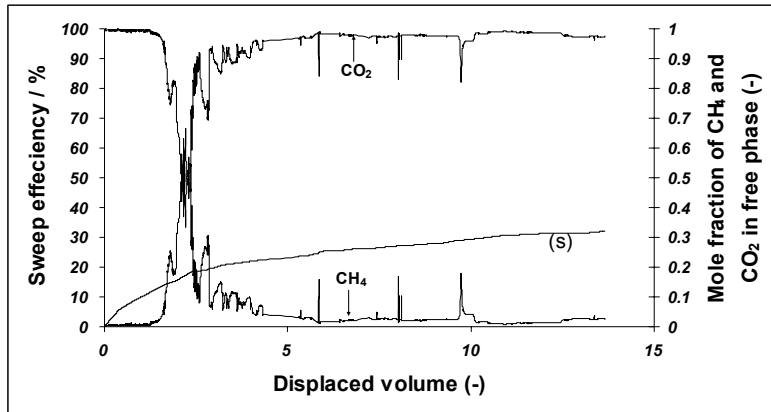
Fig. 6.9 Sweep efficiency (s) and molar concentration of the produced gas against displaced volume from Experiment III
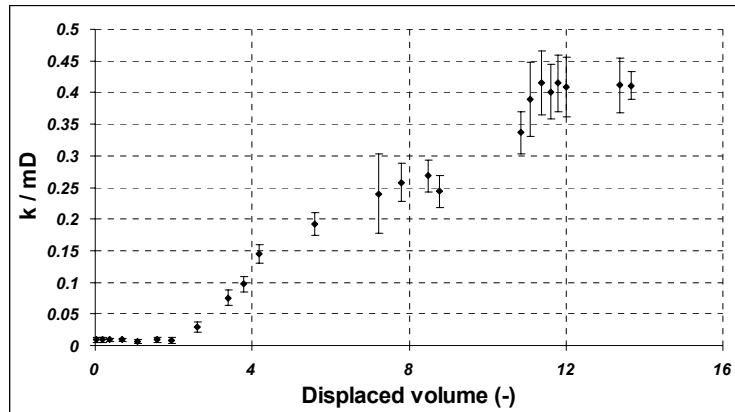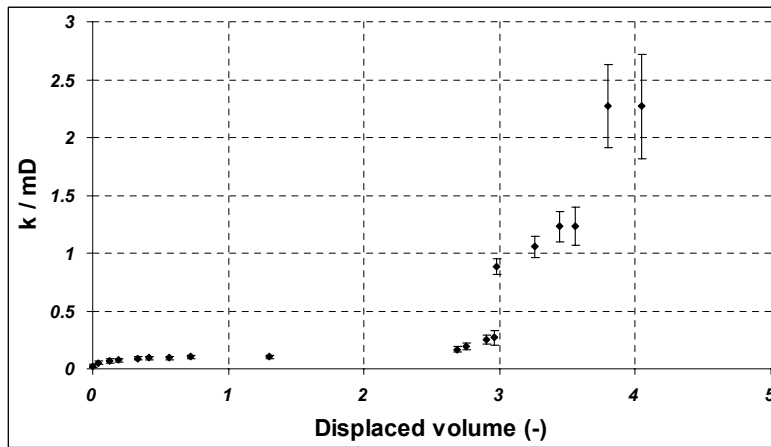

Fig. 6.10 Experimentally determined variation in permeability for the dry Silezia 315 II coal as a result of differential swelling from Experiment IV under unconstrained conditions

From Table 6.4 it is seen that there is no considerable difference in the breakthrough time for both experiments. A slightly faster breakthrough for the wet experiment can be possibly attributed to the fact, that some dissolved CO_2 is produced along with the water, which is forced out of the fracture space. Looking at the sweep efficiencies at different times from Table 6.4, the methane recovery for the relatively dry experiment is high as compared to the wet experiment. The CO_2 storage capacity does not differ much. This is also an indication that CO_2 occupies different sorption sites than CH_4. The CO_2 and CH_4 migration data for both the experiments have been shown in Figs. 6.6 and 6.9.

With the injection of CO_2 the partial pressure of CH_4 in the free phase decreased, inducing the production of methane. Whether or not CO_2 was preferentially replacing CH_4 was not clear, but from the CO_2 mass balance and from the differential swelling it was evident that the solubility of CO_2 in coal is more pronounced than that for CH_4. The term solubility has been used considering that swelling is referred to as an increase in the volume occupied by the coal as a result of the viscoelastic relaxation of its highly crosslinked macromolecular network (Larsen, 2004). Moreover all four dry experiments indicate that the amount of methane produced is greater than the methane initially there in the free phase. This was not true for the wet experiment. Consequently, under dry conditions, the incremental methane produced, is likely due to the preferential desorption of methane in the presence of CO_2. Since differential sorption is a fact as can be seen from the differential strain data, it can be concluded that CO_2 causes more strain on a unit concentration basis.
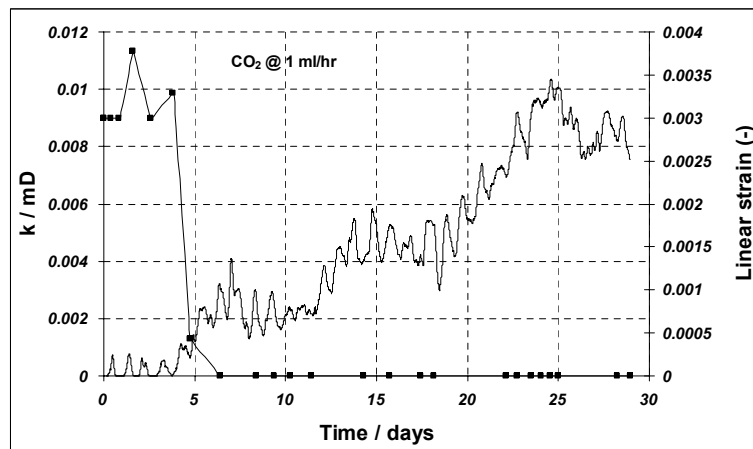

Fig. 6.11 Estimated permeability variations for dry Silezia 315 II under constrained conditions using experimentally determined permeability data from Experiment IV
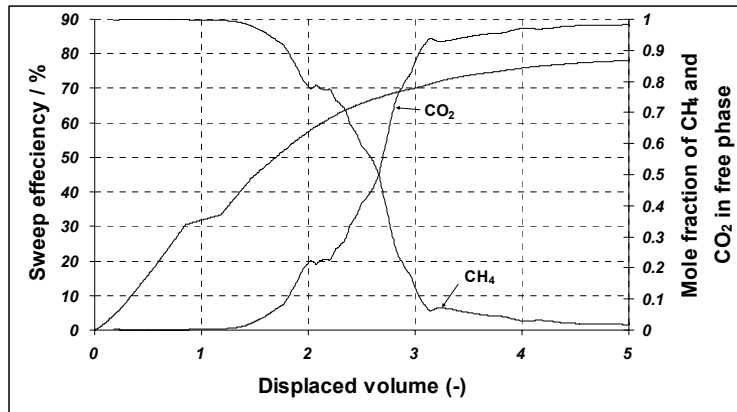
Fig. 6.12 Sweep efficiency and molar concentrations of the produced gas against displaced volume from Experiment IV
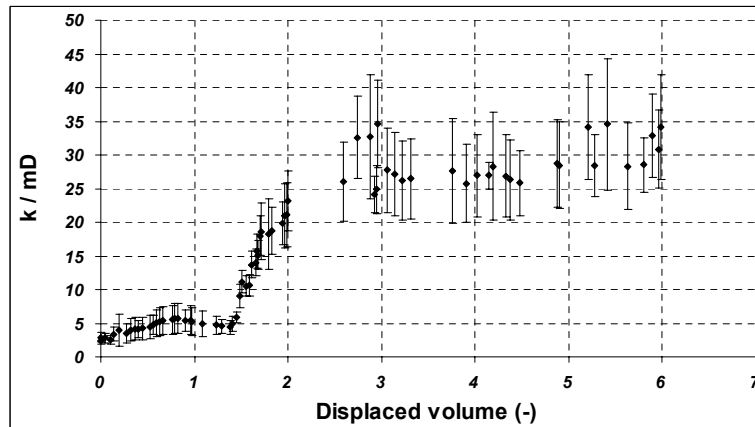
Fig. 6.13 Experimentally determined variation in permeability for the dry Tupton coal as a result of differential swelling from Experiment V under unconstrained conditions
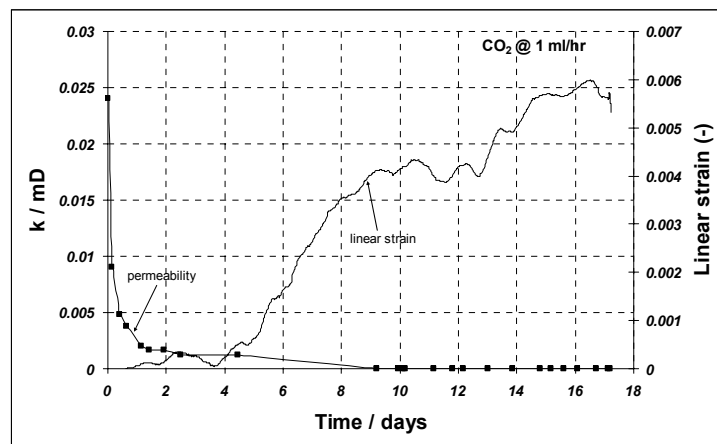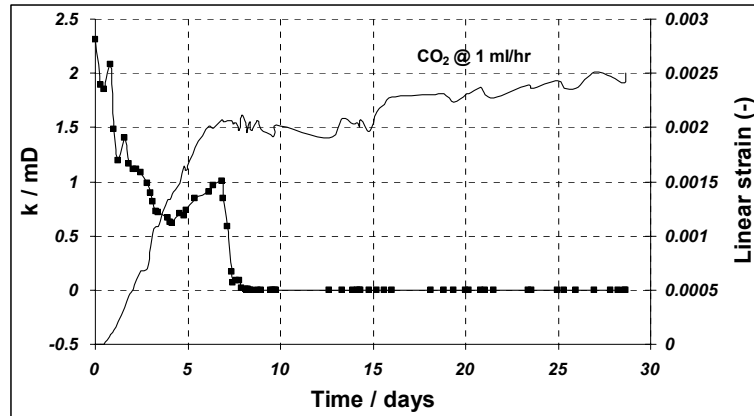
Fig. 6.14 Estimated permeability variations for dry Tupton under constrained conditions using experimentally determined permeability data from Experiment V
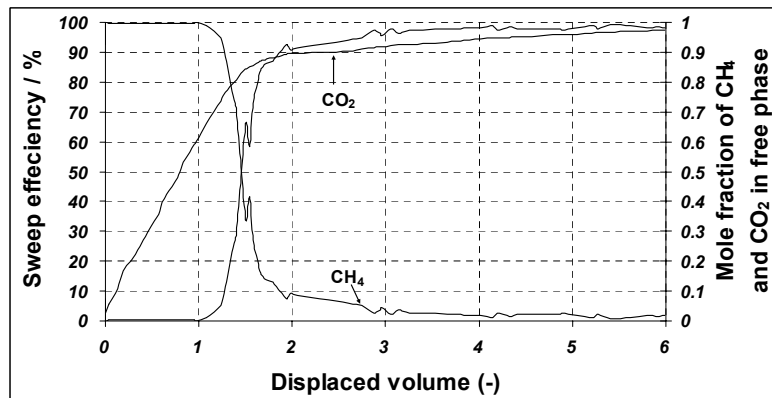
Fig. 6.15 Sweep efficiency and molar concentrations of the produced gas against displaced volume from Experiment V

Binary gas sorption experiments conducted by Prusty et al., 2004 and Laxminarayana, 2004 are different from these experiments. In those experiments, a static equilibrium was attained before each measurement was conducted. In the experiments reported here, a dynamic setup is presented, which is more realistic with respect to field applications.

The results of the permeability measurements in the laboratory are shown in the Figs. 6.4, 6.7, 6.10 and 6.13. The random errors in the permeability measurements were determined. A detail of the error analysis procedure is explained in Appendix A. Under stress, the Belgian

and the Polish coal samples have low initial permeability. All five experiments were conducted at constant mean pore pressure and at constant effective stress conditions. Since the coal core was free to swell inside the pressure cell (unconstrained swelling), the measured permeability increase corresponds to an increase in the differential strain in coal. This whole process of free swelling in the laboratory in comparison to constrained swelling in the field is analogous to thermal expansion (Shi and Durucan, 2003). A hollow steel pipe when subjected to thermal expansion encounters an increase in its free volume, which is analogous to an increase in the cleat porosity with increasing differential swelling in our case.

From the experimental results (Figs. 6.4, 6.7, 6.10 and 6.13), changes in cleat porosity were calculated. The increase in coal cleat volume due to differential swelling is considered to be equal to the decrease in cleat porosity under field conditions with constrained swelling. This assumption is valid when the total volume of coal (matrix and cleats) remains constant with injection of CO_2.

Using the experimentally determined permeability measurements under unconstrained conditions (Figs. 6.4, 6.7, 6.10 and 6.13) and assuming that permeability varies with porosity as follows,

$$\frac{k_{new}}{k_{initial}} = \left(\frac{\varphi_f^{new}}{\varphi_f^{initial}}\right)\left(\frac{\phi_{new}}{\phi_{initial}}\right)^3 \frac{(1-\phi_{initial})^2}{(1-\phi_{new})^2} \approx \left(\frac{\phi_{new}}{\phi_{initial}}\right)^n. \qquad (6.5)$$

changes in cleat porosity were calculated. In Eq. 6.5 φ_f is the volume fraction of the fractures and ϕ the cleat porosity. n in the above equation has a value of 3 for coal. In Eq. 6.5 the first and the last term drops because of very low fracture porosity. The increase in coal cleat porosity due to unconstrained swelling is considered to be equal to the decrease in cleat porosity under field conditions with constrained swelling. This assumption is valid when the total volume of coal (matrix and cleats) remains constant with injection of CO_2. With the decrease in cleat porosity calculated, the permeability variation under constrained conditions was determined. It is difficult to measure cleat porosity accurately because of the very small volume of cleats in solid coal. For a simple model like the above, any value for the initial cleat porosity returns the same estimate for the change in permeability with differential swelling of coal. The resulting variations in permeability alongside differential strain for all five experiments are shown in Figs. 6.5, 6.8, 6.11 and 6.14. For all initial porosity cases, the permeability variation corresponding to differential swelling is dependent on the differential swelling capacities of coal, for each gas, on a unit of concentration basis. Under laboratory conditions, the near zero permeability can be explained as the flow, which takes place through the coal matrix and can no longer be considered as a fracture or cleat flow. Zutshi and Harpalani, 2004 have also reported a similar analysis with a matchstick model. This problem can be anticipated at field scale injection projects in low permeability coal. Thus injecting under a near zero permeability

condition leads to a very high bottom hole pressures, which exceeds the fracture breakdown limit resulting in propagation of uncontrolled fractures.

6.5 Permeability change model for differential swelling of coal (saturated reservoirs)

Most previous researchers have rightly modeled the pressure dependent nature of coal porosity. Thus the focus has been to model the porosity change due to differential swelling as a function of the change in partial pressures using extended Langmuir formulation to model the differential strain.

For isothermal coal beds, the uniaxial strain (Appendix H) caused by coal matrix swelling upon gas adsorption is analogous to the strain due to the temperature changes for thermo-poroelastic medium (Palmer and Mansoori, 1996). The derivation makes an analogy between thermal expansion and matrix swelling associated with differential sorption in coal beds. Stress strain relationship for a thermoplastic porous media has been obtained from the available literature (Bear and Corapcioglu, 1981). In a non-isothermal body, if the temperature increases the fabric swells, leading to a decrease in the porous medium porosity. This is directly analogous to matrix swelling in coal, where the porosity decreases as a result of differential sorption of a binary gas mixture.

$$-d\phi = -\frac{1}{M}dp + \left[\frac{1}{3}\left(\frac{1+\nu}{1-\nu}\right)+f-1\right]\gamma dp - \left[\frac{1}{3}\left(\frac{1+\nu}{1-\nu}\right)-1\right]\alpha dT, \qquad (6.6)$$

where ϕ is the cleat porosity in fraction, M the constrained axial modulus in MPa, ν the Poisson's ratio, γ the grain compressibility in MPa^{-1}, α the grain thermal expansivity and f as a fraction. The term in dT is a temperature expansion / contraction term (if temperature drops, the fabric shrinks, and the cleats increase in width). This is directly analogous to matrix shrinkage, where cleat width increases as gas desorbs during pressure drawdown. By direct analogy, we can write for incremental rock volume strain (i.e., increase in strain per unit temperature or pressure change),

$$\alpha dT = \frac{d}{dp}\left(\frac{c_0 \beta p}{1+\beta p}\right)dp, \qquad (6.7)$$

Assuming that the volumetric strain curve has the same empirical form as that of the Langmuir formulation, it leads to the following equation,

$$-d\phi = -\frac{1}{M}dp + \left[\frac{1}{3}\left(\frac{1+\nu}{1-\nu}\right)+f-1\right]\gamma dp - \left[\frac{1}{3}\left(\frac{1+\nu}{1-\nu}\right)-1\right]\frac{d}{dp}\left(\frac{c_0 \beta p}{1+\beta p}\right)dp, \qquad (6.8)$$

The moduli M and Poisson's ratio v are independent of the pressure and can be measured in the laboratory. c_0 is the parameter of Langmuir curve match to volumetric strain change due to swelling. In the original Palmer and Mansoori (1996) formulation as shown above the first series of terms to the right hand side of the equation account for the pressure dependent nature of the coal porosity, while the second term accounts for the porosity change due to matrix shrinkage (in primary depletion). The second term is of interest and is open for improvement to incorporate the aspect of differential swelling reported in Chapter 6.

$$d\phi = \left[\frac{1}{3}\left(\frac{1+v}{1-v}\right)-1\right]\frac{d}{dp}\left(\frac{\varepsilon_i\beta_iX_ip+\varepsilon_j\beta_jX_jp}{1+\beta_iX_ip+\beta_jX_jp}\right)dp, \tag{6.9}$$

where $\beta_i = 1/P_{\Psi_i}$, $\beta_j = 1/P_{\Psi_j}$, $X_ip := p_i$ and $X_jp := p_j$.

The above equation has been formulated by drawing a direct analogy of differential swelling to extended Langmuir equation for multi component gas sorption. Such an analogy comes with some assumptions, which are as follows,

(i) The adsorbed gas is in equilibrium with the free gas phase in the fractures.

(ii) The differential swelling corresponding to the differential gas sorption is controlled by the change in the partial pressures ($p_{i,j}$) of the individual components.

Since an enhanced recovery project will only be taken up after primary depletion, such an injection production system would preferably be operated at a constant reservoir pressure. Any increase or decrease in the reservoir pressure would mean the addition of an extra porosity change term to accommodate the change in the effective horizontal stress normal to the cleat.

The Eq. 6.9 can be simplified by making the following replacements,

$$\alpha = \left[\frac{1}{3}\left(\frac{1+v}{1-v}\right)-1\right] \text{ and } a = \beta_iX_i; \; b = \beta_jX_j; \; x = \varepsilon_i; \; y = \varepsilon_j.$$

Integrating Eq. 6.9 with respect to the pressure (p), between p_0 and p we get,

$$\phi = \alpha\left[\frac{1}{a+b}(ax+by)+\frac{-ax-by}{(a+b)(1+ap+bp)}\right], \tag{6.10}$$

For an initially methane saturated reservoir, the mole fraction of CO_2 is zero. Thus,

$$\phi - \phi_0 = \alpha\left[\frac{ax+by}{a+b}-\frac{ax+by}{(a+b)(1+ap+bp)}\right]-\alpha\left(\frac{axp_0}{1+ap_0}\right), \tag{6.11}$$

$$\frac{\phi}{\phi_0} = 1+\frac{\alpha}{\phi_0}\left[\frac{ax+by}{a+b}-\frac{ax+by}{(a+b)(1+ap+bp)}-\frac{axp_0}{1+ap_0}\right], \tag{6.12}$$

substituting the corresponding values of α, a, b, x and y we get,

$$\frac{\phi}{\phi_0} = 1 + \frac{1}{\phi_0}\left[\frac{1}{3}\left(\frac{1+\nu}{1-\nu}\right) - 1\right]$$

$$\left[\frac{\beta_i X_i \varepsilon_i + \beta_j X_j \varepsilon_j}{\beta_i X_i + \beta_j X_j} - \frac{\beta_i X_i \varepsilon_i + \beta_j X_j \varepsilon_j}{\beta_i X_i + \beta_j X_j + 2(\beta_i X_i)(\beta_j X_j)p + (\beta_i X_i)^2 p + (\beta_j X_j)^2 p} - \frac{\beta_i X_i \varepsilon_i p_0}{1 + \beta_i X_i p_0}\right].$$

(6.13)

Assuming that permeability varies with porosity as Eq. 6.5, the permeability change can be effectively calculated as a function of elastic moduli, initial porosity and strain properties corresponding to single component gas behavior.

The input parameters for the model require separate absolute volumetric swelling experiments to be conducted on a coal sample for each gas component. These experiments will yield values for ε_i, ε_j, P_{Ψ_i} and P_{Ψ_j}. All the input parameters required to model a differential swelling experiment were only available for Experiment II, III and V. The input parameters used to model the permeability change are provided in Table 6.5. Similar model have also been developed by Mavor et al. (2004) and have been used to match data from the Fruitland coal of the San Juan Basin.

	Experiment II	Experiment III	Experiment V
ϕ_0, [-]	0.035	0.0084	0.0194
k_0, mD	0.02	0.009	2.309
ν, [-]	0.39	0.39	0.39
E, [MPa]	2.50E+03	2.50E+03	2.50E+03
β_{CH_4}, MPa^{-1}	0.189	0.189	0.189
β_{CO_2}, MPa^{-1}	0.33	0.33	0.33
ε_{CH_4}, [-]	0.0344	0.0244	0.0244
ϵ_{CO_2}, [-]	0.045	0.0427	0.042
$p_{initial}$, MPa	8.09	8.17	22.84

Table 6.5 Parameters used to model the permeability change for differential swelling experiments

The model result for Experiment II, III and V are shown in Figs. 6.16, 6.17 and 6.18. Except for Experiment III, the model results show a reasonable match with the experimental permeability values quite reasonably. The fit to the experimental data was also used to extend the model to permeability and porosity predictions under true constrained reservoir conditions. All reported sorption-induced strain data for coal use unconstrained coal samples, meaning that the coal samples were allowed to expand in all three directions without applying any external constraining force. The data shown in Fig. 6.17, where measured permeability of Experiment III is compared to model-calculated permeability, indicates that there is less strain occurring during the flooding experiment than that indicated by the measured strain curves. Similar conclusions have also been reached by Robertson et al. (2005). The model takes in as an input the change in the partial pressures of the individual components over the whole course of the experiment. The partial pressures were calculated from the measurements of the gas chromatograph. The composition of the produced gas is assumed to be the average composition of the free phase over the whole coal core. This assumption obviously for modelling purpose does not hold. The fact that the CO_2 in the core moves with a distinct front cannot be ruled out.

Fig. 6.16 Model comparison of the permeability measurements for Beringen 770 coal, used for Experiment II. Eqs. 6.5 and 6.13 have been used to model the experimental permeabilities.

Fig. 6.17 Model comparison of the permeability measurements for Silezia 315 II coal, used for Experiment III. Eqs. 6.5 and 6.13 have been used to model the experimental permeabilities.
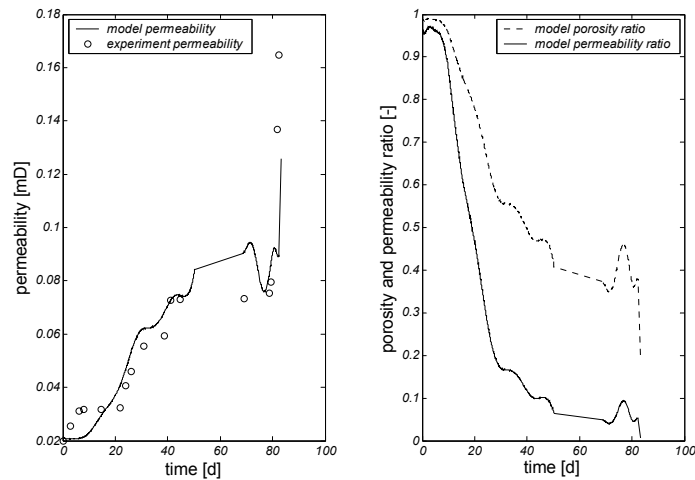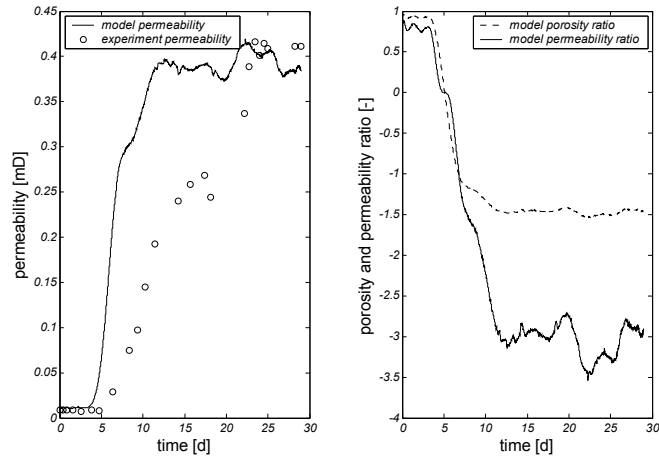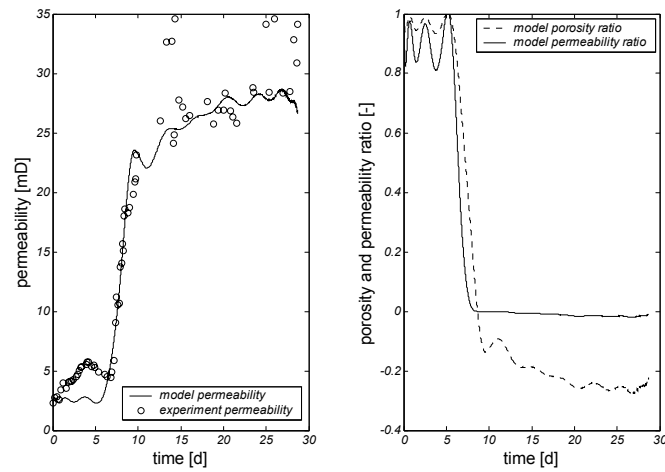

Fig. 6.18 Model comparison of the permeability measurements for Tupton coal, used for Experiment V. Eqs. 6.5 and 6.13 have been used to model the experimental permeabilities.

6.6   Conclusions

- Experiments conducted to measure the differential swelling of coal were successful. Differential strain develops as a result of the excess strain caused by the dissolution of CO$_2$ in coal when compared with CH$_4$ on a unit concentration basis. Linear strains in the order of 0.0015 to 0.006 are measured in that respect.

- The effect of the differential swelling on the fracture porosity and permeability of coal has been experimentally determined.

- The uncertainty in the measurements has been determined and shows that the pressure gradient over the core has the greatest influence on the error measurements.

- Thus differential swelling is a condition that has been measured and observed in the laboratory, where it carries a different degree of permeability change on a unit concentration basis.

- Work needs to be done to understand the chemical behavior of coal, CH$_4$ and CO$_2$ in the process of differential swelling.

Nomenclature

H_v = enthalpy of vaporization, cal

δ = solubility parameter, $cal^{0.5} cm^{-1.5}$

V = molar volume, cm^3

M = constrained axial modulus, MPa

ν = poission ratio, $[-]$

ϕ = cleat porosity, $[-]$

ϕ_0 = initial cleat porosity, $[-]$

k = permeability, mD

k_0 = initial permeability, mD

γ = grain compressibility, MPa^{-1}

p = reservoir pressure, MPa

p_0 = initial reservoir pressure, MPa

X_i and X_j = mole fraction of component i and j, $[-]$

p_i and p_j = partial pressures of component i and j, MPa

β = reciprocal of P_Ψ, MPa^{-1}

P_Ψ = gas pressure at which the matrix strain is half the maximum value, MPa

ε = maximum volumetric strain when the coal is fully saturated by a single gas component, $[-]$

q = flow rate $[m^3/\sec]$,

P_0 = production pressure $[MPa]$,

P_i = injection pressure $[MPa]$,

μ = viscosity $[Pa.s]$,

A = crossection area $[cm^2]$

L = length of the core $[m]$

7 Core flooding experiments and modelling

Part I – CO$_2$ and flue gas core flooding experiments

7.1 Introduction

In the context of the geological storage of CO$_2$ a few projects consider the direct injection of flue gases from power plants and other industries. Part of this research is to investigate the use of flue gas as an alternative to pure CO$_2$ as an injectant and how it influences the sequestrable amount of CO$_2$ in dry and water saturated coal. Flue gas primarily consists of N$_2$, which act as a stripper.

Coal is characterized by its dual porosity: it contains both primary (micro pores and meso-pores) and secondary (macro pores and natural fractures) porosity systems. The primary porosity system contains the largest part of the gas-in-place, while the secondary porosity system provides the conduit for mass transfer to the wellbore. Primary porosity gas storage is dominated by adsorption. It is relatively impermeable due to the small pore size. Mass transfer for each gas molecular species is dominated by diffusion that is driven by the concentration gradient. Flow through the secondary porosity system is dominated by Darcy flow that relates flow rate to permeability and pressure gradient.

The conventional primary CBM recovery process begins with a production well that is often stimulated by hydraulic fracturing to connect the well bore to the natural fracture system of the coal via an induced fracture (Mazumder et al., 2003). When the pressure in the well is reduced by pumping water by using artificial lift, the pressure in the induced fracture is reduced. This in turn reduces the pressure in the natural coal fracture system. When the operation starts, water begins to move in the opposite direction of the pressure gradient. When the pressure of the natural fracture system drops below the critical desorption pressure, methane starts to desorb from the primary porosity and is released into the secondary porosity system. As a result, the adsorbed gas concentration in the primary porosity system is reduced and creates a concentration gradient that results in mass transfer by diffusion through the micro and meso porosity. Adsorbed gas is released as the pore pressure drops (Reznik et al., 1984).

Enhanced recovery of coalbed methane (ECBM) uses the injection of a second gas that maintains overall reservoir pressure, while lowering the partial pressure of methane in the free gas. CO$_2$, which adsorbs more strongly than methane, is injected into the natural fracture system during the ECBM recovery process. It is preferentially adsorbed into the primary porosity system (Busch et al., 2004) and forces the CH$_4$ into the secondary porosity system. The pore pressure of the secondary porosity pressure is increased due to CO$_2$ injection and the CH$_4$ flows to the injection wells (Shi et al., 2003).

Core flood experiments were performed with varying injectants as part of this study. The experiments conducted are reported in Table 7.2. However there is an overlap of the Experiments I to IV with Chapter 6. The differential swelling measurements of these experiments have been discussed separately in the previous chapter. The objectives to perform these experiments are:

(i) Experiments I and II were conducted to compare the influence of injection pressure and injection rate on the methane recovery. Both the experiments were conducted on relatively dry coal core samples.

(ii) Experiments III and IV; experiments V and VI are compared to evaluate the influence of water on the CH$_4$- CO$_2$ exchange process in coal.

(iii) Experiment VII was conducted to compare the effects of an alternate injection of a strong (CO$_2$) and weak (N$_2$) adsorbing gas.

(iv) To compare the breakthrough time of CO$_2$ from different CO$_2$ core flood experiments.

(v) To estimate the influence of the free / dead volume over the flooding experiments.

(vi) To compare the effect of phase behavior of CO$_2$, CH$_4$, N$_2$ and water under the experimental conditions (e.g. core flood experiments conducted with liquid and super-critical CO$_2$).

(vii) To do flooding experiments with commercially available flue gas.

7.2   Equipment design

For the reasons listed below, large cores (800 cm^3 - 1000 cm^3) were used and this made the design of the setup complex. The reasons to use large core samples are: (i) The presence of a heterogeneous coal matrix and (ii) the dual porosity nature of coal is used. Taking this into consideration a high pressure core flooding setup was constructed (Fig. 7.1a). The pressure cell of 1m in length has a maximum confining pressure of 20 MPa and a maximum temperature of 150°C. The coal core is placed inside a rubber sleeve. This rubber material is able to transfer the total confining pressure onto the cylindrical coal sample. To avoid gas flow between the sleeve and the coal, irregularities on the coal surface are smoothed away with a mash of crushed coal dust and water. To prevent the gas from diffusing through the rubber sleeve into the oil, 0.2 mm lead foil was wrapped around the coal core. A schematic of the prepared sample is given in Fig. 7.1b. To simulate downhole conditions the temperature in the pressure cell was maintained at ~45°C. The pressure cell can handle samples up to a diameter of 120 mm and a core length of 500 mm. To avoid mechanical end effects and poor flow distribution, sieperm plates with a porosity of 33% and a permeability of 10^{-13} m^2 are fixed at both ends of the core. The injection and production tubing's are attached to the end plates. Leakage is checked with helium and minimized by twisted wires around the sleeve on the end pieces.
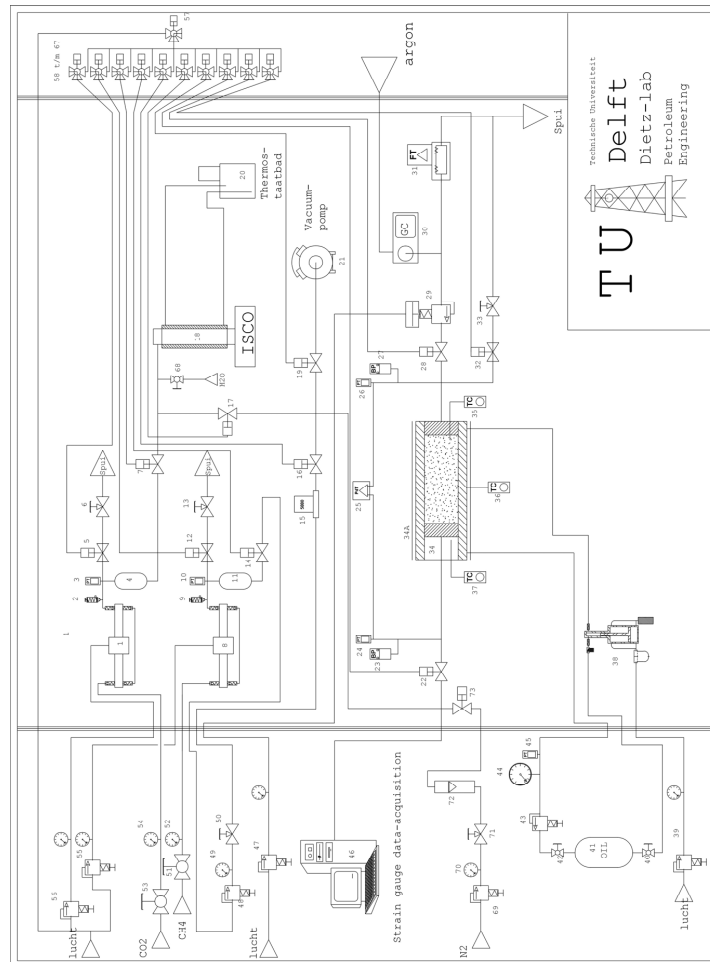
Fig. 7.1a Technical drawing of the high pressure core flooding setup. The essential components of the setup are numbered as follows: 1, 8 gas boosters; 6,13, 33, 71, 50, 51, 53 ball taps; 22, 28, 32, 16, 17, 19, 14, 5 air actuated valves; 20 thermostatic bath; 23, 27 safety valves; 25 pressure difference transducer; 24, 26 pressure transducers; 31 digital flowmeter; 30 gas chromatograph; 18 ISCO pump; 21 vacuum pump; 46 pressure and strain gauge data acquisition system; 35, 36, 37 thermocouples; 34A pressure vessel.

Following the direction of flow, the high pressure cell consists of the following peripheral
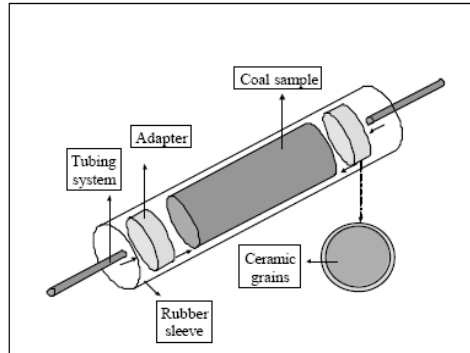
Fig. 7.1b A schematic view of all the elements that make
the coal sample for the flooding experiments

devices:

• *An ISCO TM plunger pump connected to a bottle of the required gas to be injected*. The ISCO plunger pump injects CO$_2$, CH$_4$, N$_2$ and / or flue gas into the coal core at a constant injection rate. Numbered as 18 on Fig. 7.1a (technical drawing).

• *Differential pressure gauge* measurements were used for the calculation of the Darcy permeability. A constant pressure difference was maintained during the experiment. Numbered as 25 on Fig. 7.1a (technical drawing).

• *A back pressure valve* controlled the flow out at the production end. Numbered as 29 on Fig. 7.1a (technical drawing).

• *A linear variable displacement transformer (LVDT)* measured the axial displacement of the core dimension (μ-strains) throughout the experiment. The cores were drilled parallel to the bedding plane, thus ensuring that the axial strain measured was parallel to the bedding.

• *Gas analyzer (GC).* An Agilent^{TM} 3000 micro GC with a TCD (Thermal Conductivity Detector) was used to measure the composition of the product gas. Details regarding gas chromatography are discussed in Appendix G. Numbered as 30 on Fig. 7.1a (technical drawing).

• *Flow analyzer.* At the end of the line an analog flow analyzer, i.e. an Acataris^{TM} water clock measured the remaining gases leaving the system. This type of analog flow analyzers runs at an accuracy of 0.1 ml/h. The flow rate was camera recorded and afterward used for mass balance calculations and permeability measurements. Numbered as 31 on Fig. 7.1a (technical drawing).

• *Operational panel, safety device and data acquisition system.* The operation panel, the data-acquisition system and safety devices were installed in the control room. During the test, three thermocouples were used to measure temperatures above and below the core inside the pressure cell. In addition, the (differential) pressure, tube / sample expansion and flows were registered every 30 s. Thermocouples are numbered as 35, 36 and 37 on Fig. 7.1a. The safety devices are numbered as 58 to 68 on the technical drawing. The data acquisition system is numbered as 46.

7.3   Sample description

The properties of coal put constraints on preparation and preservation of coal samples. When exposed to air, the effect of drying and weathering results in the alteration of the coal structure and the development of new fractures. The permeability and porosity values of such samples can be significantly different from the samples that are well preserved. The cores were drilled from inside of big blocks of coal (>0.25m³). Coal samples used for these experiments were kept in water to avoid contact with air and prevent drying. Once drilled the cores were put in sealed polyethylene bags and cooled to prevent oxidation and loss of moisture. The coal cores were drilled parallel to the bedding plane except for the core of Experiment VII, which was drilled vertically to the bedding plane. The length of the core varied from sample to sample. This is a result of the fact that coal is extremely fragile and is hard to drill an intact core.

The samples used for these experiments were from the Beringen coal mines (Beringen 770) in Belgium, the Silezia and the Brzeszcze coal mine in Poland and a vertical drill core from the CO$_2$ injection well (seam 401; Well MS3) in Poland. The petrographical details of the samples are shown in Table 7.1. Nine different flooding experiments were conducted on the core samples mentioned above. The details of the coal cores and their experimental conditions are in Table 7.2. The Silezia and the Brzeszcze samples were, in terms of their maceral composition, similar in rank. The Silezia coal was vitrinite rich and the Brzeszcze coal was inertinite rich. The micro-pore volumes and specific surfaces are listed in Table 7.1.

7.4   Experimental procedure

The procedure starts with volume measurements of all individual tubing segments and pressure vessels. Thereafter the coal sample (Fig. 7.1b) was built leak free in the high-pressure cell. Then again volume measurements were conducted with the sample built in the pressure cell. The details of the void volume measurements are discussed in Appendix E. The effect of the relatively large amount of dead volume is seen in the results and is discussed later in this section. All mass balance calculations for CH$_4$ and CO$_2$ take the free and the adsorbed volumes separately into account.

At the end of the volume measurement, the sample cell was, for at least a week, connected to a vacuum pump to eliminate any form of residual gas or free moisture. During this process temperature was kept constant. Experiment IV (Silezia 315 II; Dry; CO$_2$) is used as an

Sample	Rank [% R_{max}]	Maceral composition [%]		Specific surface [m^2/g]	Micropore volume [cm^3/g coal]
Beringen 770 (Belgium)	0.78	Vitrinite	37.8	151.53	0.055
		Liptinite	18.0		
		Inertinite	44.0		
		Mineral matter	0.2		
Silezia 315 II (Poland)	0.68	Vitrinite	71.6	190.00	0.064
		Liptinite	6.8		
		Inertinite	15.0		
		Mineral matter	6.8		
Brzeszcze 501; LW 405 (Poland)	0.75	Vitrinite	38.8	171.00	0.058
		Liptinite	8.0		
		Inertinite	52.8		
		Mineral matter	0.4		
Seam 401 Vertical drill core from well MS3 (Poland)	0.85	Vitrinite	53.8	not measured	not measured
		Liptinite	6.3		
		Inertinite	21.2		
		Mineral matter	18.7		

Table 7.1. Petrographical properties of the coal samples

Experiment	Length [mm]	P_{mean} [MPa]	P_{eff} [MPa]	Injection rate [ml/hr]	Free CH_4 [moles]	Adsorbed CH_4 [moles]	Sweep [%]
I (Beringen 770; Dry; CO_2)	334.0	4.3	3.61	6.0	0.43	0.61	69.1
II (Beringen 770; Dry; CO_2)	178.3	8.12	2.01	0.7	0.40	0.83	60.90
III (Silezia 315 II; Wet; CO_2)	200.5	8.325	2.25	1.0	0.13	0.29	34.00
IV (Silezia 315 II; Dry; CO_2)	200.5	9.08	1.59	1.0	0.52	0.41	78.94
V (Brzeszcze 501; Wet, CO_2)	208.0	8.78	1.77	0.5	0.44	0.58	30.18
VI (Brzeszcze 501; Dry, CO_2)	208.0	8.74	1.72	0.5	0.56	0.45	72.74
VII (Seam 401; Wet; CO_2/N_2)	229.3	8.67	1.87	0.5	0.57	0.36	37.97
VIII (Silezia 315 II; Dry; Flue gas)	200.5	8.42	2.06	1.0	0.72	0.70	35.1
IX (Silezia 315 II; Wet; Flue gas)	200.5	8.55	1.99	1.0	0.41	0.63	58.00

Table 7.2. Coal core lengths, experimental conditions and results (all core samples were 69.50 mm in diameter)

example to describe the test procedure. The flooding test, which lasted 45 days, consists of three consecutive stages (Fig. 7.2): (i) CH$_4$ loading, (ii) CO$_2$ loading, and (iii) continued CO$_2$ injection with production under a constant pore pressure and effective stress. In a typical wet experiment, the CO$_2$ loading stage is replaced by a water loading phase (Fig. 7.16). All measurements reported here are under standard temperature and pressure conditions. In the first stage (7 days), 20.76 l of CH$_4$ was injected into the system with increasing pressure cycles, till the required saturation was reached. The system pore pressure increased to 6 MPa during the first two days of injection. After each injection cycle the methane was allowed to sorb onto the coal matrix until equilibrium was reached. To meet sub-surface conditions, the difference between the annular pressure and the pore pressure was usually kept at ratios of 2:1 to 5:3. The amount of injected methane was measured with a mass flow meter. During the second stage (21 days), the system was further pressurized to 9.0 MPa, with the injection of 32.2 l of CO$_2$ at a rate of approximately 1.89 l/d. In the following injection cycle the pump was filled with CO$_2$ or flue gas and injection was started. In the final stage (17 days) 71.3 l of super-critical CO$_2$ was injected at a rate of 4.19 l/d. It brings the total amount of injected CO$_2$ to 103.5 l. During production a constant pressure gradient was kept over the core with a back pressure
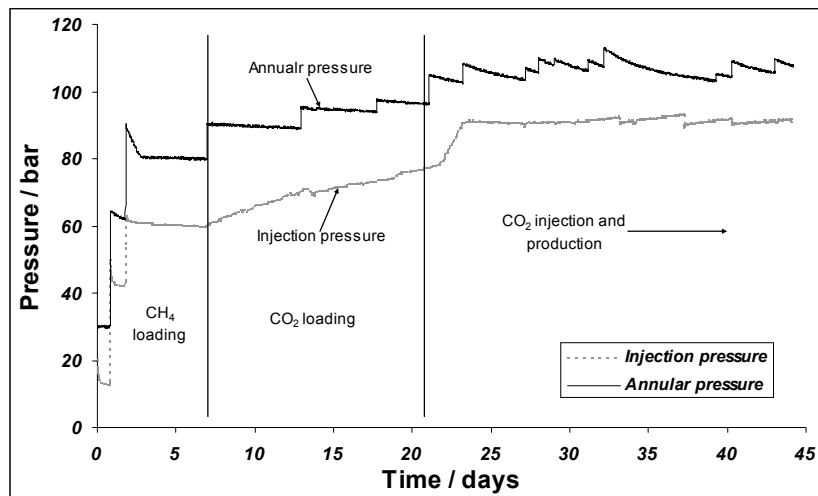

Fig. 7.2 Measured system pressure and the cumulative CO$_2$ injection during the test (typical loading curve). The purpose of the CO$_2$ loading phase was to bring up the injection pressure to super-critical conditions and to provide more residence time for CO$_2$ in the pressure cell.

valve. Throughout the final stage the system pressure was maintained at about 9 MPa.

The gas analyzer determined the relative amount of CH_4, CO_2 and N_2 (Fig. 7.3). The GC measurements are representative for the change in molar concentrations of each component in the free phase. For the CO_2 flooding experiments, the experiment was stopped when the relative amount of carbon dioxide in the product gas reached 98 mol %. It took months of injection, to produce any excess CO_2. The moisture, if present was separated using a silica gel bottle connected to a balance. Hence, for wet experiments the amount of water leaving the pressure cell was measured. During the tests, the recorded data served as an iterative feedback to compare the injected and produced volumes and to stop the experiment when the effluent CO_2 content reached 98%.

Fig. 7.3 The sweep efficiency (s) and molar concentrations of the produced gas against displaced volume from Experiment I (Beringen 770, dry, CO_2 injection at 6ml/hr). The migration data have plotted against displaced volume to make time dimensionless

7.5   Results and discussion

7.5.1   CO₂ core flood experiments

The seven different CO_2 core flood experiments range from sub-critical to super-critical CO_2 conditions. The overview of the experimental conditions and sample details are given in Table 7.2. In order to compare the experiments, the relative amount as measured by the gas analyzer and sweep efficiency are plotted against the displaced volume. The displaced volume also represents a dimensionless time. The sweep efficiency and the displaced volume are defined as follows (Bertheux et al., 2000):

$$\text{sweep efficiency}(\%) = \frac{\text{moles of } CH_4 \text{ produced}}{\text{moles of } CH_4 \text{ initially in place}} \times 100, \qquad (7.1)$$

$$\text{displaced volume} = \frac{\text{moles of } CO_2 \text{ injected}}{\text{moles of } CH_4 \text{ initially in place}}. \qquad (7.2)$$

Experiment I and II can be used to compare the effect of varying injection rate and injection pressure on the methane recovery. The results of Experiment I and II are listed in Table 7.3. The experimental conditions prior to the start of CO_2 injection are listed in Table 7.2.

CO_2 flooding (Beringen 770)	CO_2 = 1 %		CO_2 = 50 %		CO_2 = 90 %	
	Dry (6ml/hr)	Dry (0.7ml/hr)	Dry (6ml/hr)	Dry (0.7ml/hr)	Dry (6ml/hr)	Dry (0.7ml/hr)
Sweep efficiency [%]	43.6	22.9	58.8	46.7	69.1	58.7
Displaced volume [mole/mole]	0.91	1.77	1.36	5.1	2.06	10.63
Time after production [sec]	3.36×10^5	6.6×10^5	5.0×10^5	19.0×10^5	7.7×10^5	39.6×10^5

Table 7.3. The sweep efficiency, displaced volume and production time of Experiment I and II

At the temperatures and pressure the experiments were performed, methane is in the vapor phase. In Experiment I, CO_2 is in the vapor phase (4.3 Mpa, 45°C) where as in Experiment II, the CO_2 is super-critical (8.12 Mpa, 45°C). The density of CO_2 for Experiment I is 88.99 kg/m³ as compared to 248.34 kg/m³ in Experiment II. Figs. 7.3 and 7.4 show the migration history of CH_4 and CO_2 during the course of the experiment. At the beginning of Experiment I, 41 % of the CH_4 was free (59 % was adsorbed). During the experiment about 69.1 % of the methane initially injected is produced (Table 7.2). For Experiment II, 32.5 % of the initial CH_4 in-place was free, i.e, in the macropores. During the experiment about 61 % of methane was produced. Therefore it can be said that for both the experiments some of the adsorbed methane was produced. From Table 7.3 it can be seen that after breakthrough there is still a significant amount of methane production. The injection rate for Experiment I was 6 ml/h, that of Experiment II was 0.7 ml/h. The migration data, as represented in figs. 7.3 and 7.4, show that the injection pressure has some effect on the methane recovery, primarily due to the density difference of the injected CO_2. Diffusion is much faster for sub-critical than for super-critical conditions. CO_2 is also five times denser than CH_4 under super-critical conditions. The mass flow rate of Experiment I is three times larger than that of Experiment II. The coal core used in Experiment I is twice as long as that of Experiment II (Table 7.2). Table 7.3, shows that the breakthrough time for Experiment I is almost two times faster than that of Experiment II. At breakthrough (1% CO_2), almost all the free methane in the system has been produced whereas only half the free volume of methane was produced for the second case. The displaced volume data show that for methane recovery, at 90% of product CO_2 concentration, Experiment I looks

more efficient as it takes 20% of the time to remove almost a comparable amount of CH$_4$ from the system. It has to be noted that Experiment I was concluded at 90% of effluent concentration.
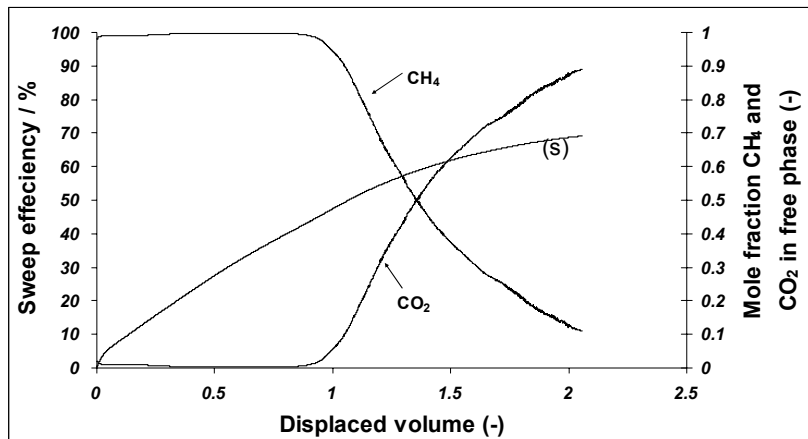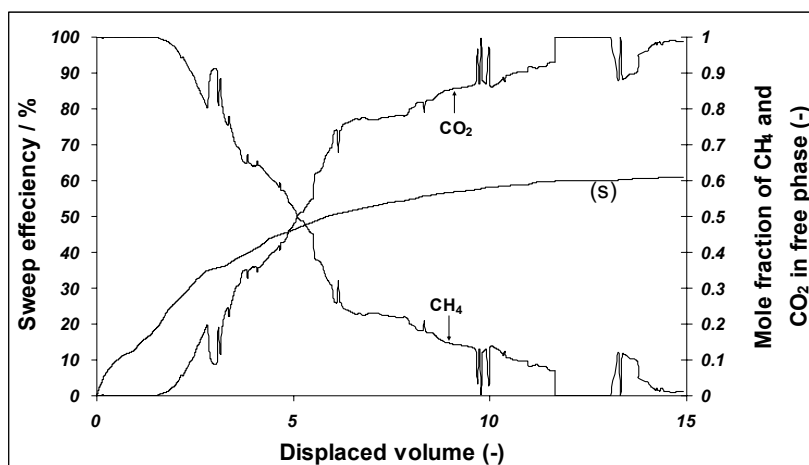

Fig. 7.4 The sweep efficiency (s) and molar concentrations of the produced gas against displaced volume from Experiment II (Beringen 770, dry, CO$_2$ injection at 0.7ml/hr). The GC response is dependent on the opening and the closure of the back pressure valve. This brings about fluctuations on the migration data. Some of the sharp events on the plot shown above are due to events like pump filling, heating failure, pressure fluctuations etc.

Experiment III and IV compare the influence of water on the CO$_2$-CH$_4$ exchange process in the coal. The effect of water on methane recovery has been predicted by Mazumder et al., 2003. The experimental conditions for these experiments are shown in Table 7.2. Both experiments were conducted on the same coal sample, with Experiment III on a wet core with excess water in the fracture system. No free water was present in the dry Experiment IV. The results of the experiments are compared in Tables 7.4 and 7.5. The duration of the wet experiment was longer than the dry one. Table 7.2 shows, that only 34% of the CH$_4$ in place was produced at the end of the wet experiment, whereas almost 79% of the CH$_4$ in place was produced from the dry experiment. Hence apart from the free methane, only 3% of the adsorbed methane was produced from the wet experiment and 50% from the dry experiment. The free methane is present in the cleats and is easier to produce than the adsorbed methane therefore we can say that during Experiment III probably only free methane was produced. After breakthrough of CO$_2$ the methane production becomes virtually nothing, all the CO$_2$ bypasses the adsorbed methane. Table 7.5 shows that there is no significant difference in the breakthrough time for both experiments. For the wet experiment the slightly faster breakthrough is either due to the dissolution of CO$_2$ in the water or due to the fact that the water acts as a thin

film and does not allow the CO$_2$ to come in contact with coal. The sweep efficiencies at different times show that (Table 7.5), the methane recovery for the relatively dry experiments, are about 3.5 times higher than those of the wet experiment. The CO$_2$ and CH$_4$ migration data for both experiments are presented in Figs. 7.5 and 7.7. Fig. 7.6 is a plot of the injection and the production details of Experiment III, showing two distinct phases of the water production. The first phase constitutes most of the free water in the fractures and it is produced in a short span of time. The second comes from the macro pores and produces at a much slower rate.

CO$_2$ flooding (Silesia 315 II)	Dry	Wet
Total amount of CO$_2$ injected [moles]	4.67	7.18
Amount of adsorbed CO$_2$ [moles]	1.604 (max)	3.83
Amount of free CO$_2$ [moles]	0.78	0.74
Total amount of CO$_2$ produced [moles]	2.28	2.62

Table 7.4. The total, free, adsorbed and produced amount of carbon dioxide in the dry and wet Silesia 315 II flooding experiment (Experiment III and IV)

CO$_2$ flooding (Silesia 315 II)	CO$_2$ = 1 %		CO$_2$ = 50 %		CO$_2$ = 90 %	
	Dry	Wet	Dry	Wet	Dry	Wet
Sweep efficiency [%]	37.2	11.6	66.25	16.5	69.8	19.5
Displaced volume [mole/mole]	1.28	1.26	2.56	2.09	2.96	2.86
Time after production [sec]	3.8×10^5	2.7×10^5	7.6×10^5	4.5×10^5	8.8×10^5	6.1×10^5

Table 7.5. The sweep efficiency, displaced volume and time of Experiment III and IV

Fig. 7.5 The sweep efficiency (s) and molar concentration of the produced gas against displaced volume from Experiment III (Silezia 315 II, wet, CO$_2$ injection at 1.0ml/hr)

Fig. 7.6 The cumulative production of all gases, water and injection of CO₂ from Experiment III (Silezia 315 II, wet, CO₂ injection at 1.0ml/hr)
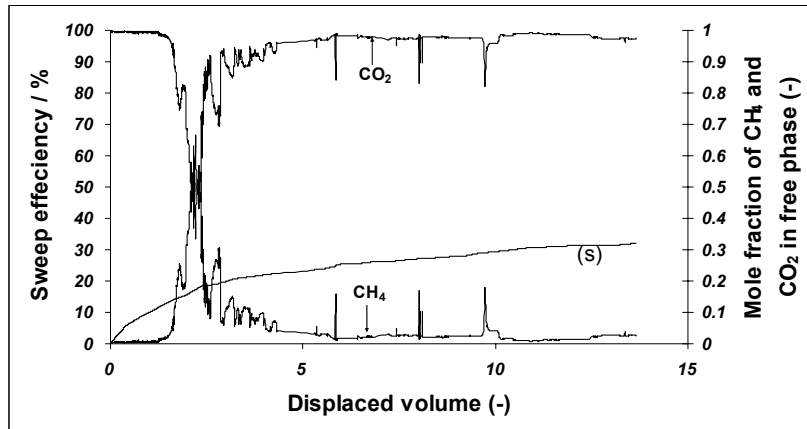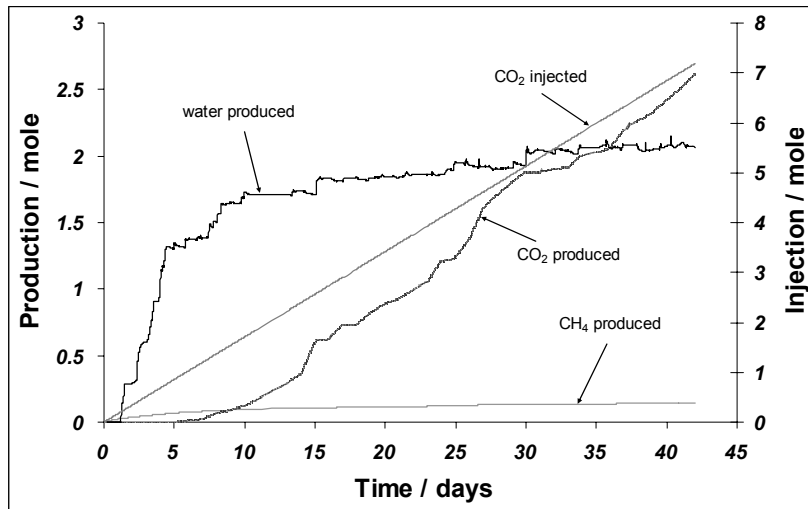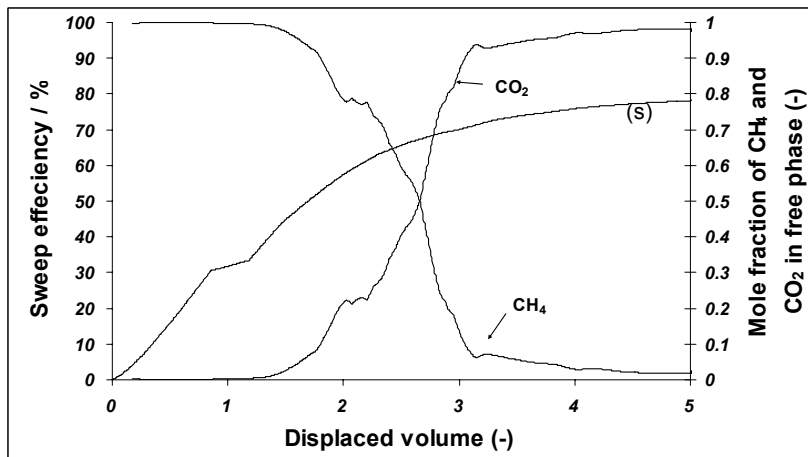

Fig. 7.7 The sweep efficiency (s) and molar concentrations of the produced gas against displaced volume from Experiment IV (Silezia 315 II, dry, CO₂ injection at 1.0ml/hr)

The coal sample of Experiment III and IV, has higher vitrinite content (71.6%) than inertinite content (15%). Experiment V and VI were done on a coal sample with a higher inertinite content (52.8%) than a vitrinite content of 38.8%. These experiments were designed to see the effect of water on methane recovery. The results of Experiments V and VI are listed in Tables 7.6 and 7.7. The migration histories are in Figs. 7.8 and 7.10. The injection and production data for Experiment V are listed in Fig. 7.9. When compared to Experiments III and IV these two experiments showed different results. Significant differences in the methane recovery was noted between the wet (Experiment V) and dry (Experiment VI) experiments (Table 7.7). It could not be inferred from the data, whether the early breakthrough was caused by inherent characteristic for an inertinite rich coal or due to a fracture which created a pathway through which the CO_2 moved directly to the production side. The injection rate for Experiment V and VI is half of those for Experiment III and IV. A close comparison of the dry Experiments IV and VI, shows that the CO_2 storage capacity for the inertinite rich coal is much higher than for the vitrinite rich coal. Comparison of Experiments III and IV with Experiments V and VI, shows that the maceral composition is correlated to the CO_2-CH_4 exchange process.

CO_2 flooding (Brzeszcze 501)	Dry	Wet
Total amount of CO_2 injected [moles]	4.7125	2.45
Amount of adsorbed CO_2 [moles]	1.033 (max)	0.423 (max)
Amount of free CO_2 [moles]	1.555	1.08
Total amount of CO_2 produced [moles]	2.1245	0.947

Table 7.6. The total, free, adsorbed and produced amount of carbon dioxide in the dry and wet Brzeszcze 501 flooding experiment (Experiment V and VI)

CO_2 flooding (Brzeszcze 501)	CO_2 = 25 %		CO_2 = 50 %		CO_2 = 90 %	
	Dry	Wet	Dry	Wet	Dry	Wet
Sweep efficiency [%]	8.83	9.2	12.97	13.5	72.62	25.4
Displaced volume [mole/mole]	0.1	0.22	0.18	0.29	4.63	1.36
Time after production [sec]	1.08×10^5	2.1618×10^5	1.92×10^5	2.86×10^5	4.959×10^6	1.33×10^6

Table 7.7. The sweep efficiency, displaced volume and production time of Experiment V and VI

Experiment VII was conducted on a sample from Poland, drilled perpendicular to the bedding plane. The effects of an alternate injection of a strong (CO_2) and weak (N_2) adsorbing gas are compared. N_2 has stripping properties when injected in coal seams. To avoid this effect, the N_2 injection was done after one pump volume (266 ml) of CO_2 injection. This procedure helped to remove all free methane from the macro pore system, before nitrogen injection. The results of Experiment VII are summarized in Tables 7.8 and 7.9. Fig. 7.11 shows

the migration of CH_4, CO_2 and N_2 through the core. As with other wet experiments the methane recovery of Experiment VII is low (38%) and the breakthrough is also early. The experiment started with the injection of one pump volume (266 ml) of CO_2 (Fig. 7.11).
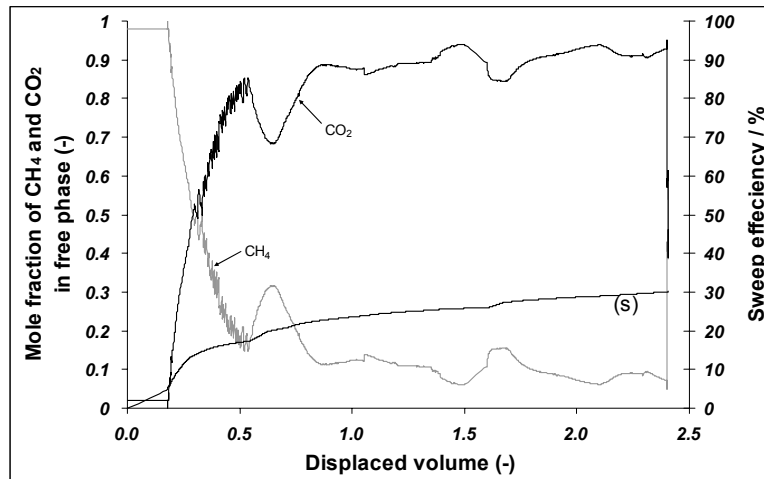

Fig. 7.8 The sweep efficiency (s) and molar concentrations of the produced gas against displaced volume from Experiment V (Brzeszcze, wet, CO_2 injection at 0.5ml/hr)
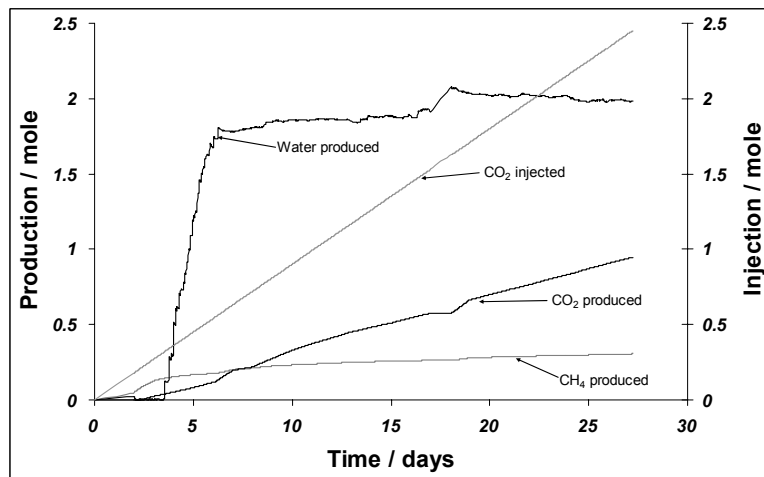
Fig. 7.9 The cumulative production of all gases, water and the injection of CO_2 from Experiment V (Brzeszcze, wet, CO_2 injection at 0.5ml/hr)

Total amount of CO_2 injected [moles]	6.76
Total amount of CO_2 produced [moles]	5.68
Total amount of N_2 injected [moles]	0.83
Total amount of N_2 produced [moles]	0.097

Table 7.8. The total, free, adsorbed and produced amount of carbon dioxide and nitrogen in sample Seam 401 (Vertical drill core from well MS3)

CO_2 / N_2 flooding (Seam 401)	CO_2 = 1 %	CO_2 = 50 %	CO_2 = 90 %
Sweep efficiency [%]	19.59	24.93	28.4
Displaced volume [mole/mole]	0.364	0.553	0.956
Time after production [sec]	3.09×10^5	4.698×10^5	8.12×10^6

Table 7.9. The sweep efficiency, displaced volume and production time of Experiment VII

Fig. 7.10 The sweep efficiency (s) and molar concentrations of the produced gas against displaced volume from Experiment VI (Brzeszcze,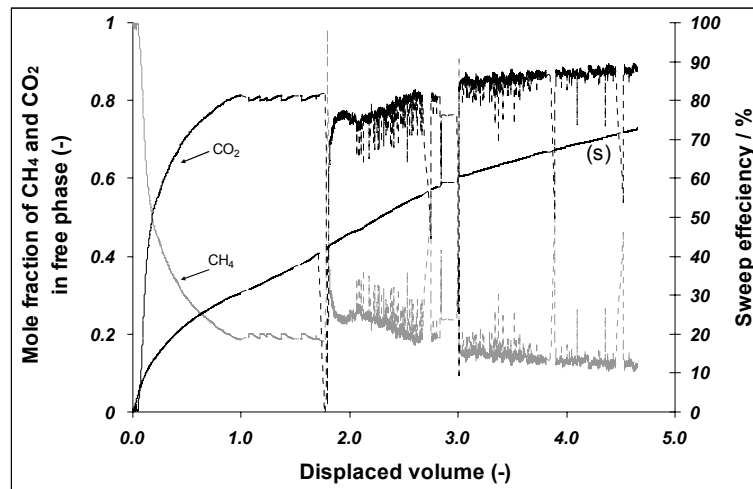 dry, CO_2 injection at 0.5ml/hr). The fluctuations on the migration data are because of the fact that the GC columns were not clean.

At a displaced volume of 2.23, N_2 injection started. After one pump volume, the CO_2 injection was resumed at a displaced volume of 3.14. A sharp increase in CH_4 production was observed alongside N_2 breakthrough. This incremental CH_4 production was consistent throughout the N_2 production. With the injection of N_2 in a CH_4 saturated coal, the partial pressures of CH_4 in the free phase is reduced. This initiate desorption of CH_4 from the coal into the free phase. Nitrogen is a natural choice for ECBM due to its availability and the fact that it tends to yield incremental recovery response relatively rapidly. Nitrogen advances more rapidly and displays a more dispersed front, in comparison to CO_2 where the displacement is more piston like under super-critical conditions. Following breakthrough significant mixing of injected N_2 and initial gas is measured at the production end.
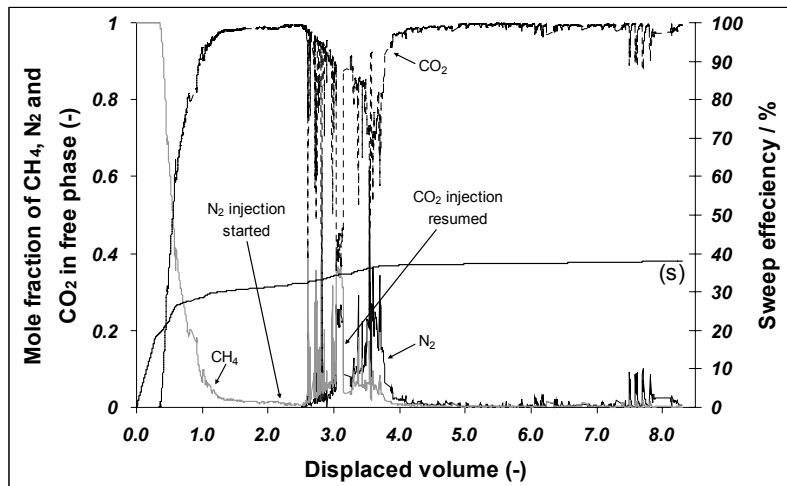

Fig. 7.11 The sweep efficiency (s) and molar concentrations of the produced gas against displaced volume from Experiment VII (Seam 401, wet, CO_2/N_2 injection at 0.5ml/hr). The alternate injection of a strong (CO_2) and weak (N_2) adsorbing gas result in the fluctuations of the concentration data between a displaced volume of 2.5 and 4.

7.5.2 Flue gas core flood experiments

As an alternative to pure gases, flooding experiments were performed with flue gas. The specifications of the flue gas are listed in Table 7.10. An equation of state (EOS) for flue gas has been developed and is discussed in Chapter 3. This EOS calculates densities for the injected flue gas. The algorithm developed by National Institute of Standards and Technology (NIST) predicts the volumetric behavior of a multi-component gas mixture in a single-phase region. The results from the algorithm are comparable to those computed with the Peng-Robinson EOS (Peng and Robinson, 1976). It performs better than the Redlich-Kwong-Soave

equation (Soave, 1972) in all cases and, in particular for the prediction of liquid phase densities, especially non-polar ones. Peng-Robinson EOS requires four input quantities per compound: critical temperature (T_C), critical pressure (P_C), acentric factor (ω) and interaction parameter (k_{ij}). The Redlich-Kwong equation is adequate for calculation of gas phase properties when the ratio of the pressure to the critical pressure is less than about one-half of the ratios of the temperature to the critical temperature.

Component name	Molar Conc. (%)	Used Column	Carrier Gas
CO_2	10.9	Porapack Q	He
CO	0.01	-	-
H_2	9.0	Mole-Sieve	Ar
CH_4	3.01	Mole-Sieve / Porapack Q	Ar/He
O_2	3.00	Mole-Sieve	Ar
SO_2	0.106	-	-
N_2	73.974	Mole-Sieve	Ar

Table 7.10. The flue gas specification and the columns/carrier gas used for chromatographic analysis and density determination.

Results from the wet and dry flue gas experiments are listed in Tables 7.11, 7.12 and 7.13. The core details and the experimental conditions are provided in Table 7.2. The pressures are the

Flue flooding (Silesia 315 II)	Dry	Wet
Total amount of flue gas injected [moles]	3.15	3.24
Amount of free flue gas [moles]	0.73	0.57
Total amount of flue gas produced [moles]	0.87	1.98

Table 7.11. The total, free, adsorbed and produced amount of flue gas in sample Silesia 315 II

	H_2		O_2		N_2		CO_2		SO_2	
	Dry	Wet	Dry	Wet	Dry	Wet	Dry	Wet	Dry	Wet
Moles injected	0.29	0.30	0.095	0.10	2.34	2.44	0.35	0.36	0.003	0.004
Moles produced	0.05	0.17	0.012	0.03	0.70	1.57	0.012	0.105	0.001	0.003
% Produced	18.20	57.11	12.14	26.44	29.72	64.56	3.5	29.15	43.00	79.22

Table 7.12. The cumulative amount of each component injected and produced during the dry and wet flue flooding experiments

same in both the dry and the wet experiments, but the dry experiment contains more methane. This is due to water injection (100.1 g) after CH_4 saturation, which displaces some methane out of the core.

Flue flooding (Silesia 315 II)	$N_2 = 1$ %		$N_2 = 50$ %		$N_2 = 73.9$ %	
	Dry	Wet	Dry	Wet	Dry	Wet
Sweep efficiency [%]	4.175	14.35	22.33	29.12	35.01	57.93
Displaced volume [mole/mole]	0.288	0.245	1.00	0.46	2.17	3.09
Time after production [sec]	5.37×10^5	2.99×10^5	1.87×10^6	5.63×10^5	4.04×10^6	3.78×10^6

Table 7.13. The sweep efficiency, displaced volume and time of the dry and wet flue flooding experiment
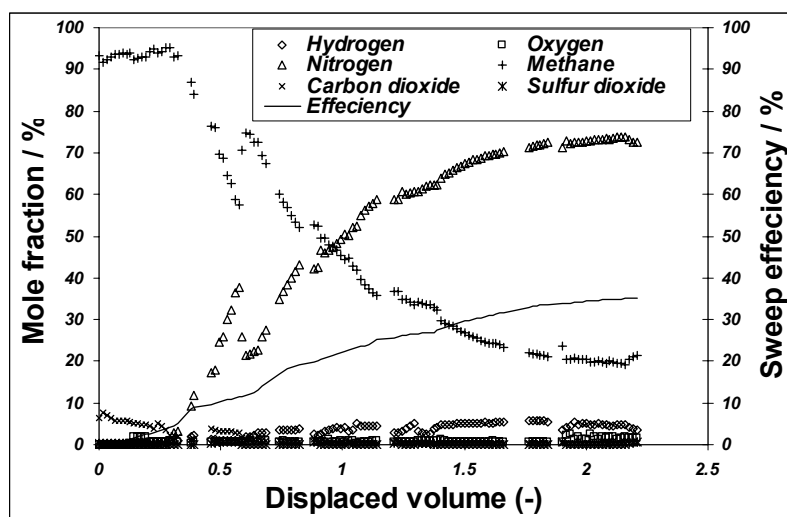

Fig. 7.12 The sweep efficiency and molar concentrations of the produced gas against displaced volume from Experiment VIII (Silezia, dry, flue gas injection at 1.0ml/hr)

The migration data of the dry experiment (Experiment VIII) in Fig. 7.12 show that the amount of free methane (0.72 mol) exceeds the net amount of CH_4 produced (0.50 mol) considerably. Hence, with an injection rate of 1ml/h, hardly any adsorbed methane is produced. Compared to the wet experiment (Experiment IX) the dry one has more free methane, which resides in the tubing system and the fracture porosity of the coal. The recovery factor of the dry experiment is 35.1%. Flue gas as an injectant gives no significant enhancement in recovery. The flue gas, primarily N_2, goes fast through the tubing system and is produced. The major part of the CO_2 in the flue gas gets adsorbed on the surface of the coal but it is unable to enhance

the production of methane. Figs. 7.13, 7.14 and 7.15 show the concentration of the individual gas components injected, produced and adsorbed respectively.
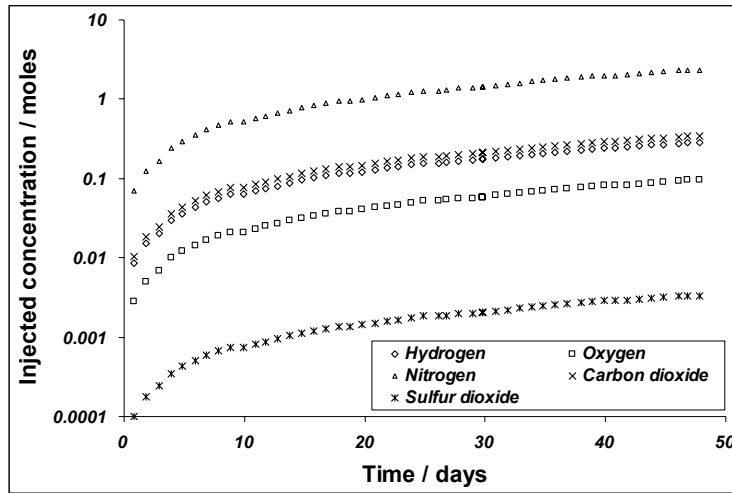

Fig. 7.13 The concentration of individual gas components injected from Experiment VIII (Silezia, dry, flue gas injection at 1.0ml/hr)
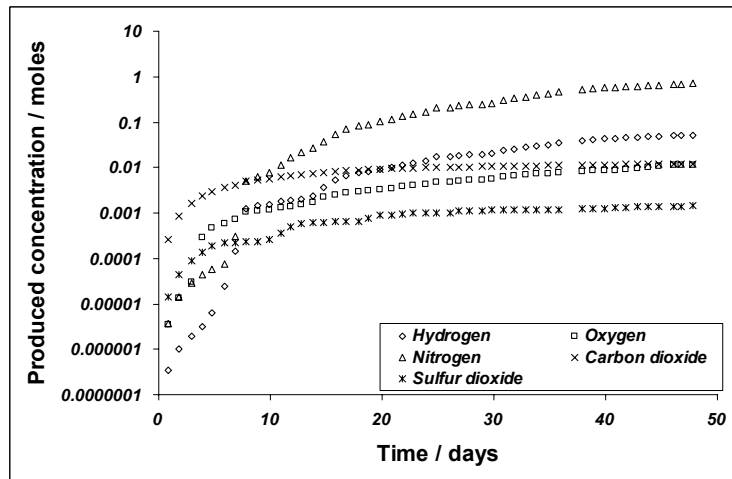

Fig. 7.14 The concentration of individual gas components produced from Experiment VIII (Silezia, dry, flue gas injection at 1.0ml/hr)
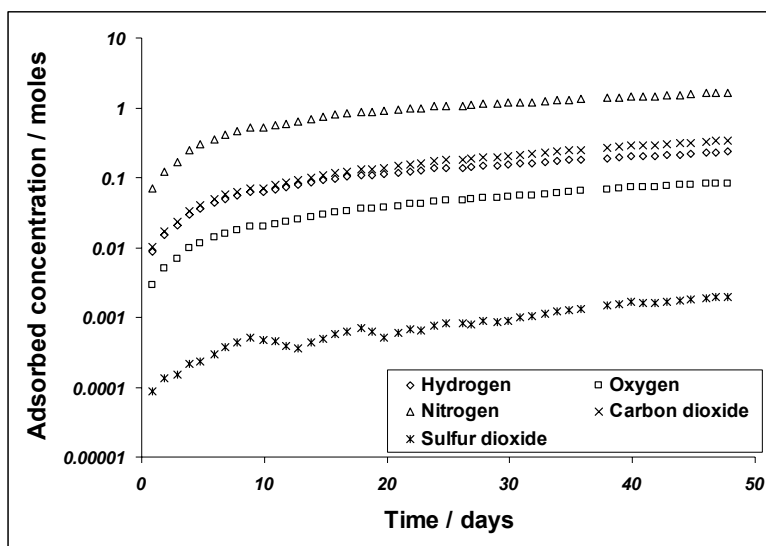
Fig. 7.15 The concentration of individual gas components adsorbed from Experiment VIII (Silezia, dry, flue gas injection at 1.0ml/hr)

In the wet experiment the methane saturation is carried out at a lower pressure (69.8 bar) compared to the dry experiment (84.35 bar). After methane saturation the sample is filled with 100.1 g of water, and consequently the pressure rises to 85.84 bars. Thereafter the flue gas was injected at a rate of 1ml/h. The loading process is shown in Fig. 7.16. The migration data of the wet experiment is shown in Fig. 7.17. The water occupied a part of the free volume in the cell, which was completely occupied by the free methane in the dry experiment. Consequently, the free methane volume in the wet experiment (0.41 mol) is less than the free methane volume in the dry experiment (0.72 mol). It is concluded that the water acts like a barrier between the free methane and the injected flue gas. This may have affected the experiment in two ways: (i) by pushing the free methane to the production side even before the start of injection, the production of free methane starts easily, and (ii) by giving the flue gas more residence time onto the surface of coal leading to better exchange. As a consequence, in the wet experiment, apart from the free methane, 30.7% of the adsorbed methane was also produced. Figs. 7.18, 7.19 and 7.20 show the concentrations of the individual gas components, which are being injected, produced and adsorbed respectively.
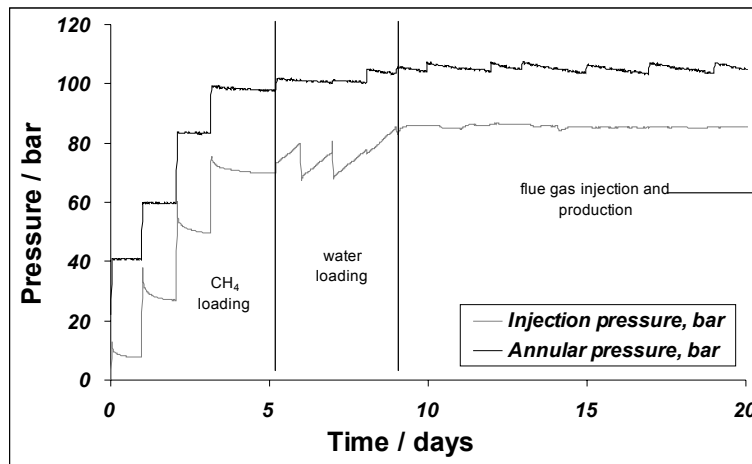
Fig. 7.16 Pressure development of the loading stages in Experiment IX
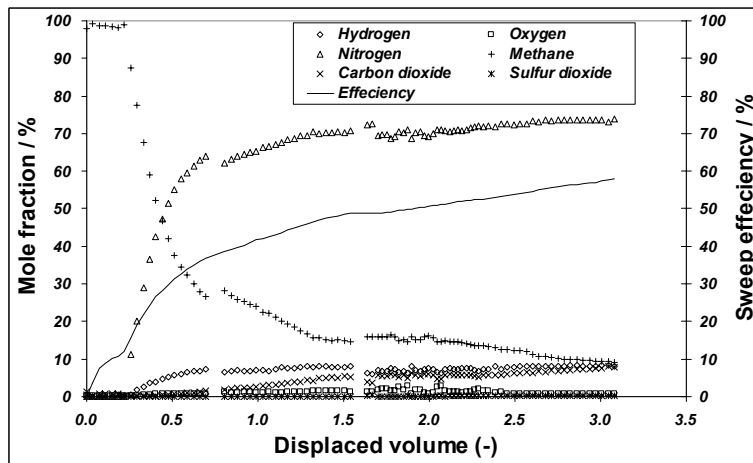
Fig. 7.17 The sweep efficiency and molar concentrations of the produced gas against displaced volume from Experiment IX (Silezia, wet, flue gas injection at 1.0ml/hr)
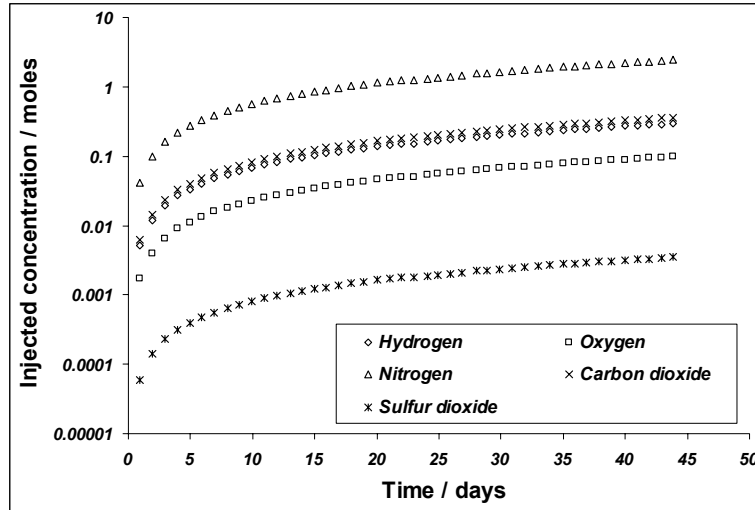
Fig. 7.18 The concentration of individual gas components injected from Experiment IX (Silezia, wet, flue gas injection at 1.0ml/hr)

Fig. 7.19 The concentration of individual gas components produced from Experiment IX (Silezia, wet, flue gas injection at 1.0ml/hr)
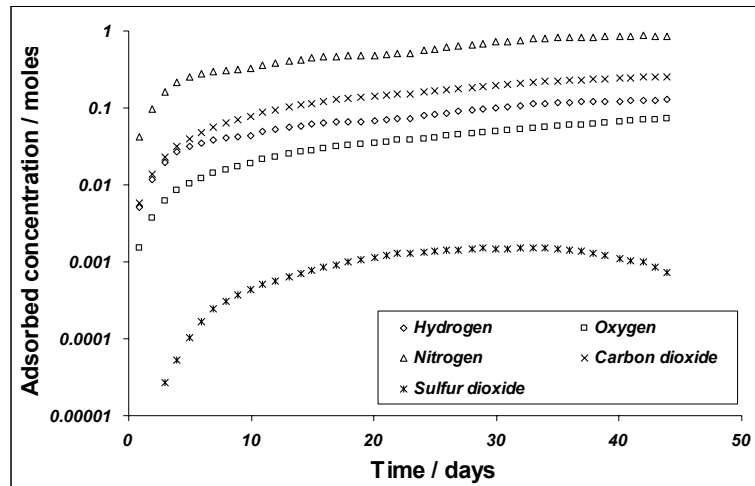
Fig. 7.20 The concentration of individual gas components adsorbed from Experiment IX (Silezia, wet, flue gas injection at 1.0ml/hr)

From the discussion above, it is clear that injecting water to saturate coal is not preferred. As an alternative the coal core can be soaked with water, shortly evacuated and then saturated with methane, but this was not done in our experiments
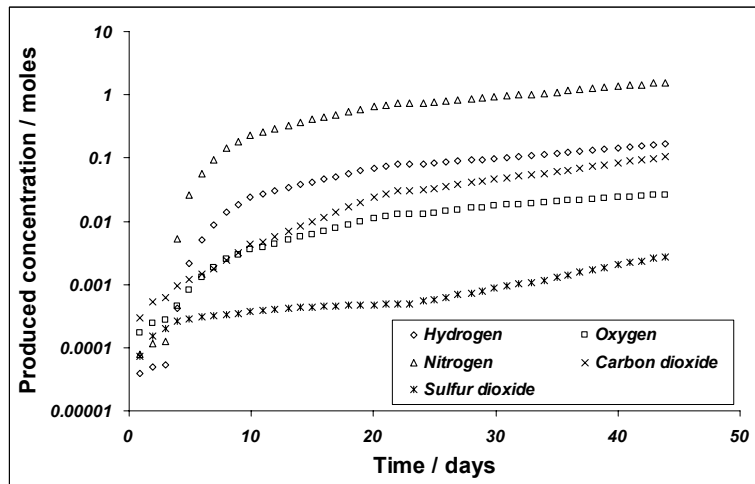
7.6   Conclusions

- Injection of CO$_2$ decreases the partial pressure of CH$_4$ in the free phase and enhances the production of methane.

- The CO$_2$ mass balance shows that the solubility of CO$_2$ in coal is more pronounced than for CH$_4$. The term solubility is used, considering that coal has a highly cross-linked macromolecular network.

- Under dry conditions, the incremental methane produced is likely due to the preferential desorption of methane in the presence of CO$_2$. Consequently, the dry experiments show that the amount of desorbed CH$_4$ is marginally greater than desorption resulting from reduction in partial pressures of methane.

- The wet experiments with pure CO$_2$ failed to produce any sorbed CH$_4$ from the coal.

- From the experiments it is clear, that on a pore scale CO$_2$ is better adsorbed compared to CH$_4$. Even though the coal was saturated with CH$_4$, under the same conditions a

class of pores that were not available for methane sorption was available for the physical sorption of the other species, preferably CO$_2$.

- The wet experiments cannot be compared to the dry experiments. All experiments can be used to understand processes under specific experimental conditions. Comparison is only possible with more data, by repeating these experiments, i.e. a consistency in the parameters is required.

- Comparing the CO$_2$ flooding experiments with the flue gas experiments under similar conditions, the latter show lower sweep efficiencies. There is hardly any production of adsorbed methane from the coal. The flue gas experiments, with N$_2$ as the main constituent can be considered as a N$_2$ stripping experiment. Comparing the thermo physical properties of N$_2$ with those of CO$_2$, the latter has higher density under reservoir conditions. The viscosities of CO$_2$ and N$_2$ are comparable. Comparing the six different components in flue gas, shows that, CO$_2$ was the most adsorbed species. Significant reduction in the CO$_2$ concentration was measured in the product gas. Using it as a process for CO$_2$ filtration seems promising.

- The displacement of CH$_4$ by CO$_2$ in a tube (Appendix F) suggests that mixing behavior for low and high pressure conditions differ significantly, and different types of mixing occur.

Part II – Numerical modelling

7.7 Physical model

The objective of this study is to conceptualize a numerical model from the physical aspect of ECBM. With so much of complexity involved in developing a numerical model and solving it, this is our first leap ahead to show the effect of effluent / water on the exchange of methane and carbon dioxide in coal. We consider the coal as a dual porosity system i.e. the large cleat system and the matrix that consists of mesocleats and micro coal particles. The large cleat system consists of parallel vertical fractures. Between the vertical fractures we have a mesocleat system of fractures that encloses the micro-pore particle system. The mesocleat system together with the coal particles is treated as a porous medium. We assume that gas and water can flow in the mesocleat system. In other words the mesocleats provide the pore space in this porous medium. The coal particles are centers of adsorption. In fact coal particles consist of aromatic particulates embedded in an aliphatic continuum. The diameter d_p of the coal particles is in the $100 \mu m$ range. The pores within the coal particles are so small ($2 - 100$ Å) that free movement of water and gas is not possible. Instead the molecules are attached to the surface and diffuse from one potential minimum on the surface to the other. In other words surface diffusion (diffusion coefficient $\mathcal{D}$) occurs. In view of the smallness of the particles the characteristic time $\tau_D \sim d_p^2 / \mathcal{D}$ for diffusion rate inside the particle is still rather fast. Therefore we only consider diffusion within the matrix. Inside the matrix also adsorption takes place. We assume that the adsorbed concentration is proportional to the free concentration $[kg/m^3]$ and that the constant of proportionality is the same for both methane and carbon dioxide. Our assumption that the adsorbed concentration is proportional to the mass concentration means that the molar adsorption ratio is equal to the molecular weight ratio i.e. 44/16. We leave more realistic adsorption behavior modeling for future work.

All flow is in the direction of the line connecting the injection and production side i.e. in one of the main directions of the large cleat system. The enhanced coal bed methane process is preceded by a de-watering phase after which the large cleat system is completely filled with methane. We assume that the matrix and large cleat is water wet and therefore there is no transfer of water from the matrix to the large cleat system. Presently we ignore the inflow of water into the system. The mesocleat system is partly filled with methane at gas saturation S_{go}^m and partly with water at $S_{wo}^m = 1 - S_{go}^m$. The coal particles have a fixed water saturation $S_w^p = S_{wo}^p$. The coal particles have an initial concentration of adsorbed methane c_{2o}^p depending on the temperature and pressure of the system The initial carbon dioxide

concentration is zero $c_{3o}^p = 0$. The flow is determined by the potential gradient due to the injection of carbon dioxide and production of gas.

In the main cleats only flow of gas occurs. In the matrix there is flow of both gas and water. At $t = 0$ carbon dioxide enters the entire system at $x = 0$. The flow rates of gas in the large cleat system and water/gas in the matrix are given below. We assume that all carbon dioxide and methane only flow in the gas phase, because the flow rate and diffusion rate in liquid water are small with respect to the rates in the gas phase. The mass balances of water, carbon dioxide and methane in the entire system need to be established. For convenience we write the balances in the main cleats and in the matrix separately with an exchange term between the two systems. The adsorbed concentrations of carbon dioxide and methane are proportional to the respective free concentrations in the gas phase in the matrix. Diffusion occurs only perpendicular to the cleat surface and is described in more detail below.

The model is two dimensional and considers a single cleat in a piece of coal matrix. The distance between the large cleats is denoted as w and the aperture of the large cleats is denoted as d^{lc}. We consider part of the coal layer that is periodic perpendicular to the large cleat planes, with a height H and a length L and a width $w/2 + d^{lc}/2$. The $x-$ and $y-$ directions of the model are shown in Fig. 7.21. The no flow boundaries in the $x-$ direction are $x = 0$ and $y = L$. In the $y-$ direction the no flow boundaries are $y = 0$ (the symmetry line) and $y = w/2 + d^{lc}/2$.
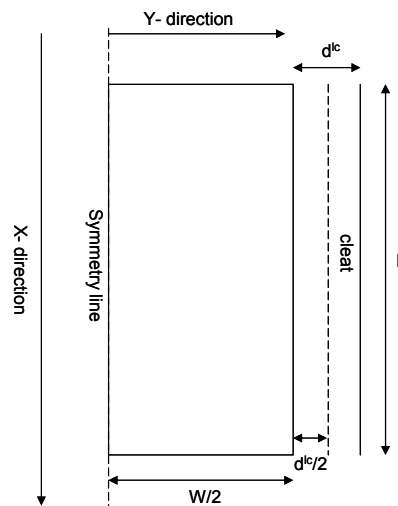

Fig. 7.21 The two dimensional model of the cleat / matrix system

Gas flow rate (Bird, 1960 and Marchesin et al., 2006) u_g^{lc} in the large cleat system is given as flow between parallel plates as

$$u_g^{lc} = -\frac{\left(d^{lc}\right)^2}{12\mu_g}\frac{\partial p}{\partial x} \tag{7.3}$$

and the gas and water flow in the meso cleat system is

$$u_g^m = -\frac{kk_{rg}}{\mu_g}\frac{\partial p}{\partial x}$$
$$u_w^m = -\frac{kk_{rw}}{\mu_w}\frac{\partial p}{\partial x} \tag{7.4}$$

where we assume that

$$k_{rw} = \left(\frac{S_w - S_{wc}}{1 - S_{wc}}\right)^2$$
$$k_{rg} = S_g^2 \tag{7.5}$$

and we use $\mu_w = 6.66 \times 10^{-4}$ [Pa s] and $\mu_g = 2.28 \times 10^{-5}$ [Pa s]. The connate water saturation is denoted by S_{wc}. Moreover k denotes the permeability and k_{rw}, k_{rg} are the relative permeability's.

Perpendicular to the cleat direction y diffusion of carbon dioxide and methane occurs both in the gas phase and the liquid water phase. However, the diffusion in the liquid phase is slower by a factor of thousand with respect to the gas phase for pressures of our interest. This means that the effective diffusion rate depends both on the water saturation and distribution in the matrix. This is a very complicated process to describe (Crank, 1966). This complexity would severely hamper the applicability of the model. Therefore we use simplifying assumptions. First we describe all diffusive processes as effective diffusion in the gas phase. The effective diffusion coefficient is a geometric average of the diffusion coefficients in the gas D_g and liquid phase D_l.

$$D_{eff} = D_l^{S_w} D_g^{1-S_w} \tag{7.6}$$

There is no convective flow in the y direction. The adsorbed concentration of carbon dioxide and methane are proportional to the free concentrations of these compounds respectively.

7.8 Model equations

We consider a part of the large cleat system that is present in the domain $\Omega_{lc} = x \in (0, L) \cup y \in \left(0, d^{lc}/2\right)$, where $x = 0$ is the injection side and $x = L$ is the production side. The part of the matrix system that we consider is in the domain $\Omega_m = \left\{ x \in (0, L) \cup y \in \left(d^{lc}/2, d^{lc}/2 + w/2\right)\right\}$.

The equation for water, methane and carbon dioxide in the matrix read i.e. in the domain Ω_m:

$$\varphi \frac{\partial S_w}{\partial t} + \frac{\partial u_{w,x}}{\partial x} = 0 \tag{7.7}$$

$$\varphi \frac{\partial \rho_{g2} S_g}{\partial t} + \varphi \frac{\partial \rho_{s2}}{\partial t} + \frac{\partial \rho_{g2} u_{g,x}}{\partial x} + \frac{\partial \rho_{g2} u_{g2,y}}{\partial y} = 0 \tag{7.8}$$

$$\varphi \frac{\partial \rho_{g3} S_g}{\partial t} + \varphi \frac{\partial \rho_{s3}}{\partial t} + \frac{\partial \rho_{g3} u_{g,x}}{\partial x} + \frac{\partial \rho_{g3} u_{g3,y}}{\partial y} = 0 \tag{7.9}$$

because we ignore dissolution of the carbon dioxide and methane into liquid water. Here $u_{g,x}$ denotes the volume averaged velocity in the gas phase (disregarding the diffusion effects) in the x-direction and $u_{g2,y}$ and $u_{g3,y}$ are the component velocities in the y-direction of methane and carbon dioxide respectively. Note that the component velocities include a contribution due to diffusion. The equations in the large cleat system will be given at the end of the section.

For the matrix we assume that there is a constant ratio between the adsorbed and free concentrations i.e.

$$\begin{aligned} \rho_{s2} &= \kappa \rho_{g2} \\ \rho_{s3} &= \kappa \rho_{g3} \end{aligned} \tag{7.10}$$

The ideal gas law leads to

$$\frac{\rho_{g2}}{M_2} + \frac{\rho_{g3}}{M_3} = \frac{P}{RT} \tag{7.11}$$

where M_2, M_3 are the molar weights of methane and carbon dioxide.

It can be shown (Bird, 1960).

$$\rho_{g3} u_{g3,y} = \rho_{g3} u_{g,y} - \varphi D_{eff} \frac{\partial \rho_{g3}}{\partial y}, \qquad \rho_{g2} u_{g2,y} = \rho_{g2} u_{g,y} - \varphi D_{eff} \frac{\partial \rho_{g2}}{\partial y}, \tag{7.12}$$

where $u_{g,y}$ is the volume averaged velocity in the y-direction. These expressions are only valid when pressure and temperature are considered constant i.e. the pressure gradient causing flow is small with respect to system pressure divided by the inter-well distance. We substitute in the equations above and find for carbon dioxide

$$\varphi \frac{\partial \rho_{g3} S_g}{\partial t} + \varphi k \frac{\partial \rho_{g3}}{\partial t} + \frac{\partial \rho_{g3} u_{g,x}}{\partial x} + \frac{\partial \rho_{g3} u_{g,y}}{\partial y} = \varphi D_{eff} \frac{\partial}{\partial y} \frac{\partial \rho_{g3}}{\partial y} \qquad (7.13)$$

and the same equation for methane with the index 3 replaced by 2. We assume a constant pressure gradient $\frac{\partial P}{\partial x}$.

$$\frac{\partial P}{\partial x} = -\frac{P_{inj} - P_{prod}}{L} := P_x \qquad (7.14)$$

where L is the distance between injection and production well and P_{inj}, P_{prod} are the injection and production pressure respectively. This equation replaces the pressure equation that can be derived by a weighted sum of Eqs. 7.7, 7.8 and 7.9. This equation ignores that more carbon dioxide molecules are adsorbed than methane molecules are desorbed. However, in our preliminary model our interest is focused on the effect of water and we leave a more realistic assumption of the space dependence of the pressure gradient for future work. Below we compute the methane density from the carbon dioxide density with Eq. 7.11.

Next we can solve the equation to obtain the saturation distribution, which with the application of Darcy's law assumes the form

$$\varphi \frac{\partial S_w}{\partial t} + \frac{kP_x}{\mu_w} \frac{\partial k_{rw}}{\partial x} = 0 \qquad (7.15)$$

Finally we solve Eq.

$$\varphi \frac{\partial \rho_{g3} S_g}{\partial t} + \varphi k \frac{\partial \rho_{g3}}{\partial t} + \frac{kP_x}{\mu_g} \frac{\partial \rho_{g3} k_{rg}}{\partial x} = \frac{\partial}{\partial y}\left(\varphi D_{eff} \frac{\partial \rho_{g3}}{\partial y} \right) \qquad (7.16)$$

In the large cleat system only carbon dioxide and methane are present in the gaseous phase. We can compute the methane density from the carbon dioxide density with Eq. 7.11. The carbon dioxide equation in Ω_{lc} reads

$$\frac{\partial \rho_{g3}}{\partial t} + \frac{\left(d^{lc}\right)^2}{12\mu_g} P_x \frac{\partial \rho_{g3}}{\partial x} + \frac{2\varphi D_{eff}}{d_{lc}} \left(\frac{\partial \rho_{g3}}{\partial y} \right)_{y=d^{lc}/2+0} = 0, \qquad (7.17)$$

where $y = d^{lc}/2 + 0$ denotes a position just inside the matrix. Eqs. 7.16 and 7.17 are averaged in the z−direction i.e. between $z = 0$ and $z = H$.

7.9 Numerical model

In order to solve the model equations, we use the finite volume approach. The coal system is split up into grid blocks and after each time step integration is performed over the grid blocks. For the sake of stability, we use the upstream weighting approximation, forward on time. The entire domain is split up in $(nx + 1) \times (ny + 1)$ grid cells see Fig. 7.22. The column $(ny + 1)$ represents the cleat and columns 1 to ny represent the matrix. CO_2 is injected in the cleat into grid cell $((ny + 1), 1)$ and gas flows out of the system at cell $((nx + 1), (ny + 1))$.
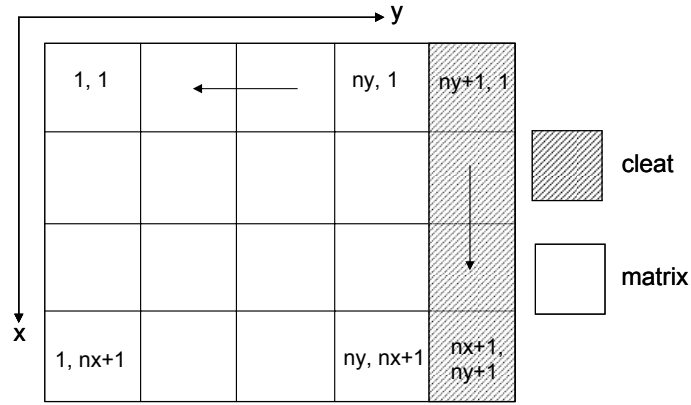
Fig. 7.22 Schematic representation of the grid blocks and of the positive orientation directions

We apply a finite volume method to perform numerical calculations for the water we write

$$S_{w,i}\left(t + \Delta t\right) = S_{w,i}\left(t\right) + \frac{1}{\varphi}\left(\left(\frac{kk_{rw}P_x}{\mu_w}\right)_{i-1} - \left(\frac{kk_{rw}P_x}{\mu_w}\right)_i\right)\frac{\Delta t}{\Delta x} \qquad (7.18)$$

and for carbon dioxide we write

$$\left(\rho_{g3}\left(S_g + k\right)\right)_{t+\Delta t}^{i,j} = \left(\rho_{g3}\left(S_g + k\right)\right)_t^{i,j} + \frac{1}{\varphi}\left(\left(\frac{kk_{rg}\rho_{g3}P_x}{\mu_g}\right)_{i-1} - \left(\frac{kk_{rg}\rho_{g3}P_x}{\mu_g}\right)_i\right)\frac{\Delta t}{\Delta x} +$$

$$\left(D_{eff}^{i,j}\left(\rho_{g3,i;j+1} - \rho_{g3,i;j}\right) - D_{eff}^{i-1,j}\left(\rho_{g3,i;j} - \rho_{g3,i;j-1}\right)\right)\frac{\Delta t}{\left(\Delta y\right)^2}$$

$$(7.19)$$

In the large cleat (denoted with $i, j = 0$) we have the equation

$$
\left(\rho_{g3}\right)_{t+\Delta t}^{i,0} = \left(\rho_{g3}\right)_{t}^{i,0} + \frac{\left(d^{lc}\right)^2}{12\mu_g} P_x \frac{\left(\rho_{g3}\right)_{t}^{i-1,0} - \left(\rho_{g3}\right)_{t}^{i,0}}{\Delta x} \Delta t +
$$

$$
\frac{4\varphi D_{eff}, i, 1 \left(\rho_{g3}\right)_{t}^{i,1} - \left(\rho_{g3}\right)_{t}^{i,0}}{d_{lc}} \frac{}{\Delta y} \Delta t
$$

(7.20)

where the additional factor of 2, leading to the factor 4 in the last term arises because the density $\left(\rho_{g3}\right)_{t}^{i,0}$ occurs at the boundary of cell $(i, 1)$.

7.10 Results of the Simulations

Experimental results of core flood experiments with CO_2 do suggest the effect of water in terms of low sweep efficiencies. One of the objectives to this numerical study is to show the effect of effluent / water on the exchange of CH_4 and CO_2 in coal, and to see what impact it has over the methane recovery. The simulator has been tested for different water saturations, for different cleat aperture and for different injection rates. Changing effective horizontal stress conditions has considerable impact on the flow characteristics of coal as a result of the opening and closing of the cleat aperture. The matrix volume of the coal swells / shrinks when CO_2 / CH_4 adsorb or desorb. Matrix swelling could cause the fracture aperture width to decrease, causing an immense reduction in permeability.

7.10.1 Input parameters

The simulator simulates the enhanced coalbed methane process in a relatively wet or dry coal, with one single cleat running for a length of 1 m. The width (distance between the cleats) is 0.01 m and the height of the coal layer is 0.2 m. The matrix has been divided into grid cells in both x and the y directions respectively. The grid sizes thus become, $dx = 0.1$ m; $dy = 0.0005$ m. The constants used in the simulations are shown in Table 7.14.

Transport in the coal matrix is governed by the velocity with which the de- and adsorption processes take place and by the diffusion rate. Porosity influences both parameters in the way that more pore space increases the effective diffusion in the matrix and enhances the transport of the free gases through the coal matrix. A minor role is played by the matrix porosity, which stays more or less unaltered during stress built up and release. The cleat aperture is an important parameter in the flow characteristics of coal. Together with the injection velocity the cleat aperture governs the displacement characteristics of methane by carbon dioxide in this model. In general, we focus in this study on the changing flow

characteristics as a result of changing stress conditions and changing water saturations in the matrix. Therefore, in this numerical model only the parameters that are influenced by changing stress conditions and water content are altered.

7.10.2 Base Case

For the base case of the simulation we use a matrix porosity of 3 % and a cleat opening of 1×10^{-4} m. The velocity of injection is 0.00012 m/s. The base case water saturation is

Parameter	value	unit	description
P	8.5	MPa	in-situ gas pressure
T	318	K	in-situ temperature
R	8.314	J/mol,K	gas constant
L	1	m	length
d^{lc}	1.0×10^{-4}	m	cleat aperture
u_g^{lc}	1.2×10^{-4}	m/s	flow in single cleat
w	0.01	m	distance between cleats
dx	0.1	m	grid cell length
dy	5.0×10^{-4}	m	grid cell width
μ_w	6.66×10^{-4}	Pa s	water viscosity
μ_g	2.28×10^{-5}	Pa s	gas viscosity
S_g	0.05	-	initial gas in meso-cleats
D_l	1.0×10^{-9}	m²/s	diffusion in liquid phase
D_g	7.24×10^{-6}	m²/s	diffusion in gas phase
k	1.0×10^{-15}	m²	permeability in meso-cleats
$u_{g,y}$	1.2×10^{-9}	m³/s	flow in meso-cleats
S_{wc}	0.2	-	connate water in meso-cleats
Φ	0.03	-	matrix porosity
ρ_{g2}	57.21	kg/m³	initial CH₄ density
ρ_{g3}	281.81	kg/m³	initial CO₂ density

Table 7.14. Overview of the parameters used in the base case simulation

equal to 0.95. The other parameters are given in Table 7.14. The results of the base case simulation are presented in Figs. 7.23 and 7.24. The results give an idea of the development of a displacement front during injection of carbon dioxide. The lowermost row of the figures represents a cleat; the rest of the rows represent the matrix. The injected gases enter the system in the left lowermost grid block and flow to the right.

It is expected to create a plug-like displacement of the methane throughout the whole sample. This plug-like displacement would theoretically cause a concentration profile comparable with a piston moving from the left of the imaginary sample to the right. But then again in the figures we see a gradual increasing concentration of carbon dioxide from right to left in stead of an abrupt change. Besides the front between carbon dioxide and methane is not a straight vertical front, but a curved one.

The water saturation, injection velocity and the cleat aperture influences the form of the front. For higher water saturations, injection velocity and cleat apertures, the transport through

the cleat go much faster than diffusion through the matrix. The result is a curved concentration profile. Fig. 7.24 shows that at CO_2 break the recovery is as low as 41%. Thus in the light of higher matrix water saturation, this result is not very encouraging as has also been confirmed by the experiments.
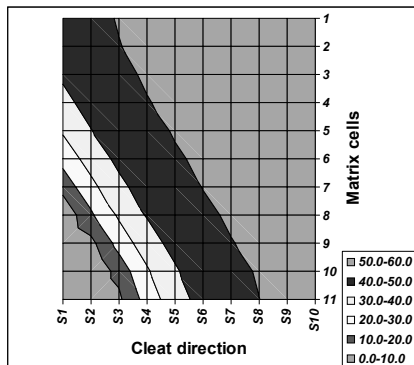

Fig. 7.23 (Base case) Development of the CO_2 displacement front after 11 h of injection; recovery: 24.8 %; injection velocity: 1.2e⁻⁴ m/s
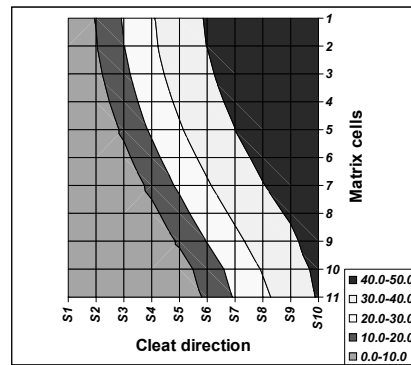

Fig. 7.24 (Base case) Elapsed time at CO_2 breakthrough: 41 h; recovery: 57.4 %; injection velocity: 1.2e⁻⁴ m/s

7.10.3 Cleat aperture

To simulate the change of effective stress in the subsurface the only tool in this model is the cleat opening. From the performed experiments it is concluded that the cleat closes when effective horizontal stress increases. The rest of the coal does hardly vary in volume because the micro pores do not change as a result of changing stress conditions. A lower cleat aperture would mean a smaller flux through the cleats.

Compared to the base case, the only parameter altered is d^{lc}, the cleat aperture. For the four different simulations the values of d^{lc} are 10 μ, 50 μ, 70 μ, and 200 μ. The base case value is 100 μ. These cleat apertures reflect the in situ situation. In Fig. 7.25 the solution is shown for a cleat opening of 10 μ. The displacement fronts of the this simulation are straight and the width of the concentration profile is the smallest of all. It can be concluded that it approaches the favorable plug flow displacement the most. The results for an aperture of 50 μ, 70 μ, and 200 μ are given in Figs. 7.26, 7.27 and 7.28 respectively. It is obvious that as a result of the larger aperture to flow, the process develops faster when compared with the 10 μ scenario. The 50 μ cleat aperture scenario (Fig. 7.26) takes the most time for a CO_2 break (130 h), also resulting in a higher recovery (72.2%). The 200 μ cleat aperture scenario (Fig. 7.28) posted the least recovery (50%) and a much faster CO_2 break (18 h).

7.10.4 Injection velocity

As mentioned before, the injection velocity alongside water saturation is a leading parameter in the process we try to model. The injection velocity to a great extent determines whether the displacement of the methane is piston like or that the injection gas slips right through to the production end. The lower the velocity, the more the process can be considered semi-steady state.

Again, four different simulations were run. During the laboratory experiments an injection rate of 1 ml/h was used over a core whose diameter was 70 mm. With a cleat spacing of 10 mm, there can be 6 large cleats at the maximum. This may result in a minimum injection velocity of 0.00012 m/s (base case). In an extreme situation where there is only one large cleat the injection velocity can be as high as 0.00072 m/s. The runs with four different injection velocities can be found in Figs. 7.29, 7.30, 7.31 and 7.32.

The most conspicuous difference between the four simulations is the shape of the concentration front. With increasing velocity the front becomes more curved. The result is that carbon dioxide is produced at an earlier stage of the process with higher velocities then with lower velocities. A higher velocity leads to a fast decrease in methane concentration at the production end. It can be seen that injection velocities higher than or equal to 0.00024 m/s, yields similar kind of recovery factor although the breakthrough times for CO_2 are different. An injection velocity of 0.00006 m/s yielded a recovery of 71.7% after 130 h of CO_2 injection and also resulting in a CO_2 break.

7.10.5 Water saturation

Presence of immobile water in the matrix can hinder the exchange process considerably. Diffusion coefficients in water are at least two orders of magnitude lower than diffusion coefficients in the gas phase. Most naturally occurring coal seams have very high water content and it is this water which is to be removed by the process of dewatering, before the methane production reaches its peak.

Four different simulations have been run with water saturation values ranging from 0.4 to 1.0. The results of the migration process are shown in Figs. 7.33, 7.34, 7.35 and 7.36. Lower water saturations (Figs. 7.33 and 7.34) can result in almost piston like flow through the system. Very high water saturations (Fig. 7.36) would result in an early CO_2 break and lower recovery factor. It should be noted that for the above simulations the injection velocity is kept low to obtain better results. A combined effect of higher injection velocity alongside high water saturations can be very detrimental for a sequestration project. A system where the coal has been rendered CO_2 wet instead of being water wet, can yield much better results in terms of both storage and recovery.
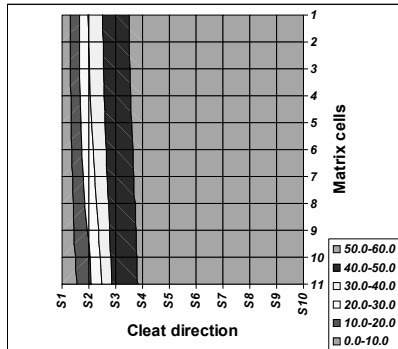
Fig. 7.25 Cleat aperture: 10 micron; elapsed time (no CO_2 breakthrough): 127 h; recovery: 24.5 %; injection velocity: $1.2e^{-4}$ m/s

Fig. 7.26 Cleat aperture: 50 micron; elapsed time at CO_2 breakthrough: 130 h; recovery: 72.2 %; injection velocity: $1.2e^{-4}$ m/s

Fig. 7.27 Cleat aperture: 70 micron; elapsed time at CO_2 breakthrough: 77 h; recovery: 66.4 %; injection velocity: $1.2e^{-4}$ m/s

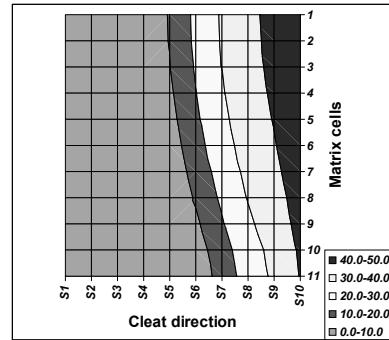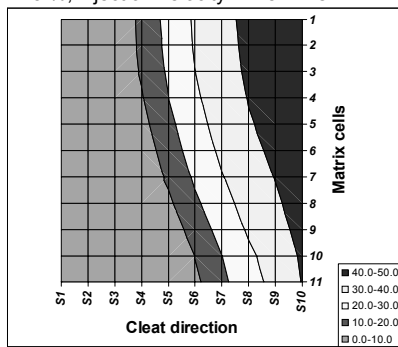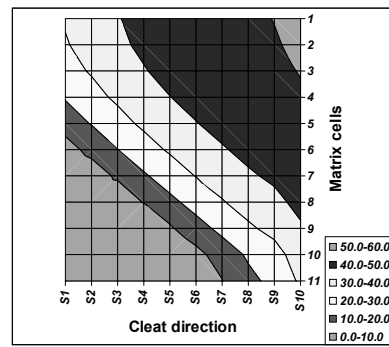Fig. 7.28 Cleat aperture: 200 micron; elapsed time at CO_2 breakthrough: 18 h; recovery: 50 %; injection velocity: $1.2e^{-4}$ m/s
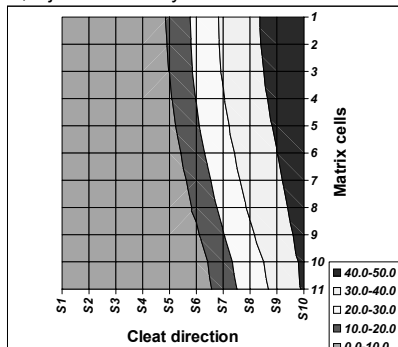
Fig. 7.29 Injection velocity: 0.6 e-4 m/s; cleat aperture: 100 micron; elapsed time at CO_2 breakthrough: 130 h; recovery: 71.7 %
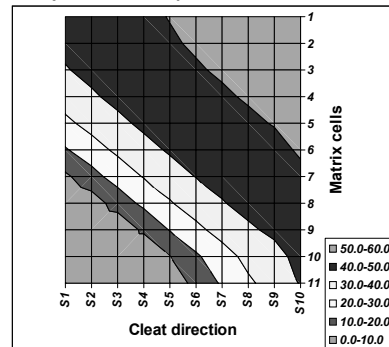
Fig. 7.30 Injection velocity: 2.4 e-4 m/s; cleat aperture: 100 micron; elapsed time at CO_2 breakthrough: 11 h; recovery: 38.2 %
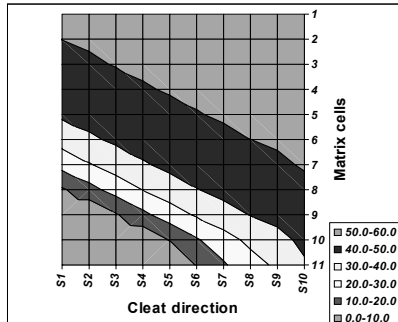
Fig. 7.31 Injection velocity: 3.6 e^{-4} m/s; cleat aperture: 100 micron; elapsed time at CO_2 breakthrough: 5.55 h; recovery: 32.4 %
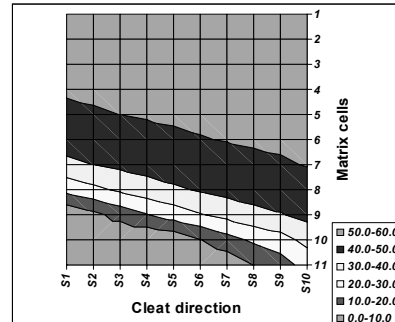
Fig. 7.32 Injection velocity: 7.2 e^{-4} m/s; cleat aperture: 100 micron; elapsed time at CO_2 breakthrough: 2.77 h; recovery: 31.8 %
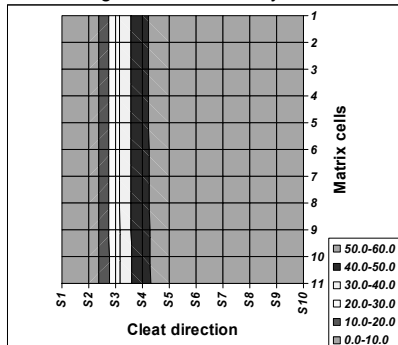
Fig. 7.33 Water saturation: Sw = 0.4; elapsed time: 27 hours (no CO_2 breakthrough); recovery: 32.8 %; injection velocity: 1.2 e^{-4} m/s; cleat aperture: 100 micron
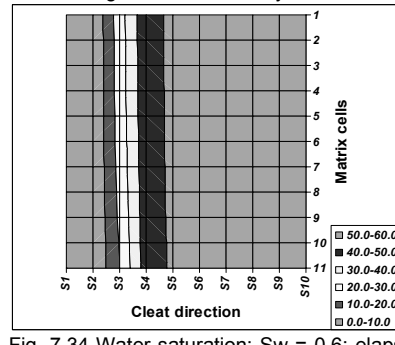
Fig. 7.34 Water saturation: Sw = 0.6; elapsed time: 27 hours (no CO_2 breakthrough); recovery: 34 %; injection velocity: 1.2 e^{-4} m/s; cleat aperture: 100 micron
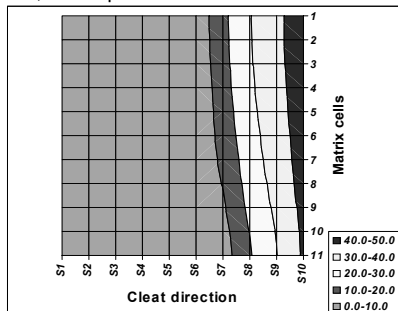
Fig. 7.35 Water saturation: Sw = 0.8; elapsed time at CO_2 breakthrough: 83 hours; recovery: 52.4 %; injection velocity: 1.2 e^{-4} m/s; cleat aperture 100 micron
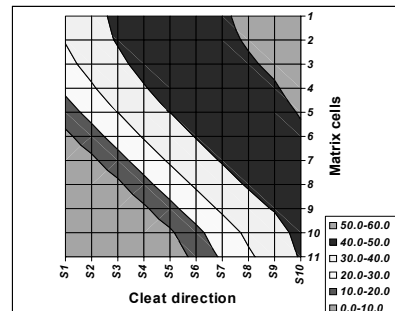
Fig. 7.36 Water saturation: Sw = 1.0; elapsed time at CO_2 breakthrough: 27 hours; recovery: 44 %; injection velocity: 1.2 e^{-4} m/s; cleat aperture: 100 micron

7.11 Conclusions

- The results generated out of the numerical model seem to clearly depict the effect of the effluent on the exchange process.

- Coal with low porosity can store more carbon dioxide then coal with a higher porosity, when the rest of the parameters are kept constant.

- To maintain a high methane concentration at the production end for as long as possible, a low injection velocity should be used.

- With a small cleat aperture and lower water saturations the plug flow is best approximated.

Nomenclature

We denote the CO_2 as component 3, CH_4 as component 2, and H_2O as component 1. We denote all the concentrations of carbon dioxide (3) and methane (2) as $\rho_{\alpha,j}$ where $j = 2,3$ is the component and α is the phase i.e. the gas (g) or the solid (s) phase. The concentrations in the solid phase are expressed in terms of unit mass per unit pore volume. The concentrations in the gas phase are expressed in terms of unit mass per unit volume available to the gas.

Appendix A

Estimate of the experimental error in measuring the permeability

The experimental error in measuring the permeability was estimated. The error measurement is based on the concept of calculating the uncertainty in the final value of the calculated parameter from the uncertainties of each measured variables (Holman, 1994; Taylor, 1997). The effects of each measured variables on the final calculated variable value is derived from the concept of propagation of errors. The concept is best explained by the following example:

For evaluation of the uncertainty in the value of parameter R, where R is a function of independent variables (x_i), i.e.:

$$R = R(x_1, x_2, x_3, \ldots \ldots \ldots x_n),$$ (A-1)

Let U_R denote the uncertainty in the result R and, U_i is the uncertainty in each variable x_i. Then the uncertainty U_R is given by

$$U_R = \left[\left(\frac{\partial R}{\partial x_1}U_1\right)^2 + \left(\frac{\partial R}{\partial x_2}U_2\right)^2 + \ldots \ldots \ldots + \left(\frac{\partial R}{\partial x_n}U_n\right)^2\right]^{\frac{1}{2}}.$$ (A-2)

Applying this concept for our case and starting with the permeability equation (Eq. 6.2), the measured independent variables are: q, L, P_o and P_i. All the other terms have been put as a constant in the term θ.

$$k = \frac{\theta q L P_o}{P_i^2 - P_o^2}.$$ (A-3)

Taking partial derivative of k with respect to the above mentioned independent variables, the uncertainty in permeability is then derived as

$$U_k = \sqrt{\begin{bmatrix} \left(\frac{\theta L P_o}{P_i^2 - P_o^2}\partial q\right)^2 + \left(\frac{\theta q P_o}{P_i^2 - P_o^2}\partial L\right)^2 + \\ \left(\frac{\theta q L (P_i^2 + P_o^2)}{(P_i^2 - P_o^2)^2}\partial P_o\right)^2 + \\ \left(\frac{-2\theta q L P_i P_o}{(P_i^2 - P_o^2)^2}\partial P_i\right)^2 \end{bmatrix}}.$$ (A-4)

All error measurements of the experimental permeability data have been presented as +/- error bars. This is shown in the Figs. 6.4, 6.7, 6.10 and 6.13. More than 95 % of the random

error in the permeability measurements was introduced by the uncertainty in the injection and the production pressures.

Nomenclature

k = permeability, mD

p = reservoir pressure, MPa

q = flow rate $[m^3/\sec]$,

P_0 = production pressure $[MPa]$,

P_i = injection pressure $[MPa]$,

μ = viscosity $[Pa.s]$,

A = crossection area $[cm^2]$

L = length of the core $[m]$

Appendix B

Numerical solution of the Case II diffusion problem

Finite volume equation

We like to solve the equation

$$\frac{\partial \phi}{\partial t} = \frac{\partial}{\partial x}\left(D\frac{\partial \phi}{\partial x}\right) + \frac{1}{B}\frac{\partial}{\partial x}\left(D\phi\frac{\partial}{\partial x}\left(\exp(-m\phi)\frac{\partial \phi}{\partial t}\right)\right). \tag{B-1}$$

Integrating over the grid cell leads to

$$\frac{\partial \phi}{\partial t}\Delta x = \left(\left(D\frac{\partial \phi}{\partial x}\right)_{eb} - \left(D\frac{\partial \phi}{\partial x}\right)_{wb}\right)$$
$$- \frac{1}{mB}\left(\left(D\phi\frac{\partial}{\partial x}\left(\frac{\partial \exp(-m\phi)}{\partial t}\right)\right)_{eb} - \left(D\phi\frac{\partial}{\partial x}\left(\frac{\partial \exp(-m\phi)}{\partial t}\right)\right)_{wb}\right).$$

Hence we obtain the finite difference form as

$$\frac{\phi_P^{k+1} - \phi_P^k}{\Delta t}\Delta x - D\left\{\frac{\phi_P^{k+1} + \phi_E^{k+1}}{2}\right\}\frac{\phi_E^{k+1} - \phi_P^{k+1}}{\Delta x} + D\left\{\frac{\phi_P^{k+1} + \phi_W^{k+1}}{2}\right\}\frac{\phi_P^{k+1} - \phi_W^{k+1}}{\Delta x}$$
$$- \frac{1}{m}\left(\frac{\left(\phi_P^{k+1} + \phi_E^{k+1}\right)D\left\{\frac{\phi_P^{k+1} + \phi_E^{k+1}}{2}\right\}}{2B}\right)_{eb} \times$$
$$\left(\frac{\exp\left(-m\phi_E^{k+1}\right) - \exp\left(-m\phi_E^k\right)}{\Delta t\Delta x} - \frac{\exp\left(-m\phi_P^{k+1}\right) - \exp\left(-m\phi_P^k\right)}{\Delta t\Delta x}\right) +$$
$$+ \frac{1}{m}\left(\frac{\left(\phi_P^{k+1} + \phi_W^{k+1}\right)D\left\{\frac{\phi_P^{k+1} + \phi_W^{k+1}}{2}\right\}}{2B}\right)_{wb} \times$$
$$\left(\frac{\exp\left(-m\phi_P^{k+1}\right) - \exp\left(-m\phi_P^k\right)}{\Delta t\Delta x} - \frac{\exp\left(-m\phi_W^{k+1}\right) - \exp\left(-m\phi_W^k\right)}{\Delta t\Delta x}\right) = 0,$$

where we use the harmonic average for the diffusion coefficient. The Jacobian can be obtained straightforwardly by differentiating versus ϕ_P^{k+1}, ϕ_E^{k+1} and ϕ_W^{k+1}.

The Newton-Raphson equation for this system reads

$$f_P\left(\phi_P^{k+1},\phi_E^{k+1},\phi_W^{k+1}\right) + \frac{\partial f_P}{\partial \phi_P^{k+1}}\Delta\phi_P^{k+1} + \frac{\partial f_P}{\partial \phi_W^{k+1}}\Delta\phi_W^{k+1} + \frac{\partial f_P}{\partial \phi_E^{k+1}}\Delta\phi_E^{k+1} = 0.$$

Boundary conditions

At $x=0$ we have a concentration $\phi(x=0,t)=\phi_g(t)$, which can be derived from Eq. 4.14. At $x=L$ we have the boundary condition

$$D\frac{\partial \phi}{\partial x} + \frac{1}{B}D\phi\frac{\partial}{\partial x}\left(\exp(-m\phi)\frac{\partial \phi}{\partial t}\right) = 0$$

This can be rewritten as

$$D\frac{\partial \phi}{\partial x} - \frac{1}{mB}D\phi\frac{\partial}{\partial x}\left(\frac{\partial \exp(-m\phi)}{\partial t}\right) =$$
$$D\frac{\partial \phi}{\partial x} - \frac{1}{mB}D\phi\frac{\partial}{\partial t}\left(\frac{\partial \exp(-m\phi)}{\partial x}\right) =$$
$$D\frac{\partial \phi}{\partial x} + \frac{1}{B}D\phi\frac{\partial}{\partial t}\left(\exp(-m\phi)\frac{\partial \phi}{\partial x}\right) = 0$$

The equation is satisfied when $\frac{\partial \phi}{\partial x}=0$. The initial condition is $\phi(x,t=0)=0$ and $\partial\phi(x,t=0)/\partial t = 0$.

Sherwood and Pigford approach

In Bird, (1960), the following approach is indicated. In order to use the same equations as in (Bird, 1960), we use $c=\tilde{c}-c_s$, where $\tilde{c}$ is the conventional concentration. We have the following boundary and initial conditions

$$\begin{array}{lll} \text{I.C:} & c(z>0,t=0)=0 & \\ \text{B.C. 1:} & c(z=0,t)=c_o & \\ \text{B.C. 2.3:} & c(z=z_R(t)-\varepsilon,t)=c(z=z_R(t)+\varepsilon,t)=c_s & \text{(B-2)} \\ \text{B.C. 4:} & D_1\frac{\partial c}{\partial z}((z=z_R(t)-\varepsilon,t))=D_2\frac{\partial c}{\partial z}((z=z_R(t)+\varepsilon,t)) & \\ \text{B.C. 5:} & c(z\to\infty,t)=0. & \end{array}$$

The following solution is proposed

$$\frac{c}{c_o} = C_1 + C_2 \operatorname{erf} \frac{z}{\sqrt{4D_2 t}} \quad \text{for} \quad 0 < z \le z_R(t)$$
$$\frac{c}{c_o} = C_3 + C_4 \operatorname{erf} \frac{z}{\sqrt{4D_1 t}} \quad \text{for} \quad z_R(t) < z < \infty ,$$

(B-3)

where D_2 is the diffusion in the rubber state, whereas D_1 is the diffusion in the glass state. Note that $D_2 >> D_1$. We have the following equations when implementing some boundary conditions and the initial condition in Eq. B-3a

$$C_1 = 1$$
$$C_1 + C_2 = 0\,?$$
$$1 + C_2 \operatorname{erf} \frac{z_R(t)}{\sqrt{4D_2 t}} = \frac{c_s}{c_o},$$

and when implementing some boundary conditions and the initial condition in Eq. B-3b we obtain

$$C_3 + C_4 = 0 \text{ and } C_4 = -\frac{c_s / c_o}{\operatorname{erf} c \frac{z_R}{\sqrt{4D_1 t}}}$$

Note that D_1 is the glass diffusion and D_2 is the rubber diffusion. Hence we find

$$\frac{c}{c_o} = 1 + \left(\frac{c_s}{c_o} - 1\right) \frac{\operatorname{erf} \frac{z}{\sqrt{4D_2 t}}}{\operatorname{erf} \frac{z_R(t)}{\sqrt{4D_2 t}}} \quad \text{for} \quad 0 < z \le z_R(t)$$
$$\frac{c}{c_o} = \frac{c_s / c_o}{\operatorname{erf} c \frac{z_R}{\sqrt{4D_1 t}}} \operatorname{erf} c \frac{z}{\sqrt{4D_1 t}} \quad \text{for} \quad z_R(t) < z < \infty ,$$

(B-4)

Application of BC-4 in Eq. B-2 leads to (noting that common terms cancel)

$$\sqrt{D_2}\left(\frac{c_s}{c_o} - 1\right) \frac{\exp - \frac{z^2}{4D_2 t}}{\operatorname{erf} \frac{z_R(t)}{\sqrt{4D_2 t}}} = -\sqrt{D_1} \frac{c_s / c_o}{\operatorname{erf} c \frac{z_R}{\sqrt{4D_1 t}}} \exp - \frac{z^2}{4D_1 t}$$

where we use that $\frac{d}{dx} \operatorname{erf} c\langle ax \rangle = -\frac{2a}{\sqrt{\pi}} e^{-a^2 x^2}$. We observe that $z_R(t)$ increases as $\sqrt{t}$. Also the adsorption rate is proportional to $\sqrt{t}$. Assuming that $z_R = \beta\sqrt{t}$ we obtain an implicit equation for β

$$\left(\frac{c_s}{c_o} - 1\right) \frac{\exp - \frac{\beta^2}{4D_2}}{\operatorname{erf} \frac{\beta}{\sqrt{4D_2}}} = \sqrt{\frac{D_1}{D_2}} \frac{c_s / c_o}{\operatorname{erf} c \frac{\beta}{\sqrt{4D_1}}} \exp - \frac{\beta^2}{4D_1},$$

Laplace solution of linearized equation

We like to solve a linearized form of Eq. B-1 in which we substitute

$$\phi = \phi^{(0)} + \omega,$$

where ω is small. Retaining only first order terms, we obtain

$$\frac{\partial \omega}{\partial t} = \frac{\partial}{\partial x}\left(D\frac{\partial \omega}{\partial x}\right) + \frac{1}{B}\frac{\partial}{\partial x}\left(D\phi^{(0)}\frac{\partial}{\partial x}\left(\exp\left(-m\phi^{(0)}\right)\frac{\partial \omega}{\partial t}\right)\right). \tag{B-5}$$

Assume that the initial concentration is $\phi^{(0)}$, and that the boundary concentration is $\phi^{(b)}$.

Laplace transforming leads to (assuming a constant diffusion coefficient)

$$s\widehat{\omega} = D\left(\frac{\phi^{(0)}s\exp\left(-m\phi^{(0)}\right)}{B} + 1\right)\frac{\partial^2 \widehat{\omega}}{\partial x^2} =: \Lambda\frac{\partial^2 \widehat{\omega}}{\partial x^2}.$$

The solution of this is

$$\widehat{\omega} = \frac{\left(\phi^{(b)} - \phi^{(0)}\right)}{s}\exp\left(-\sqrt{\frac{s}{\Lambda}}x\right)$$

Dimensionless form

Eq. 4.10 can be rescaled using $D_g t / L^2 \to t$, $D / D_g \to D$, $x / L \to x$ and we obtain

$$\frac{\partial}{\partial t}\phi = \frac{\partial}{\partial x}\left(D\frac{\partial}{\partial x}\phi\right) + \beta\frac{\partial}{\partial x}\left(D\phi\frac{\partial}{\partial x}\exp\left(-m\phi\right)\frac{\partial}{\partial t}\phi\right), \tag{B-6}$$

where $\beta = \Omega D_g\eta_o / \left(kTL^2\right)$, showing that for long time, i.e., large sample length L the relaxation term becomes negligible. This is also confirmed by the numerical solutions. Neglecting the relaxation term allows an analytical solution, which shows $\sqrt{t}$ behavior.

Appendix C

Stress dependent permeability of coal

The impact of increasing triaxial stress on permeability of coal samples has been investigated by a number of researchers (Somerton et al., 1975; Durucan and Edwards, 1986). Experimental measurements indicate that permeability of coal decreases exponentially with increasing effective stress. Theoretical support for this exponential relationship was later provided by McKee et al. (1987) and Seidle et al. (1992), based upon the assumption that solid grains are incompressible.

The permeability of the cleat structure in coal may vary in three basic ways. The first is by phase relative permeability effects, whereby the degree of saturation will affect the gas and water relative permeability's of the reservoir. The second and one of the most important way by which the permeability may vary is by a change in the effective stress within the seams. The effective stress is the total stress minus the seam fluid pressure. The effective stress tends to close the cleats and to reduce permeability within the coal. It is very likely that the permeability is related particularly to the "*effective normal stress*" (Gray, 1987) across the cleats because these appear to conduct most seam fluids. The "*effective normal stress" is* defined as, the total stress normal to the cleat, minus the fluid pressure. Under field disposition the "*effective normal stress"* can also be termed as the "*effective horizontal stress"* (Shi et al., 2003) because the cleat system is sub-vertically oriented to the bedding plane and is orthogonal to each other. Under these circumstances the permeability variations brought about by variations in fluid pressures are anisotropic, depending on the nature, frequency, and direction of the cleats. Such opening and closing of the cleats is also likely to change the phase relative permeability's and capillary pressures within the coal. The third most important way by which the permeability may vary is by the process of shrinkage while methane is being desorbed or swelling while carbon dioxide is being injected. This aspect of permeability variation is being dealt with separately.

Permeability models

Two permeability models were selected from the literature to model our laboratory permeability data. Palmer and Mansoori published their model in 1998, and Shi and Durucan published theirs in 2003.

The Palmer-Mansoori Model is perhaps the most widely discussed permeability model in the literature and other models are based on it. The Palmer-Mansoori Model assumes Reiss's cubic relationship between permeability and porosity for fractured media. The macro porosity change equation for this model was given as:

$$\frac{\phi}{\phi_0} = 1 - \frac{1}{M\phi_0}(\sigma - \sigma_0) + \frac{\varepsilon}{\phi_0}\left(\frac{K}{M} - 1\right)\left(\frac{P}{P_\Psi + P} - \frac{P}{P_\Psi + P_0}\right), \qquad \text{(C-1)}$$

where M is the constrained axial modulus, K is the bulk modulus, and ε as the volumetric Langmuir strain constant. The bulk modulus and the constrained axial modulus can be written in terms of Young's moldulus and Poisson's ratio.

$$K = \frac{E}{3(1-2\nu)}, \ and \ M = \frac{E(1-\nu)}{(1+\nu)(1-2\nu)}. \qquad \text{(C-2)}$$

In the original Palmer and Mansoori (1996) formulation as shown above the first series of terms to the right hand side of the equation account for the pressure dependent nature of the coal porosity, while the second term accounts for the porosity change due to matrix shrinkage (in primary depletion). All parameters in the equation can be either measured or approximated except the initial porosity, which can have a large effect on the outcome of the model. However, initial porosity values can be obtained by judiciously fitting the above equation to permeability data unaffected by sorption-induced strain.

The Shi-Durucan Model began with the derivation for permeability by Seidle et al. (1992) and derived an expression for the change in effective stress:

$$\frac{k}{k_0} = \exp\left\{-c_f\left[\frac{3\nu}{(1-\nu)}(\sigma - \sigma_0) + \frac{E}{(1-\nu)}\varepsilon\left(\frac{P}{P_\Psi + P} - \frac{P}{P_\Psi + P_0}\right)\right]\right\}, \qquad \text{(C-3)}$$

where the fracture compressibility, c_f, is obtained by fitting the experiments to the formulation shown below:

$$c_f = \frac{1}{3}\left[\frac{2}{E}(1-2\nu) - \frac{\left(\ln k_{f_2} - \ln k_{f_1}\right)}{(\sigma_{e2} - \sigma_{e1})}\right], \qquad \text{(C-4)}$$

where σ_e is the effective stress and k_f the fracture permeability of coal Seidle et al. (1992).

Permeability measurements

Experimental work reported here used coal core samples confined by an effective stress with nitrogen flow along the axis of the sample. The core being a vertical drill core, the flow is along the axis of the conceptualized bunch of matchsticks. The test procedure in the laboratory involved confining a 20 cm long and 7 cm in diameter coal core sample under a number of isotropic stress levels in the cell and passing nitrogen through the sample at a steady pressure until the flow came to equilibrium. Two hours to two days were required to reach equilibrium. Because gas pressure varied across the specimen, the average of the two end gas pressures was used in the calculation of the effective stress. The equation used to calculate core permeability is after Gray (1987) and have been referred to in Chapters 5 and 6.

The permeability measurements were conducted on three different samples. A vertical drill core sample (Seam 401) from the Silezia basin of Poland. This sample was used to conduct experiment VII, reported in Chapter 7. The other one was of an anthracitic coal sample (Selar Cornish) with a vitrinite reflectance of 2.41%. This sample was used to conduct absolute swelling experiments and the details of which have been reported in Chapter 5. The third sample was a Silezia coal core used to do core flooding experiments as reported in Chapter 7. The results of experiments and the respective model fits have been shown in Figs. C-1, C-2 and C-3 respectively. For the Seam 401 drill core, permeability changes resulting from the varying effective stress as shown in Fig. C-1. Along with the actual permeability data, the Palmer-Mansoori and Shi-Durucan models are shown. Because pore pressure was kept constant, sorption-induced strain was eliminated, which allowed these data to be used to calculate the initial porosity and the fracture compressibility constants. Both of these models were fitted to the experimental data using a least squares method. The calculated initial porosities (using the P-M model) were 0.3, 0.16 and 0.18% respectively for the three experiments. The calculated fracture compressibilities, c_f (using the S-D model) were 0.04, 0.113 and 0.113 MPa^{-1} respectively.

Both the models seem to give a reasonable fit to the experimental data except for the third experiment (Fig. C-3) where the S-D model fit returns a very high Poisson's ratio, which is not very natural for coal. The value of the Young's modulus was determined experimentally and is as follows: E = 2.5 x 10^{+3} MPa. All three experiments predict a very low initial porosity value for all coal samples used. While the P-M model yielded values for the initial porosity, the S-D model gave values for the fracture compressibility.
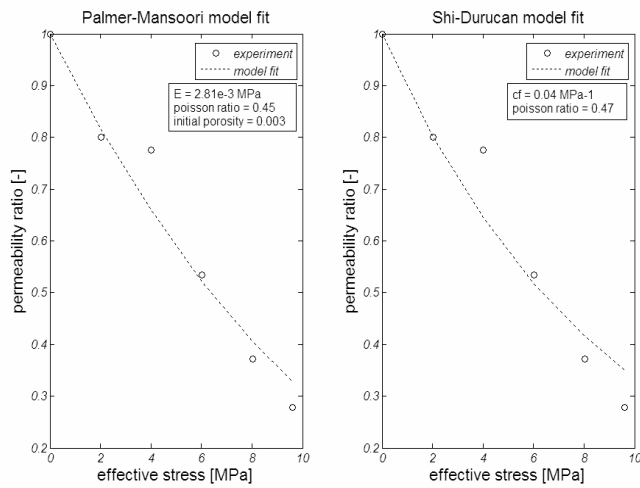
Fig. C-1 Permeability measurements in relation to effective stress for the Polish drill core (Seam 401) and its model fit.
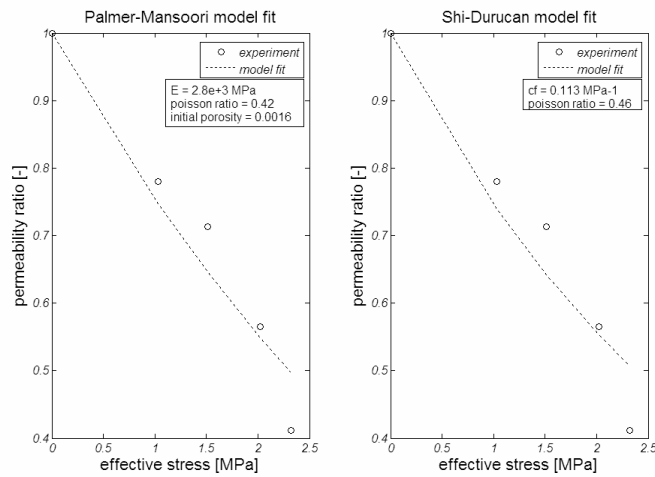

Fig. C-2 Permeability measurements in relation to effective stress for the high rank Selar Cornish coal and its model fit.
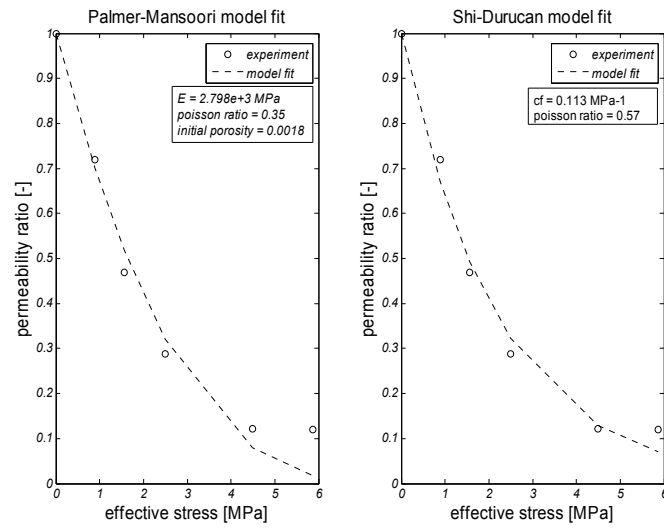
Fig. C-3 Permeability measurements in relation to effective stress for the low rank Silezia coal.

Appendix D

Swelling, structure and coal rank

Coal is a complex and heterogeneous material produced by the biological and geothermal degradation of organic components of ancient plant matter. This heterogeneity leads to difficulties in accurately characterizing its structure. Evidences to prove the highly crosslinked macromolecular nature of coal has been presented, mostly as contribution by previous researchers. In this work a molecular diffusion-deformation problem in coal is of interest. Experimental evidences have been put forward to prove the non-Fickian / anomalous diffusion process in coal. A model has been proposed based o the fact that the diffusive process is strongly coupled to the mechanical response of coal. This happens in a sense that the rate at which the penetrant is absorbed must be compatible with the swelling rate, controlled by the creep deformation of the surrounding coal. It is a diffusion which is stress driven.

Coalification is defined as the gradual increase in carbon content of fossil organic material from peat through lignite to bituminous coal and ending with anthracite. It is important to emphasize that not all coals derive from the same precursor materials, so that lignite and anthracite do not necessarily represent different stages of the same coalification process. The hydrogen content remains rather constant throughout coalification to the bituminous coals, but decreases during the formation of anthracite. The reactions contributing to this loss include aromatization of cycloalkanes or hydroaromatics, and condensation of isolated ring structures into polycyclic systems (Schobert, 1989). With a carbon content approaching 90 % and the formation of large sheets of aromatic rings, increased coalification among the very high rank coals lead to structures that become increasingly like graphite (Schobert, 1989).

Coalification is principally governed by temperature, time and pressure. Pressure promotes "physico-structural" coalification, whilst temperature promotes "chemical" coalification. Products of the lowest rank have a strongly hydrophilic character and high moisture content. It is not until the bituminous coal stage is reached that the moisture content becomes low and the coal substance becomes hydrophobic. This is probably due to the gradual elimination of polar functional groups, especially hydroxyl (-OH) groups, which are reduced in the early stages of coalification. Besides hydroxyl groups, carboxyl (-COOH), methoxyl (-OCH₃) and carbonyl (>C=O) groups, as well as ring oxygen, are decomposed and so the carbon content gradually increases (Stach et al., 1982). In the later stages of coalification, volatile matter, which consists predominantly of the non-aromatic fraction of coal, falls rapidly due to both the removal of aliphatic and alicyclic groups and the increasing aromatization of humic complexes.

Porosity, internal surface area and moisture content decrease with increasing rank from brown coal to the medium volatile bituminous coals, where a minimum is reached, and then increase again to anthracite. The increase in these properties from low volatile bituminous coals to anthracite is due to the progressive removal of the bitumens from the porous coal structure (caused by increasing temperatures).

Since the H/C ratio is low, and becomes lower still during the final stages of coalification, suggests a high and increasing degree of aromaticity. Considering that graphite is the final link in the evolution of coal, the aromaticity, and the degree of condensation of the aromatic rings, increases throughout the coalification process. However based on very early solid state C^{13}-NMR work, Whitehurst (1978) disagrees that the mole ratio of H/C is a clear indication of aromatic carbon content. He prefers to regard coal as "...a highly crosslinked amorphous polymer, which consists of a number of stable aggregates connected by relatively weak crosslinks". Stach et al., (1982) describe the structure of low rank bituminous coals as comprising randomly dispersed stacks of two or three aromatic layers, with each layer being composed of 5 to10 aromatic rings. The stacks are linked together by non-aromatic groups that inhibit the development of close and constant interlayer spacing. The wide spread of interlayer spacing thus characteristic of low rank coals decreases with increasing rank as the aliphatic groups and oxygen disappear (Stach et al., 1982).

On the basis of X-ray structural analysis, Hirsch (referenced in van Krevelen, 1961) developed a model that distinguished between three types of structures; an "open structure" charasteristic of low rank coals, a "liquid structure" typical of bituminous coals, and an "anthracitic structure" (Fig. D.1). In the open structure, the lamellae are connected by crosslinks. They have a low degree of orientation, thus constituting a highly porous system. In the liquid structure the lamellae show a higher degree of orientation and the number of crosslinks decreased considerably. Pores are practically absent. In the anthracitic structure, the crosslinks disappear completely and the degree of orientation of the lamellae increases significantly.

Coal as a highly crosslinked macromolecular network

Green et al. (1982) presented several compelling reasons as to why coal should be considered as comprising a macromolecular structure. Firstly, coals are insoluble. Although a significant part of coal is extractable in various solvents, the bulk of most coals will not dissolve. This is indicative of a crosslinked, or highly entangled, macromolecular structure. Secondly, coals swell in the presence of CO_2 and other good solvents. They are capable of contracting to its original volume. Finally, coals are viscoelastic, i.e. they deform under an applied stress and are able to recover partly on removal of the applied stress, indicating a macromolecular network with extensive crosslinking. The dimensional change of a coal during swelling is due to

the reorientation of macromolecular chains, with the driving force coming from the free energy of mixing of the solvent and the coal network.
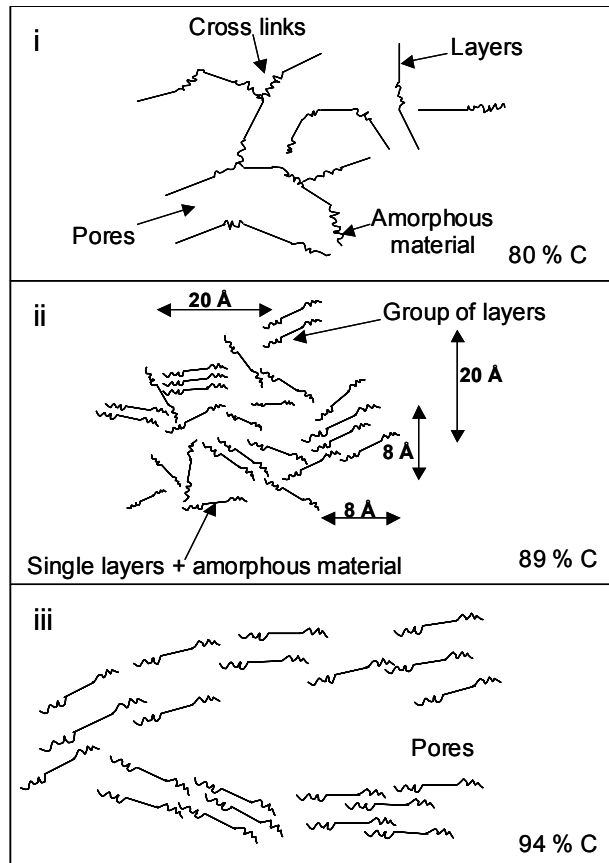
Fig. D.1 Structural model of coal according to Hirsch (after van Krevelen, 1961).
[i = "Open structure"; ii = "Liquid structure"; iii = "Anthracitic structure"]

Bodily et al. (1989) used sequential swelling (from poor to good swelling solvents) to illustrate the crosslinked nature of a high volatile bituminous coal. When the coal was first swollen in cyclohexane (a poor swelling solvent), and then, after removal of the preceding solvent, in methanol, acetone, and tetrahydrofuran, the swelling was the same as that of a coal swollen independently in each of the solvents. When the order of solvent treatment was reversed, a dramatic increase in swelling induced by the weaker solvents was observed. It was concluded that polar crosslinks broken by the better solvents, were not entirely reformed after

removal of the solvent. The weaker solvents were now able to swell the coal in the absence of some of the constraints previously present in the form of polar crosslinks (i.e. hydrogen bonds). van Krevelen (1961) showed in experiments with model substances that when the number of bridges between monomer units are less than unity, the model substance was completely soluble in solvents. As soon as the number of linkages between monomer units increases slightly above unity (i.e. crosslinking), complete solubility was no longer possible. As crosslinking became more pronounced the substance became completely insoluble. Since coal does not dissolve, even in solvents that are able to swell it to more than twice its original volume, it must be three dimensionally crosslinked or it has to consist of such large macromolecules that entanglements cannot be easily separated. Evidence for the existence of permanent crosslinks between macromolecular chains is from the fact that coals swollen in good solvents do not continue to swell indefinitely. Instead they reach a limiting size. The fact that low rank coals swell to a greater extent than high rank coals do, may be either a consequence of a lower initial crosslink density or of a greater degree of the crosslink interactions in low-rank coal to be ruptured by good solvents.

Larsen and Kovac (1978) used strain - time curves to argue that bituminous coals must be considered as covalently crosslinked macromolecules. Weak associative forces such as hydrogen bonding and van der Waals forces only provided a small contribution to the macromolecular association. Swelling of coal by all non - polar gases like CO_2 and CH_4 is caused by the dispersion force interaction between the gas species and the coal macromolecular network.

Reucroft and Patel (1986) used the solubility parameter theory (commonly used for crosslinked macromolecular network) to predict that swelling has a significant effect on the measured specific surface area of coals. Considering coal to be a three dimensional highly crosslinked macromolecular structure, the swelling properties of different gas species primarily depend on the sorption capacity of coal (Chikatamarla et al., 2004) and on the basis of their interaction with the various types of effective bridging bonds in coal. The effective bridging bonds in coal are formed through (i) covalent bonding, (ii) ionic bonding, (iii) hydrogen bonding and (iv) charge transfer complexing (Larsen at al., 1981). Swelling in coal is caused by disrupting (breaking or extending) one or more of these bonds. The extent of swelling depends on the type of bonds predominant in a particular rank of coal and the nature of the sorbent. Covalent bonds are not likely to be broken by common sorbents in coal. Only ionic interactions, hydrogen bonding and charge transfer complexing are important in the swelling phenomenon. Ionic and hydrogen bonds are believed to be significant in low rank coals because of the presence of relatively large numbers of polar functional groups. Charge transfer complexing is expected to be predominant only in high rank coals because of their higher aromatic content than the low rank coals.

The macromolecular model is widely accepted, with the framework occluding some tar like extractable components (Nishioka, 1992). He proposed that the macromolecular structure is a polycyclic aromatic ring like system, linked by carbon and heteroatom bridges. A simple conceptualization is shown in Fig. D.2. Hydrogen bonds are primarily considered in addition to relatively weak van der Waal's forces, which have to be broken as a result of dissolution by CO_2 and other gas species. The relatively strong secondary interactions are highly dependent on coal rank (Nishioka et al., 1990). It is estimated that the columbic force is predominant in low rank coal due to ionized groups. The charge-transfer complexes involving non - ionizable but transferable electrons are important in medium rank coal, and dispersion forces involving polarizable $\pi-$electrons in the polycyclic aromatics ($\pi-\pi$ interactions) are major contributors in high rank coal. This concept is well depicted in Fig. D.3.
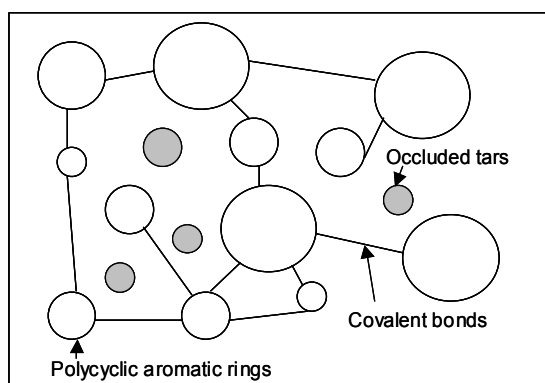
Fig. D.2 A covalently cross-linked model of coal structure (Nishioka, 1992)

Considering the previous explanations of coal compositions and its relation to gases may give the following CO_2- polymer relation. A CO_2 molecule placed between the polymer chains of coal, disrupts partly the original structure if the sorption takes place in locations where the available volume between the chains is smaller than the actual volume of the CO_2 molecule. This disruption requires energy to overcome attractive forces between the chains, which can be described in the form of Lennard-Jones potentials and columbic electrostatic potentials. Furthermore, the energy which is required to change the conformation of the polymer chains: rotational alterations of sp^3- bonds and out-of-plane bending of sp^2-bonds will be responsible for the change of the chain conformation.
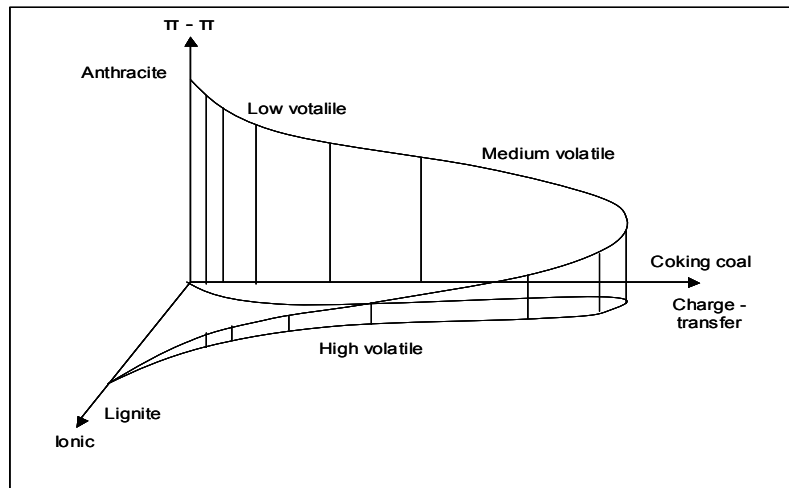
Fig. D.3 Dependence of relatively strong intra- and intermolecular interactions on coal rank (Nishioka, 1992)

Appendix E

Void volume measurements

For better comparison of the results, a schematic of the set-up is shown in Fig. E-1. The whole set-up is divided into four parts. Valves enclose the major part of the volume in the set-up. Volume measurements have been conducted by using helium expansion.

Starting from left to right, (Fig. E-1), the first section of the volume includes the volume of the pump, including a part of the tubing from the pump to the injection side. This volume ends at valve 1, which is an air actuated valve and is open only when the pump is injecting. The volume of this section is 283.02 ml, out of which the syringe pump itself has a volume of 266.50 ml. Of the total 283.02 ml only 266.50 ml can be displaced during the experiment, and this volume gives no contribution to the absolute free volume of the set-up.

The second section is the part of the tubing enclosed between valve 1 and valve 2. This part has a volume of 44.04 ml, and contributes to the absolute free volume of the set-up.

The third section, the volume between valve 2 and valve 3, comprises the volume of the in going and out going tubing of the pressure cell, the tubing to the differential pressure transducer (over the core) and the pore volume of the coal core. This volume differs with coal samples. For Experiment I the volume is 137.97 ml, of which the pore volume of the core is 63.35 ml. As shown in the figure, the volume of the tubing to the differential pressure transducer is static. The tubing diameter (OD) of this part is 3.14 mm and the volume   5 ml. This static volume interacts with the flow stream by diffusion. The diffusion rates being small, this volume is neglected. Apart from the porous coal the two end plates attached to the core are the major contributors to the volume of this section. These end plates and the tubing volume cannot be eliminated, as they are vital in the construction of the set up. Subtracting the porous volume of the coal (63.35 ml) from the total free volume, gives us the tubing volume (74.62 ml). Likewise for experiment II and VII, the total volume for this part is 108.44 ml and 142.28 ml respectively. For Experiments III, IV, VIII and IX this volume is 135.48 ml and for experiments V and VI the volume is 132.01 ml.

The fourth section is between valve 3 and the back pressure valve, with a volume of 46.73 ml, and contributes to the free volume of the set up.

During production with injection, the injected fluid first displaces the tubing volume on the production side. This volume is 84.03 ml in total. For example when CO_2 / flue gas is injected at a rate of 1ml/h, assuming that equilibrium was attained; it takes around 3.5 days to replace the gas. Since the pressure in the cell remains constant, it is assumed that the core produced at the speed of the injection. Thus the first 3 to 4 days of production data will have the information related to the void volume after the sample.
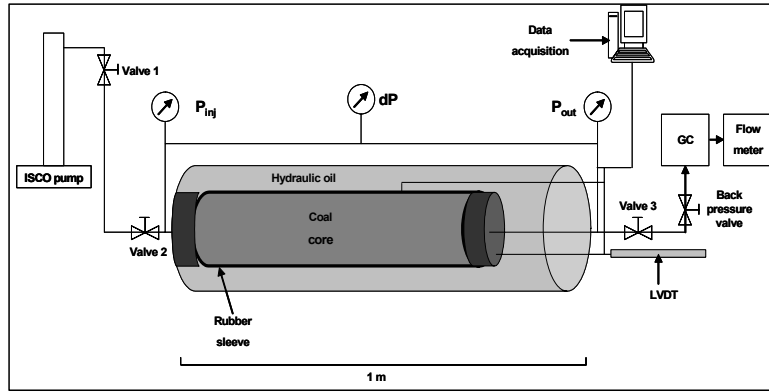
Fig. E-1 Schematic of the high pressure flow cell

Appendix F

Displacement of CH₄ by CO₂ in a tube

The aim of these experiments was to observe the mixing behaviour, while replacing methane by carbon dioxide in a tube. Knowledge on the mixing behaviour in a tube is required for correct interpretation of the flooding experiments. To determine the mixing behaviour in the tube, the composition of the produced gas was analyzed. Four experiments were performed: one experiment with both CH_4 and CO_2 in as a gas, and three experiments with CO_2 as a liquid phase and CH_4 as a gas. The mixing behaviour can be theoretically described in two extremities: piston-like displacement and perfect mixing. In piston-like displacement the diffusion is much slower than the displacement process. This behaviour would occur, if the displacing and displaced fluids are immiscible. A piston-like displacement is described by a step function, with the fractional composition as a function of the translated time. For a perfect mixing it has to showed that convective dispersion combines with transverse molecular diffusion in what is known as "Taylor Dispersion". Here the concentration is dispersed symmetrically about a plane that moves with the mean flow velocity and can be written for a step input (Carslaw and Jaeger, 1986),

$$c = c_0 + \frac{1}{2}(c_1 - c_0)\left\{erfc\left[\frac{x-ut}{2(\eta t)^{1/2}}\right] + \exp^{ux} erfc\left[\frac{x+ut}{2(\eta t)^{1/2}}\right]\right\}, \qquad \text{(F-1)}$$

where c is the concentration at distance x, c_0 the base concentration, c_1 the injected concentration, u the mean velocity of the flow, t the time and η the net longitudinal dispersivity. Horne and Rodriguez (1983) used a method similar to Taylor's to derive an expression for the net longitudinal dispersivity, η, for flow in a fracture.

$$\eta = \frac{2}{105}\frac{b^2 u^2}{D}, \qquad \text{(F-2)}$$

where b is the fracture half-width, u the mean flow velocity and D the coefficient of molecular diffusion. Fig. F-1 shows the fractional composition of the displaced and the displacing phase for both piston-like displacement and completely miscible displacement (perfect mixing). In the case of perfect mixing the diffusion process is much faster than the displacement process and the two components are completely miscible.

Methods

Fig. E-1 (Appendix E) shows the experimental setup used for the displacement experiments. All experiments were performed at room temperature. Between valve 2 and valve 3, the setup was replaced by a ¼" tubing. The volume of this tubing was 58 ml. At the start of

the experiment this tubing was filled with CH_4. Thereafter CO_2 was injected with a constant rate. The system was kept at a constant pressure with a backpressure valve. The composition of the produced gas was analyzed at constant time intervals with a micro gas chromatograph.

Results

Table F-1 displays the details of the different experiments. Fig. F-2 shows for Experiment A (low pressure) the measured compositions versus time. Fig. F-3 shows for Experiments B, C and D (high pressure) the measured compositions versus time. The three experiments agree within the experimental uncertainty, indicating that the specific experimental conditions have no discernible influence.

	Pressure [bar]	Time [hrs]	Injection rate [ml/hr]
Experiment A	~ 20	22.9	5
Experiment B	~ 80	13.7	10
Experiment C	~ 80	22.6	10
Experiment D	~ 80	22.9	10

Table F-1. Details of the displacement experiments

Experiment A (Fig. F-2) shows good agreement with the perfectly mixed displacement model. The initial deviation between model and experiment is that the diffusion apparently requires approximately 2 hours. The observed behaviour of Experiment B, C and D varies considerably from the suggested simple theoretical models. Piston-like displacement or perfect mixing does not describe the behaviour. Two phases in the tube, some CO_2 evaporates into the gaseous CH_4 phase, and some CH_4 dissolves into the liquid CO_2 phase. The observed behaviour suggests that the composition has three distinct regimes with time (Fig. F-3):

• Regime I is the production of the CH_4 by piston-like displacement with some addition of CO_2 by gas diffusion.

• Regime II is the diffusive displacement front with its two high diffusion flanks. An estimate shows that the diffusive front is around 5 cm in length.

• Regime III is the production of almost pure CO_2 with a little CH_4 added by diffusion.
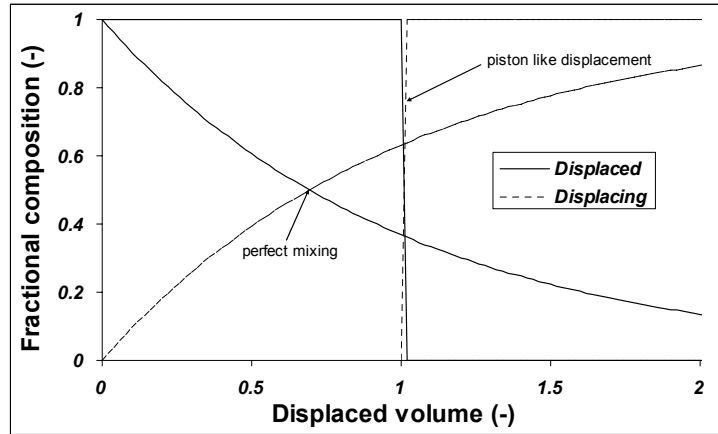
Fig. F-1 The fractional composition of the produced gas with displaced volume for perfect mixing and piston-like displacement (Appendix F).
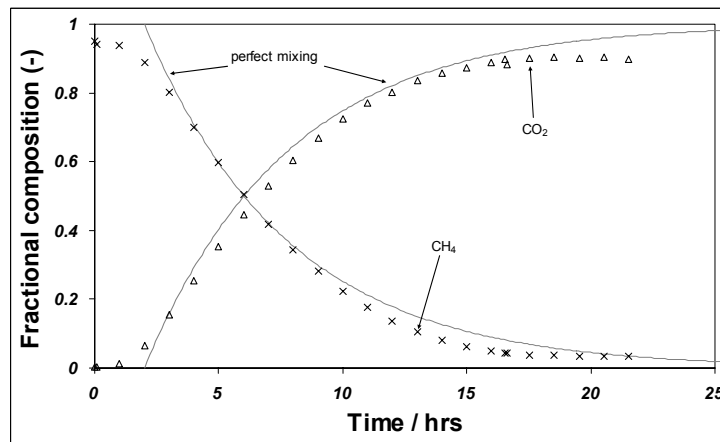

Fig. F-2 The fractional composition against time for Experiment A (~20bar, 5ml/hr)
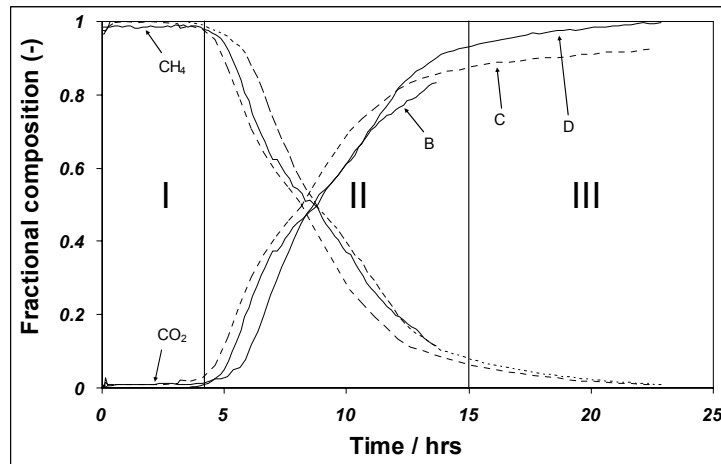
Fig. F-3 The fractional composition against time for Experiments B, C and D (~80bar, 10ml/hr)

Appendix G

Micro Gas Chromatography

The gas chromatograph used for gas analysis is an Agilent 3000 Micro GC with a TCD (Thermal Conductivity Detector). The micro GC is fitted with, a Molsieve column and a Poraplot U column. For data acquisition and analysis "Agilent Cerity^{TM}" was used. The carrier gas for all measurements was helium. Another option was argon. With argon CO could not be measured because it had approximately the same thermal conductivity as that of argon. On the molsieve column the following gases were measured; H$_2$, O$_2$, N$_2$, CH$_4$ and CO. On the Poraplot U column the following gases could be separated and measured; CO$_2$, ethylene, ethane, acetylene and sulphur dioxide. Both the above-mentioned columns were cleaned for at least 12 h on a weekly basis. The micro-GC was calibrated repeatedly with the Universal Gas Calibration Standard, whose composition is as shown in Table G-1.

The area measurement of the calibration sample was associated to an amount of moles by using the sample volume of the micro-GC (+/- 0.853 l) at ambient conditions (P=1bar, T =25°C) and the amount of mole in the standard gas of every gas species. The ratio of the amount of moles in the flue gas and the area, gives the reference factor. This reference factor multiplied with the area value for all later by the micro-GC measurements, gave the gas

Components	Concentration
Helium	0.10%
Neon	0.05%
Hydrogen	0.10%
Oxygen	0.05%
Nitrogen	0.10%
Methane	99.05%
Ethane	0.05%
Ethylene	0.05%
Carbon Dioxide	0.05%
Carbon Monoxide	0.10%
Acetylene	0.05%
Propane	0.05%
Methyl Acetylene	0.05%
n-Butane	0.05%
n-Hexane	0.05%
n-Heptane	0.05%

Table G-1. The Composition of the Universal Gas Calibration Standard

concentration in moles for that measurement. Every gas component had its own reference factor. This kind of calibration is referred to as a single level calibration. In order to develop the

most dependable calibration, the calibration procedure was kept strictly uniform in comparison to the measuring procedure. The micro-GC set points used is shown in Table G-2.

GC set-points	Molsieve	Poraplot U
Sample Inlet Temperature (°C)	60	60
Injector Temperature (°C)	60	60
Column Temperature (°C)	60	60
Sampling Time (s)	10	10
Inject Time (ms)	30	30
Run time (s)	240	240
Post Run Time (s)	120	60
Pressure equilibration time (s)	15	60
Column pressure (psi)	30.00	15.00
Post Run Pressure (psi)	40.00	25.00
Detector Filament	Enabled	Enabled
Detector Sensitivity	Standard	Standard
Detector Data Rate (Hz)	50	50
Baseline Offset (mV)	0	0
Back flush time (s)	n/a	n/a

Table G-2. The Selected micro-GC set-points as used for gas analysis

Every measurement was taken under the same conditions as from the calibration. The micro GC was connected directly to the flow out vent of the autoclave and thus samples were taken automatically from the flow stream. The actual volume analyzed is estimated to be +/- 0.853l. The volume used for each analysis was 2.39 +/- 0.1 ml. The volume used is much larger than the volume analyzed. An amount of gas was needed by the micro-GC to rinse the tubing, which connects the sample inlet to the analyzer. A sample response of the micro-GC is shown in Fig. G-1.
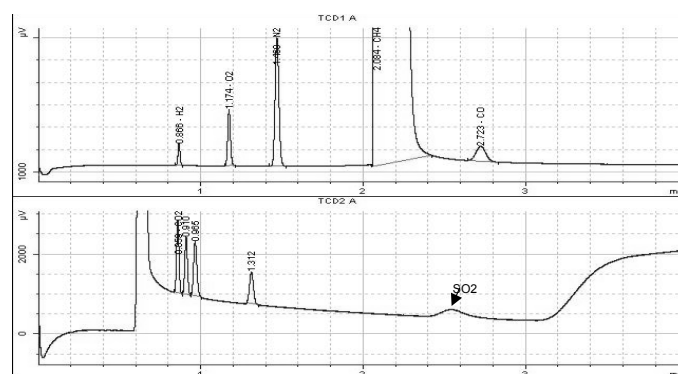

Fig. G-1 A typical sample response from the micro-GC, with time (min) on the x-axis and thermal conductivity (µV) on the y-axis.

Appendix H

Uniaxial strain reference state

An uniaxial strain reference state is based on the postulated boundary condition that strain is constrained at zero across all fixed vertical planes (Jaeger and Cook). Such a boundary condition leads to a stress state, which approximates newly deposited sediments in a sedimentary basin: the state of stress arising from uniaxial strain (Fig. H-1). Uniaxial strain is used as the model for the stress state describing the effect of overburden load on rocks at depth assuming these rocks develop fixed elastic properties at some point after deposition. σ_1 is the vertical stress arising from the weight of overburden. If rocks were unconfined in the horizontal direction the response to an addition of overburden weight would be a horizontal expansion. Because rocks are confined at depth in the crust, it is suggested that horizontal expansion is restricted by adjacent rock so that in the ideal case, $\varepsilon_2 = \varepsilon_3 = 0$. The assumption is that there is no displacement perpendicular to the σ_1- axis; stresses σ_2, σ_3 perpendicular to this axis are called into play to prevent displacement. This case arises in the simplest attempt to calculate stress below the earth's surface on the assumption that there are no lateral displacements. Upon initiation of tectonic processes, horizontal stresses can vary widely from those calculated using the uniaxial reference state. During erosion and removal of overburden weight, lack of contraction in the horizontal direction by uniaxial strain behavior also leads to large changes in horizontal stresses.

For the case of uniaxial strain, $\varepsilon_1 \neq 0$, $\varepsilon_2 = \varepsilon_3 = 0$, the equations of elasticity are written as,

$$\sigma_1 = (\lambda + 2\zeta)\varepsilon_1 \qquad\qquad \text{(H-1)}$$

$$\sigma_2 = \sigma_3 = \lambda\varepsilon_1 \qquad\qquad \text{(H-2)}$$

where λ and ζ are elastic properties of the rock, known as the Lame's constants. ζ is commonly known as the modulus of rigidity, the ratio of shear stress to simple shear strain. $\lambda + 2\zeta$ relates stress and strain in the same direction, and λ relates stress with strain in two perpendicular directions.

From Eqs. H-1 and H-2, the relationship between vertical ($S_v = \rho g z = \sigma_1$) and horizontal stresses ($S_H = S_h = \sigma_2 = \sigma_3$) are given in terms of the Poisson's ratio

$$S_H = S_h = \left[\frac{\upsilon}{(1-\upsilon)}\right] S_v = \left[\frac{\upsilon}{(1-\upsilon)}\right]\rho g z \qquad\qquad \text{(H-3)}$$

where ρ is the integrated density of the overburden, g is the gravitational acceleration, and z is the depth within the earth. Major deviations from this reference state may signal that the uniaxial strain model is not a particularly effective model for state of stress in the lithosphere. Assuming a $\upsilon = 0.2$, the $S_h = 0.25\ S_v$. This stress state is illustrated by the Mohr's circle in Fig. H-1.

A: $\quad \sigma_n = \dfrac{\sigma_1 + \sigma_3}{2} + \dfrac{\sigma_1 - \sigma_3}{2}\cos 2\theta$

B: $\quad \tau = \dfrac{\sigma_1 - \sigma_3}{2}\sin 2\theta$

C: The center of the Mohr's Circle - $\dfrac{\sigma_1 + \sigma_3}{2}$

D: The radius of the Mohr's Circle - $\dfrac{\sigma_1 - \sigma_3}{2}$
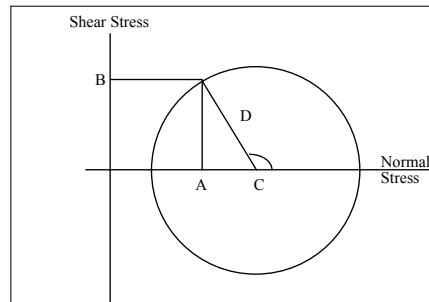
Fig. H-1 On the Mohr diagram, θ is represented by measuring 2θ counter clockwise from the maximum normal stress, σ_1. In general, θ will be approximately 60° so that the $\cos 2\theta$ will be a negative number. The significance of this is that the normal stress on active fault planes is less than the mean stress (i.e., A < C)

Bibliography

Alfrey, T., Gurnee, E. F. and Lloyd, W. G., "Diffusion in glassy Polymers", Journal of Polymer Sciences (C) 12, 249-261, 1966.

Ammosov, I.I., Eremin, I.V., "Fracturing in Coal", IZDAT Publishers, Office of Technical Services, Washington, DC, 109 pp, 1963.

Argon, A.S., Cohen, R.E., Patel, A.C., "A mechanistic model of case II diffusion of a diluent into a glassy polymer", Polymer 40, 6991-7012, 1999.

Arri, L. E., Morgan, W. D., Yee, D., Jeansonne, M. W., "Modelling coalbed CH$_4$ production with binary gas sorption" SPE Rocky Mountain Regional Meeting, Casper Wyoming, SPE 24363, 1992.

Arri, L. E., Yee, D., Morgan, W. D., Jeansonne, M. W., "Modelling coalbed methane production with binary gas sorption", SPE 24363, SPE Rocky Mountain Regional Meeting, Casper Wyoming, 1992.

Barrer, R. M., "Diffusivities in Glassy Polymers for the Dual Mode Sorption Model", Journal of Membrane Science, 18, 25-32, 1984.

Bear, J. and Corapcioglu, M. Y., "A mathematical model for consolidation in a theroelastic aquifer due to hot water injection or pumping", Water Resources Research., 17, 723 - 736, 1981.

Bertheux, W.B., "Enhaced Coalbed Methane Production by Carbon Dioxide Injection in Water Saturated Coal", Novem Technical Report, Contract no.222103/2008, 106 pp, 2000.

Bertheux, W., "Enhanced CBM production by CO$_2$-injection in water saturated coal: experiments, image analysis and simulations", M.Sc. Thesis, Delft University of Technology, The Netherlands, 2000.

Bird, R.B., Stewart, W.E., and Lightfoot, E.N., "Transport Phenomena", John Wiley & Sons 1960.

Bodily, D. M., Wann, J. P. and Kopp, V., "The Effect of Solvent Swelling on Coal Structure", Proc. Int. Conf. Coal Sciences, Vol. I, Tokyo, October, 1989.

Brooks, R.H., and Corey, A.T., "Properties of porous media affecting fluid flow", J.Irr. Drain. Div., Proc., Am. Soc. Civ. Eng., 61-88, 1966.

Busch, A., Gensterblum, Y., and Krooss, B. M., "CH$_4$ and CO$_2$ sorption and desorption measurements on dry Argonne premium coals: pure components and mixtures", International Journal of Coal Geology 55, 205-224, 2003.

Busch, A., Gensterblum Y., Krooss B.M., Littke, R., "Methane and carbon dioxide adsorption-diffusion experiments on coal: upscaling and modelling", International Journal of Coal Geology 60, 151-168, 2004.

Carslaw, H.S., and Jaeger, J. C., "Conduction of Heat in Solids", Oxford University Press, USA, 1986

Chaback, J. J., Morgan, W. D., and Yee, D., "Sorption of N$_2$, CH$_4$, CO$_2$ and their mixtures on bituminous coals at in-situ conditions", Fluid Phase Equilibria 117, 289-296, 1996.

Chikatamarla, L, Xiaojun, CUI and Bustin, R.M., "Implications of volumetric swelling / shrinkage of coal in sequestration of acid gases" International Coalbed Methane Symposium, May 3-7, Alabama, USA, 2004.

Clarkson, C. R, Bustin, R. M., "Binary gas adsorption/desorption isotherms: effect of moisture and coal composition upon CO$_2$ selectivity over CH$_4$", International Journal of Coal Geology 42, 241-271, 2000.

Clarkson, C.R., Bustin, R.M., "The Effect of Pore Structure and Gas Pressure Upon the Transport Properties of Coal: A Laboratory and Modeling Study. 2. Adsorption Rate Modeling", Fuel 78(11), 1345, 1999.

Clarkson, C. R., Bustin, R. M., and Levy, J. H., "Application of the mono/multilayer and adsorption potential theories to coalbed CH$_4$ adsorption isotherms at elevated temperature and pressure", Carbon 35, 1689-1705, 1997.

Close, J.C., Mavor, M.J., "Influence of coal composition and rank on fracture development in Fruitland coal gas reservoirs of San Juan Basin", In: Schwochow, S., Murray, D.K., Fahy, M.F. (Eds.)., Coalbed Methane of Western North America, Rk. Mt. Assoc. Geol., Field Conf., 109—121, 1991.

Crank, R.H*.,* "Diffusion", J. Irr. Drain. Div., Proc., Am. Soc. Civ. Eng., 61-88, 1966.

Crank, C.J., "The mathematics of diffusion", Oxford University Press, Oxford, 1976.

Cui, X., Bustin, R.M., Dipple, G., "Selective Transport of CO$_2$, CH$_4$, and N$_2$ in Coals: insights from Modeling of Experimental Gas Adsorption Data", Fuel 83:293-303, 2003.

Dake, I.P., "Fundamentals of Reservoir Engineering", Elsevier Science Publishers, Amsterdam, 1978.

DeGance, A. E., Morgan, W. D., and Yee, D., "High pressure adsorption of CH$_4$, N$_2$ and CO$_2$ on coal substrates", Fluid Phase Equilibria 82, 215-224, 1993.

De Haan, M.F.E., "Enhanced coalbed methane production by carbondioxide injection; theory, experiments and simulations" M.Sc. Thesis, Student number: 292843, TUDelft, 1998

Diamond, L. W., Akinfiev, N. N., "Solubility of CO$_2$ in water from - 1.5 to 100^0 C and from 0.1 to   100 MPa : evaluation of literature data and thermodynamic modeling", Fluid Phase Equilibria 208, 265-290, 2003.

Dullien, F.A.L., "Porous media; Fluid Transport and Pore Structure", Academic Press Inc. San Diego, USA, 1992.

Durucan, S., Edwards, J. S., "The Effects of stress and fracturing a permeability of coal", Mining Science and Technology, Vol. 3, 205 -- 216, 1986.

Durning, C., "Differential sorption in visco-elastic fluids", Journal of Polymer Sciences (B) 23, 1831—1855, 1985.

Gall, T.P., Kramer, E.J., "Diffusion of deuterated toluene in polystyrene", Polymer 32, 265-271, 1991.

George, J.D, Barkat, M.A., "The change in effective stress associated with shrinkage from gas desorption in coal", International Journal of Coal Geology, 45, 105-113, 2001.

Gilman, A., Beckie, R., "Flow of Coal-Bed Methane to a Gallery", Transport in Porous Media, 41, 1 – 16", 2000.

Govindjee, S., Simo, J.C., "Coupled stress-diffusion: Case II", J. Mech. Phys. Solids 41, 863-887, 1993.

Gray, I., "Reservoir Engineering in coal Seams: Part 1-The physical process of gas storage and movement in coal seams", paper SPE 12514, 1987.

Greaves, K.H., Owen, L.B., McLennan, J.D., "Multi-component gas adsorption--desorption behavior of coal", Proc. of the 1993 Int. Coalbed CH_4 Symp., Tuscaloosa, AL, pp. 197—205, 1993.

Green, T., Kovac, J., Brenner, D., Larsen, J.W., "The Macromolecular Structure of Coals", Academic Press, 199-282, 1982.

Hall, F. E., Chunhe, Z., Gasem, K. A. M., Robinson, R. L and Yee, D., "Adsorption of pure CH_4, N_2, and CO_2 and their binary mixtures on wet Fruitland coal", Eastern Regional Conference and Exhibition, Charleston, SPE 29194, 1994.

Harpalani, S., Zhao, X., "An investigation of the effect of gas desorption on coal permeability formation", Proc. Coalbed Methane Symposium, Tuscaloosa, Alabama, 57-64, 1989.

Harpalani, S., Pariti, U.M., "Study of coal sorption isotherms using a multicomponent gas mixture", Proc. of the 1993 Int. Coalbed CH_4 Symp., Tuscaloosa, AL, pp. 151—160, 1993.

Harpalani, S., Schranfnagel, R., "Shrinkage of coal matrix with release of gas and its impact on permeability of coal", *Fuel*, 69, 551 -- 556, 1990.

Harpalani, S., Chen, G., "Effect of gas production on porosity and permeability of coal", In: Beamish, B. B., Gamson, P. D. (Eds.), Symposium on Coalbed Methane, Townsville, Australia, 67, 1992.

Harpalani, S., Chen, G., "Influence of gas production induced volumetric strain on permeability of coal", *Geotech. Geol. Eng.,* 15, 303 -- 325, 1997.

Harpalani, S. & Chen, G., "Estimation of changes in fracture porosity of coal with Gas Emission", *Fuel*, 74, 10, 1491, 1995.

Harpalani, S., Schranfnagel, R., "Shrinkage of coal matrix with release of gas and its impact on permeability of coal", Fuel, 69, 551 -- 556, 1990.

Harpalani, S., Chen, G., "Effect of gas production on porosity and permeability of coal", In: Beamish, B. B., Gamson, P. D. (Eds.), Symposium on Coalbed Methane, Townsville, Australia 4, 67, 1992*.*

Harpalani, S., Chen, G., "Influence of gas production induced volumetric strain on permeability of coal", Geotech. Geol. Eng*.,* 15, 303 -- 325, 1997.

Harpalani, S. & Chen, G., "Estimation of changes in fracture porosity of coal with Gas Emission:*,* Fuel, 74, 10, 1491, 1995.

Holman, J. P., "Experimental Methods for Engineers", 6th Edition McGraw - Hill Inc, 1994.

Horne, R.N. and Rodriguez, F., "Dispersion in Tracer Flow in Fractured Geothermal Systems", Geoph. Res. Let. , Vol. 10, no. 4, 289-292, 1983.

Hsieh, S. T. and Duda, L. J., "Probing coal structure with organic vapour sorption", Fuel 66, 170-178, 1987.

Hui, C.-Y., Wu, K.-C., Lasky, R. C. and Kramer, E. J., "Case-II diffusion in polymers. I. Transient swelling. Journal of Applied Physics 61, 5129-5136, 1987.

Hui, C.-Y., Wu, K.-C., Lasky, R. C. and Kramer, E. J., "Case-II diffusion in polymers. II. Steady-state front motion", Journal of Applied Physics 61, 5137-5149, 1987.

IEA Greenhouse Gas R&D Programme: Information Sheets, 2004

IEA Special Report on Carbon Dioxide Capture and Storage, Final Draft, Oct. 2005

IPCC, 2005: Special report on Carbon Dioxide Capture and Storage, UNFCCC, 2005

Jou, D., Casas-Vazquez, J., Lebon, G., "Extended Irreversible Thermodynamics", Springer-Verlag, Heidelberg, 2001.

Karacan, C. O., "Heterogeneous Sorption and Swelling in a Confined and Stressed Coal during CO_2 Injection", Energy & Fuels 17, 1595-1608, 2003.

Karacan, C.Ö., Okandan, E., "Fracture / cleat analysis of coals from Zonguldak Basin (northwestern Turkey) relative to the potential of coalbed methane production", International Journal of Coal Geology 44, 109—125, 2000.

Keller, A., "High resolution, non-destructive measurement and characterization of fracture apertures", International Journal of Rock Mechanics and Minning Sciences 35, 1037-1050, 1998

Kendall, P.E., Briggs, H., "The formation of rock joints and the cleat of coal", Proc. R. Soc. Edinburgh 53, 164—187, 1933.

Koros, W. J., "Model for Sorption of Mixed Gases in Glassy Polymers", Journal of Polymer Science: Polymer Physics 18, 981-989, 1980.

Krooss, B. M., van Bergen, F., Gensterblum, Y., Siemons, N., Pagnier, H. J. M. and David, P., "High-pressure CH_4 and CO_2 adsorption on dry and moisture-equilibrated Pennsylvanian coals", International Journal of Coal Geology 51, 69 – 92, 2002.

Landau, L.D., Lifshitz, E. M., "Fluid Mechanics", Pergamon Press. Oxford, 1975.

Lasky, R.C., Kramer, E.J., Hui, C-Y., "The initial stages of Case II diffusion at low penetrant activities", Polymer 29, 673-679, 1988.

Larsen, J. W., "The effects of dissolved CO_2 on coal structure and properties", International Journal of Coal Geology, 57, 63-70, 2004.

Larsen, J.W., Green, T.K., Choudhury, P., Kuemmerle, E.W., "The effect of reagent access on the reactivity of coals, in coal structure", Advances in chemistry series 192, American Chemical Society, Washington, 1981.

Larsen, J.W., Kovac, J., "Polymer structure of bituminous coals", ACS Symp. Series 71, 36-49, 1978.

Laubach, S.E., Marrett, R.A., Olson, J.E., Scott, R.A., "Characteristics and origins of cleat: a review", International Journal of Coal Geology 35, 175—207, 1998.

Law, B.E., "The relation between coal rank and cleat spacing: implications for the prediction of permeability in coal", Proc. Int. Coalbed Methane Symp., II, 435—442, 1993.

Law, B.E., and Rice, D., "Hydrocarbons from coal", AAPG Studies in Geology 38, 1993.

Levine, J.R., "Model study of the influence of matrix shrinkage on absolute permeability of coal bed reservoirs", Coalbed Methane and Coal Geology, Geologic Society Special Publication, 109, 197-212, 1996.

Levy, J., Day, S.J., Killingley, J.S., "CH$_4$ capacity of Bowen Basin coals related to coal properties", Fuel 74, 1 – 7, 1997.

Lucht, L. M. and Peppas, N. A., "New Approaches in Coal Chemistry", ACS Symposium Series, 43, 169, 1981.

Marchesin, D., Bruining, J., "Diffusion mechanisms in steam drive recovery of oil", European Conference on the Mathematics of Oil Recovery X, Amsterdam, Sept. 2006.

Martin-Martinez, J. M., Torregrosa-Marcia, R., and Mittelmeijer-Hazeleger, M. C., "Mechanisms of adsorption of CO$_2$ in the micropores of activated anthracite", Fuel 74, 111-114, 1995.

Mavor, M. J., Gunter, W. D., "Secondary Porosity and Permeability of Coal vs. Gas Composition and Pressure", SPE 90255, SPE Annual Technical Conference and Exhibition, Houston, Texas, 2004.

Mavor, M.J., Owen, L.B., Pratt, T.J., "Measurement and evaluation of coal sorption isotherm data", SPE 20728, SPE 65th Annual Technical Conference and Exhibition, New Orleans, Louisiana, September 23—26, 1990.

Mazumder, S., Bruining. J., Wolf, K. H. A. A., "Swelling and Anomalous Diffusion Mechanisms of CO$_2$ in coal", 0601, Proceedings of The International Coalbed Methane Symposium, Tuscaloosa, U.S.A, (2006).

Mazumder, S., Willem-Jan Plug., & J. Bruining., "Capillary Pressure and Wettability Behavior of Coal – Water – Carbon dioxide System", SPE 84339, SPE Annual Technical Conference and Exhibition held in Denver, Colorado, U.S.A., 5 – 8 October 2003.

Mazumder, S., Willem-Jan Plug., & J. Bruining., "Capillary Pressure and Wettability Behaviour of Coal – Water – Carbon dioxide System", Proceedings of the International Congress on Carboniferous and Permian Stratigraphy, MS ICCP-XV-5, 2005.

Mazumder, S., Wolf, K-H. A. A., & van Hemert, P., "Laboratory experiments on environmental friendly means to improve coalbed methane production by carbon dioxide / flue gas injection" Accepted for "Transport in Porous Media", submitted 22nd February, 2006.

Mazumder, S., K-H. A. A Wolf and P. van Hemert,. "CO$_2$ and Flue-Gas Coreflood Experiments for Enhanced Coalbed Methane" Accepted for "SPE Journal", submitted 22nd February, 2006.

Mazumder, S., R. Ephraim, K-H. A. A Wolf and Elewaut, K.,. "Application of X-Ray Computed Tomography for analysing cleat spacing and cleat aperture in coal samples", International Journal of Coal Geology 68, 205 - 222, 2006.

Mazumder, S., P. van Hemert, A. Busch, K-H. A. A Wolf and P Tejera Cuesta.,. "Flue gas and pure CO$_2$ sorption properties of coal: A comparative study", International Journal of Coal Geology 67, 267 - 279, 2005.

Mazumder, S., Siemons, N., and K-H. A. A Wolf.,. "Differential swelling and permeability change of coal in response to CO$_2$ injection for ECBM", In Press for SPE Journal, SPE-98475-USMS, submitted 7th June, 2005.

Mazumder, S., Karnik, A., and K-H. A. A Wolf.,. "Swelling of Coal in Response to CO$_2$ Sequestration foe ECBM and its Effect on Fracture Permeability", SPE Journal, SPE-97754-RMS, September, 2006.

Mazumder, S., P. van Hemert, J. Bruining, K-H. A. A Wolf., & Drabe, K. "Insitu CO$_2$ - Coal reactions in view of carbon dioxide storage in deep unminable coal seams", Fuel 85, 1904 - 1912, 2006.

Mazumder, S., K.H.A.A. Wolf; "An overview of the potentials and prospects of coalbed methane exploration and exploitation in the permo-carboniferous coal measures of the Barakar Formation, the Jharia basin, India" Geologica Belgica, 7/3-4, 147 – 156, 2004.

Mazumder, S., vanHemert, P., Wolf, K.H.A.A., & Bruining, J., "Flue gas – CH$_4$ – H$_2$O chemistry in coal", Final Report, Contract nr 4600000549, C25B15, 2004.

Mazumder, S. & Wolf, K-H A.A., "CO$_2$ Injection for Enhanced CH$_4$ Production from Coal Seams: Laboratory Experiments and Simulations", 329, Proceedings of Petrotech, New Delhi, 2003.

Mazumder, S., Hemert. P. Van., Bruining. J., & Wolf, K-H A.A., "A Preliminary Numerical Model of CO$_2$ Sequestration in Coal for Improved Coalbed Methane Production", 0331, Proceedings of The International Coalbed Methane Symposium, Tuscaloosa, U.S.A, 2003.

McKee, C. R., Bumb, A. C., and Koenig, R. A., "Stress Dependent Permeability and porosity of coal. Proc.", International Coalbed Methane Symposium, Tuscaloosa, Alabama, 183, 1987.

Myers, A. L., Prausnitz, J. M., "Thermodynamics of mixed-gas adsorption", AIChE Journal 11, 121-127, 1965.

Nishioka, M., "The associated molecular nature of bituminous coal", Fuel 71, 941-948, 1992.

Nishioka, M., Larsen, J.W., "Association of aromatic structures in coals", Energy and Fuels 4, 100-106, 1990.

Ozdemir, E., Morsi, B. I., and Schroeder, K., "CO$_2$ Adsorption Capacity of Argonne Premium Coals", Fuel 83, 1085-1094, 2004.

Palmer, I, Mansoori, J., "How permeability depends on stress and pore pressure in coalbeds: A new Model", SPE 36737, Oct., 1996.

Pekot, L.J., & Reeves, S.R., "Modelling coal matrix shrinkage and differential swelling with CO$_2$ Injection for enhanced coalbed methane recovery and carbon sequestration applications", Tropical Report, Advanced resources International, Texas, Nov., 2002.

Peng, D. Y. and Robinson, D. B., "A new two-constant equation of state", Ind. Eng. Chem. Fundam. 15, 59-64, 1976.

Peppas, N. A., Ritger, P. L., "Transport of penetrants in the macromolecular structure of coals", Fuel, 66, 815-826, 1987.

Peterlin, A., "Plastic deformation of crystalline polymers", Polymer Engineering and Science 17, 183-193, 1977.

Prusty, B. K., Harpalani, S., "A laboratory study of methane / CO$_2$ exchange in an enhanced CBM recovery Scenario", International Coalbed Methane Symposium, May 3-7, Alabama, USA, 2004.

Puri, R., Yee, D., "Enhanced coalbed methane recovery", SPE paper 20732, SPE 65th Annual Technical Conference and Exhibition, New Orleans, Louisiana, 1990.

Reeves, S. R. and Pekot, L., "Advanced Reservoir Modeling In Desorption-Controlled Reservoirs", SPE 71090, SPE Rocky Mountain Petroleum Technology Conference, Colorado, 2001.

Reeves, S. R., Davis, D. W. and Oudinot, A. Y., "A Technical and Economic Sensitivity study of Enhanced Coalbed Methane Recovery and Carbon Sequestration in Coal", *Topical Report* 2004, Advanced Resources International Inc., Houston, TX

Reiss, L. H., "The Reservoir Engineering Aspects of Fractured Formations", Editions Technip, France., 1980.

Reucroft, P. J. & Patel, H., "Gas induced swelling in Coal", Fuel, 65, 816 – 820, 1986.

Reznik, A. A., Singh, P. K., Foley, W. L., "An Analysis of the Effect of CO$_2$ Injection on the Recovery of In-Situ Methane From Bituminous Coal: An Experimental Simulation" SPE 10822, Oct., 1984.

Rice, D., "Coalbed Methane--An Untapped Energy Resource and an Environmental Concern", Energy Resource Surveys Program, U.S. Geological Survey, USGS Fact Sheet FS-019-97,1997

Ritger, P. L. and Peppas, N. A., "Transport of penetrants in the macromolecular structure of coals", Fuel 66, 815-826, 1987.

Robertson, E. P., Christiansen, R. L., "Modelling Permeability in Coal using Sorption-Induced Strain Data", SPE 97068, SPE Annual Technical Conference and Exhibition, Dallas, Texas, 2005.

Sawyer, W. K., Paul, G. W., and Schraufnagel, R. A., "Development and Application of a 3D Coalbed Simulator", Paper CIM / SPE, Proc. Petroleum Society CIM, Calgary, 90 – 119, 1990.

Schobert, H.H., „The Geochemistry of Coal", Journal of Chemical Education 66, 290-293, 1989.

Seidle, J.P., et al., "Experimental Measurement of Coal Matrix Shrinkage due to gas desorption and implications for cleat permeability increases", paper SPE 30010, 1995.

Seidle, J.P., et al., "Application of Matchstick Geometry To Stress Dependent Permeability in Coals", paper SPE 24361, 1992.

Shi, J.Q & Durucan, S., "Changes in permeability of coalbeds during primary recovery -- Part 2: Model Validation and field application", International Coalbed Methane Symposium, May 5-9, Alabama, USA, 2003.

Shi, Ji-Quan., Mazumder, S., Wolf, K-H. A. A., & Durucan, S., "Competitive Methane Desorption by Supercritical CO$_2$ Injection in Coal", Accepted for "Transport in Porous Media", submitted 22nd May, 2006.

Shi, J.Q. and Durucan, S., "A Bidisperse Pore Diffusion Model for Methane Displacement Desorption in Coal by CO$_2$ Injection," Fuel 82:1219, 2003.

Soave, G., "Equilibrium Constants from a Modified Redlich-Kwong Equation of State", Chem. Eng. Sci. 27, 1197-1203, 1972.

Somerton, W., et al., "Effect of stress on permeability of coal", International Journal of Rock Mechanics and Mining Sciences, vol. 12, 129 -- 145, 1975.

Span, R., Lemmon, E.W., Jacobsen, R.T, Wagner, W., Yokozeki, A., "A reference equation of state for the thermodynamic properties of N$_2$ for temperatures from 63.151 to 1000 K and pressures to 2200 Mpa", J. Phys. Chem. Ref. Data 29, 1361-1433, 2000.

Stach, E., Mackowski, M-Th., Teichmuller, M., Taylor, G.H., Chandra, D., Teichmuller, R., "Coal Petrology", Gebruder Borbtraeger, Berlin, 1982.

Stevenson, M.D., Pinczewski, W.V., Somers, M.L., Bagio, S.E., "Adsorption / desorption of multicomponent gas mixtures at in-seam conditions", SPE paper 23026, Presented at the SPE Asia-Pacific Conference, Perth, Western Australia, 741—755, 1991.

Stach, E., Mackowsky, M.Th., Teichmüller, M., Taylor, G.H., Chandra, D., Teichmüller, R., "Stach's Textbook of Coal Petrology", Gebrüder Borntraeger, Berlin, 535 pp, 1982.

Taylor, J. R., "An Introduction to Error Analysis", 2nd Edition University Science Books, Sausalito, California, 1997.

Thomas, N., Windle, A., "A theory of case II diffusion", Polymer 23, 529—542, 1982.

Ting, F.T.C., "Origin and spacing of cleats in coalbeds", Journal of Pressure Vessel Technical Transactions ASME 99, 624—626, 1997.

Tremain, C.M., Laubach, S.E., Whitehead, N.H., "Coal fracture cleat patterns in Upper Cretaceous Fruitland formation, San Juan Basin, Colorado and New Mexico: implications for exploration and development", In: Schwochow, S., Murray, D.K., Fahy, M.F. (Eds.)., Coalbed Methane of Western North America. Rocky Mtn. Assoc. Geol, 49—59, 1991.

Vandersteen, K., Busselen, B., Van Den Abeele., Carmeliet, J., "Quantitative characterization of fracture apertures using microfocus computed tomography", In: Mees, F., Swennen, R., Van Geet, M., Jacobs, P. (Eds.)., "Applications of X-ray Computed Tomography in the Geosciences", Geol. Soc. Spec. Publ., 215, 61—68, 2003.

Van Geet, M., "Optimization of microfocus X-ray computer tomography for geological research with special emphasis on coal components (macerals) and fractures (cleats) characterization", PhD thesis, K. U. Leuven, Belgium, 2001.

van Krevelen, D.W., "Coal", Elsevier Publishing Co., Amsterdam, 1961.

Verhelst, F., Vervoort, A., De Bosscher, PH., Marchal, G., "X-ray computerized tomography: determination of heterogeneities in rock samples", Proceedings of the 8th International Congress on Rock Mechanics. Balkema, Rotterdam, 105-108, 1995.

Vrentas, J.S., Jarzebski, C.M., Duda, J.L., "A Deborah number for diffusion in polymer--solvent systems", AIChE J 21, 894—901, 1975.

Vrentas, J. S., Duda, J. L., "Diffusion in polymer-solvent systems. III. Construction of Deborah number diagrams", J. Polym. Sci. Polym. Phys. Ed. 15, 441-453, 1977.

Weast, R.C., "*CRC* Handbook of Chemistry and Physics", 58th edition, CRC Press, Inc. 1977

Whitehurst, D.D., "A Primer on the Chemistry and Constitution of coal", ACS Symp. Series 71, 1978.

Willem-Jan Plug., Mazumder, S. & J. Bruining., "Capillary Pressure and Wettability Behaviour in the Coal – Water – Carbon dioxide System at High Pressures", 0606, Proceedings of The International Coalbed Methane Symposium, Tuscaloosa, U.S.A, (2006).

World Energy Assessment, 2004: Overview: 2004 Update. J. Goldemberg and T.B. Johansson (eds), United Nations Development Programme, New York

Wolf, K.H.A.A., Bruining, J., Ephraim, R., Mazumder, S., & Siemons, N., "Reduction of CO$_2$ emission by means of CO$_2$ storage in coal seams in the Silesian Coal Basin of Poland", CONFIDENTIAL Report to RECOPOL, Contract nr ENKCT-2001-00539, C24B15, 2005

Wolf, K.H.A.A., Bruining, J., Siemons, N., & Mazumder, S., "Development of advanced reservoir Characterisation and simulation tools for improved coalbed methane recovery", ICBM-Project, Contract nr ENK6-2000-00095, Project nr. NNE5-1999-20174. Final Report, C25B07, 2005.

Wolf, K.H.A.A., J. Bruining, S. Mazumder, P. vanHemert and Drabe, K., "Innovative use of Dutch coals: CO$_2$ injection and storage, combined with CH$_4$ – production: In-situ CO$_2$ reactions" Novem Contract 0234-01-01-50-0002, Final Report, C25B14, 2004.

Wolf, K. H. A. A., Ephraim, R., Siemons, N., Bosie-Codreanu, D., "Analysing the cleat angle in coal seams using drilling cuttings and image analysis techniques", Geologica Belgica 7, 3-4, 2004.

Wolf, K.H.A.A., Hijman, R., Barzandji, O., Bruining, J., "Laboratory experiments and simulations on the environmentally friendly improvement of CBM-production by carbon dioxide injection", Proc. Int. Coalbed Methane Symp., Tuscaloosa, Alabama, 279-290,1999.

Wolf K.H.A.A., Hijman, R., Barzandji, O., Bruining, J., "Feasibility study on CO$_2$-sequestration and CBM-production", Novem Report on modeling work, economics and related lab experiments, Contr.nr. 234130/9001, TU Delft, Delft, 1999.

Wolf K.H.A.A., Barzandji, O., Bertheux, W., Bruining, J., "CO$_2$-sequestration in The Netherlands. CO$_2$-injection and CH$_4$-production as related to the Dutch situation: Laboratory experiments and field simulation", Proc. 5th Int. Conf. on Greenhouse Gas Control Technologies, Cairns, Australia, 1-6, 2000.

Zutshi, A & Harpalani, S., "Matrix Swelling with CO$_2$ Injection in CBM Reservoirs and its Impact on Permeability of Coal", International Coalbed Methane Symposium, May 3-7, Alabama, USA, 2004.

Summary

The mechanisms, by which the coal seams sorb, retain and store gases needs, to be understood. The results presented in this thesis give an insight into the dynamics of CO$_2$ and other flue gas components in coal that are related to operation feasibility of ECBM projects. The main issues relate to the permeability behavior and the flue gas/ CO$_2$ sorption.

The cleat network in coal seams provides the principal source of permeability for fluid flow. Understanding and predicting the cleat attributes is necessary for creating a flow model. A methodology for determining the cleat spacing is proposed, which uses a Gaussian point spread function. Using this method, the cleat apertures were measured with the aid of CT images. In addition, a method to determine the cleat orientation and cleat spacing distribution from CT scans of coal samples was developed. Regarding the cleat orientation and relevant cleat spacing, we observe configuration dependent spacing distributions, which can be used for fracture modeling in coal specimens, up to one cubic foot in size. The method combines these two different techniques, and gives a better understanding of the cleat framework. Up-scaling to seam size was not investigated. This combined procedure also proves that it is possible to distinguish the face cleat, the butt cleat and the bedding system. However, no measurement can be exact in the sub-pixel level, including the method described above. At best, choosing the right method can reduce the error in the approximations.

Flue gas and pure CO$_2$ sorption experiments were carried out to compare the sorption capacity of a single and multi-component gas. CO$_2$ compared to CH$_4$ is the most preferred adsorbed component in both the wet and dry experiments: CO$_2$ shows the largest decrease in concentration at the end of the adsorption experiment (increasing pressure steps) and shows the largest increase (preferentially desorbed) at the end of the extraction steps (decreasing pressure steps). The preference decreases with the addition of water to the coal. Consequently, a considerable amount of CO$_2$ can be stripped off the flue gas by making it sorb onto coal at high pressures. For the injection of flue gas on an industrial scale, it means that coal may be successfully used to filter the CO$_2$ out. Large volumes of flue gas can be directly sequestered in coal. Enhancement of CH$_4$ production via flue gas adsorption was not established in these experiments. For the first time density measurements of a flue gas has been successfully performed, suggesting a close resemblance to the pure N$_2$ behavior.

As part of this thesis an experimental study was conducted to estimate the porosity and permeability impairment caused by the volumetric swelling of coal due to the injection of CO$_2$. This permeability decrease can result in serious injectivity problems near the wellbore. Swelling of coal is rank dependent and a major conclusion from the results on swelling behavior is the comparison of the coal structure with that of glassy polymers. From the experimental work, it

can be concluded that on a unit concentration basis, absorption of CO$_2$ causes excess strain when compared to CH$_4$. This effect has been named as differential swelling. An Extended Langmuir type formulation coupled with Palmer-Mansoori equation for uniaxial strain conditions were used to model the experiments, resulting in an average match. Plasticization of coal may be a possible reason. Moreover models used in commercial simulators based on uniaxial strain reservoir conditions, might not work under complex stress regimes.

The effect of plasticization, on diffusion processes in coal has been modeled. A theory that accounts for anomalous diffusion, with CO$_2$ and swelling of bituminous coal, is introduced. The theory explains the process in terms of the contrast in the diffusion coefficients and the viscosity of the original coal. Experiments have been conducted to support this theory by estimating diffusion coefficients, which show anomalous diffusion process. The model has been derived from conservation law, combined with mass transport both due to concentration and stress gradients. Moreover, the derivation involves a stress that is proportional to the mass flux gradient, which is typical for extended non-equilibrium thermodynamics. Parameter estimation for the model corresponding to the diffusion of CO$_2$ in coal has been done and sharp concentration fronts in line with the theory of Case II diffusion has been observed in the simulation results.

Core flooding experiments were conducted with CO$_2$, N$_2$ and flue gas as an injectant under reservoir conditions. Conditions of these experiments were varied from sub-critical to super-critical and from relatively wet to relatively dry cores. Under dry conditions, the incremental methane produced is likely due to the preferential desorption of methane in the presence of CO$_2$. Consequently, the dry experiments show that the amount of desorbed CH$_4$ is marginally greater than desorption resulting from reduction in partial pressures of methane. The wet experiments failed to produce any sorbed CH$_4$ from the coal. The water acted as a barrier and probably hindered the exchange process by either blocking the sites or by reducing the diffusivities by at least two orders of magnitude. From the experiments it is clear, that at a pore level CO$_2$ is adsorbed better, when compared to CH$_4$. Comparing the CO$_2$ flooding experiments with the flue gas experiments under similar conditions, the latter show lower sweep efficiencies. There is hardly any production of adsorbed methane from the coal. The flue gas experiments, with N$_2$ as the main constituent can be considered as a N$_2$ stripping experiment. Nitrogen is a natural choice for ECBM due to its availability and the fact that it tends to yield incremental recovery response relatively rapidly. Nitrogen advances more rapidly and displays a more dispersed front, in comparison to CO$_2$ where the displacement is more piston like under super-critical conditions. A numerical model was developed to understand the physical process on a single cleat scale. The results of the numerical model show the effect of the effluent on the exchange process.

Samenvatting

Het is belangrijk dat de mechanismen waarmee steenkool gas sorbeert, vasthoudt en opslaat, worden begrepen. De resultaten in dit proefschrift geven inzicht in de dynamiek en rookgas componenten in kool. Deze zijn van belang voor de operationele mogelijkheden van ECBM projecten. De belangrijkste onderwerpen hebben te maken met het permeabiliteitsgedrag en de rookgas/ CO$_2$ sorptie van steenkool.

Het netwerk van scheuren (cleats) geeft de meest belangrijke permeabiliteit voor stroming van gassen en vloeistof door steenkool. Het is dus noodzakelijk om de eigenschappen van deze scheursystemen te begrijpen en hun bijdrage te kunnen voorspellen bij het maken van een goed stromingsmodel. Hiervoor wordt een methodiek voorgesteld, die voor de bepaling van de afstand tussen cleats gebruik maakt van de Gaussische punt spreiding functie. De grootte van de opening van de scheuren werd bepaald met behulp van CT scans. Daarnaast werd er een methode ontwikkeld om met dezelfde CT-scans de oriëntatie van en de afstand tussen de scheuren te meten. Configuratie afhankelijke ruimtelijke verdelingen zijn waargenomen voor zowel de oriëntatie van de scheuren als de afstand tussen de scheuren. Deze resultaten kunnen worden gebruikt voor het modelleren van breuken tot 1 m schaalgrootte, met behulp van de twee verschillende technieken en geeft een beter begrip van het netwerk van scheuren. Het opschalen van dit model naar steenkool laag grootte is niet onderzocht. De gecombineerde procedure bewijst ook dat het mogelijk is de 'face cleat', 'butt cleat' en de gelaagdheid te onderscheiden. Echter, metingen op subpixelgrootte zijn nooit exact, ook deze niet. Deze methode kan in het gunstigste geval de fouten in de benaderingen verkleinen.

Experimenten met rookgas en pure CO$_2$ zijn uitgevoerd om de sorptie capaciteit van enkel- en multi-component gas te bepalen. In vergelijking met CH$_4$ is CO$_2$, in zowel natte als droge experimenten, de meest geadsorbeerde component en CH$_4$ wordt geproduceerd. In dit soort sorptie-experimenetn toont CO$_2$ de grootste vermindering in concentratie aan het eind van adsorptie experimenten en de grootste toename aan het eind van de extratie stappen (preferente desorptie). Deze preferentie neemt af als een water-gesatureerde steenkool wordt gebruikt. Dus een behoorlijke hoeveelheid CO$_2$ kan worden verwijderd uit het schoorsteengas door het te laten sorberen aan steenkool bij hoge drukken. Dus injectie van rookgas in steenkoollagen kan worden gebruikt om op industriële schaal CO$_2$ te filteren en achter te houden en grote hoeveelheden rookgas direct op te slaan in steenkool. In vergelijkbare laboratorium experimenten met behulp van rookgas adsorptie is geen verbetering van de CH$_4$ productie gemeten.Voor het eerst zijn dichtheidbepalingen van rookgas succesvol uitgevoerd. Deze bepalingen tonen een grote gelijkenis met de dichtheid van puur N$_2$.

Een deel van dit proefschrift bestaat uit een verkennend onderzoek naar de afname van porositeit en permeabiliteit als gevolg van zwelling van steenkool. Deze zwelling wordt veroorzaakt door de injectie van CO_2. De afname in permeabiliteit kan in de buurt van de put ernstige injectie-problemen veroorzaken. De mate van zwelling van de steenkool is afhankelijk van de type steenkool en een belangrijke conclusie van het onderzoek is de grote overeenkomst tussen de struktuur van steenkool en die van glazige polymeren. Uit experimenteel onderzoek blijkt dat de uitzonderlijke zwelling, ook wel "excess strain" of "differential swelling" genoemd, wordt veroorzaakt door de absorptie van CO_2. Het syteem is gemodelleerd met behulp van een extended Langmuir formulatie gekoppeld aan een Palmer Mansoori vergelijking voor uniaxiale strain condities. De uitkomsten van het model komen voor een groot deel overen met de experimentele resultaten. De geconstateerde afwijking tussen het model en de experiment wordt mogelijk veroorzaakt door plastificatie van de steenkool.

Abnormale diffusie is waargenomen bij zwelling van bitumineuze steenkool in CO_2. Het effect van plastificatie van steenkool, als gevolg van diffussie processen, is gemodelleerd, waarbij een theorie voor abnormale difusie is geintroduceerd. Deze theorie verklaart het proces in termen van het verschil in de diffusie coëfficienten en viscositeit van geexpandeerde steenkool met de oorspronkelijke steenkool. Deze theorie wordt bevestigd met behulp van de experimentele bepaling van de diffusie coëfficienten en suggereert een abnormaal diffusie-proces. Het model is afgeleid van een welke conservatie wet en gecombineerd met concentratie en stress gradiënten gedreven massa transport. De afleiding van het model gebruikt verder een proportioneel verband tussen stress en de massa flux, een typisch resultaat van uitgebreide niet-evenwicht thermodynamica (extended non-equilibrium thermodynamics). Als resultaat is er een schatting van de parameters voor het CO_2 diffusie model uitgevoerd. De met deze parameters gesimuleerde resultaten tonen een scherp concentratie front, wat overeenkomt met de theorie van Case II diffusion.

Onder reservoir condities zijn doorspoel-experimenten op CH_4-gesatureerde kolenkernen uitgevoerd, waarbij CO_2, N_2 en rookgas zijn gebruikt als geïnjecteerd gas. De CO_2-condities van deze experimenten variëren van subkritisch tot superkritisch. De kernen variëren van droog tot deels water gesatureerd. De stijging in de methaan productie van droge kernen wordt veroorzaakt door de preferente desorptie van methaan in de aanwezigheid van CO_2. De droge experimenten tonen aan dat de hoeveelheid gedesorbeerde CH_4 onder in-situ condities marginaal groter is dan de desorptie van methaan door de reductie van de partiële druk van methaan. In experimenten met water gesatureerde kernen was van productie van aan steenkool gesorbeerde CH_4 nauwelijks sprake. Het water functioneert als een barrière en hindert het uitwisselingsproces de hechtingsplekken ('sites') te blokkeren en/of door de diffusiviteit met (minstens) twee ordes van grootte te verlagen. De experimenten laten duidelijk zien dat op porie-schaal CO_2 beter adsorbeert dan CH_4. Een klasse van poriën was niet beschikbaar voor methaan sorptie, maar wel beschikbaar voor physische sorptie van andere

gassoorten (bij voorkeur CO$_2$), ook al was de kern met CH$_4$ gesatureerd. Doorspoel-experimenten met rookgas resulteren onder vergelijkbare condities in een lagere 'sweep efficiëntie' dan experimenten met CO$_2$. Er is nauwelijks productie van aan steenkool geadsorbeerde methaan. De schoorsteengas experimenten kunnen beschouwd worden als N$_2$ 'stripping' experimenten. Een numeriek model van een enkele cleat is ontwikkeld om de fysische processen te begrijpen. De resultaten van het numerieke model geven duidelijk aan wat de effecten van de vloeistof zijn.

Acknowledgements

A very challenging and dynamic four years of research has resulted in this dissertation. Little less than five years ago, I took a daring decision to quit one of the prized jobs in India and venture into the world of Enhanced Coalbed Methane better known as ECBM. Believe me I never repented in taking that decision. My period of stay in Delft took me beyond the realms of my research and sharpened many a facet of my professional and personal self. This would have not been possible without the influence of those wonderful people, whom I met during this period of five years. Here is my opportunity to thank you all who have directly or indirectly contributed to this piece of work.

Firstly I want to express my gratitude towards my supervisors, Karl Heinz Wolf and Hans Bruining and my promoter Cor van Kruijsdijk. Thanks a lot for accepting me as a PhD student at the Faculty of Geotechnology. This research program was sponsored by NWO / SenterNovem. I extend my heartiest thanks to Harry Schreurs for providing the necessary support. This work was also funded by the EU funded CO_2 sequestration project "RECOPOL" and the Dutch "CATO" programme. This opportunity gave me the much desired possibilities to work on conceptual design, modeling and complex experiments under true reservoir conditions. I must admit that Karl Heinz scared me a bit during the lab tour that he gave me on my first trip to The Netherlands. Thank you very much for fostering and stimulating my interests in experimental work and to think about simplifying complex issues in reservoir engineering. Karl Heinz, thank you for the flexibility and freedom you provided me in this research program that allowed me to approach the outstanding research issues from different perspectives. Those Monday morning meetings to discuss and flush experimental bottlenecks were immensely helpful. Hans, my modeling guru, I had a great time with you over these years in Delft. Thank you for your guidance and effort in solving those complex modeling issues. Special regards to those tiring, though fruitful late evening sessions at Hans's place. Although nightmarish at times, but the warmth and the inspiring technical discussions did make me attend those sessions quite regularly.

The Dietz Lab and the High Pressure Lab, is where I spent most of my time, as the experimental facilities were located here. Let me begin, with thanking all the technical staff: Henk van Asten, Leo Vogt, Rudy Ephraim, Andre Hoving, Paul Vermeulen, Jan Etienne, Gerard Mathu, Peter de Vreede, Gerard Sigon and Karel Heller. My special thanks to Henk van Asten, Leo Vogt and Rudy Ephraim. While Henk worked tirelessly to see all my experiments run for months together, Leo did all the hard work in bringing those conceptual designs to reality. Rudy was instrumental in getting me through, with one of the most difficult piece of work on cleat attributes. His image analysis skills were exceptional. I commend Rudy's wonderful

hospitality in making brilliant coffee, which surely provided the necessary thrust to carry out those thoughtful discussions.

Another important group were the students and fellow researchers who played a core role in contributing towards different aspects of this work. Patrick, Nikolai, Willem, Koen, Amit, Nicolas and Inge, thank you all. Patrick, you came to grips with the sorption experiments and I'm glad that your work has found its way into my thesis. Willem Jan, it was great working with you as you got yourself so dynamically involved in unraveling the capillary pressure and wettability behavior of coal-CO_2-water under high pressures.

As for the spirit of Dietz lab, we had an interesting mix of folks from different parts of the globe. Firas, Quoc, Talal, Renato, Koen, Rouhi, Nikolai, Tristan and Mohammed are just a few of them. My life outside India wouldn't have been as exciting, adventurous and happening if it weren't for the many 'gezellige borrels', BBQ, squashing, lunch meets, spare rib meets and many other social events that were always running through Dietz Lab. I would also like to thank all academic staff, other fellow PhD students, and MSc. students.

I'd also like to thank our industrial partner Shell, who financially supported various modules of this research. Over the period of this research, my cooperation with various universities and research organizations like Aachen, Imperial College, University of Southern Illinois, TNO, University of Utrecht, University of Leiden, IFP, CSIRO and ARI have been of immense importance.

A big "Shukriya" to all the Indian folks in Delft and in The Netherlands who provided me a home away from home. Be it getting together for the DIYA parties or for the Diwali, Ganeshotsav get-togethers, or for the weekend Bollywood movie shows, I had a great time with you guys – Premendra, Vikas, Anand, Vikas Kumar, Diganta, Sachin, other TUDIndians and the inmates of Gildestraat. Thanks also to my squash-mates, Patrick, Camilo, Abhilash, Bert Rik, Leo and Karel, for providing me the necessary break from work.

Thank you all.

About the Author

Saikat Mazumder was born on February 6, 1973 in Durgapur (West Bengal), India. After finishing his high school studies (1990) from St. Xavier's School, Durgapur, he joined DAV Model School, Durgapur to pursue his higher secondary school in science. On completion of this in 1992, he began an undergraduate study in Geology at Durgapur Government College, University of Burdwan. As part of this study, he did extensive geological field work in different depositional and structural settings of India.

In 1996 he graduated from the University of Burdwan as a Bachelor in Science and went on to Indian School of Mines to pursue a three year postgraduate study in the field of Applied Geology. As part of this program he did his Masters' thesis on coal cleat development and its effect on Coalbed Methane (CBM) production.

Thereafter in the year 1999 he joined Oil and Natural Gas Corporation Ltd. (ONGC), India as a Production Geologist to work in drilling and production testing of primary Coalbed Methane wells. During his three years at ONGC he worked extensively on gas content determination of coal, sorption-diffusion experiments, mechanics of triple-porosity/dual-permeability coal reservoirs, well test analysis (pre fracturing and pressure build-up), production forecasting using probabilistic models and on complete seam level geological representation of coal.

Then he joined Delft University of Technology to pursue a PhD program in the field of Enhanced Recovery of Coalbed Methane (ECBM). He worked on high pressure experiments and modeling to understand the dynamics of CO_2 in coal, the major part of which is presented in this thesis. The research results have been published (accepted) in various international journals and presented at various refereed conferences in the field of CBM and ECBM.

He is currently working as a technical leader for global coalbed methane aspirations of Shell Exploration and Production.